# ESTIMATING THE NEUTRON BACKGROUND TOWARD THE MEASUREMENT OF NEUTRINO MIXING ANGLE $\theta_{13}$ WITH THE DOUBLE CHOOZ DETECTOR.

by

DEEPAK SHRESTHA

B.Sc., Tribhuvan University, Kathmandu, 1997
M.Sc., Tribhuvan University, Kathmandu, 2000

---

AN ABSTRACT OF A DISSERTATION

submitted in partial fulfillment of the
requirements for the degree

DOCTOR OF PHILOSOPHY

Department of Physics
College of Arts and Sciences

KANSAS STATE UNIVERSITY
Manhattan, Kansas
2013

# Abstract

Double Chooz is a reactor neutrino experiment which has shown evidence of electron anti-neutrino disappearance at 1 km distance. It has been able to exclude the no-oscillation hypothesis at 99.8% CL ($2.9\sigma$) with only one detector. From a rate plus spectral shape analysis, the value of $\sin^2 2\theta_{13}$ was found to be $0.109 \pm 0.030(\text{stat}) \pm 0.025(\text{syst})$. Correlated events mimicking an anti-neutrino event are one of the most important backgrounds for a reactor neutrino experiment like Double Chooz which measured the neutrino mixing angle $\theta_{13}$. Cosmic muons passing through the rock surrounding the detector produce fast neutrons which give rise to correlated events through proton recoil followed by a neutron capture. Muons stopping around the chimney region subsequently decay into Michel electrons also contributing to the correlated background. Measurement of the shape and rate of this background is very important for the precise measurement of $\theta_{13}$. Experimental techniques to estimate of the shape and rate of this background in the Double Chooz far detector are presented in this thesis.

# ESTIMATING THE NEUTRON BACKGROUND TOWARD THE MEASUREMENT OF NEUTRINO MIXING ANGLE $\theta_{13}$ WITH THE DOUBLE CHOOZ DETECTOR.

by

DEEPAK SHRESTHA

B.Sc., Tribhuvan University, Kathmandu, 1997
M.Sc., Tribhuvan University, Kathmandu, 2000

---

A DISSERTATION

submitted in partial fulfillment of the
requirements for the degree

DOCTOR OF PHILOSOPHY

Department of Physics
College of Arts and Sciences

KANSAS STATE UNIVERSITY
Manhattan, Kansas
2013

Approved by:

Major Professor
Prof. Dr. Glenn Horton-Smith

# Copyright

# Abstract

Double Chooz is a reactor neutrino experiment which has shown evidence of electron anti-neutrino disappearance at 1 km distance. It has been able to exclude the no-oscillation hypothesis at 99.8% CL ($2.9\sigma$) with only one detector. From a rate plus spectral shape analysis, the value of $\sin^2 2\theta_{13}$ was found to be $0.109 \pm 0.030(\text{stat}) \pm 0.025(\text{syst})$. Correlated events mimicking an anti-neutrino event are one of the most important backgrounds for a reactor neutrino experiment like Double Chooz which measured the neutrino mixing angle $\theta_{13}$. Cosmic muons passing through the rock surrounding the detector produce fast neutrons which give rise to correlated events through proton recoil followed by a neutron capture. Muons stopping around the chimney region subsequently decay into Michel electrons also contributing to the correlated background. Measurement of the shape and rate of this background is very important for the precise measurement of $\theta_{13}$. Experimental techniques to estimate of the shape and rate of this background in the Double Chooz far detector are presented in this thesis.

# Table of Contents

# List of Figures

# List of Tables

# Acknowledgments

I feel very proud to have been involved in a pioneering experiment like Double Chooz. I would like to thank my advisor Prof. Dr. Glenn Horton-Smith for giving me the opportunity. I can never thank Dr. Horton-Smith, or just "Glenn" to all of us, enough for being so patient with me while I was going up the learning curve. In addition to being a great mentor for all these years, I have learnt equally from him as an extremely kind and family loving person.

I want to thank Dr. David McKee for all those conversations and discussions in his office, often initiated by my naive questions. He, along with his wife Melissa, are two of the nicest people I have ever met. I would like to thank Dr. Lindley Winslow and Dr. Alessandra Tonazzo for all their guidance during my learning period. My stay and learning at APC, Paris would not have been so smooth had it not been for the constant support of Dr. Tonazzo along with Dr. Jaime Dawson. I must thank Dr. Jerome Busenitz and Dr. Zelimir Djurcic for all the useful suggestions during the analysis. I have always been inspired by two of my colleagues, Dr. Igor Ostrovskiy and Dr. Kazuhiro Terao, along with whom I was a member of the so called "Neutron Gang", for all those phone meetings and discussions over a beer. I want to thank Dr. Kyohei Nakajima for the useful discussion during the analysis.

My parents, who have sacrificed so much to let me achieve what I wanted in life, are my biggest source of inspiration. I would not have made it to this day if it were not for their constant encouragement even while they were struggling with various aspects of life. I would like to thank all the mentors since my childhood who always saw the good in me and worked hard to shape me into an honest individual. Finally I would like to thank my wife Akriti for always putting my career ahead of hers. Her confidence and poise have been a constant source of strength for me.

# Dedication

To my mom and dad.

# Chapter 1

# Neutrino in the Standard Model

This chapter will attempt to take the reader through the introduction of neutrinos in the Standard Model (SM) of particles, explain neutrino oscillations and establish the importance of measuring the neutrino mixing angle $\theta_{13}$. The experimentally observed behaviors of most particles are described by the so called Standard Model (SM). The SM is a theory of interacting fields, including the electromagnetic, weak and strong interactions between the particles. It is a quantum field theory of quarks and leptons which is based on the special theory of relativity and quantum mechanics. Neutrinos are the second most abundant particles in the universe after photons according to the standard model of Big Bang cosmological model [14] with approximately 340 neutrinos per cubic centimeter on average in the universe. In the SM the neutrinos are massless, electrically neutral spin $\frac{1}{2}$ leptons accompanying the charged leptons in the decay of W-Bosons. For example, in the decay of the W-particle, as shown below

$$W^+ \rightarrow l_\alpha^+ + \nu_\alpha, \tag{1.1}$$

The neutrino, $\nu_\alpha$, emitted together with the charged lepton $l_\alpha$, where $\alpha = e$, $\mu$ or $\tau$, is called a neutrino of "flavor" $\alpha$. Hence the "state" of a flavor neutrino $\nu_\alpha$ can be defined as the state which describes a neutrino detected in a charged current weak interaction process with a charged lepton $l_\alpha$ in the final state. However, recent discoveries have shown that neutrinos have non-zero masses and that they show leptonic mixing which means that these flavor states $\nu_\alpha$ are not states of definite masses. In reality, the process shown in (1.1) produces

a quantum-mechanical superposition of mass-states $\nu_j$ each time, which could be any of a spectrum of the "mass" states $\nu_j, j = 1, 2, \ldots$ . If $U^*_{\alpha j}$ is the amplitude for the production of a given $\nu_j$, the neutrino flavor state corresponding to the lepton of given flavor $\alpha$ is given by

$$|\nu_\alpha\rangle = \sum_{j=1}^{3} U^*_{\alpha j} |\nu_j\rangle. \tag{1.2}$$

Here the quantities $U_{\alpha i}$ form the elements of the neutrino mixing matrix called the "PMNS" matrix as discussed in Section 1.1.1. The PMNS matrix is unitary which ensures that the flavor states are orthogonal and normalized and each of them have a distinct energy and momentum, so that a neutrino of a given "flavor" state is associated with a lepton of the same "flavor" via W-exchange. The "mass" states are the eigenstates of the Hamiltonian, a Hermitian operator, which makes them orthogonal to each other also. Since there are 3 such neutrino flavor states, corresponding to the 3 leptons, one can form 3 orthogonal linear combinations out of them representing 3 orthogonal neutrino mass states $\nu_j$ of definite masses,

$$|\nu_j\rangle = \sum_{\alpha=1}^{3} U^*_{\alpha j} |\nu_\alpha\rangle, \tag{1.3}$$

obtained by inverting Eq. (1.2). The possibility of the existence of more than three neutrino mass eigenstates will be discussed in Section 1.7.3.

## 1.1 Neutrino Oscillations

The term "neutrino oscillation" means the change in flavor of a neutrino in its flight from the source to the detector [50]. A neutrino of a given flavor ($\nu_\alpha$) produced along with a corresponding lepton ($l_\alpha$), upon interaction in a detector after travelling a distance, might produce a lepton of different flavor ($l_\beta$) with $\alpha \neq \beta$. This means that, during the course of its journey the neutrino has transformed from $\nu_\alpha$ to $\nu_\beta$.

To establish the theory of "neutrino oscillations" the fact that must be take into account is that the neutrino "mass" states of Eq. 1.3 evolve with time as plane waves. The Schrödinger time-dependent equation describing the propagation of these mass states is

$$\frac{\partial}{\partial t}|\nu_j(t)\rangle = H_v|\nu_j(t)\rangle, \tag{1.4}$$

For the energy eigen-states $E_j$ of the vacuum Hamiltonian $H_v$, the solution of Eq. (1.4) is

$$|\nu_j(t)\rangle = e^{-iE_jt}|\nu_j\rangle. \tag{1.5}$$

So from Eq. (1.2) the time evolution of a flavor state can be written as

$$|\nu_\alpha\rangle = \sum_{j=1}^{3} U_{\alpha j} e^{-iE_jt}|\nu_j\rangle, \tag{1.6}$$

which after using Eq. (1.3) becomes

$$|\nu_\alpha\rangle = \sum_{\beta=1}^{3}\sum_{j=1}^{3} U_{\beta j} e^{-iE_jt}|\nu_\beta\rangle. \tag{1.7}$$

The transition probability of the neutrino flavor "$\alpha$" into "$\beta$" is given by,

$$P_{\nu_\alpha\to\nu_\beta} = \left|\langle|\nu_\beta|\nu_\alpha\rangle\right|^2 = \left|\sum_{j=1}^{3} U_{\alpha j}U^*_{\beta j}e^{-iE_jt}\right|^2. \tag{1.8}$$

Expanding Eq. (1.8) and separating the real and imaginary parts, the general transition probability becomes

$$\begin{aligned} P_{\nu_\alpha\to\nu_\beta} = \delta_{\alpha\beta} &- 4\sum_{i>j}\Re(U_{\alpha i}U^*_{\beta i}U_{\alpha j}U^*_{\beta j})\sin^2\left(\frac{\Delta m^2_{ij}L}{4E}\right) \\ &+ 2\sum_{i>j}\Im(U_{\alpha i}U^*_{\beta i}U_{\alpha j}U^*_{\beta j})\sin^2\left(\frac{\Delta m^2_{ij}L}{2E}\right) \end{aligned} \tag{1.9}$$

### 1.1.1 Two-flavor Oscillations

The Oscillation between any two flavors $\alpha$ and $\beta$ with mass states 1 and 2 can be viewed as a 2-dimensional rotation

$$\begin{pmatrix} \nu_\alpha \\ \nu_\beta \end{pmatrix} = \begin{pmatrix} \cos\theta_{jk} & \sin\theta_{jk} \\ -\sin\theta_{jk} & \cos\theta_{jk} \end{pmatrix} \begin{pmatrix} \nu_j \\ \nu_k \end{pmatrix}. \tag{1.10}$$

Here the matrix

$$U = \begin{pmatrix} \cos\theta_{jk} & \sin\theta_{jk} \\ -\sin\theta_{jk} & \cos\theta_{jk} \end{pmatrix}$$

is the "rotation" or "mixing" matrix called the PMNS matrix as in Fig. 1.1.

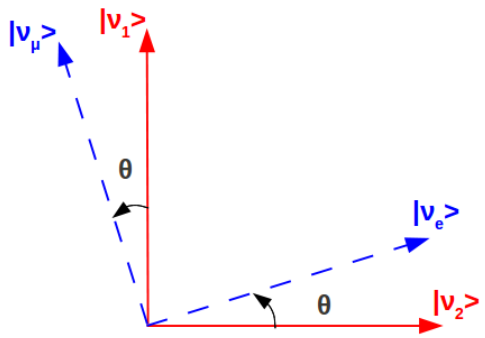


Figure 1.1: 2-flavor neutrino oscillation.

Use Eq. (1.9), for the two neutrino case we get

$$P_{\nu_\alpha \to \nu_\beta} = \sin^2\theta \cos^2\theta \left| e^{-iE_1 t} - e^{-iE_2 t} \right|^2 \tag{1.11}$$

where $\theta_i = \theta_{12}$ is the mixing angle.

Since the neutrinos are relativistic and travel at close to the speed of light, one can approximate $E^2 = p^2 + m^2$, by $E \approx p + \frac{m^2}{2p}$ and also use $t \approx L$ (distance from the source). Using these into Eq. (1.11) results in

$$P_{\nu_\alpha \to \nu_\beta} = \sin^2\theta \cos^2\theta \left(1 - e^{-i\frac{\Delta m^2 L}{2p}}\right)\left(1 - e^{i\frac{\Delta m^2 L}{2p}}\right) = \sin^2 2\theta \sin^2\left(\Delta m^2 \frac{L}{4E}\right) \tag{1.12}$$

where $\Delta m^2$ is the difference between the squared masses of the states: $\Delta m^2 = \Delta m_1^2 - \Delta m_2^2$. See Fig. 1.2 for illustration example.

Re-introducing the $\hbar$'s and c's give for the survival probability for a neutrino flavor $\alpha$ of energy $E$ after travelling a distance $L$

$$P_{\nu_\alpha \to \nu_\alpha} = 1 - \sin^2 2\theta \sin^2 \left( \frac{\Delta m^2 c^4}{4\hbar c} \frac{L}{E} \right), \tag{1.13}$$

which in more useful units is

$$P_{\nu_\alpha \to \nu_\alpha} = 1 - \sin^2 2\theta \sin^2 \left( 1.27 \Delta m^2 \frac{L(m)}{E(MeV)} \right) \tag{1.14}$$

This implies that for neutrino oscillations to happen $\Delta m^2 = -\Delta m_1^2 - \Delta m_2^2 ! = 0$ so at least one of the two states must have mass or in other words neutrinos must be massive.

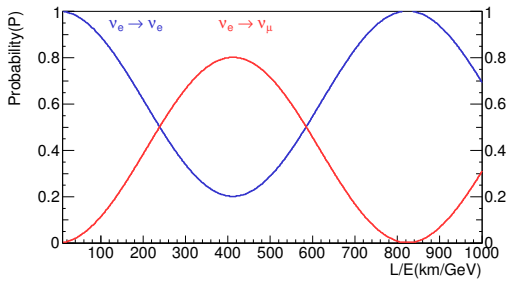


Figure 1.2: Example of 2-Flavor neutrino oscillation between $\nu_e$ and $\nu_\mu$

### 1.1.2 Three-flavor Oscillations

Two flavor neutrino oscillations described in the previous section can be extended to a more general oscillation between all three flavors of neutrinos by introducing the Dirac CP-violating phase $\delta$ in the form

$$D = \begin{pmatrix} 1 & 0 & 0 \\ 0 & 1 & 0 \\ 0 & 0 & e^{i\delta} \end{pmatrix}. \tag{1.15}$$

The three flavor neutrino mixing matrix is then

$$U = \begin{pmatrix} 1 & 0 & 0 \\ 0 & c_{23} & s_{23} \\ 0 & -s_{23} & c_{23} \end{pmatrix} D \begin{pmatrix} c_{13} & 0 & s_{13} \\ 0 & 1 & 0 \\ -s_{13} & 0 & c_{13} \end{pmatrix} D^\dagger \begin{pmatrix} c_{12} & s_{12} & 0 \\ -s_{12} & c_{12} & 0 \\ 0 & 0 & 1 \end{pmatrix} \tag{1.16}$$

$$= \begin{pmatrix} c_{12}c_{13} & s_{12}c_{13} & s_{13}e^{-i\delta} \\ -s_{12}c_{23} - s_{13}s_{23}c_{12}e^{i\delta} & c_{12}c_{23} - s_{12}s_{13}s_{23}e^{i\delta} & s_{23}c_{13} \\ s_{12}s_{23} - s_{13}c_{12}c_{23}e^{i\delta} & -s_{23}c_{12} - s_{12}s_{13}c_{23}e^{i\delta} & c_{13}c_{23} \end{pmatrix} \tag{1.17}$$

where $c_{ij} = \cos_{ij}$ and $s_{ij} = \sin_{ij}$. The oscillation between all three flavors can be written as

$$\begin{pmatrix} \nu_e \\ \nu_\mu \\ \nu_\tau \end{pmatrix} = \begin{pmatrix} U_{e1} & U_{e2} & U_{e3} \\ U_{\mu 1} & U_{\mu 2} & U_{\mu 3} \\ U_{\tau 1} & U_{\tau 2} & U_{\tau 3} \end{pmatrix} \begin{pmatrix} \nu_1 \\ \nu_2 \\ \nu_3 \end{pmatrix}, \tag{1.18}$$

where the mixing matrix is

$$\begin{pmatrix} U_{e1} & U_{e2} & U_{e3} \\ U_{\mu 1} & U_{\mu 2} & U_{\mu 3} \\ U_{\tau 1} & U_{\tau 2} & U_{\tau 3} \end{pmatrix} = \begin{pmatrix} c_{12}c_{13} & s_{12}c_{13} & s_{13}e^{-i\delta} \\ -s_{12}c_{23} - s_{13}s_{23}c_{12}e^{i\delta} & c_{12}c_{23} - s_{12}s_{13}s_{23}e^{i\delta} & s_{23}c_{13} \\ s_{12}s_{23} - s_{13}c_{12}c_{23}e^{i\delta} & -s_{23}c_{12} - s_{12}s_{13}c_{23}e^{i\delta} & c_{13}c_{23} \end{pmatrix} \tag{1.19}$$

See Fig. 1.3.

For the special case of $\nu_e \to \nu_e$, the survival probability is

$$\begin{aligned} P_{\nu_e \to \nu_e} = 1 &- 4|U_{e1}|^2|U_{e2}|^2 \sin^2\left(1.27\frac{\Delta m^2_{21}L}{E}\right) \\ &- 4|U_{e1}|^2|U_{e3}|^2 \sin^2\left(1.27\frac{\Delta m^2_{31}L}{E}\right) \\ &- 4|U_{e2}|^2|U_{e3}|^2 \sin^2\left(1.27\frac{\Delta m^2_{32}L}{E}\right), \end{aligned} \tag{1.20}$$

which, using Eq. (1.19), becomes

$$\begin{aligned} P_{\nu_e \to \nu_e} = 1 &- \cos^4\theta_{13}\sin^2 2\theta_{12}\sin^2\left(1.27\frac{\Delta m^2_{21}L}{E}\right) \\ &- \cos^2\theta_{12}\sin^2 2\theta_{13}\sin^2\left(1.27\frac{\Delta m^2_{31}L}{E}\right) \\ &- \sin^2\theta_{12}\sin^2 2\theta_{13}\sin^2\left(1.27\frac{\Delta m^2_{32}L}{E}\right). \end{aligned} \tag{1.21}$$

The three flavor oscillation with contributions from all three mixing angles will be described in the Reactor Neutrino Experiments Section 1.4.

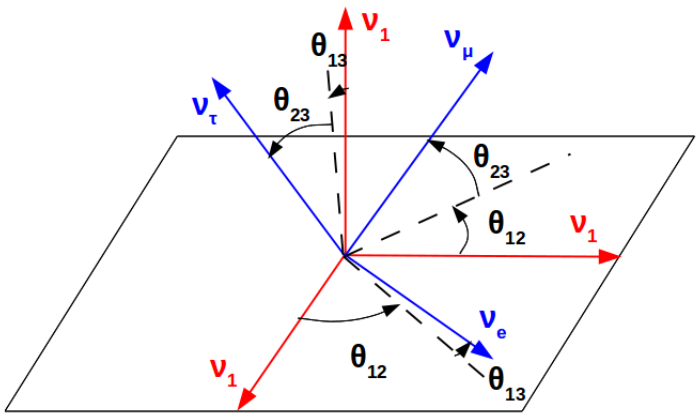


Figure 1.3: 3-flavor neutrino oscillation as 3-D rotation. [2]

## 1.2 Matter Effect

The general neutrino oscillation case was discussed in the previous section. In general, however, the neutrinos travel in a medium, of albeit low but non zero density, which slightly complicates the situation. In this case neutrinos acquire an extra interaction potential energy due to Charge Cuirrent (CC) and/or Neutral Current (NC) interactions with the atomic electrons or with the nucleons in the nucleus of the matter in the medium in which the neutrinos are propagating.

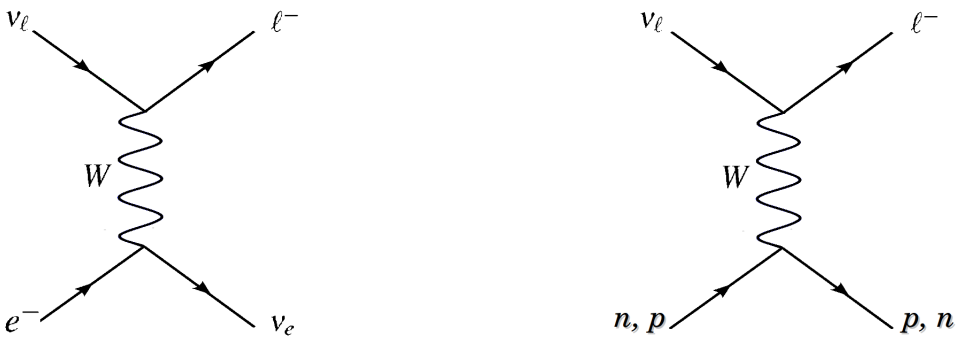


Figure 1.4: Charged current interactions via W-Boson exchange

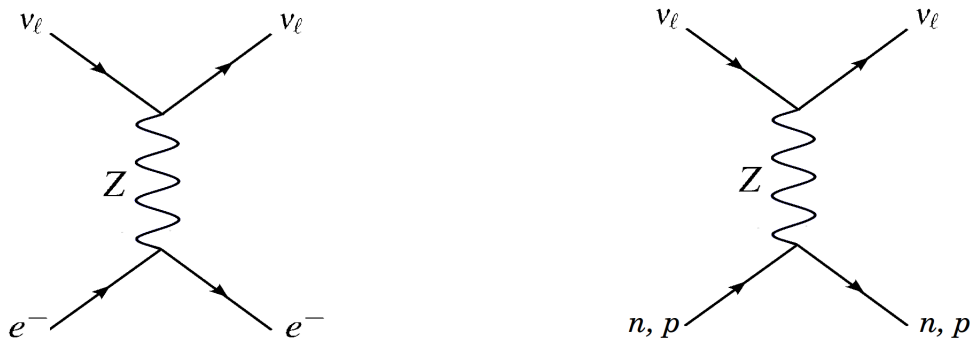


Figure 1.5: Neutral current interactions via Z-Boson exchange

The Hamiltonian in the presence of these interactions in the presence of matter is

$$H_m = H_v + H_I \tag{1.22}$$

The first term, the vacuum Hamiltonian can be written as

$$H_v = \langle \nu_\beta | H_v | \nu_\alpha(t) \rangle = \sum_{j=1}^{3} U_{\alpha j} E_j U^*_{\alpha j} \tag{1.23}$$

### 1.2.1 Two-flavor Case

In the two flavor case, as described in Section 1.1.1, the vacuum Hamiltonian can be written as

$$H_v = \frac{\Delta m^2}{4E} \begin{pmatrix} -\cos 2\theta & \sin 2\theta \\ \sin 2\theta & \cos 2\theta \end{pmatrix} + E \begin{pmatrix} 1 & 0 \\ 0 & 1 \end{pmatrix}. \tag{1.24}$$

The second term in Eq. (1.24) only adds a constant phase to all the neutrino flavors and so does not affect the differences between the eigenvalues of $H_v$. Hence it has no role in the intererence between the flavor states.

The interaction Hamiltonian in Eq. (1.22) is [50],

$$H_I = \begin{pmatrix} V_W & 0 \\ 0 & 0 \end{pmatrix} + \begin{pmatrix} V_Z & 0 \\ 0 & V_Z \end{pmatrix}. \tag{1.25}$$

Here the interaction potential energies, $V_W$ and $V_Z$, gained in the two above processes

for the neutrinos and anti-neutrinos, are

$$\begin{aligned} V_W &= \pm\sqrt{2}G_F N_e, \\ V_Z &= \mp\frac{G_F N_n}{\sqrt{2}}, \end{aligned} \tag{1.26}$$

Where $G_F$ is the Fermi coupling constant and $N_e$ and $N_n$ are the electron and neutron number densities in the medium. In an electrically neutral medium, the NC potentials of the protons and electrons cancel each other.

The interaction potential due to the Z exchange affects all flavors equally, therefore its contribution to $H_m$ is a multiple of the identity matrix and consequently it can be dropped [50] and Eq. (1.25) can be approximated as

$$H_I = \frac{V_W}{2}\begin{pmatrix} 1 & 0 \\ 0 & -1 \end{pmatrix} + \frac{V_W}{2}\begin{pmatrix} 1 & 0 \\ 0 & 1 \end{pmatrix}. \tag{1.27}$$

Here the term due to W exchange has been divided into a term that is not proportional to the identity and a term that is proportional to it. Dropping the latter term as previously, from Eq. (1.24) and Eq. (1.27), the total Hamiltonian in the presence of matter can be written as

$$H_m = \frac{\Delta m^2}{4E}\begin{pmatrix} -\cos 2(\theta - x) & \sin 2\theta \\ \sin 2\theta & \cos 2(\theta - x) \end{pmatrix}, \tag{1.28}$$

where

$$x \approx \frac{V_W/2}{\Delta m^2/4E} = \frac{2\sqrt{2}G_F N_e E}{\Delta m^2}. \tag{1.29}$$

It is interesting to note that the sign of the potential is different for neutrinos and anti-neutrinos, giving rise to a difference in the total potential between them. This creates a false CP violation, but the matter effect is negligible for

$$[\sqrt{2}G_F N_e][\Delta m^2/2E] \ll 1.$$

## 1.3 Significance of $\theta_{13}$

As illustrated in the earlier sections, $\theta_{13}$ is as an important parameter in the global neutrino puzzle as well as in the measurement of CP violation in leptonic sector.

### 1.3.1 CP Violation

One can show that for the conjugate channels $\nu_\alpha \to \nu_\beta$ and $\bar{\nu}_\alpha \to \bar{\nu}_\beta$:

$$P_{\bar{\nu}_\alpha \to \bar{\nu}_\beta}(U) = P_{\nu_\alpha \to \nu_\beta}(U^*) \tag{1.30}$$

Hence the probability for the anti-neutrinos can be obtained by simply replacing the mixing matrix $U$ by its complex conjugate $U^*$. So using Eq. (1.9) results in [50]

$$\begin{aligned} P_{\substack{(-)\\ \nu_\alpha \to \nu_\beta}^{(-)}} = \delta_{\alpha\beta} - 4\sum_{i>j} \Re(U_{\alpha i}U^*_{\beta i}U_{\alpha j}U^*_{\beta j}) \sin^2\left(\frac{\Delta m^2_{ij}L}{4E}\right) \\ \underset{(-)}{+} 2\sum_{i>j} \Im(U_{\alpha i}U^*_{\beta i}U_{\alpha j}U^*_{\beta j}) \sin\left(\frac{\Delta m^2_{ij}L}{2E}\right). \end{aligned} \tag{1.31}$$

Here the negative sign is for the anti-neutrinos. Eq. (1.31) shows that that if the PMNS matrix $U$ is real then the transition probability for the neutrinos and the anti-neutrinos are the same. On the other hand if $U$ is complex then the two transition probabilities are in general different and a direct measurement of CP violation can be expressed in a parameterization-invariant way by the asymmetry $A^{\alpha\beta}_{CP}$ as:

$$\Delta P^{\alpha\beta}_{CP} = A^{\alpha\beta}_{CP} = P_{\nu_\alpha \to \nu_\beta} - P_{\bar{\nu}_\alpha \to \bar{\nu}_\beta} = 4\sum_{i>j} \Im(U_{\alpha i}U^*_{\beta i}U^*_{\alpha j}U_{\beta j}) \sin\left(\frac{\Delta m^2_{ij}}{2E}L\right). \tag{1.32}$$

The quantity

$$J^{ij}_{\alpha\beta} = \Im(U_{\alpha i}U^*_{\beta i}U_{\alpha j}U^*_{\beta j}) = \sin\theta_{12}\cos\theta_{12}\sin\theta_{23}\cos\theta_{23}\sin\theta_{13}\cos^2\theta_{13}\sin\delta_{CP} \tag{1.33}$$

is known as the Jarslkog invariant [46]. From Eq. (1.33), one can get the symmetry relations [1]

$$\begin{aligned} J^{ij}_{\alpha\beta} &= -J^{ji}_{\alpha\beta}, \\ &= -J^{ij}_{\beta\alpha}. \end{aligned} \tag{1.34}$$

Also, using the unitary properties of the $U$ matrix, the following relations can be obtained

$$\begin{aligned}\sum_{i=1}^{3} J^{ij}_{\alpha\beta} &= \delta_{\alpha\beta}\Im(U^*_{\alpha j}U_{\beta j}) = 0 \\ \sum_{\alpha=e,\mu,\tau} J^{ij}_{\alpha\beta} &= \delta_{ij}\Im(U^*_{\alpha j}U_{\beta j}) = 0.\end{aligned} \tag{1.35}$$

Using equations (1.34) and (1.35) give the cyclic relation

$$J^{21}_{\alpha\beta} = J^{13}_{\alpha\beta} = J^{32}_{\alpha\beta} \tag{1.36}$$

as well as the cyclic relation

$$J^{ij}_{e\mu} = J^{ij}_{\mu\tau} = J^{ij}_{\tau e} \tag{1.37}$$

Therefore from Eq. (1.36) and (1.37),

$$J^{ij}_{e\mu} = J^{ij}_{\mu\tau} = J^{ij}_{\tau e} = J^{21}_{e\mu}. \tag{1.38}$$

Using Eq. (1.37) in Eq. (1.32) gives,

$$\Delta P^{\alpha\beta}_{CP} = 16 J^{21}_{e\mu}\left(\sin\frac{\Delta m^2_{12}}{2E}L + \sin\frac{\Delta m^2_{23}}{2E}L - \sin\frac{\Delta m^2_{13}}{2E}L\right). \tag{1.39}$$

which after using $\Delta m^2_{13} = \Delta m^2_{12} + \Delta m^2_{23}$ results in the relation;

$$\begin{aligned}\Delta P^{e\mu}_{CP} =& 2\cos\theta_{13}\sin 2\theta_{13}\sin 2\theta_{12}\sin 2\theta_{23}\sin\delta_{CP} \\ &\times \sin\left(\Delta m^2_{31}\frac{L}{4E}\right)\sin\left(\Delta m^2_{32}\frac{L}{4E}\right)\sin\left(\Delta m^2_{21}\frac{L}{4E}\right).\end{aligned} \tag{1.40}$$

Fig. 1.6 shows the difference in the two probabilities calculated in Eq. (1.40). This shows that to have a chance of measuring the CP-violating Dirac phase $\delta$ all the mixing angles must be non-zero. With the mixing angles $\theta_{12} = 34 \pm 1^\circ$ and $\theta_{23} = 40 - 45^\circ$, it becomes all the more important to know whether $\theta_{13}$ is non-zero and there in lies the importance of the Double Chooz experiment.

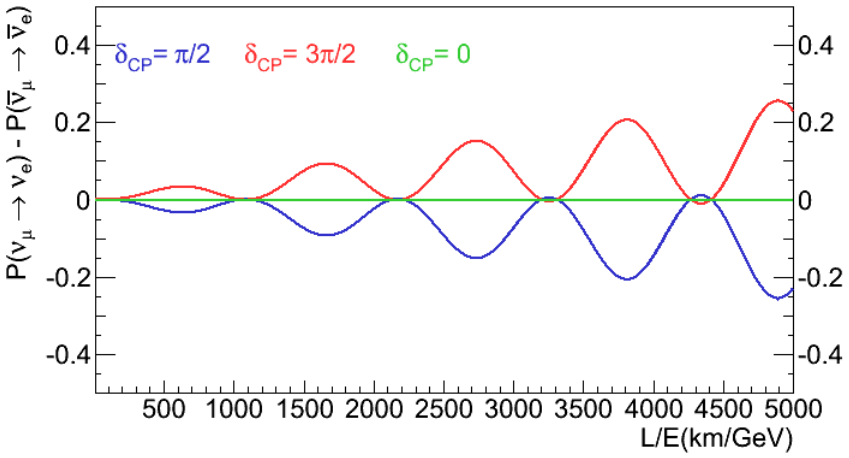


Figure 1.6: An example of a direct measurement of CP violation from $P_{\nu_\alpha \to \nu_\beta} - P_{\bar{\nu}_\alpha \to \bar{\nu}_\beta}$ with a constant $E$ =1GeV.

### 1.3.2 CP Violation in Matter

Eq. (1.28) shows that the presence of matter affects the neutrinos and anti-neutrinos differently, by raising the effective mass of the neutrinos while lowering that for the anti-neutrinos. This is induces a "fake CP violation" in the presence of matter, different from the true "vacuum CP violation". Furthermore this "fake CP violation" is also sensitive to the mass hierarchy of the neutrinos as shown in Fig. 1.7.

The total difference between the CP-conjugate channels $\nu_\mu \to \nu_e$ and $\bar{\nu}_\mu \to \bar{\nu}_e$ in matter is given by [67]

$$P_{\nu_\mu \to \nu_e} - P_{\bar{\nu}_\mu \to \bar{\nu}_e} = P_m s_{23}^2 - \Delta P_{CP}. \tag{1.41}$$

Here $P_m$ is the matter-induced difference between the two quantities given as

$$P_m = (1 - 2s_{13}^2) c_{13}^2 s_{13}^2 \left( \frac{16a}{\Delta m_{31}^2} \sin^2 \frac{\Delta m_{31}^2 L}{4E} - \frac{4aL}{2E} \sin^2 \frac{\Delta m_{31}^2 L}{4E} \right). \tag{1.42}$$

while the true CP-violating part in vacuum $\Delta P_{CP}$ is the same as $P_{CP}^{e\mu}$ in Eq. (1.40).

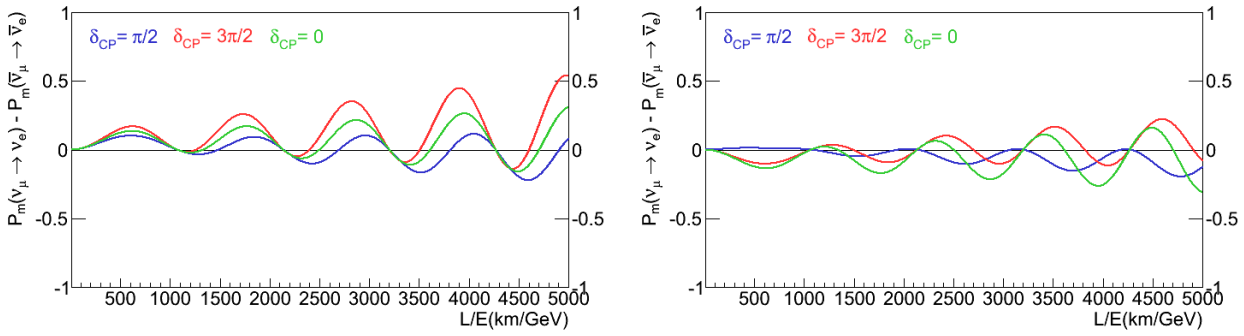


Figure 1.7: An example of a direct measurement of CP violation by $P_{\nu_\alpha \to \nu_\beta} - P_{\bar{\nu}_\alpha \to \bar{\nu}_\beta}$ with a constant $E = 1$GeV in matter of constant density, for the two mass orderings of the neutrinos, the normal (and inverted) hierarchies in left (right) panels.

It must be noted in Fig. 1.7 that the pure effect of the matter can be seen in the green curve for case when the the CP-violating phase $\delta = 0$. Here $a = 2\sqrt{2}G_F n_e E = 1.5 \times 10^{-3}$ eV$^2$ has been calculated for the reference setup of $L = 732$ km and $E = 7$ GeV.

## 1.4 Reactor Neutrino Experiments

In principle $\theta_{13}$ can be measured using a long baseline accelerator experiment as well as a short baseline nuclear reactor experiment. On the one hand, the neutrino oscillation probability in case of a long baseline accelerator experiment depends upon the CP phase $\delta$, the sign of $\Delta m^2_{31}$ as well as the matter effect. The reactor-based short baseline experiments, on the other hand, are free of such ambiguities and provide a unique method of measuring the angle $\theta_{13}$. Since the energy of the neutrinos from the reactor are limited to below 8 MeV (with the peak ocurring at 3 MeV), only the disappearance channel can be probed in such an experiment. Nuclear reactors are copius sources of isotropic low energy electron anti-neutrinos ($\bar{\nu}_e$), primarily below 8 MeV. The $\bar{\nu}_e$ undergo oscillation and their disappearance can be measured with the help of a detector at a distance of the order of 1 km. The detection method for these $\bar{\nu}_e$ is based upon the "Inverse Beta Decay (IBD)" in which an $\theta_{13}$ interacts with a free proton inside the detector to produce a positron and a neutron as shown below:

$$\bar{\nu_e} + p \rightarrow e^+ + n \tag{1.43}$$

The principle of neutrino oscillation and their detection described as illustrated in Fig. 1.8.

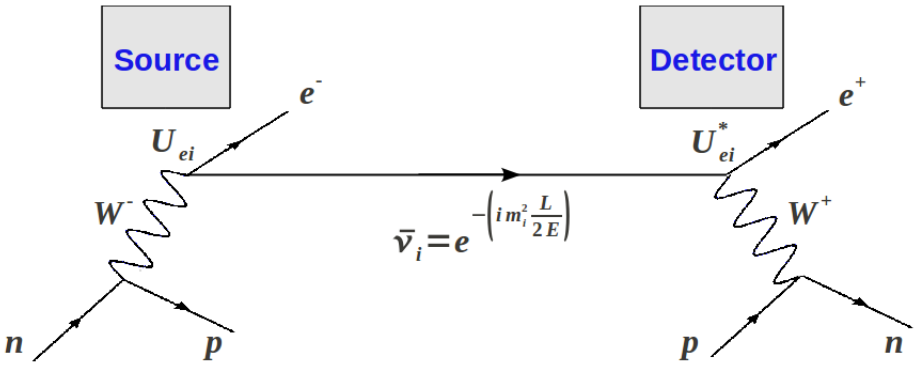


Figure 1.8: Neutrino flavor change in-flight and detection by inverse beta decay at the detector.

From Eq. (1.43) it can be seen that the survival probability of an $\bar{\nu}_e$ depends on their energies. Also the interaction cross section of the anti-neutrinos inside the detector depends upon the energy as [57]

$$\sigma_{V-A}\left(E_e\right) = \kappa p_e E_e (1 + \delta_{\text{rec}} + \delta_{\text{wm}} + \delta_{\text{rad}}). \tag{1.44}$$

Here $\kappa = 2\pi^2/m_5^2 f^R \tau_n$, with $m_e$ being the electron mass, $\tau_n$ the neutron mean lifetime and $f^R$ the phase-space factor for the beta decay of the free neutron. Also $\delta_{rec}$ (recoil), $\delta_{wm}$ (weak magnetism) and $\delta_{rad}$ (radiative) are the various corrections to the positron energy. The positron energy is in turn related to the neutrino energy through

$$E_\nu = E_e + \Delta + \frac{E_e(E_e + \Delta)}{M} + \frac{1}{2}\frac{\Delta^2 - m_e^2}{M}, \tag{1.45}$$

where $M$ is the mass of the nucleon and $\Delta = m_n - m_p$ is the difference of the neutron and proton masses.

From the kinematics of the inverse beta decay, the four momenta for the initial state can be written as: $p_\nu^\mu = (E_\nu, P_\nu)$ and $p_p^\mu = (m_p, 0)$, which results in

$$s_{\text{initial}} = (p_\nu^\mu + p_p^\mu)^2 \approx m_p^2 + 2E_\nu m_p. \tag{1.46}$$

Also, for the final state after neglecting neutron recoil $p_{e^+}^\mu = (m_e, p_e^+)$ and $p_n^\mu = (m_n, 0)$ which gives

$$s_{final} = (p_{e^+}^\mu + p_n^\mu)^2 \approx (m_{e^+} + m_n)^2 \tag{1.47}$$

Hence for the case when the positron is produced with zero momentum, the energy threshold for the reaction is given by

$$E_\nu^{thres} \approx \frac{(m_{e^+} + m_n)^2 - m_p^2}{2m_p} = 1.806\text{MeV} \tag{1.48}$$

The values of the three mixing angles are $\theta_{12} = 34.06^{+1.16}_{-0.84}$ degrees [15], $\theta_{23} \approx 40^\circ$ to $45^\circ$, $\theta_{13} \approx 9^\circ$ [23], while the values of the various mass splittings can be given as $\Delta m_{32}^2 \approx 2.244 \times 10^{-3} eV^2$, $\Delta m_{31}^2 = 2.32^{+0.12}_{-0.08} \times 10^{-3} eV^2$ [32] and $\Delta m_{21}^2 = 7.59^{+0.20}_{-0.21} \times 10^{-5} eV^2$ [15]. With this parameterisation one can safely make an assumption that $\Delta m_{32}^2 \approx \Delta m_{31}^2$. Hence the survival probability for the electron neutrinos can be approximated as [68]

$$\begin{aligned} P_{\nu_e \to \nu_e} = 1 &- 4|U_{e1}|^2|U_{e2}|^2 \sin^2\left(1.27\frac{\Delta m_{21}^2 L}{E}\right) \\ &- 4(|U_{e1}|^2 + U_{e2}|^2)|U_{e3}|^2 \sin^2\left(1.27\frac{\Delta m_{32}^2 L}{E}\right). \end{aligned} \tag{1.49}$$

Using the unitary properties of the $U$ matrix,

$$|U_{e1}|^2 + |U_{e2}|^2 + |U_{e3}|^2 = 1, \tag{1.50}$$

Eq. (1.49) becomes

$$\begin{aligned} P_{\nu_e \to \nu_e} = 1 &- 4|U_{e1}|^2|U_{e2}|^2 \sin^2\left(1.27\frac{\Delta m_{21}^2 L}{E}\right) \\ &- 4(1 - |U_{e3}|^2)|U_{e3}|^2 \sin^2\left(1.27\frac{\Delta m_{32}^2 L}{E}\right), \end{aligned} \tag{1.51}$$

$$P_{\nu_e \to \nu_e} = 1 - \cos^4 \theta_{13} \sin^2 2\theta_{12} \sin^2 \left(1.27 \frac{\Delta m^2_{21} L}{E}\right) - \sin^2 2\theta_{13} \sin^2 \left(1.27 \frac{\Delta m^2_{32} L}{E}\right) \quad (1.52)$$

Furthermore, for a short baseline of $L \approx 1$ km and low energies of order $E \approx 1$ MeV, $\Delta m^2_{21} L/E \approx 0$.

Hence the expression for the survival probability of an electron anti-neutrino is given by

$$P_{\bar{\nu}_e \to \bar{\nu}_e} \approx 1 - \sin^2 2\theta_{13} \sin^2 \left(1.27 \frac{\Delta m^2_{32} L}{E}\right). \quad (1.53)$$

Eq. (1.21) is graphed in Fig. 1.9.

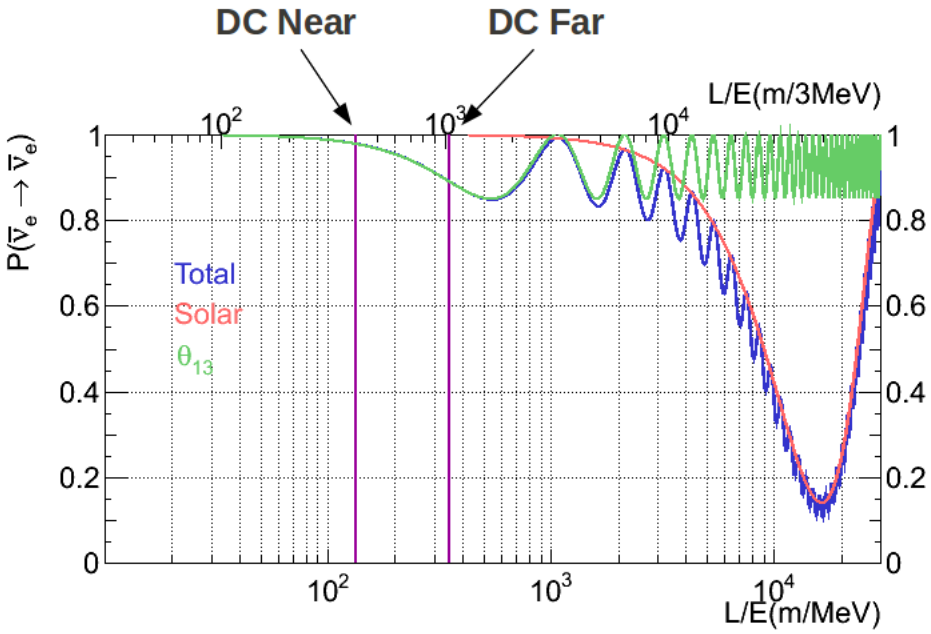


Figure 1.9: Three flavor oscillation for reactor anti-neutrinos with the Double Chooz Far and Near detector positions, shown for $E = 3$ MeV and $\sin^2 2\theta_{13} = 0.15$ (CHOOZ upper limit).

Modern day reactor experiments take advantage of multiple detectors by placing one detector close to the source to maximize the flux and minimize the oscillation while placing the far detector close to the first maximum of the oscillation, as shown in Fig. 1.9. By

comparing the measured fluxes at the two detectors and comparing it to the expected $1/r^2$ fall off, a measurement of $\theta_{13}$ free of reactor-induced uncertainties can be performed.

## 1.5 Accelerator Neutrino Experiments

An accelerator experiment measures the appearance of $\nu_e$ ($\bar{\nu}_e$) in a $\nu_\mu$ ($\bar{\nu}_\mu$) beam of a few GeV energy. The high energy neutrino beams are produced by colliding intense proton beams with fixed targets. We saw earlier that such a transition depends upon the CP-violating phase $\delta$ as well as on the sign of $\Delta m^2_{31}$. Due to the longer distance travelled through earth, matter induced effects can also be significant.

Since accelerator experiments are essentially appearance experiments, they have the advantage of being able to detect electrons from anti-electron neutrino interactions in the detector and measure the $\nu_\mu \to \nu_e$ oscillation without potential ambiguity that might be caused by the posible existence of sterile neutrinos. The formula used to measure $\theta_{13}$ through the appearance channel $\nu_\mu \to \nu_e$ is [2]

$$\begin{aligned} P_{\nu_\mu \to \nu_e} = & \sin^2 2\theta_{13} \sin^2 \theta_{23} \sin^2 \left(1.27 \frac{\Delta m^2_{32} L}{E}\right) - \cos\theta_{13} \sin 2\theta_{12} \sin 2\theta_{23} \sin 2\theta_{13} \sin\delta \\ & \times \sin\left(1.27 \frac{\Delta m^2_{21} L}{E}\right) \sin\left(1.27 \frac{\Delta m^2_{31} L}{E}\right) \sin\left(1.27 \frac{\Delta m^2_{32} L}{E}\right) \\ & + 4 \cos\theta_{13} \sin\theta_{12} \sin 2\theta_{13} \sin\theta_{23} (\cos\theta_{12} \cos\theta_{23} \cos\delta + 4 \sin\theta_{12} \sin\theta_{13} \sin\theta_{23}) \\ & \times \sin\left(1.27 \frac{\Delta m^2_{21} L}{E}\right) \sin\left(1.27 \frac{\Delta m^2_{31} L}{E}\right) \cos\left(1.27 \frac{\Delta m^2_{32} L}{E}\right), \end{aligned} \tag{1.54}$$

which is plotted in Fig. 1.10.

## 1.6 Knowledge about $\Theta_{13}$ Before Double Chooz

Limits on the value of the mixing angle $\theta_{13}$ before Double Chooz came from the reactor experiments CHOOZ and Palo Verde. Lately the T2K experiment, which is an accelerator experiment, also published its result on $\theta_{13}$. The following sections will provide short descriptions of each of these experiments and their results.

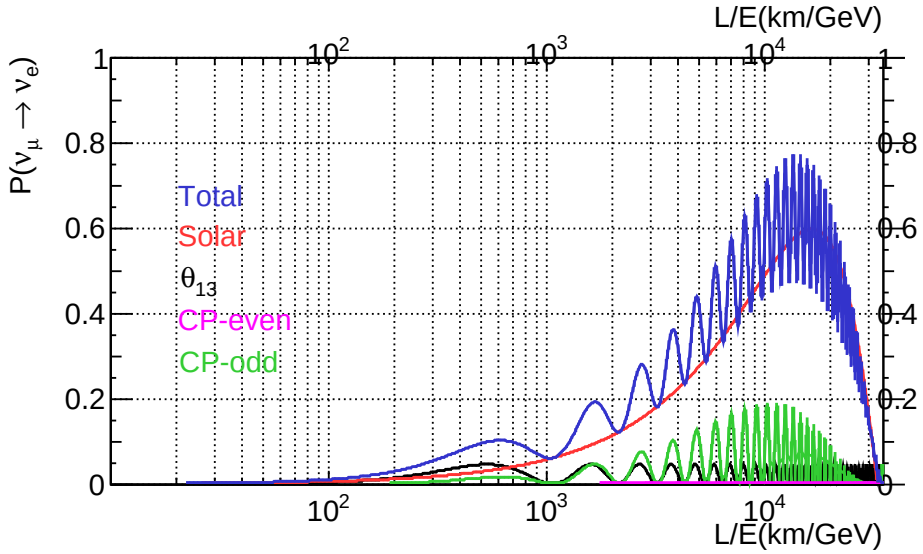


Figure 1.10: Oscillations of 1 GeV neutrinos in the channel $\nu_\mu \to \nu_e$ as given in Eq. (1.54)

### 1.6.1 CHOOZ

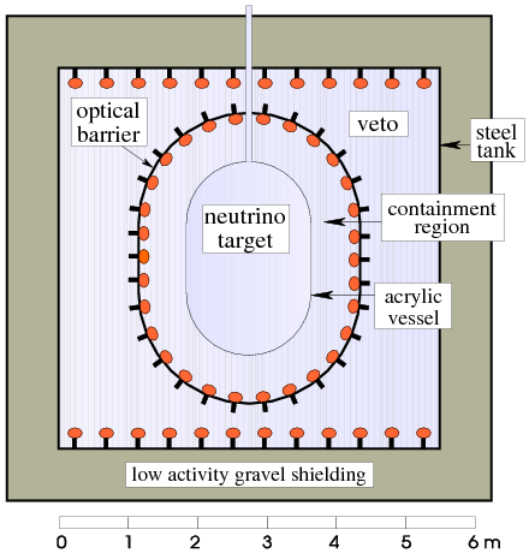


Figure 1.11: CHOOZ detector schematics [23].

Fig. 1.11 shows the CHOOZ detector. The detection principle for the neutrinos was

based on the inverse beta decay reaction described previously. The criteria used for selecting neutrino candidates were:

- Positron energy: $E_e^+ < 8$ MeV.
- Neutron energy: 6 MeV $< \mathrm{E_n} <$ 12 MeV.
- Distance from geode boundary: $d_e^+ > 30$ cm, $d_n^+ > 30$ cm.
- Relative positron-neutron distance: $d_{e^+n} < 100$ cm.
- Neutron delay: $2\mu\mathrm{s} < \mathrm{t_{e^+n}} < 100\mu$ s.
- Neutron multiplicity: $\mathrm{N_n} = 1$.

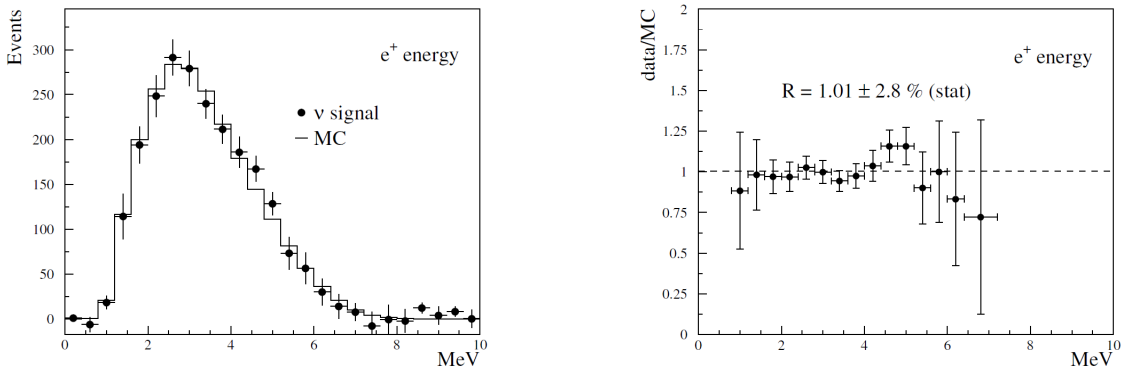


Figure 1.12: Comparison of expected MC positron spectrum in the case of no-oscillation to the measured spectrum [23].

### 1.6.2 Palo Verde

The experiment was built in the Palo Verde Nuclear Generating Station in Arizona and it consisted of three PWR (Pressurized Water Reactor) reactors with a total thermal power of 11.63 GW of thermal power. The detector shown in Fig. 1.13, consisted of Gd-loaded liquid scintillator and the method of neutrino detection was the inverse beta decay. The

event selection criteria required that each prompt($e^+$) delayed($n$) event have at least one hit with energy greater than 1 MeV and two additional hits with energies greater than 30 KeV. Any event with hits greater than 8 MeV were discarded. Further a muon veto of 150$\mu$s and a time lapse of $5\mu s < t_n < 200\mu s$ between any two subevents was required [19].

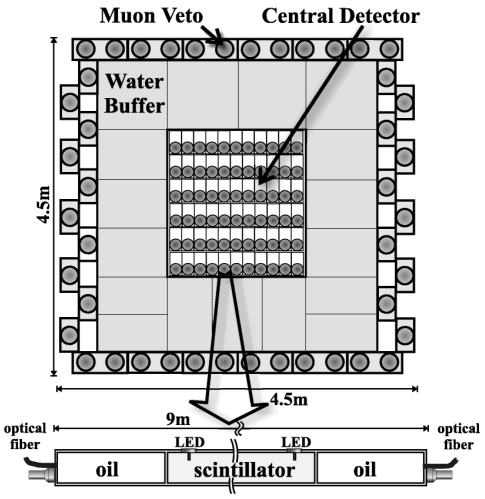


Figure 1.13: Palo Verde detector design

The combined results of CHOOZ, Palo Verde and Kamiokande (a solar neutrino experiment located in Kamioka, Japan) are shown in Fig. 1.14: The best limit for the value of the angle $\theta_{13}$ can be taken from CHOOZ [23] and is

$$\sin^2 2\theta_{13} \leq 0.15 \text{ at } 90\% \text{ CL}, \ \Delta m^2 = 2.5 \times 10^{-3} \text{eV}^2. \tag{1.55}$$

### 1.6.3 T2K

The T2K (Tokai to Kamioka) experiment is a long-baseline (LBL) neutrino experiment in Japan. The T2K experiment sends an intense beam of $\nu_\mu$ from Tokai to Kamioka, at a distance of 295 km as shown in Fig. 1.15. It uses two detectors, the near detector "ND280", and the "Superkamiokande" detector as the far detector. Both the detectors are 2.5° away from the neutrino beam axis. The off-axis positioning provides a narrow range of neutrino

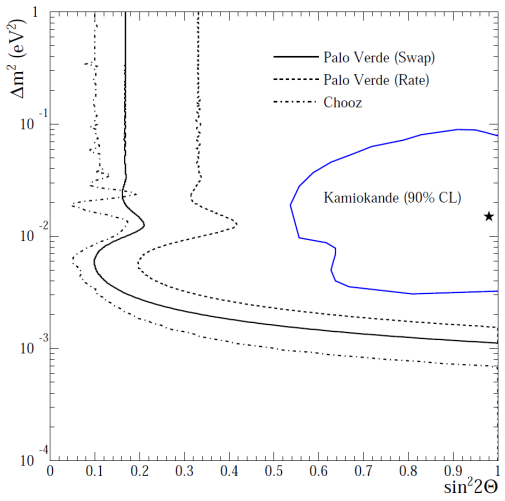


Figure 1.14: Limits on $\theta_{13}$ from CHOOZ, Palo Verde and Kamiokande

energies meaning a higher fraction of neutrinos oscillate by the time they reach the far detector. It also allows for more accurate measurement of the neutrino energy.

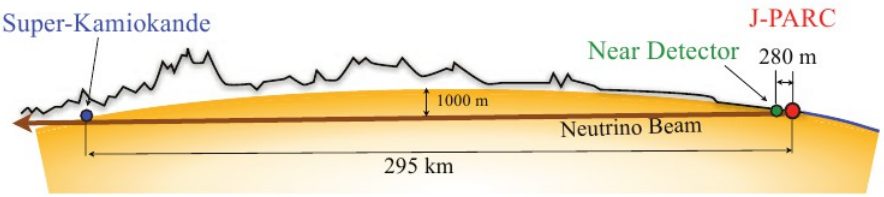


Figure 1.15: T2K experiment schematic [9].

T2K published their first result in 2011 from appearance data in the $\nu_\mu \rightarrow \nu_e$ channel. They found 6 $\nu_e$ events in the beam of $\nu_\mu$ above the 1.5 events expected with no-oscillation hypothesis. The J-PARC Main Ring (MR) accelerator provides the beam of 30 GeV protons which is focused on a graphite target. The on-axis Interactive Neutrino GRID (INGRID) detector monitors the intensity, direction and profile of the neutrino beam. The ND280 near detector measures the $\nu_\mu$'s in the beam before any oscillations occur. Both the INGRID as well as ND280 detectors are 280 m downstream from the target. The Superkamiokande water Cherenkov detector, which is 295 km away from the target at Tokai, acts as the far detector for the T2K experiment.

The largest contribution to the signal comes from the charged-current quasi-elastic interactions (CCQE) due to $\nu_\mu \rightarrow \nu_e$ oscillations while the major source of background is $\nu_e$ contamination in the beam and the misidentified $\pi^0$ from neutral-current (NC) interactions.

The T2K result shows a best fit value for $\theta_{13} = 0.11(0.14)$ for $|\Delta m^2_{32}| = 2.4 \times 10^{-3} eV^2$ for the normal (inverted) hierarchy. Fig. 1.16 shows the global constraint on $\theta_{13}$ before the Double Chooz data.

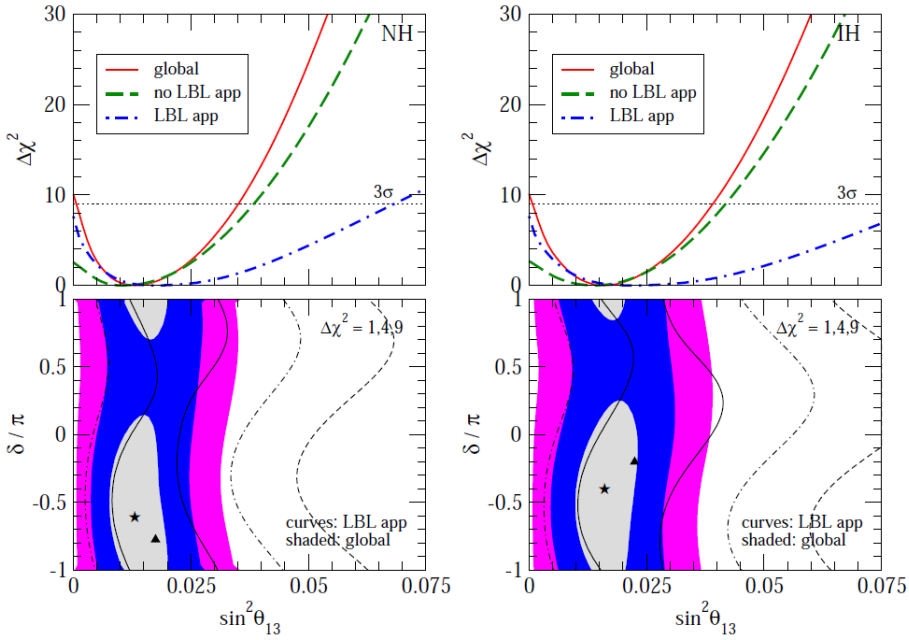


Figure 1.16: Global analysis of $\theta_{13}$ with data both including and excluding T2K+MINOS [65].

## 1.7 Open Questions about Neutrinos

Besides the efforts to measure $\theta_{13}$ there are quite a few other challenges in the field of neutrino physics. A number of these are briefly discussed here.

### 1.7.1 Neutrino Mass Hierarchy

Assuming three neutrino generations, the measured differences of squared masses that have been used in the previous sections do establish the ordering of the masses of the three mass eigenstates. It remains to be established whether the mean mass of the solar doublet $(\nu_1, \nu_2)$ is smaller or larger than the atmospheric neutrino mass state $(\nu_3)$. Depending upon whether the mass of the solar doublet is smaller or larger, their mass ordering is called "normal" or "inverted" respectively. The two possible situations are shown in Fig. 1.23.

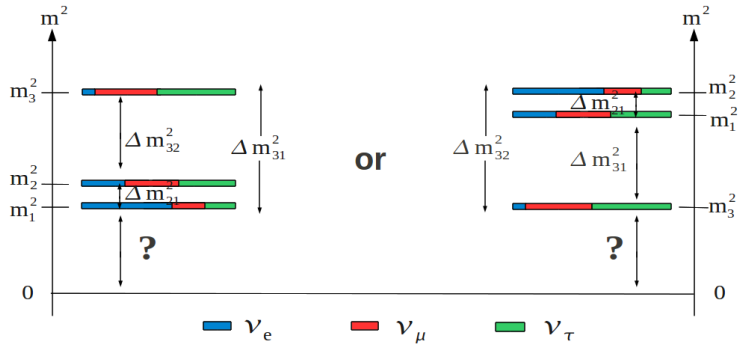


Figure 1.17: Possible neutrino mass orderings: Normal (left) and Inverted (right)

The matter effect raises the effective mass for neutrinos while lowering that for anti-neutrinos see Eq. (1.42) and Fig. 1.18, could be used in a long-baseline accelerator experiment, to differentiate between the oscillation probabilities for the $\nu$'s and the $\bar{\nu}$'s and might be able to experimentally distinguish between the normal and inverted hierarchy.

### 1.7.2 Absolute Neutrino Mass

If neutrinos are massive then in a beta-decay experiment the beta spectrum will be slightly distorted at the end point, see Fig. 1.19. Kinematics of the beta decay reaction tells us that to achieve high resolution at the end point, there must be very low Q-value for the reaction as well as high decay rate (short half-life). This is is achieved by using the decay of Tritium

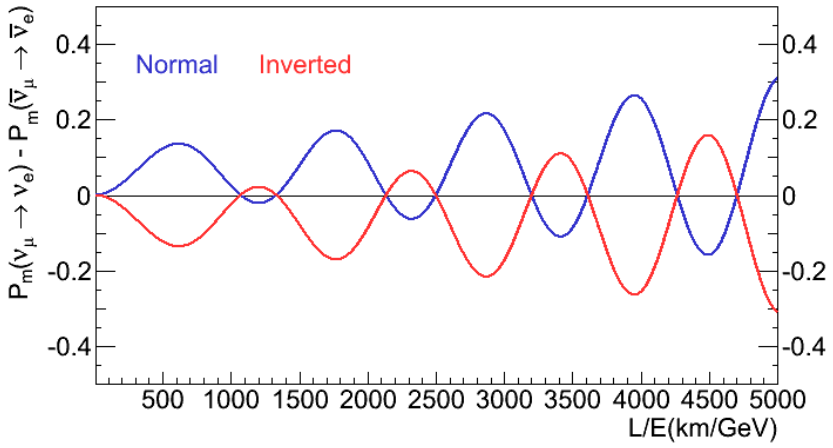


Figure 1.18: Neutrino mass ordering affects the transition probabilities for the neutrinos and the antineutrinos differently in matter with $\delta_{CP} = 0$ from Eq. (1.42).

($^3H$) with a Q-value of 18.6KeV and half-life of 2.3 years. The current best limit on the $\nu_e$ mass is $m_{\nu_e} < 2.3$ eV (90% C.L.) [8].

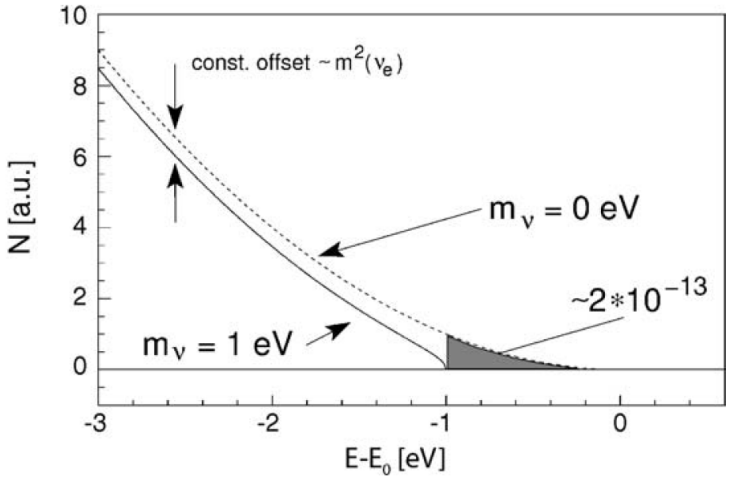


Figure 1.19: Expanded differential rate N(a.u.) of tritium-$\beta$-decay around its endpoint. The difference between the two curves is proportional to $\Delta m^2_{\nu_e}$ [62]

### 1.7.3 Are Neutrinos Their Own Antiparticles?

With the discovery of neutrino oscllation, we definitely know that neutrinos have mass. Also, from the tritium decay end point experiments described in the above section, we have the uppper limit on the electron neutrino mass, $m_{\nu_e} < 2.3$ eV (90% C.L.) [8]. In the Standard Model (SM) of particle physics, the neutrinos are massless. It requires a left handed neutrino $\nu_L$ as well as its right handed charge conjugate $\nu_R$ to construct the Dirac mass term $L_D = m_D \bar{\nu}_L \nu_R$ where $m_D$ is the SM Higgs. The right handed neutrino is not part of the SM, which just has a left handed neutrino field $\nu_L$ and a right handed antineutrino field $\bar{\nu}_R$. Here the Higgs mechanism that gives the neutrinos their masses is the same one that gives all other Fermions their masses. Due to the electrically neutral nature of the neutrinos it is also possible to write down another mass term, from the existing left handed neutrino field $\nu_L$ and its charge conjugate $\nu_L^c$, a left handed mass term $L_M = m_R \bar{\nu_L} \nu_L^c$ in which the mass operator $m_R$ annihilates a left handed neutrino and creates a right handed antineutrino. Such a mass term is called a Majorana mass term. As the neutrino is electrically neutral, the Majorana mass term conserves electric charge but neither conserves the weak isospin symmetry nor the lepton number $L$ defined as

$$L(\nu) = L(l^-) = -L(\bar{\nu}) = -L(l^+) = 1$$

. It can be shown that the existence of a Majorana mass term for neutrinos can result in the neutrinos becoming their own antiparticles.

One can add neutrino mass to the SM by introducing a right handed neutrino field $v_L^c$ into the SM to form a Dirac mass term $m_D \nu_L \nu_L^c$ and a Majorana mass term $\frac{1}{2} M \nu_L^c \nu_L^c$ without violating the local symmetries of the SM. The operator $M$ does not participate in weak interactions and can result in a tiny mass for the left handed neutrinos as observed experimentally. With this formulation the complete mass term in the Lagrangian is

$$L = m_D \nu_L \nu_L^c + \frac{1}{2} M \nu_L^c \nu_L^c, \tag{1.56}$$

and the neutrino mass matrix $M$ can be written as

$$M = \begin{pmatrix} 0 & m_D \\ m_D & M \end{pmatrix}$$

The eigenvalues of the mass matrix $M$ can be interpreted as the masses for a "light" and a "heavy" neutrino with $m_{\nu_{\text{light}}} \approx m_D^2/M$ and $m_{\nu_{\text{heavy}}} \approx M$ for the neutrino fields of $\nu_L$ and $\nu_L^c$ respectively. This mechanism is known as the "See-Saw" mechanism and can explain the large difference between the much lighter neutrino masses and the much heavier masses of the Fermions in terms of the GUT scale. Neutrino oscillations cannot distinguish between Dirac and Majorana neutrinos as they are lepton number conserving processes and further Majorana phases do not appear in the oscillation formula. The only possible way to establish whether the neutrinos are Dirac or Majorana particles is to look for the so-called "Neutrinoless Double Beta Decay ($0\nu 2\beta\beta$)" see Fig. 1.20. The observation of neutrinoless double beta decay would confirm the Majorana nature of the neutrinos as well as the existence of a Majorana mass term for neutrinos.

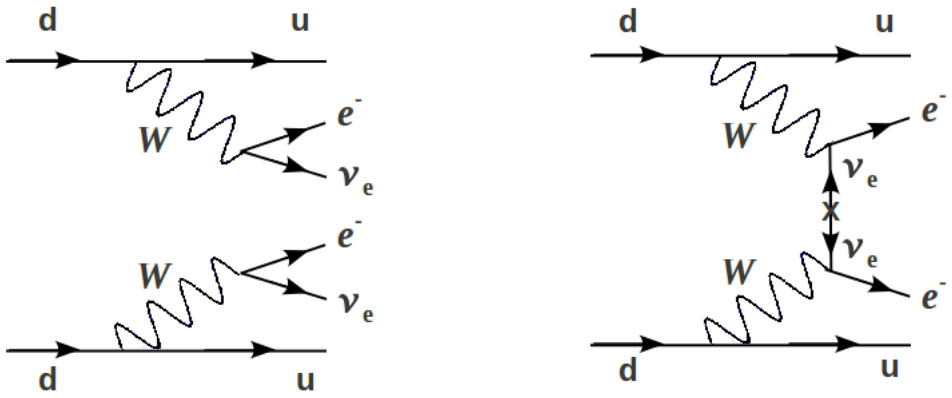


Figure 1.20: Double Beta Decay (left) and Neutrinoless Double Beta Decay (right) [63]

### 1.7.4 Are There More Than Three Generations of Neutrinos ?

Any new species of neutrinos other than the current three mass eigenstates are known as the "Sterile Neutrinos". A sterile neutrino is a neutral lepton which does not interact through

weak interactions, except those induced by neutrino mixing. In this section we will briefly discuss various tentative experminetal hints about the possible existence of sterile neutrinos.

### LSND Result

LSND was an experiment designed to search for $\bar{\nu}_\mu \to \bar{\nu}_e$ oscillation with high sensitivity. In its first result, the experiment reported an excess of $87.9 \pm 22.4 \pm 6.0$ $\bar{\nu}_e$ events at $3.8\sigma$. This excess could be explained with oscillation at a much higher neutrino mass $0.3\text{eV}^2 < \Delta m^2_{\text{LSND}} < 3\text{eV}^2$ from the atmospheric ($\Delta m^2_{\text{atmos}} = 2.5 \times 10^{-3}$) $\text{eV}^2$ and solar ($\Delta m^2_{\text{solar}} = 7 \times 10^{-5}$) $\text{eV}^2$ mass squared differences . The existence of three independent $\Delta m^2$'s hints at the existence of a fourth and much heavier neutrino generation.

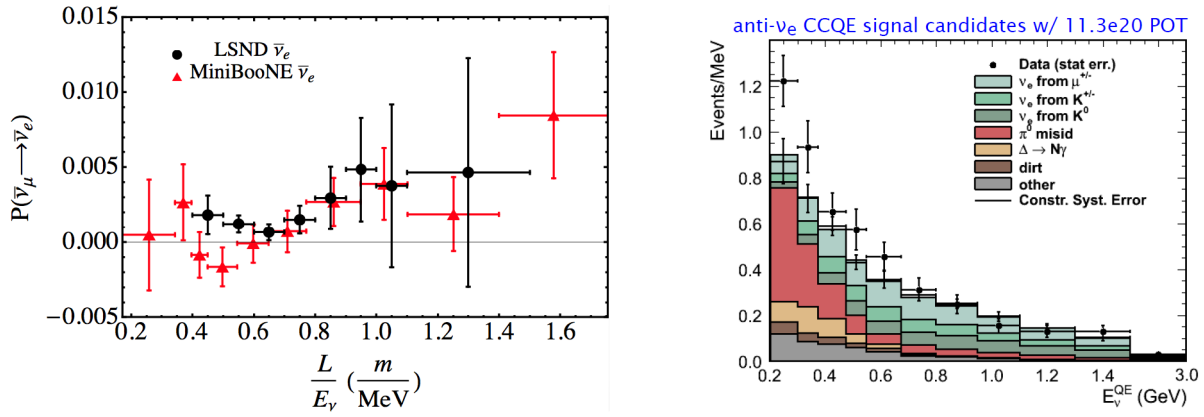


Figure 1.21: LSND and MiniBooNE $\bar{\nu}_e$ results (left) and the low energy excess as seen in MiniBooNE (right) [63].

In 2007, the MiniBooNE experiment, that was conducted to test the LSND result, reported no descrepancies with the present three-neutrino oscillation framework by looking into the $\nu_\mu \to \nu_e$ channel. It excluded the LSND result at 98% C.L., assuming the oscillations of neutrinos and anti-neutrinos are the same. The result however contained an excess of events at energies in the 200 - 475 MeV region. It is yet not known if the excess events are due to oscillations or the neutral current $\gamma$-background. In their most recent release, MiniBooNE presented their $\bar{\nu}_\mu \to \bar{\nu}_e$ analysis and the results are quite consistent with their $\nu_\mu \to \nu_e$ result with the excess events concentrated in the 200 - 475 MeV region [63].

### Reactor Neutrino Anomaly

Recent re-evaluaion of the reactor anti-neutrino flux finds the $\bar{\nu}_e$ flux from nuclear reactors increased by $\approx 3.5\%$. Additionally there is a $\approx 1\%$ increase in the neutrino interaction cross-section due to the decrease in experimental value for the neutron lifetime and another $\approx 1\%$ increase to account for the accumulation of long-lived isotopes in the nuclear reactors which do not reach equilibrium. So the overall expectation value of the anti-neutrino interaction in a nuclear reactor increased by roughly 6% [22]. The new oscillation fits performed are compatible with neutrinos of mass $\Delta m^2_{\text{new}} \gtrsim 1$ eV$^2$ at a distance of $\gtrsim 15$ m [57].

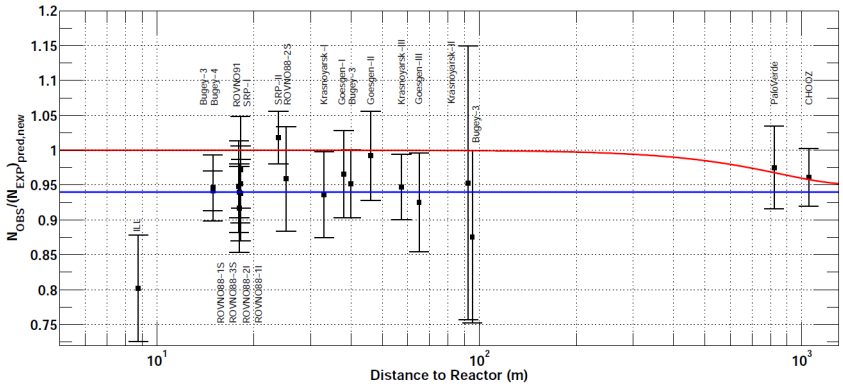


Figure 1.22: The red line shows a possible three-active-neutrino mixing solution with $\sin^2(2\theta_{13}) = 0.06$. The blue line displays a solution including a new neutrino mass state, with $|\Delta m^2_{\text{new,R}}| >> 1eV^{\ 2}$ and $\sin^2(2\theta_{\text{new,R}}) = 0.12$ (for illustration purpose only) [57].

### Gallium Anomaly

Recent source calibrations done for the Gallium based radio-chemical solar neutrino experiments by placing sources $^{52}$Cr and $^{37}$Ar sources inside the detector have shown a deficit of $\bar{\nu}_e$ with the observed to expected ratio being $R_B^{Ga} = 0.86 \pm 0.5$ at 2.8 $\sigma$. An analysis shows neutrino oscillation at an amplitude $\sin^2 2\theta \gtrsim 0.07$ and $\Delta m^2 \gtrsim 0.35$ eV$^2$ at 99% C.L. [37]

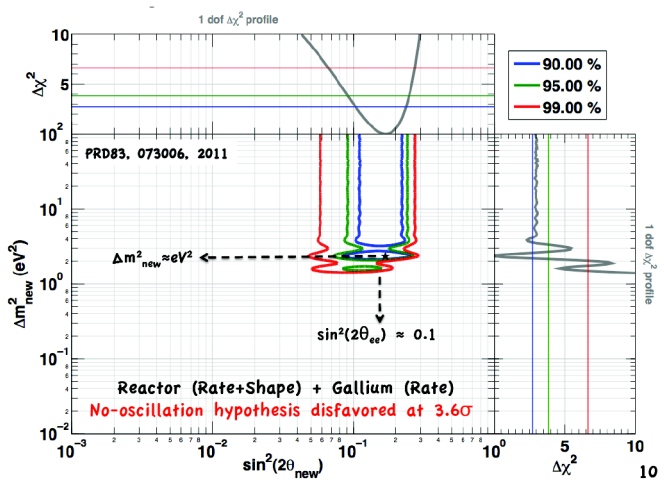


Figure 1.23: Combined Reactor and Gallium analysis [52]

### Cosmology

The relation between the temperature $T_\gamma$ of the relic photons and $T_{nu}$, that of the relic neutrinos after $e^+e^-$ annihilation is

$$T_\nu = \left(\frac{4}{11}\right)^{\frac{1}{3}} T_\gamma. \tag{1.57}$$

From entropy conservation, the number density of the neutrinos can be related to that of the photons as

$$n_\nu + n_{\bar{\nu}} = \frac{3}{11} n_\gamma = 112\, cm^{-3}. \tag{1.58}$$

In the limit of relativistic neutrinos ($m_\nu << T_\nu$), $\rho_\nu$, the energy density of one family of neutrinos is

$$\rho_\nu = \frac{7\pi^2}{120} T_\nu^4 = \frac{7\pi^2}{120}\left(\frac{4}{11}\right)^{4/3} T_\gamma^4. \tag{1.59}$$

In the radiation dominated universe the expansion rate (H) depends upon the energy density of photons and neutrinos. If $N_{\text{eff}}$ is the effective number of neutrinos then from the Friedmann equation, in the above limit, including the energy density of $N_{\text{eff}}$ families of relativistic neutrinos results in

$$H^2 = \frac{8\pi G}{3}(\rho_\gamma + \rho_\nu) = \frac{8\pi G}{3}\left[\rho_\gamma + \frac{7\pi^2}{120}\left(\frac{4}{11}\right)^{4/3} N_{\text{eff}} T_\gamma^4\right]. \tag{1.60}$$

Using $\rho_\gamma = \pi^2 T_\gamma^4/15$, this becomes

$$H^2(t) = \frac{8\pi G}{3}\left[1 + \frac{7}{8}\left(\frac{4}{11}\right)^{4/3} N_{\rm eff}\right]\rho_\gamma. \tag{1.61}$$

The value of $\rho_\gamma$ is very well known from the measurements of Cosmic Microwave Background (CMB) temperature. Hence, in principle, depending on the value of $H(t)$, this can constraint $N_{\rm eff}$. Observationally, CMB anisotropy and other data are used to constrain $N_{\rm eff}$. For example a recent analysis based on the WMAP 9 year CMB anisotropy in conjunction with small scale CMB anisotropy a Hubble prior of $H_0 = 69.32 \pm 0.80\ s^{-1}\mathrm{Mpc}^{-1}$ as

$$N_{\rm eff} = 3.26 \pm 0.35\ (\text{ at } 68\%\ \text{CL}) \tag{1.62}$$

which is consistent with the standard model value of $N_{\rm eff} = 3.04$.

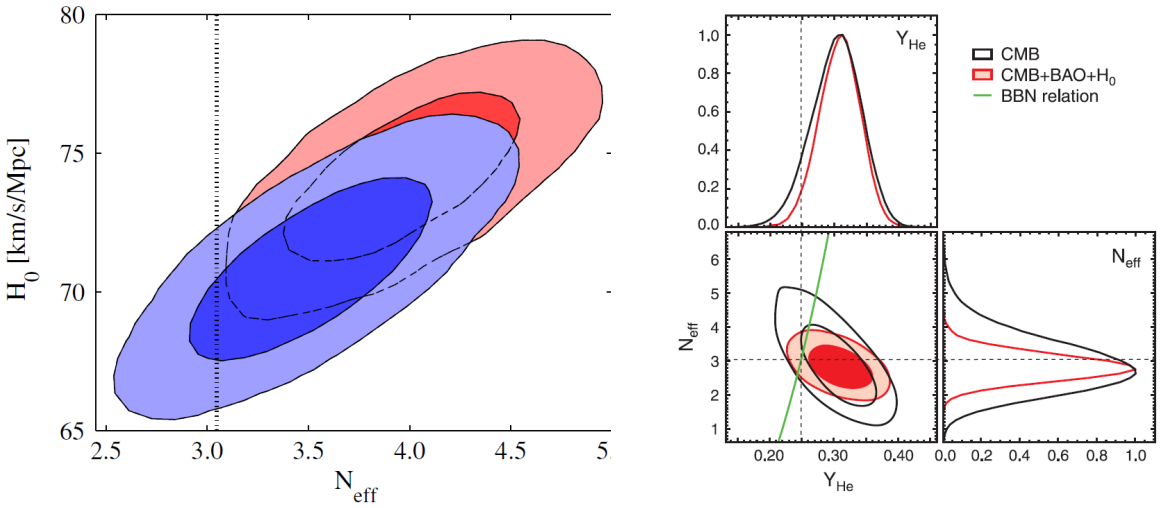


Figure 1.24: Left panel: Constraints on the Hubble parameter $H_0$ and effective number of neutrino species ($N_{\rm eff}$) [17]. Red contours and regions (closer to the upper right corner) assume a Hubble constant of $H_0 = 73.4 \pm 2.4$ km/s while blue contours and regions (closer to the lower left corner) assume $H_0 = 68 \pm 2.8$ km/s. The dotted black vertical line corresponds to $N_{\rm eff} = 3.046$. Right panel: Constraints on the primordial helium abundance $Y_{\rm He}$ and $N_{\rm eff}$ [20].

Baryon accoustic oscillation of the Hubble constant measured with the latest results, emphasize the importance of the $H_0$ prior in establishing the existence of any new neutrino

species. As shown in Fig. 1.24, the value of $N_{\rm eff}$ is correlated to $H_0$ and $Y_{\rm He}$ and better constraints on $N_{\rm eff}$ will follow from a definitive determination of the value of $H_0$.

# Chapter 2

# The Double Chooz Experiment

## 2.1 Overview of the Experiment

The Double Chooz experiment is an $\bar{\nu}_e$ disappearance experiment designed to measure the neutrino mixing angle $\theta_{13}$. The Double Chooz experiment was the first to measure the angle $\theta_{13}$ with high precision. Compared to the previous experiments, it achieved this feat based upon higher statistics, lower background and improved systematics with a single detector [28] and [29]. The Double Chooz collaboration consists of institutions from USA, France, Germany, Japan, Italy and Russia. The Double Chooz experiment is located in the Chooz village of northern France. The detector concept consists of two identical detectors; namely the far and near detectors. The far detector is located at the same experimental hall as the predecessor experiment called CHOOZ at a distance of 1 km(approximately) from the reactor. The near detector will be at a distance of 300 m(approximately) from the reactors and is currently under construction. The source of antineutrinos for the experiment are the pair of Chooz nuclear reactors. The following sections will describe the Chooz nuclear reactor as well as the Double Chooz experiment in detail including both the hardware and software components of the system:


Figure 2.1: Double Chooz experiment site [72]

### 2.1.1 The Chooz Nuclear Reactors

The Chooz nuclear reactors are a pair of pressurized power reactors (PWR), each of thermal power 4.27 $GW_{th}$. The fuel used by the reactors is of type $UO_x$. A nuclear reactor produces power by a contolled fission of mainly $^{235}U$ nuclei with an emission of about 3 neutrons. The neutron undergo subsequent $\beta$-decays to produce 6 $\bar{\nu_e}$ on average. The control is achieved by using water as a moderator to decrease the kinetic energy of the neutrons as well as by using the control rods to absorb some of the neutrons. The fission fragments then undergo $\beta$-decay to produce the $\bar{\nu_e}$.

In a reactor core, a fraction of the neutrons produced is actually captured by the dominant $^{238}$U isotope rsulting in the production of the new fissile isotope $^{239}$Pu and $^{241}$Pu. Hence during this so-called burn-up process a core is burning $^{238}$U and accumulating $^{239}$Pu. In a PWR reactor the fission rates from both isotopes, $^{238}$U and $^{239}$Pu, become comparable at the end of a cycle [57].

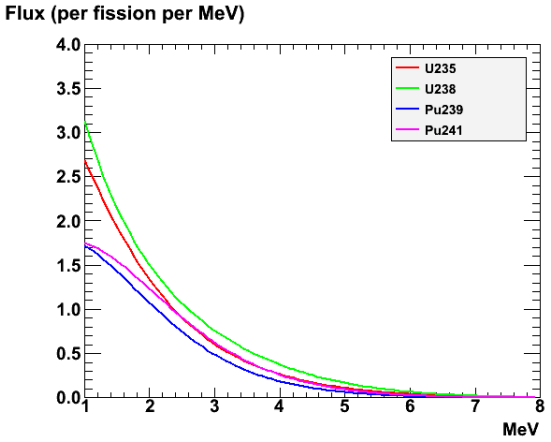


Figure 2.2: Reactor $\bar{\nu}_e$ Flux [41].

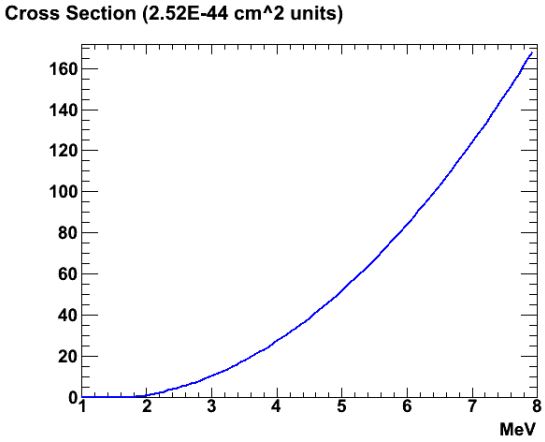


Figure 2.3: Reactor $\bar{\nu}_e$ Cross-Section [41].

Fig 2.2 and Fig 2.3 show the typical $\bar{\nu}_e$-flux and cross-section from a reactor due to $^{235}$U, $^{238}$U, $^{239}$Pu and $^{241}$Pu. The typical, $\beta$-decay cross-section weighted, $\bar{\nu}_e$-spectra are shown in Fig. 2.4.

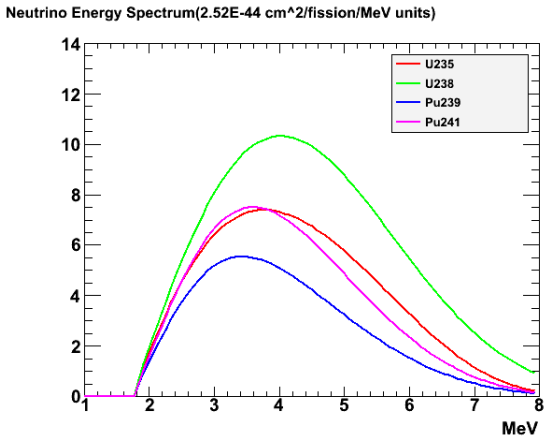


Figure 2.4: Reactor $\bar{\nu}_e$ spectrum from the various fissile nuclei.

### 2.1.2 Detector Description

Fig. 2.5 is a schematic of the Double Chooz detector system. The various detector components are labeled briefly with a more detailed description each given in this section. The Double Chooz detector system consists of a main detector along with an Outer Veto. The Outer Veto has two layers of plastic scintillators above the main detector. The main detector system, shown in Fig. 2.5, is made up of an hierarchy of four concentric cylinders which are described next, starting with the innermost cylinder, the Target.

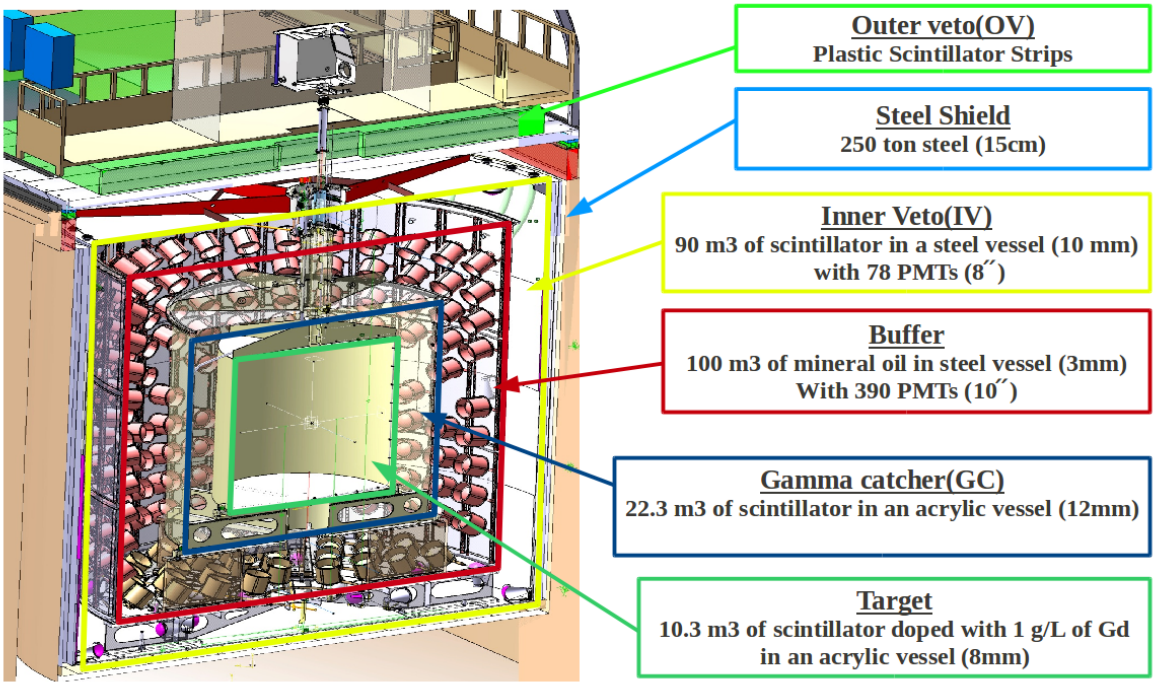


Figure 2.5: Schematic of diagram of Double Chooz detector [71].

### Target

The target is at the center of the hierarchical detector volumes. The target vessel is made up of acrylic and is filled with 10.3 $m^3$ of liquid scintillator with a density of 0.8 gm/l. The liquid scintillator consists of a mixture of n-dodecane (80%) and o-PXE (20%) with 1.32 mg/cc of PPO (fluor) and 20$\mu$g/cc (wavelength shifter). The scintillator is doped with 1 mg/l of gadolinium (Gd) which has one of the highest capture cross-sections for thermal neutrons. Neutron capture of Gd provides a cascade of 2.2 MeV gammas with a mean capture time of about 30 $\mu$s. The total gamma energy peaks around 8 MeV which is far away from natural radioactivity. This is one of the main technique of background rejection in Double Chooz.

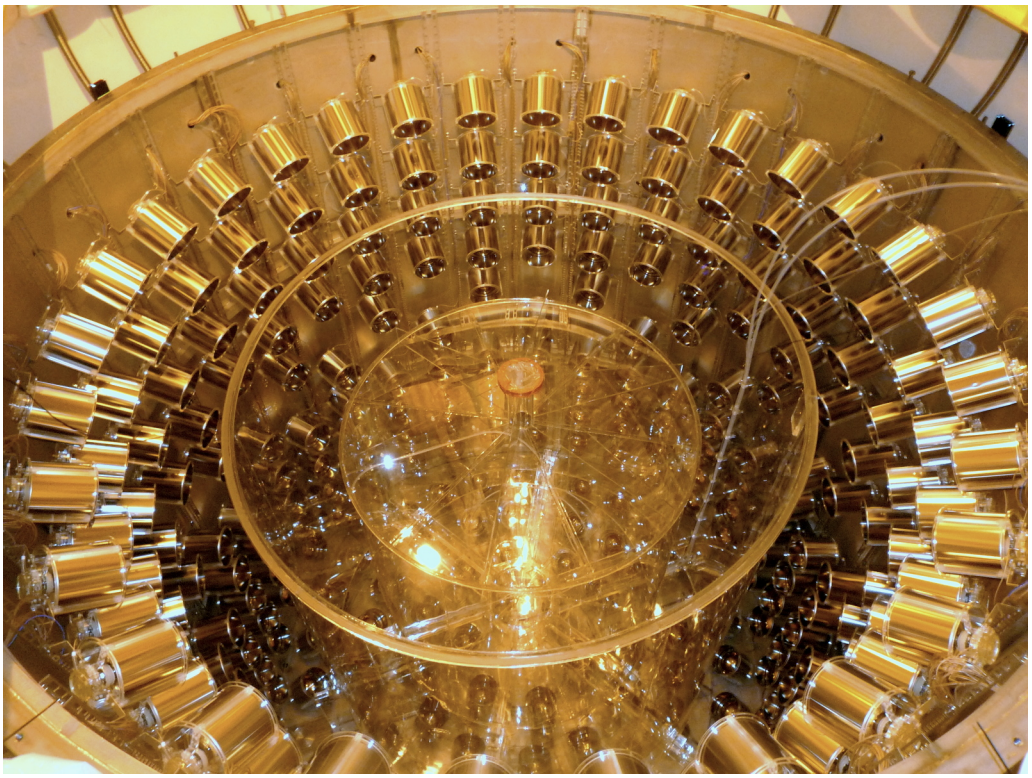

Figure 2.6: Various detector volumes in the Double Chooz main detector [43].

### Gamma Catcher

The Gamma Catcher consists of an acrylic vessel filled with liquid scintillator surrounding the target volume. The scintillator consists of Dodecane (30%), Ondina909 (66%), o-PXE (4%) with 2mg/l of PPO (fluor) and 20 $\mu$g/l of Bis-MSB (wavelength shifter). The gamma catcher captures the gammas that "spill out" during the neutrino interactions inside the target volume. The gamma catcher scintillator density matches that of the target scintillator within 1%. In addition to that it also has a very similar light yield to that of the target scintillator.

### Buffer Region

The Buffer volume is a stainless steel vessel surrounding the gamma catcher tank. The buffer is filled with 100 $m^3$ of non-scintillating liquid consisting of 47.2% of CobersolC70 and 52.8% of Ondina917. 390 photo multiplier tubes(PMT) each of 10" diameter are attached to the walls of the buffer tank. The non-scintillating nature of the buffer liquid supresses the natural radioactivity coming from the radioactive impurities in the PMTs.

### Inner Veto

The outer most volume in the detector hierarchy of the Double Chooz far detector is the Inner Veto (IV). The IV is a steel tank consisting of 78 PMTs, each of 8" diameter. The IV is filled with scintillating liquid consisting of 48.4% LAB and 51.6% Cobersol70 along with 2 mg/l of PPO and 20$\mu$g/l of Bis-MSB. The inner veto acts as a software muon tagging system. Cosmic muons passing through the nearby rock can produce fast neutrons which travel into the sensitive volume of the detector causing correlated backgrounds. Muons passing through the detector can, reduce long lived radioactive isotopes like $^{9}$Li, $^{11}$Li and $^{8}$He through spallation on $^{12}$C which are also important sources of correlated backgrounds. Hence the correct tagging of the muons is very important in order to understand these processes as well as apply a reasonable veto on the muons.

### Steel Shielding

The Double Chooz detector volumes are placed inside a 15 cm thick steel shield to protect the detector from external gammas coming from the rock radioactivity.

### Outer Veto

The Outer Veto system shown in Fig. 2.7,provides additional muon identification for the Double Chooz detectors. Since the muon-induced backgrounds are the major source of backgrounds for the experiment, it is very important to identify the muons that produce neutrons of other radioactive isotopes. The combination of the upper and lower panels of the outer veto will provide tracking information for the muons passing through or missing the target. It will also be able to track the muons clipping the inner veto which are the most dangerous of all.

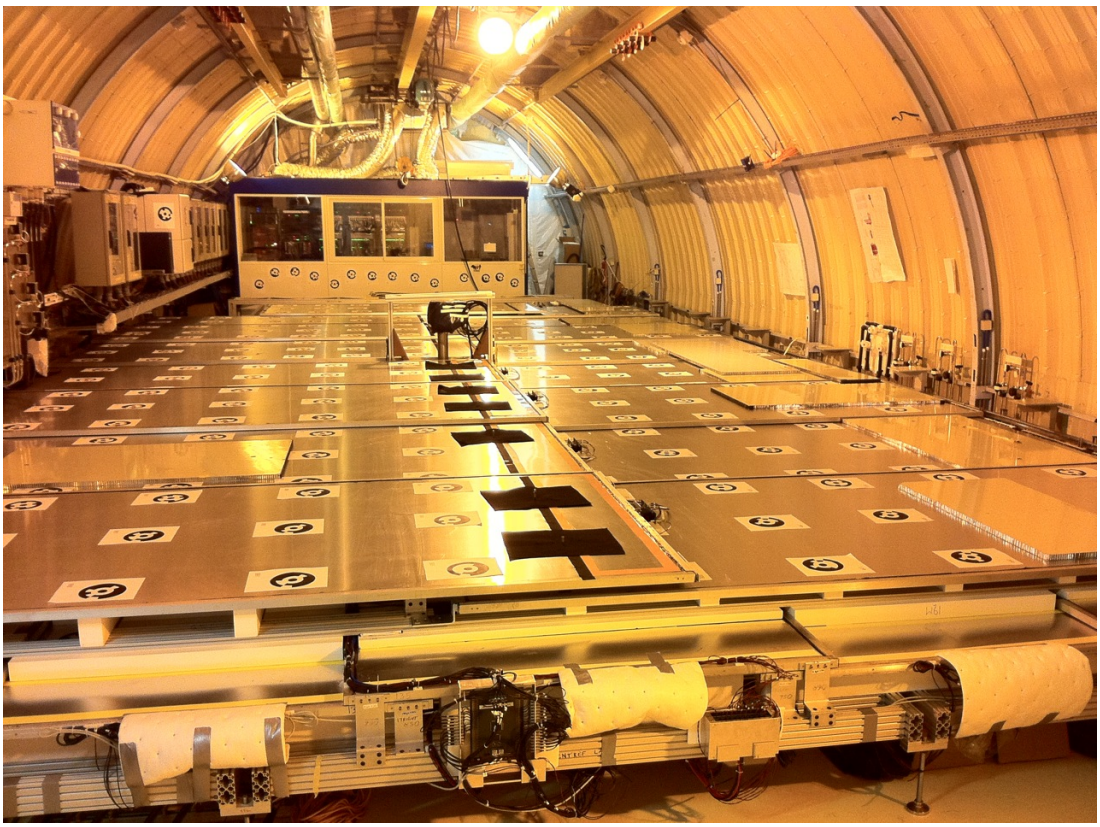

Figure 2.7: Double Chooz outer veto system [12]

## 2.2 Double Chooz Offline Group Software(DOGS)

The offline software package for the Double Chooz experiment is called the name Double Chooz Offline Group Software (DOGS). It consists of individual packages dedicated to specific tasks such as Monte Carlo simulation, data production, the read-out system, position and energy reconstruction. The packages are written in C++ and have external dependancies on Geant4, a toolkit for simulation of the passage of particles through matter, and on ROOT, a data analysis framework [3]. Fig. 2.8 shows the optical model with the construction of Photo Multiplier Tube (PMT) in GLG4sim.

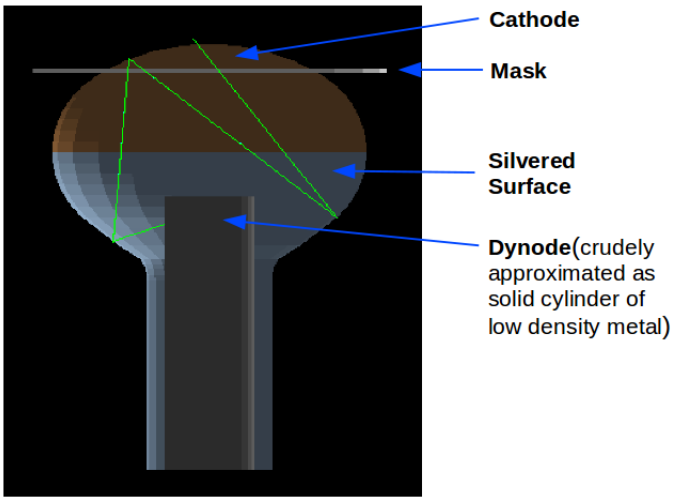


Figure 2.8: PMT Optical model in GLG4sim [42]

### 2.2.1 Monte Carlo Simulation

The Double Chooz Monte Carlo simulation package is called DCGLG4sim (Double Chooz Generic Liquid Scintillator Geant4 Simulation). It is a Double Chooz specific adaptation of the Geant4-based package called GLG4sim similar to the one used by the KamLAND collaboration called KLG4sim. It is used to model the Double Chooz detector and to simulate the generation of the particles, their tracking and energy deposition and the whole process

of the optical photon production by the photoelectron (PE) emission at the photomultiplier tube(PMT) surfaces. Several Monte Carlo event generator packages are included in DCGLG4sim to generate events radioactive decay of nuclei such as $^{252}$Cf, $^{241}Am-Be$, $^{69}$Ge, $^{60}$Co and $^{137}$Cs as well as muons and neutrons. For illustration purpose, we can show Fig. 2.9 as detector model in DCGLG4sim while 2.10 shows the simulation of 1MeV electrons in the target volume of the detector.

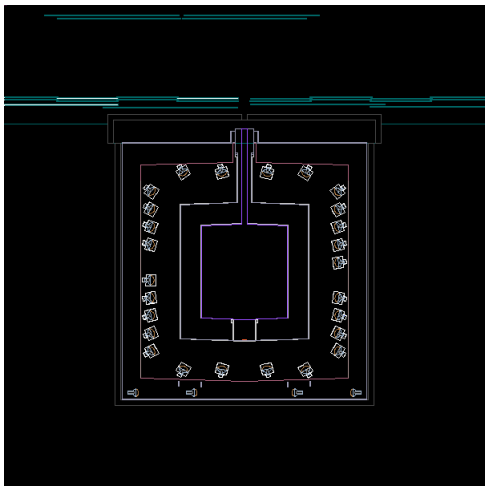

Figure 2.9: Double Chooz Detector Geometry in DCGLG4sim [42]

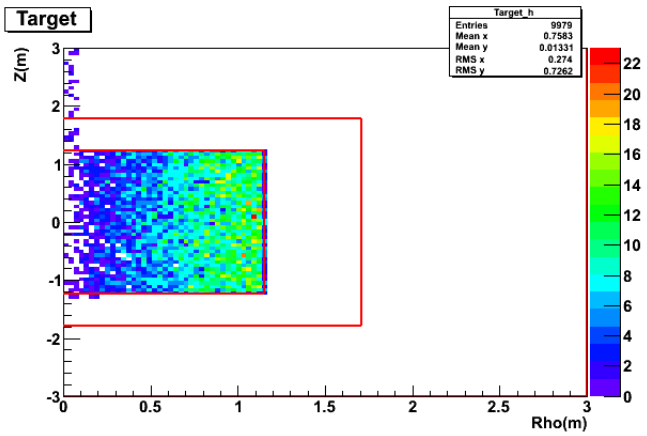


Figure 2.10: Simulation of 1MeV electrons filling the target volume with DCGLG4sim [40]

### 2.2.2 Read-Out Software

The Double Chooz Read-Out System Simulation (RoSS) simulates the detector response of the readout system to the Monte Carlo data generated by DCGLG4sim with a given quantum efficiency. The package includes all the aspects of the real world readout system, such as PMT gain, threshold and time-windows to reproduce simulated data as close to the real data as possible. As stated earlier, DCGLG4sim also simulates the PE production at the PMTs. RoSS takes these PEs and converts them into digitized electrical signals with some collection efficiency. The readout system software is independant of Geant4 and has dependancy only on ROOT. RoSS takes its input from dedicated test-bench experiments designed to characterize the various responses. The Double Chooz readout system developed

from the Monte Carlo techniques using RoSS is shown in Fig 2.11.

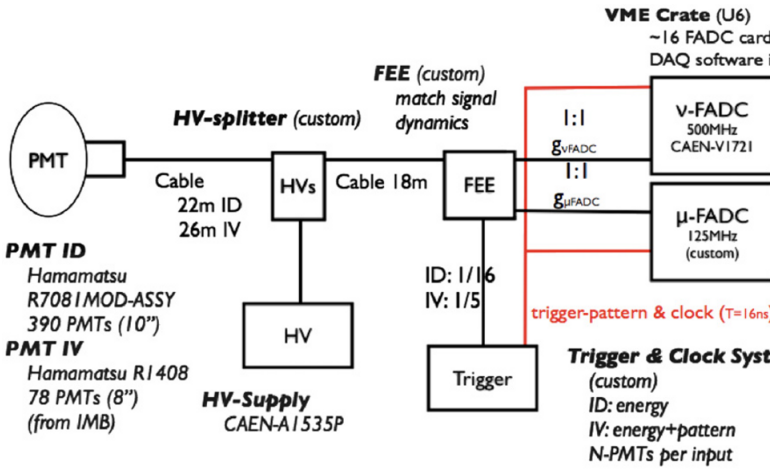


Figure 2.11: Schematic diagram of the Double Chooz readout system [29]

### 2.2.3 Pulse Reconstruction

The pulse reconstruction and pedestal analysis for Double Chooz is done by the package DCRecoPulse [24] which provides the charge collected in any readout channel along with the characteristic time of the pulse. When using Monte Carlo data, DCRecoPulse is applied after RoSS and before the vertex and energy reconstruction. The DCRecoPulse package contains several reconstruction algorithms, namely:

- Peaks Window Algorithm which analyzes continuous regions of amplitude above the pedestal so that the size of the time window depends on the shape of the pulse,
- Maximum Window Algorithm: which places an asymmetric time window of fixed size around the waveform maximum.
- Sliding window Algorithm which searches for a fixed-size time window that maximizes the integral.

  These are illustrated in Fig. 2.12.

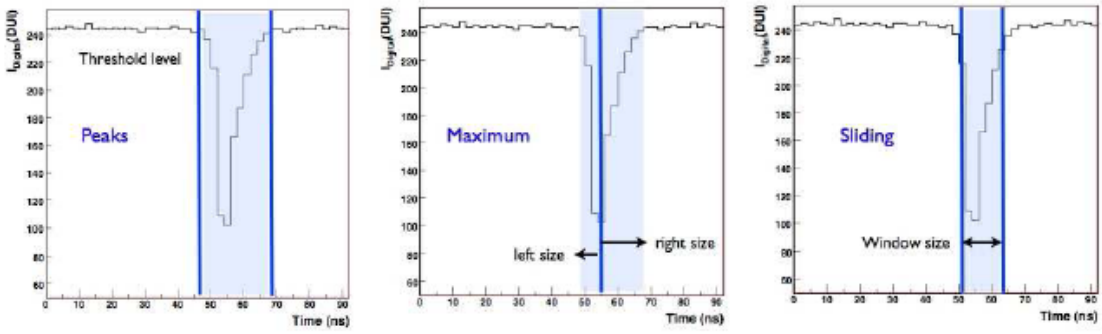


Figure 2.12: Definition of reconstruction time window for the various algorithms. Left: Peak window algorithm. Middle: Maximum window algorithm. Right: Sliding window algorithm.

### 2.2.4 Vertex Reconstruction

The vertex reconstruction for Double Chooz is based upon the likelihoods of measuring a set of PMT charges ($q_i$) or times ($t_i$) or both in the Double Chooz detector [29]. The charge likelihood function depends upon the expected number of photoelectron(PEs) reaching a PMT. Assuming an isotropic distribution of scintillation light from an event inside the detector, the average number of PEs, $\mu_i^{\text{expected}}$ reaching a PMT of quantum efficiency $\epsilon_i$, at a distance $r_i$ from the event vertex and subtending a solid angle $\Omega_i$ is given by

$$\mu_i^{expected} = \epsilon_i \; \Omega_i \; \Phi \; \exp(-r_i/\lambda)$$

where $\Phi$ is the number of photons per steradian. The time likelihood for any hit PMT is a function of the corrected time, $t_{\text{corr}}^{(i)}$ as well as the charge at that particular PMT. Here $t_{\text{corr}}^{(i)}$ is given by

$$t_{\text{corr}}^{(i)} = t_i \text{ - } t \text{ - } r_i/c_n,$$

where $t_i$ is the measured time at the PMT, $c_n$ is the speed of light in the medium and $t$ is the event time.

The vertex reconstruction is performed by maximizing the charge likelihood or the time likelihood or both, between the expected and observed hit distributions.

# Chapter 3

# Simulation Study for Physical Environment Monitoring

## 3.1 Description of the System

The Double Chooz slow monitoring system consists of an ensemble of hardware and software to read out as well as record data from devices measuring slowly varying conditions such as temperature, humidity and magnetic field. The sensors are deployed in the Buffer volume as well as in the Inner Veto. Additionally there are underground sensors to monitor the overall changes to the surroundings of the detector. The components that go into making the monitoring instruments are often contaminated with radioactive substances. The author of this thesis has, along with Dr. David McKee, contributed to the development of this system by assessing the risks of installing the sensors especially inside the sensitive Buffer volume of the Double Chooz far detector, called the Buffer Monitors (BMon).

### 3.1.1 Montecarlo Study for the Radioactive Contamination of the Sensors

Based on the bench measurements of the radioactive components of the sensors and cables at Lawrence Livermore National Laboratory, a Monte Carlo study of the rates of the triggers inside the active volume of the detector was performed.

| Isotope | ppm (Sensor) | ppm (Cable) |
|---|---|---|
| $^{238}$U | $0.085 \pm 0.006$ | $< 0.007$ |
| $^{232}$Th | $0.40 \pm 0.02$ | $< 0.015$ |
| $^{40}$K | $< 20$ | $27 \pm 0.03$ |

Table 3.1: Amounts of radiaoctive isotopes in the sensors and cable.

Table 3.1 shows the measured amounts of radioactive isotopes in the sensors and cable. The trigger rates inside the active volume of the detector was simulated using the isotopes mass fractions, their half lives and the calculated decay rates. A Geant4-based model of the sensors with cable was created within the DOGS framework and enough Monte Carlo data was generated at each proposed site of the sensors. The model was studied with two different configurations of the sensors: 1. Sensors facing away from the buffer tank wall. 2. Sensors facing toward the buffer tank wall. The assembly of the sensors along with the acrylic base on which they are mounted can be understood from the cartoon of a Buffer temperature and magnetic field Monitor (BMon) is shown in the Fig. 3.1.

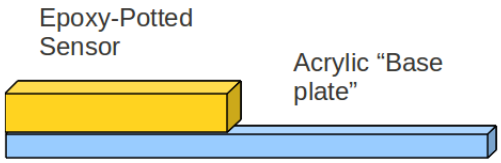


Figure 3.1: A cartoon of a BMon

### 3.1.2 Sensors Facing Away from the Buffer Wall

The configuration in which the sensors are pointing away from the walls of the buffer vessel, is the desired one as this enables the sensors to be closest to the face of the PMTs to accurately measure the magnetic field surrounding the PMTs. Fig. 3.2 shows the vertical and transverse section of the detector with the sensors in this configuration.

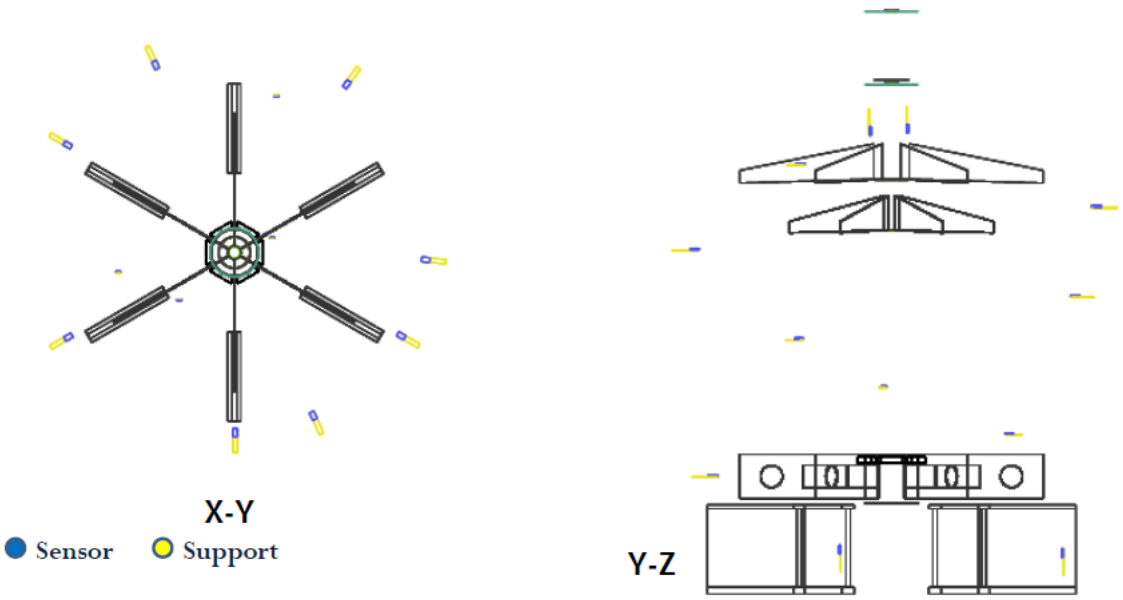


Figure 3.2: Sensors facing away from the Buffer wall.

The trigger rates inside the active volume of the detector above various detection thresholds with this configuration of the sensors is given in Table 3.2.

| Isotope | Event rate (Hz) at trigger threshold | | |
|---|---|---|---|
| | 0.5 MeV | 0.7 MeV | 0.9 MeV |
| $^{238}$U | 0.0068±0.00011 | 0.0048±0.00009 | 0.0035±0.00008 |
| $^{232}$Th | 0.011±0.00017 | 0.0075±0.00014 | 0.056±0.00012 |
| $^{40}$K | 0.0044±0.00021 | 0.0036±0.00020 | 0.0027±0.00017 |

Table 3.2: Trigger rates with the BMons facing away from the buffer wall.

### 3.1.3 Sensors Facing Toward the Buffer Wall

The configuration with the sensors facing toward the buffer wall, shown in FIg. 3.3, was studied just in case the rates in the first case were too high. One caveat of this configuration was that the sensors would be further away from the PMT faces and the magnetic field measurements would be less accurate compared to the previous configuration.

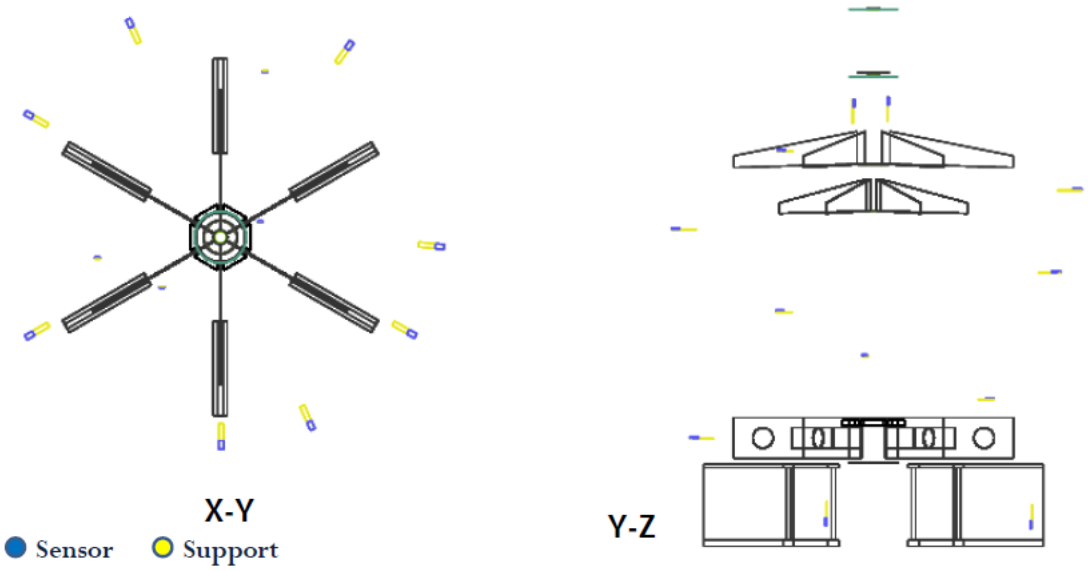


Figure 3.3: BMons facing towards the buffer wall.

The trigger rates in the active volume for the above BMon configuration are shown in Table 3.3 below

| Isotope | Event rate(Hz) at trigger threshold | | |
|---|---|---|---|
| | 0.5 MeV | 0.7 MeV | 0.9 MeV |
| $^{238}$U | 0.00056±0.00003 | 0.00041±0.000027 | 0.00030±0.000023 |
| $^{232}$Th | 0.0014±0.000060 | 0.0011±0.00005 | 00083±0.000050 |
| $^{40}$K | 0.000041±0.0000065 | 0.000029±0.0000054 | 0.000019±0.0000045 |

Table 3.3: Trigger rates with the BMons facing the buffer wall.

### 3.1.4 Trigger due to the cables

The trigger rates due to the connecting cables were simulated by assuming that the cables form a thin layer outside the buffer tank wall, see Fig. 3.4. This was done by using the "skin" option in the DCGLG4sim. The trigger rates are shown in Table 3.4.

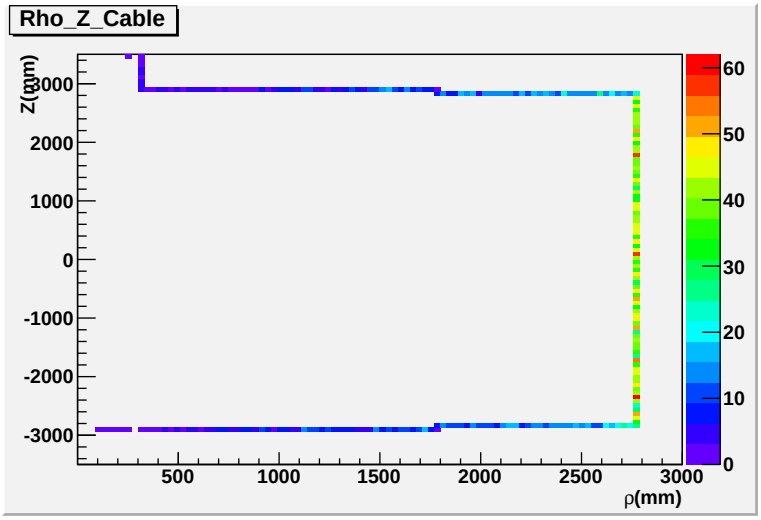


Figure 3.4: An approximation of the BMon cable around the buffer tank

| Isotope | Event rate(Hz) at trigger threshold | | |
|---|---|---|---|
| | 0.5 MeV | 0.7 MeV | 0.9 MeV |
| $^{238}U$ | 0.00012±0.000016 | 0.000090±0.000014 | 0.000084±0.000013 |
| $^{232}Th$ | 0.00041±0.000037 | 0.00033±0.000033 | 0.00030±0.000031 |
| $^{40}K$ | 0.000011±0.0000037 | 0.0000074±0.0000030 | 0.0000037±0.0000021 |

Table 3.4: Trigger rates due to the BMons cables.

The trigger rates due to the cables were very low for all the trigger thresholds considered.

### 3.1.5 Conclusion

The Monte Carlo simulations of the trigger rates due to the sensors and the connecting cables, in various configurations and trigger thresholds were studied. The rates were found to be low enough and the sensors were considered safe enough to be installed inside the Buffer volume of the detector.

# Chapter 4

# PMT Pointing

## 4.1 PMT Pointing Study

In this chapter, I describe work done by the author of this thesis along with his advisor Dr. Glenn Horton-Smith, to optimize the positioning for the Buffer PMTs for the Double Chooz experiment. This Monte Carlo based study is aimed at reaching a model for the PMT pointing with optimum light yield and coverage of the detector for the 390 PMTs placed on the walls of the Buffer volume. All the simulations were done with 1 MeV electrons distributed uniformly in the target volume. The study started with three main PMT distributions described below. The 10 inch PMTs studied had the magnetic shields. The main focus was on light collection, detector response uniformity in the target and gamma-catcher region and the mechanical constraints. Our was helped a lot by the previous work of Carmen Palomares [6]. Our work can be divided into two major parts: (A) Comparative PMT pointing study, and, (B) "Good Enough" PMT pointing study.

## A. A Comparative PMT Pointing Study

In this part we study a few different models for the pointing angles and $z$-positions of the PMTs and test them comparatively for light yield and channel-wise PMT response. The comparative study of the pointing models will be divided into two parts, before and after the suggestions made from similar studies done in [6].

## 4.2 First Stage

The three main models studied in the first stage first are:

- Model "C" refers to the "Spherical (or radial)" PMT pointing with the PMTs pointing to a common spherical center except for the 3 central rings pointing horizontal.
- Model "D" refers to the "Spherical (or radial)" PMT pointing.
- Model "E" refers to "Cylindrical" pointing with the PMTs pointing angles normal to the nearest wall.

The above three models differ from each other in terms of the pointing angles for the PMTs of various $z$-positions. A cartoon, explaining these two variables (pointing angle and $z$-position) for a PMT, is shown below in Fig. 4.1:

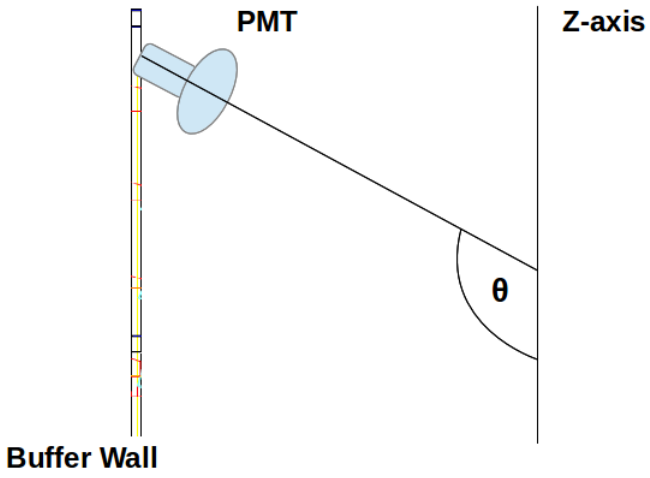


Figure 4.1: Cartoon showing the PMT pointing angle($\theta$) vs $z$-position, measured relative to the central plane.

The performance of any model depends upon the position as well as the pointing angles of the PMTs. The different models studied in the first stage with different pointing angles for the PMTs and their $z$-positions are shown in Figs. 4.2 - 4.4

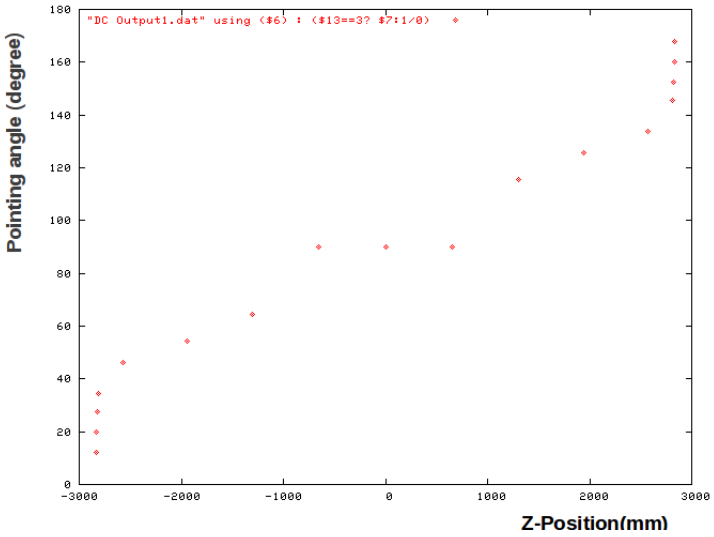


Figure 4.2: Model "C" with spherical coordinates except for the central three rings.

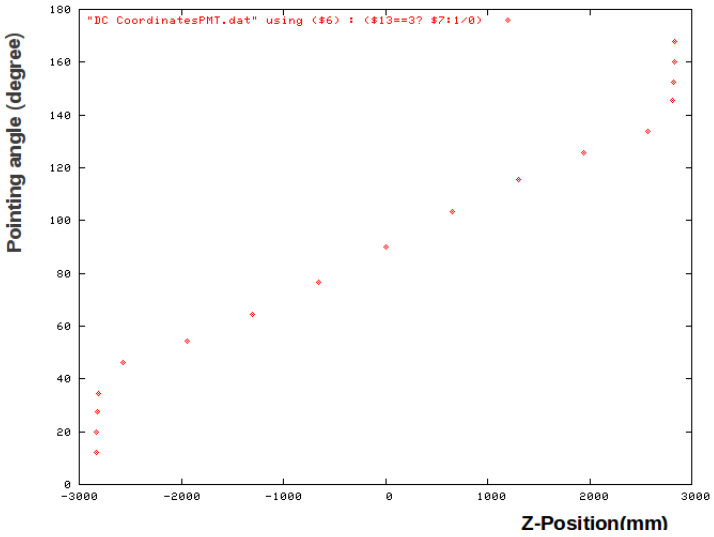


Figure 4.3: Model "D" with spherical coordinates.

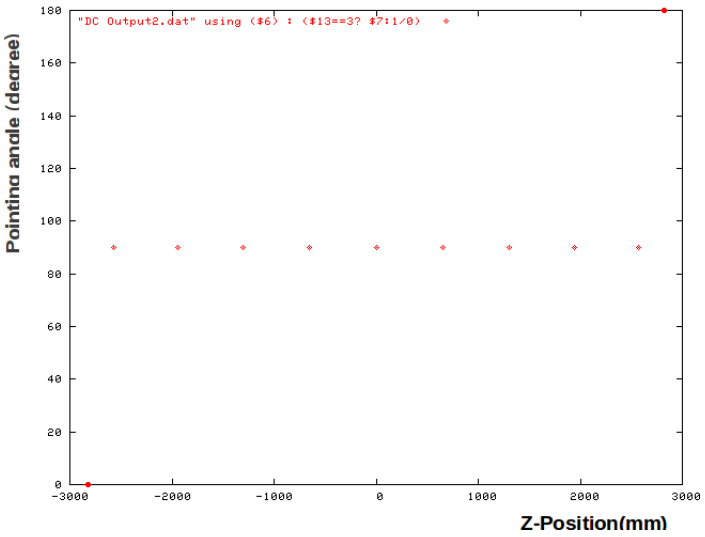


Figure 4.4: Model "E" with cylindrical coordinates.

Fig. 4.5 shows the histogram comparing the total number of photoelectron hits on the PMTs for the three models described above. As described earlier, the simulations were done with 1 MeV electrons distributed uniformly in the target volume.

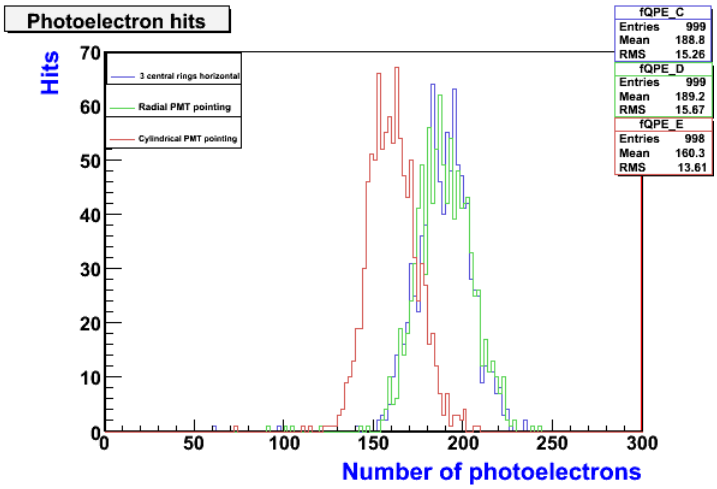


Figure 4.5: Total number of photoelectron hits for models: C (Blue), D (Green) and E (Red).

The small changes in the PMT pointing between models "C" and "D" have almost no effect; the larger the changes in the pointing of the corner and the top tubes in "E" the

longer the reduction in light yield and the worse the resolution.

To prove that the re-tilting of the PMTs really changed the distribution of incident photons hitting the tubes, the following comparisons of the hit distribution in the PMT's local "Y" axis (equivalent to the global Z axis for the side tubes) were done for the various rings. The PMT rings 5, 6 and 7 with PMT number 90-120, 120-150 and 150-180 respectively were chosen. The results are shown in Fig 4.12

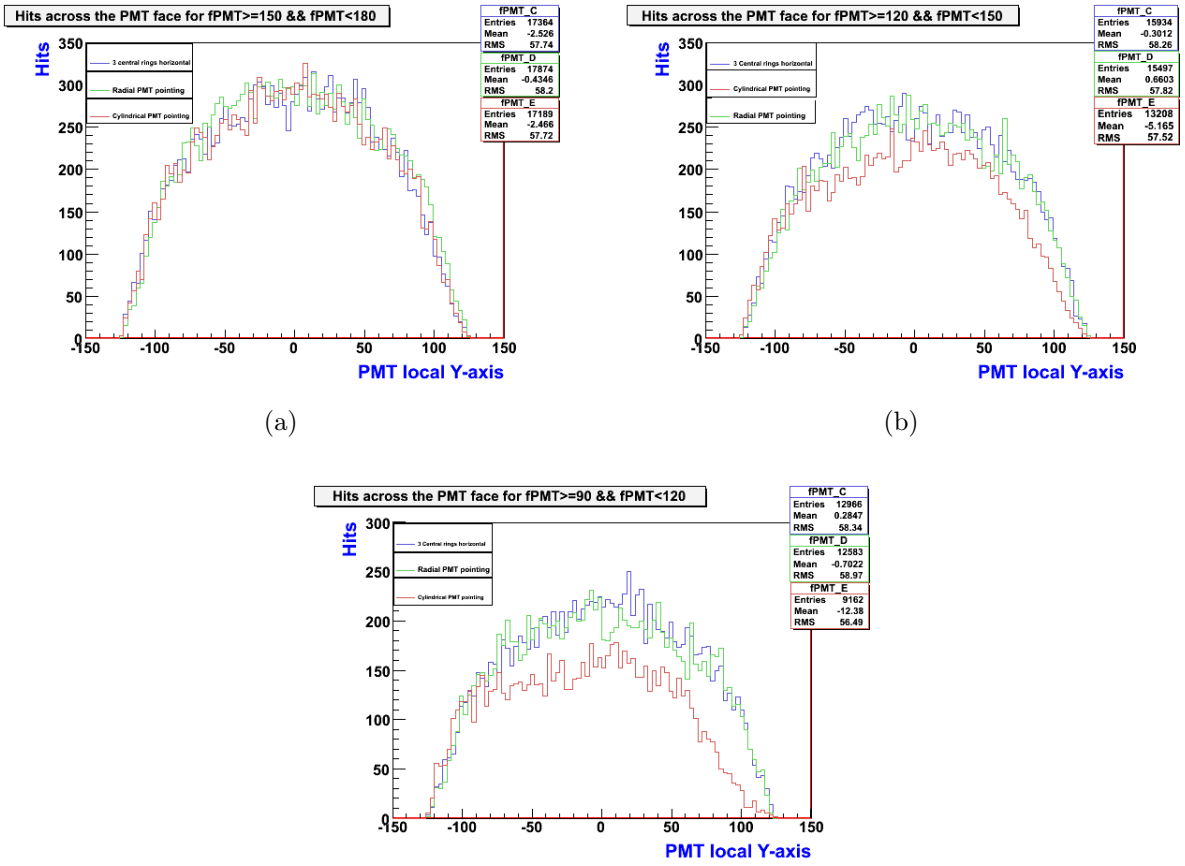


(a) (b)

(c)

Figure 4.6: Distribution of hits along the local Y-axis of the PMTs (equivalent to global Z-axis for the side PMTs for (a) Ring #5 with PMT #(90-120) (b) Ring #6 with PMT #(120-150) (c) Ring #7 with PMT #(150-180)

**Observations:** Small changes in pointing angles have very little effect while larger changes for the corner and top tubes seriously reduce the light yield and worsen resolution.

## 4.3 Second Stage

The same process, as performed in the previous section, was repeated but now using the improved optical data with bench measurements about properties of the scintillators as of 2008/01/08. The pointing angles and positions for the PMTs studied at this stage were either the "Carmen proposed" PMT pointing and positioning as suggested in [6] or some variations of it. From hereon this will be called the model "F".

The details of the three pointing models studied at this stage were:

- Model "F" uses modified spacing between the PMT rings with the pointing angles that follow the spherical model used in model "D" earlier.
- Model "F1" is basically the same as model "F" except that the 4 central rings pointing horizontally (like model "C" above).
- Model "F2" has the same spacing as in model "F" but with the PMTs pointing angles normal to the nearest wall (like model "E" above). It must be noted that it caused a geometry conflict between the side and top/bottom tubes near the corner.

These models are shown in Fig. 4.7 through 4.9.

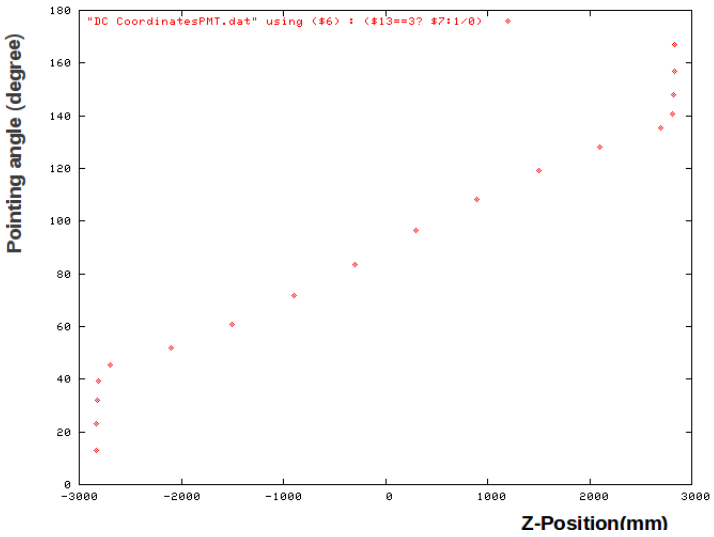


Figure 4.7: PMT Pointing Model "F"

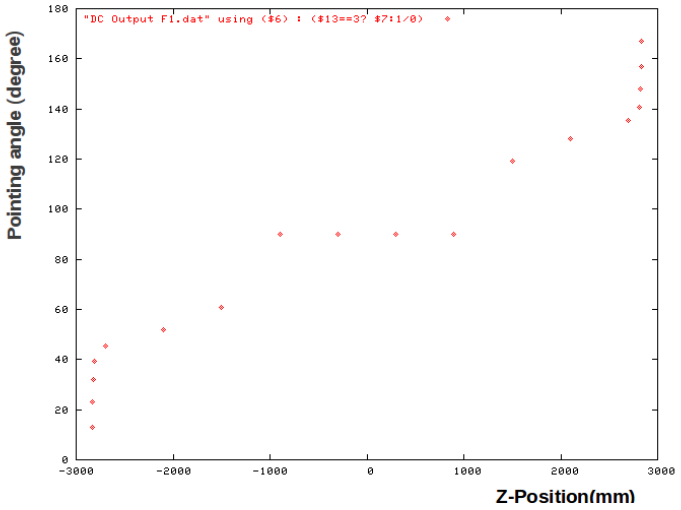


Figure 4.8: PMT pointing model "F1"

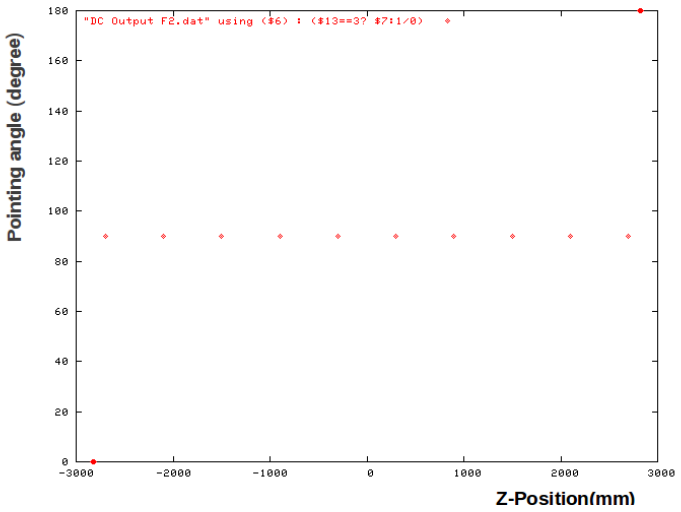


Figure 4.9: PMT pointing model "F2"

Fig. 4.10 compares the total number of photoelectrons per unit energy deposited (in MeV), for the three models discussed above while Fig. 4.11 shows the comparison of the PMT hit pattern for the three models.

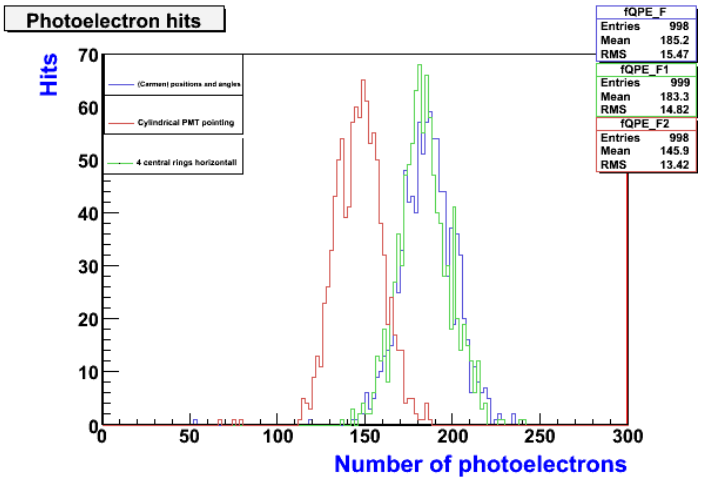


Figure 4.10: Total number of photoelectron hits for the three models: F (Blue), F1 (Green) and F2 (Red).

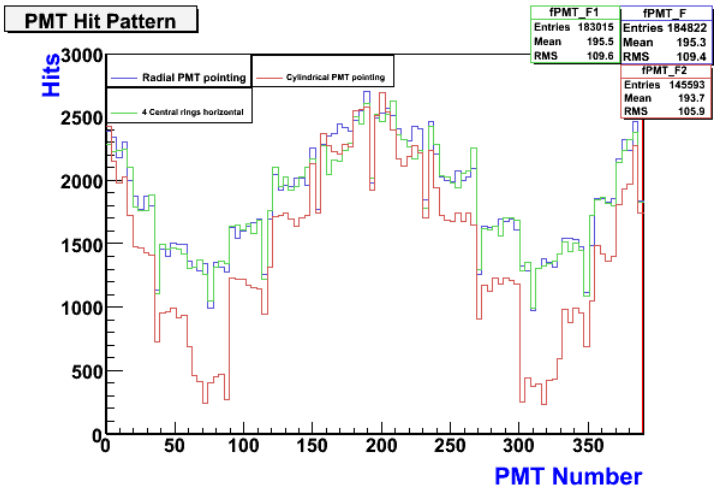


Figure 4.11: PMT hit pattern for the models: F, F1 and F2.

**Observations:** Similar to the results seen in the first stage, models "F" and "F1", which differed little in terms of pointing angles give similar results while model "F2" is significantly different apart from the some geometry conflict.

## 4.4 Another Look

In the previous sections, the study of the various models only included the Monte Carlo events generated in the central target volume. In this section, we present the comparison of the cases of uniformly distributed events in the target (black) vs. gamma-catcher (blue), using the improved optical data in all cases with modified PMT positions or angles, see Fig. 4.12. The model obtained by modifiying model "F", called model "G", has the Z-spacings changed for only the side PMTs from 600 mm to 500 mm and with the angles like in models "F2" or "E". This modification removed any geometry conflict among the corner PMTs.

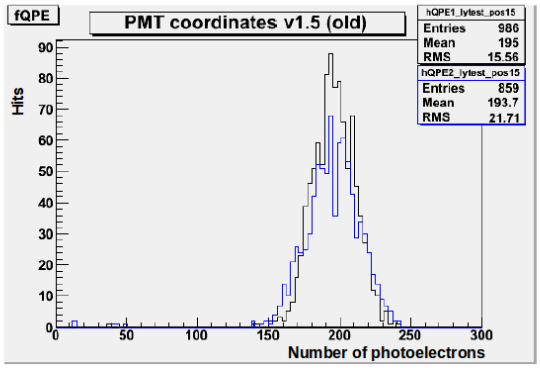


(a)

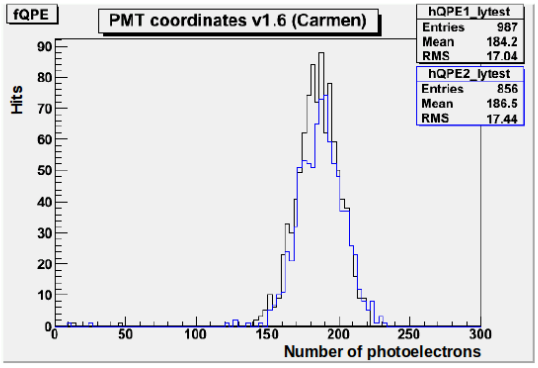


(b)

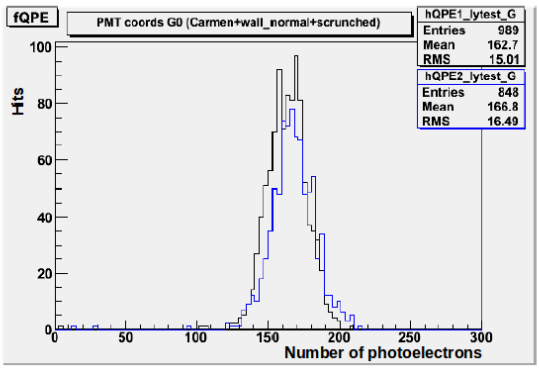


(c)

Figure 4.12: Total number of photoelectrons for: (a): pre-F coordinates (b): Model F coordinates and (c): G coordinates (Note the large loss of light yield in the G distribution.)

The PMT coordinates distribution for the pre-F model is shown in Fig. 4.13

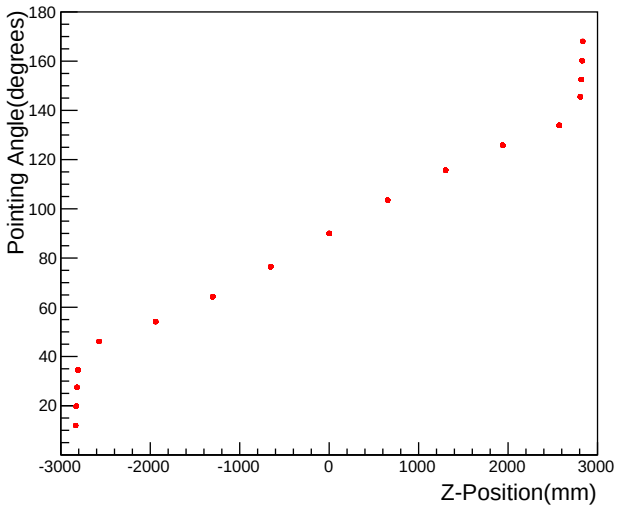


Figure 4.13: PMT configuration before model "F"

It must be noted here that the model "F" coordinates seem to achieve more consistency between target and gamma catcher distributions at some expense of light yield and resolution compared to the large loss of light yield in the "G" distribution.

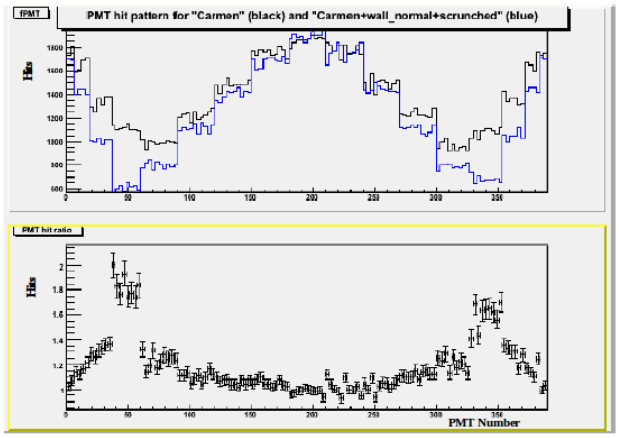


Figure 4.14: PMT hit distribution comparison between "F" and "G" for target events.

The PMT hit distributions for the two models, "F" and "G" for the target events are shown in Fig. 4.14.

**Observations:** The "G" distribution results in slightly better resolution and light yield matching between the target and gamma catcher while the "F" distribution had superior light yield.

## 4.5 "Photomultipier Wall" study

To better understand the ideal pointing for the PMTs at a given position, the inner detector phototubes were eliminated and the code base was modified to record the position and direction of all photons stopping on the buffer tank wall, creating a 100% coverage, 100% quantum efficiency, direction and position-sensitve "Photomultiplier Wall"

Fig. 4.15 shows the arrival direction vs. Z position on the side walls, where the thin black boxes show the 2-D distribution data, thick black lines indicate the cuts used to select events for finding average theta at each Z, blue shows the average theta data and fit, and red shows the radial angle (corresponding to pointing directly at the center of the tank).

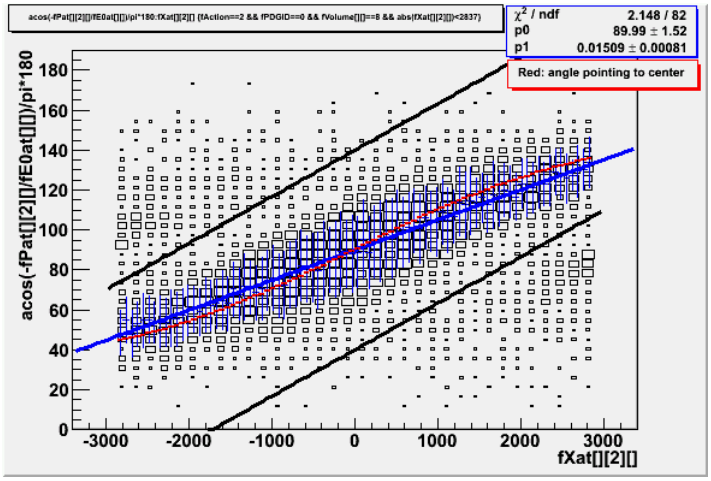


Figure 4.15: Arrival direction vs. $(x^2 + y^2)^{1/2}$ position on the tank top and bottom (angle flipped for top)

**Observations:** It seems that tilting is needed, as setting the corner PMTs normal to

the walls would cut off a significant number of photons given the angular acceptance of the shields.

## 4.6 G2 PMT distributions

G2 is a modified F with modified positions and pointing for the side PMTs accomplished by changing the Z spacing from 600 mm to 500 mm and using mean angles from the theta vs. Z-hit-on-wall fit from the "Photo-Wall" study of the previous section. The top and bottom tube positions and angles are the unmodified model F ones.

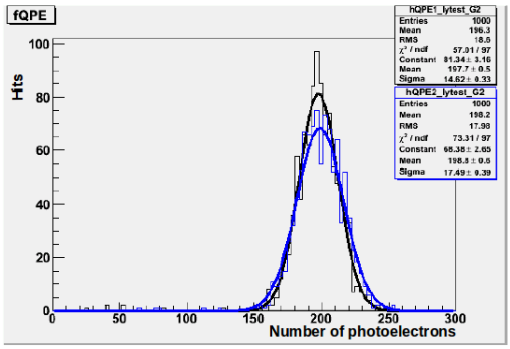


Figure 4.16: Target events

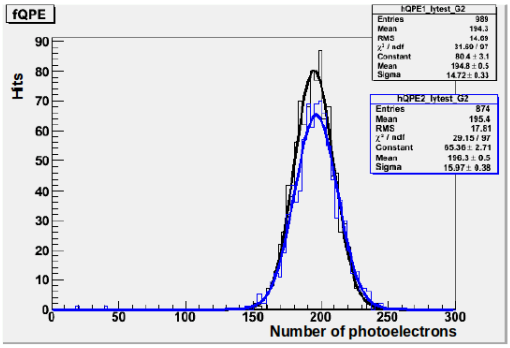


Figure 4.17: Gamma Catcher events

Figure 4.18: Photoelectron hit distributions for the G2: Target (black) and Gamma Catcher (blue).

**Observations:** This seems to have recovered the light yield of the pre-Carmen PMT distribution and improved the light yield of the target events without degrading the gamma catcher event resolution. In addition, there are no mechanical conflicts between the side and top/bottom tubes at the corners.

**Overall observations:**

By modifying the positions and angles in the ways described, the 1 MeV "QPE" resolution can vary from 7% to 11% (where 7% is essentially Poisson statistics), and the overall yield can vary by approximately +5%/-15%. Tilting seems necessary, presumably due to the

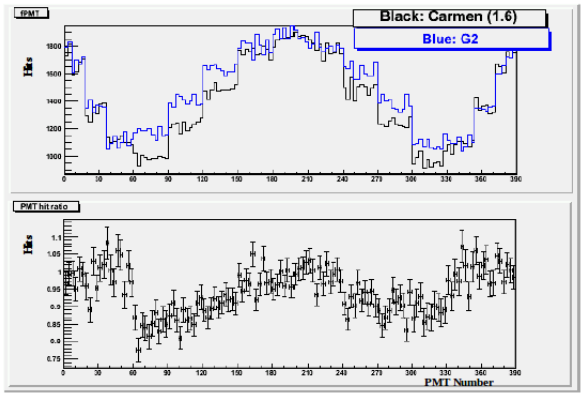


Figure 4.19: PMT hit pattern for Target events: (a) F coordinates (black) (b) G2 coordinates (blue).

acceptance limits of the cylindrical shields. Varying the angle of the tubes near the equator as much as 10 degrees from their optimum doesn't have much effect, but repointing "corner" tubes by about 30 degrees or more has a large effect. This might be the satisfactory solution that achieves better resolution, gamma catcher-target uniformity and the light yield, all at the same time, while avoiding gross mechanical conflicts.

## B. The "Is it Good Enough?" PMT Pointing Study

After studying several configurations of phototube positions and orientations in the "Comparative PMT Pointing Study" we now consider one PMT configuration in an attempt to show that it is both good enough and near optimal. For this, we perform similar analysis as done in the first part but now with higher statistics (10k events in the target volume and 20k events in the gamma catcher) and make 2-D plots by using Geant4.7.1 or 9.0. The configuration studied is based on the "G2" model, adjusted to include mechanical and other corrections provided by the Madrid group. We call our final configuration G3.

## 4.7 Summary of the G3 Configuration

The G3 configuration is summarized graphically in Fig. 4.20 provided by Enrique Calvo Alamillo [7]

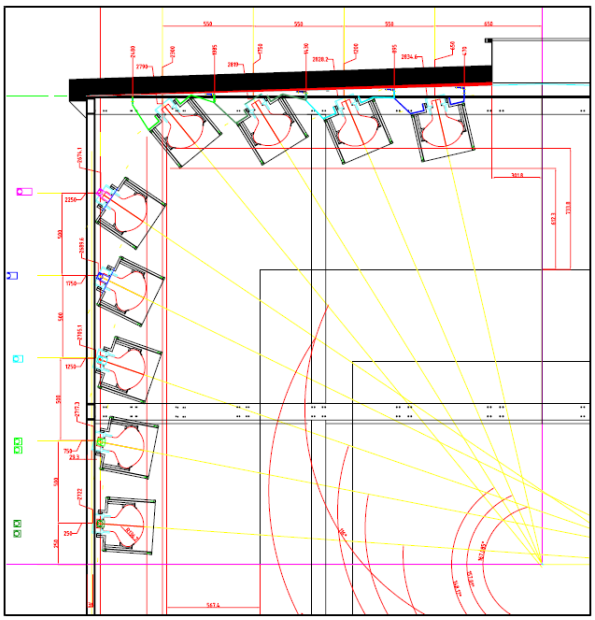

Figure 4.20: G3 configuration

The configuration cosists of 4 rings of PMTs on the top and bottom at radii of 650, 1200, 1750 and 2300 mm plus 10 rings on the sides at z positions $\pm 2504$, $4 \pm 7503$, $3 \pm 1250$ and $\pm 2250$ mm. The PMTs on the lid and the floor are pointed at the center of the target, and the PMTs on the side are pointed according to the equation $\theta = 90° + 0.0151°$ (z/mm), obtained by the pointing angles and the mechanical design. This configuration differs from the G2 configuration described previously in the following ways: PMTs in the outermost rings on the lid and floor are adjusted 20 mm in z toward the middle to avoid conflict, the radial position of the lower 5 rings on the wall were corrected to be symmetric with the top 5 rings and, the numbering of the rings on the floor was corrected.

## 4.8 Comparison between the Geant4 Versions

Two Geant4.9.0.p01 runs, of 10,000 events each, were produced with 1 MeV electrons starting at positions uniformly filling the target and the gamma catcher, using the G3 PMT coordinates. Similarly 10,000 event runs were produced usingthe the G2 PMT coordinates with both Geant4 7.1 and Geant4 9.0 p01. No differences were seen between the results of the two Geant4 versions.

## 4.9 Photoelectrons Plots

Next we check the light collection efficiency, consistency between gamma catcher and target and the effect of non-uniformity of the number of photoelectrons (the most naive energy estimate), by plotting the number of photoelectrons per unit energy (MeV) per event and comparing the target and GC distributions with the G3 and G2 PMT coordinates. The resulting histograms are shown below in Fig. 4.21 and 4.22.

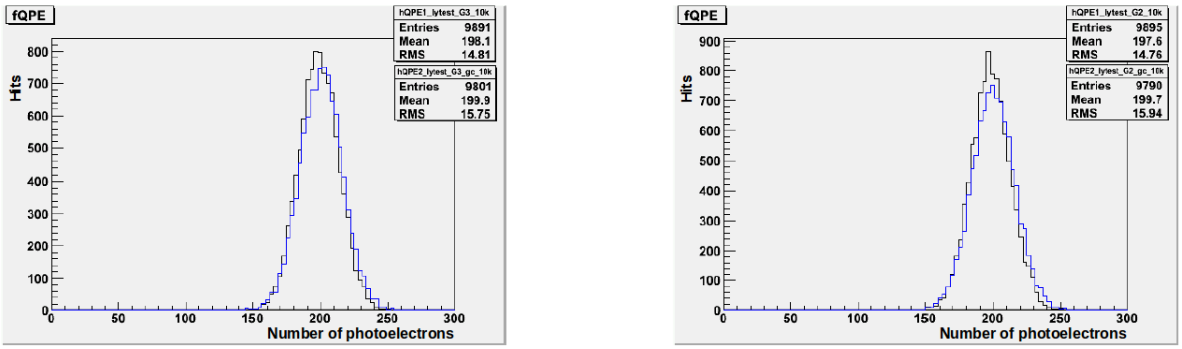


Figure 4.21: Photoelectrons per unit energy (MeV) for Target (black) and Gamma-Catcher (blue) with the G3 coordinates(Left) and G2 coordinates (Right).

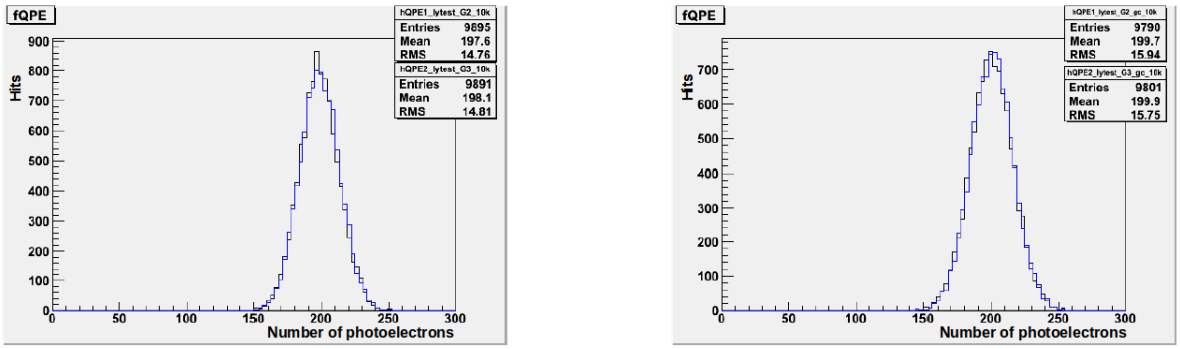


Figure 4.22: Plot comparing photoelectrons per unit energy (MeV) for G2(black) and G3(blue) ditributions for Target events (Left) and Gamma-Catcher events (Right)

## 4.10 Statistical breakdown

Table 4.1 shows the statistical quantities to demonstrate the optimum light yield and sensitivity as well as the uniformity of detector coverage, see Fig. 4.23 and 4.24, achieved with the configurations discussed thus far. The column marked "RMS-NPC" gives the non-Poissonian contribution to the RMS. The width of the distribution is dominated by the Poisson statistics in both volumes. The RMS/Mean is very close to the design energy resolution of 7% assumed in the sensitivity calculations done by Guillaume in his thesis and for the Letter of Intent [LOI].

Table 4.1

| Region | Mean | RMS | RMS/Mean[%] | 1/sqrt(mean)[%] | RMS-NPC(*)[%] |
|---|---|---|---|---|---|
| Target | 198.1 | 14.81 | 7.5 | 7.1 | 2.3 |
| Gamma Catcher | 199.9 | 15.75 | 7.9 | 7.1 | 3.5 |

The RMS/Mean is also better than that of the PMT configuration previously used for calibration simulations. The means of the distribtions differ by less than 2 PE/MeV, less than 1% of the mean and less than 1/4 of the RMS.

## 4.11 2D Uniformity Plots

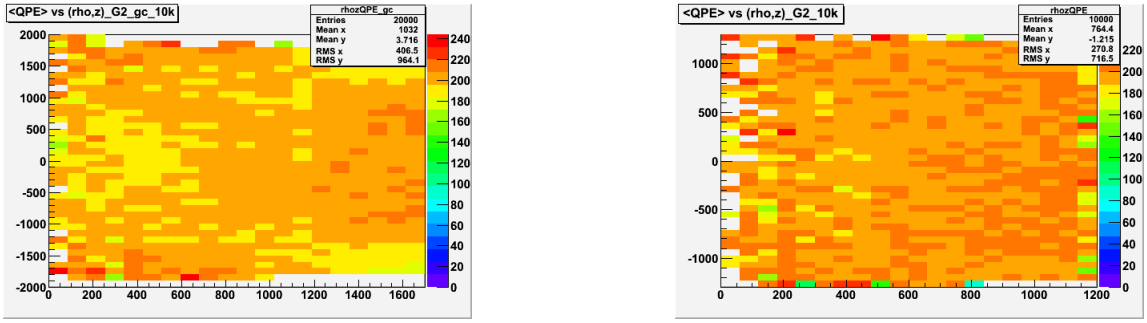


Figure 4.23: Fine grain, low statistics/bin view of "Gamma Catcher + Target" and "Target" photoelectron per unit energy deposited.

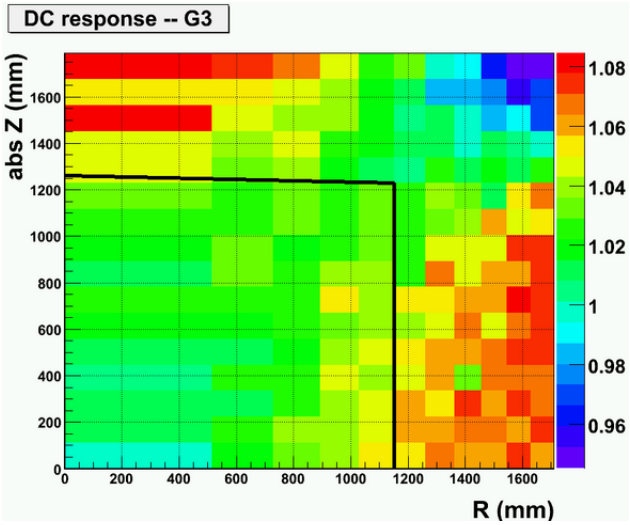


Figure 4.24: Coarser grain, higher statistics/bin view of the Gamma Catcher + Target uniformity.

## 4.12 Conclusion

The G3 design was free of any mechanical conflicts and the collected photoelectron distribution matched the collected photoelectron distributions of events in the target and gamma catcher to be better than 1%. Furthermore, the pointing was optimized for maximum light

collection, and the average phtoelectron yield seems to be at or near the maximum available without sacrificing uniformity. Hence the results were found acceptable for the Double Chooz physics results and the design was deemed to be good enough to be adopted for the Double Chooz experiment.

# Chapter 5

# Neutrino Event Selection

The selection of the actual antineutrino events ocurring in the detector depends on carefully excluding events that are not antineutrino events from the candidate list. This involves removing the random noise events in the detector (of radioactive or electrical origin), understanding the correct energy scale inside the detector as well as removing the sources of backgrounds. These will be discussed in the following sections.

## 5.1 Energy Reconstruction

The visible positron energy $E_{\text{vis}}$ is the measure of the actual energy deposited in an antineutrino interaction. $E_{\text{vis}}$ is a function of the total number of photoelectrons detected by the PMTs after calibration with the additional corrections factors due to the position of the event in the detector and the change in the gain of the PMTs with time. [29]

$$E_{vis} = PE^m(\rho, z, t) \times f_u^m(\rho, z) \times f_s^m(t) \times f_{\text{MeV}}^m. \tag{5.1}$$

Here $PE = \Sigma_i pe_i = \Sigma_i q_i/\text{gain}(q_i)$ for each good channel $i$, $\rho$ and $Z$ are the radial and vertical coordinates in the detector and $t$ is the time. Also $pe_i$ is the number of photoelectrons and $q_i$ is the raw charge on a PMT. The letter $m$ refers to data or Monte Carlo (MC). Eq. (5.1) contains the correction factors $f_u$, $f_s$ and $f_{\text{MeV}}$ for spatial uniformity, time stability and $PE/\text{MeV}$ calibrations respectively.

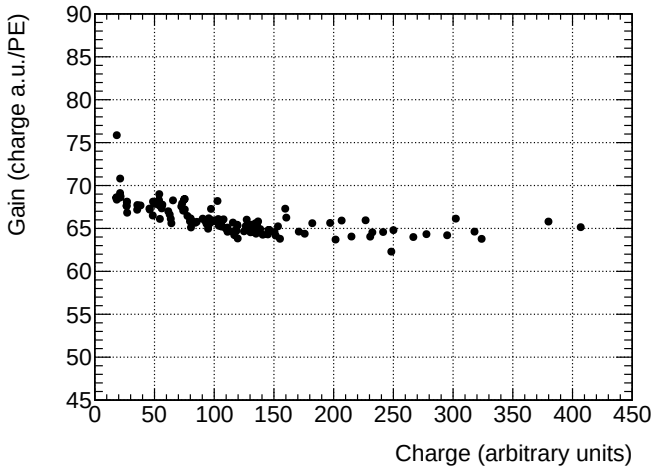


Figure 5.1: Linear PE calibration for one channel (Left) [29].

All this makes the visible energy ($E_{vis}$) independent of time, event position and consistent between both data and MC. An example of a gain curve used to calibrate the charge vs *PE* for each good channel is shown in Fig. 5.1. A similar curve is used in the case of MC also, so that the *PE* calibrated charge can be defined as $pe_i = q_i/\text{gain}_i(q_i)$. The number of *PE*'s for each event depends upon the the position of the event inside the detector.

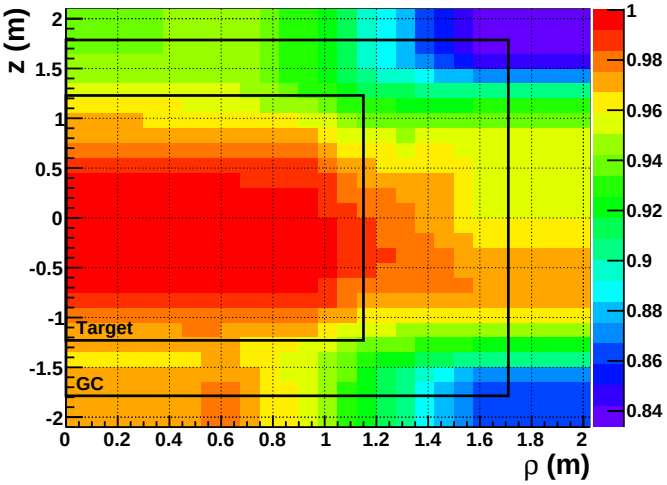


Figure 5.2: Detector calibration map with spallation neutron capture on hydrogen across the inner detector [29].

A calibration map, shown in Fig. 5.2, created with the help of spallation neutron capture

on hydrogen, with a capture peak at 2.223MeV in the target as well as the gamma catcher, is used to convert the PE created in an event at a position into its response as if measured at the detector center ($\rho = 0, z = 0$) through $PE^m_\odot = PE^m(\rho, z) \times f^m_u(\rho, z)$.

Separate calibration maps were created for data and MC to calculate the correction factor $f^m_u(\rho, z)$ and maximize the position dependence consistency between data and MC. The detector response stability varies with time due to the change in the readout gain and scintillator response as well as due to the omission of problematic channels which reduces the overall gain. There is no need of time stability correction for the MC and in the case of the data, any response $PE_\odot$ is convertd to the equivalent response at $t_0$ as: $PE_{\odot t_0} = PE_\odot(t) \times f^m_s(t)$

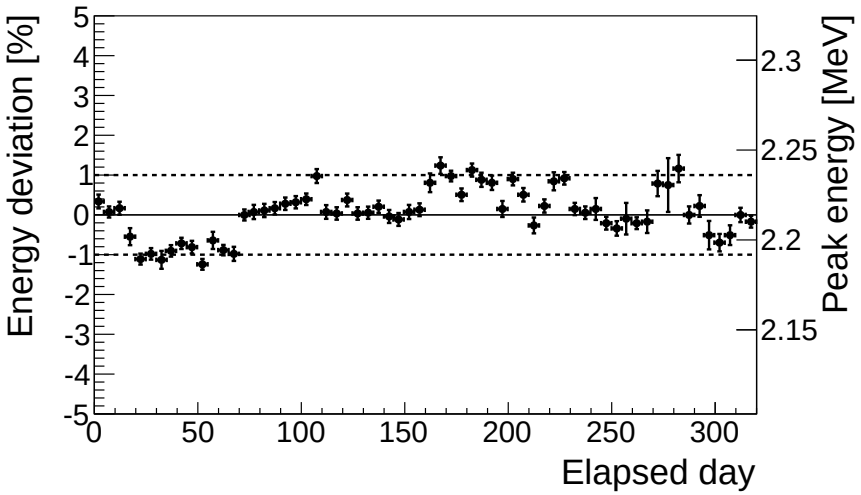


Figure 5.3: Time stability of the reconstructed energy with spallation neutron capture on hydrogen [29].

## 5.2 Neutrino candidate selection

The detection principle for the anti-neutrino events in the Double Chooz detector is based upon "Inverse Beta Decay (IBD)" described in Section 1.4. The selection scheme for each IBD candidate event is based on the 'Delayed Coincidence' method in which an early or

"prompt" positron signal is followed by a "delayed" neutron capture signal, with the two signals separated by the typical capture time of neutrons in gadolinium. The physical threshold, for positron ($e^+$) event is 1.022MeV (twice the rest mass of an electron), for the case when the kinetic energy of the positron is zero. The selection cut threshold for the $e^+$ events is lowered lowered to 0.7MeV. This low threshold does not result in any loss in trigger efficiency but it significantly reduces the trigger related systematics. Two special cuts to reduce excess noise events due to the increased activity of the PMTs are: (1) $Q_{\text{max}}/Q_{\text{tot}}$ cut which utilises the ratio of maximum charge of a PMT to the total charge collected in the inner detector to remove noisy events, and (2) RMS($t_{\text{start}}$) cut which uses the standard deviation of the arrival time of the light at the PMTs to cut out events which havea large spread in the start of the first pulse on each PMT. Here $Q_{\text{max}}$ is the maximum charge recorded by a single PMT and $Q_{\text{tot}}$ is the total inner detector charge collected in a trigger [29]. The various cuts to select the prompt-delayed pairs of a signature neutrino event are summarized as follows:

- Energy Cuts:
  - Prompt Energy Cut: 0.7 MeV $< E_{\text{prompt}} <$ 12.2 MeV.
  - Delayed Energy Cut: 6.0 MeV $< E_{\text{prompt}} <$ 12 MeV.
- Prompt-Delayed Coincidence:
  - Time between consecutive prompt and delayed triggers $2\mu s < \Delta T < 100\mu s$
  - No spatial coincidence.
- Light Noise Cut:
  - RMS($t_{\text{start}}$) $<$ 40 ns.
  - $Q_{\text{max}}/Q_{\text{tot}} < 0.09$ (Prompt events).
  - $Q_{\text{max}}/Q_{\text{tot}} < 0.055$ (Delayed events).

- Multiplictiy and Isolation Cuts:
  - No addtional triggers from $100\mu s$ preceding the prompt signal to $400\mu s$ after it.
- Muon Event:
  - Total charge in Inner Veto $>$ 10000 DUQ (Digital Unit of Charge, an arbitrary unit).
  - Energy in the Inner detector $>$ 30 MeV
- Post-muon Cut:
  - To reject the neutrons and other short-lived spallation products following a muon, a 1 ms veto is applied after the previous muon, which introduces a deadtime of about 4.4%.
- Additional Cuts:
  - To reject those candidates which are correlated, in time, to a showering muon ($E_\mu > 600$ MeV), an additional veto of 0.5 s is applied after each showering muon.
  - Also the candidates whose prompt signal are coincident with an Outer Veto trigger, initiated by a muon passing through the Outer Veto, are excluded.

### 5.2.1 Daily Rates

Neutrino candidates were selected based upon the above cuts from data as well as from Monte Carlo simulation. A total of 8249 anti-neutrino candidates were selected from a total detector livetime of 227.93 days. The total expected number of candidates from anti-neutrino Monte Carlo simulation for the same livetime, for $\theta_{13} = 0$, is 8937 [29]. A mesurement of $\theta_{13}$ based upon these candidates is presented in Chapter 9.

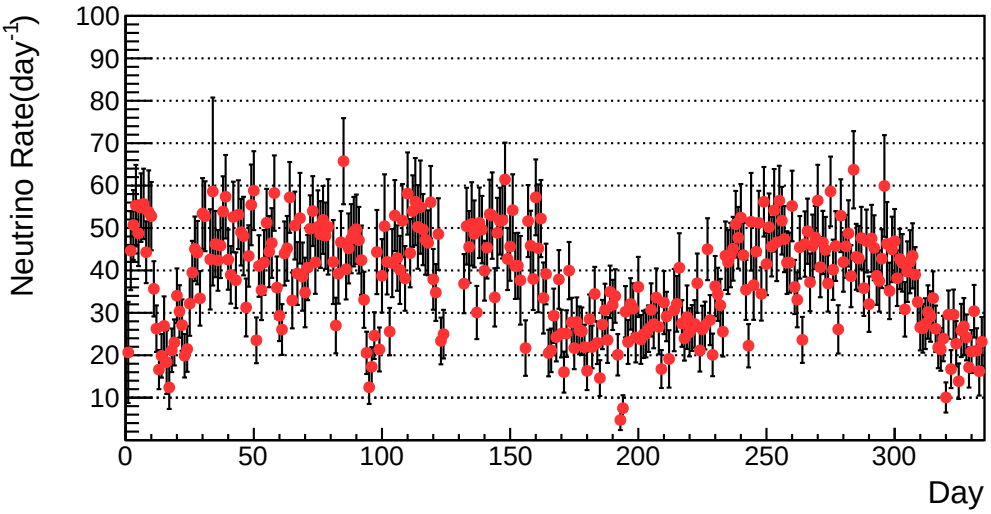


Figure 5.4: Daily variation of neutrino candidates before any background subtraction or veto anti-coincidence

Figs. 5.4 - 5.7 shows the effect of thier selection in various daily rates. The variations of the daily rates of the selected anti-neutrino events represents the variations in the combined power for the two reactors. The average rate of anti-neutrino candidates comes out to be $36.2 \pm 0.4$ events day$^{-1}$ since the start of data taking on April 13, 2011.

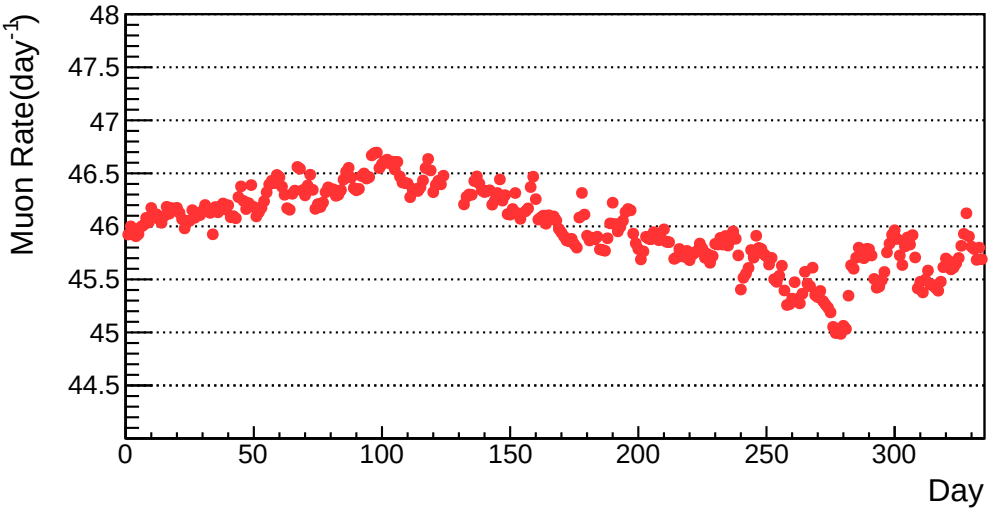


Figure 5.5: Daily variation of muon rate

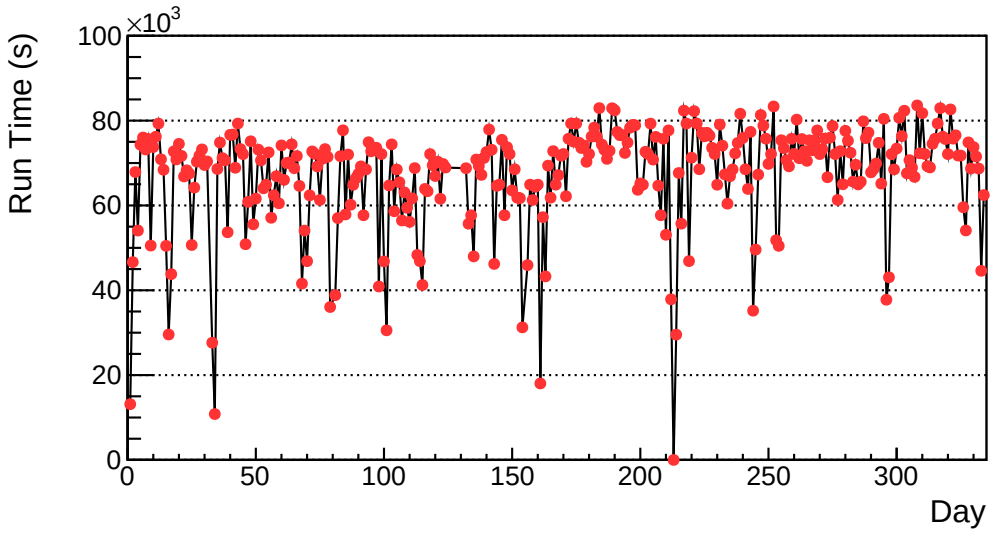


Figure 5.6: Daily variation of the runtime for neutrino candidate selection.

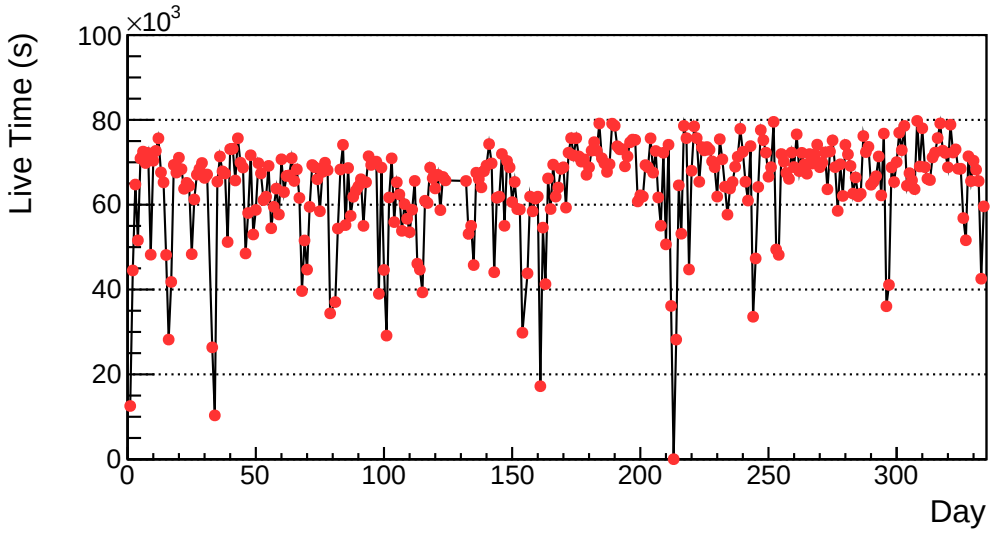


Figure 5.7: Daily variation of the livetime for neutrino candidate selection after applying the veto corrections.

### 5.2.2 Candidate Characteristic Plots

Various characteristic plots for the selected anti-neutrino candidates are given in this section.

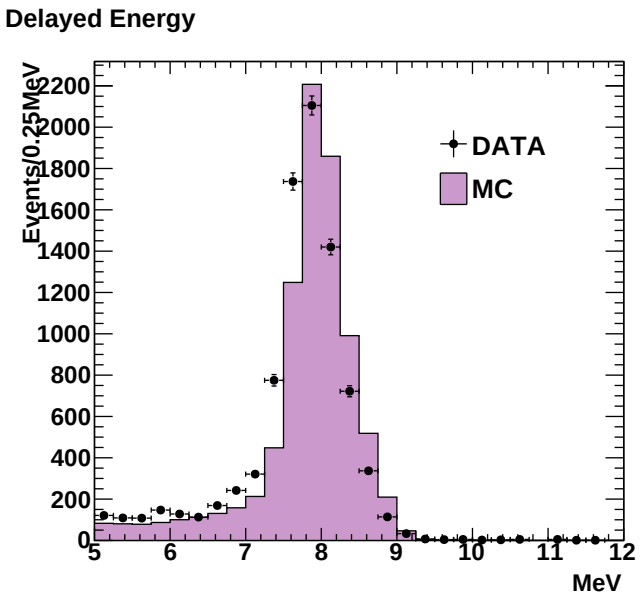


Figure 5.8: Delayed energy epectrum of the 8249 neutrino candidate events selected with the official set of cuts as per the Double Chooz second publication [29].

In Fig. 5.10, the lower cut of 2$\mu$s helps to reduce the correlated background while the upper cut of 100$\mu$s determines the end of the tail of the neutron capture on gadolinium [29].

Although the anti-neutrino candidate selection for Double Chooz does not include a fiducial cut on the distance between the prompt and the delayed events, Fig. 5.11 shows a good agreement between the data and Monte Carlo for the prompt-delayed distance. Figs. 5.12 - 5.15 show the 2-dimensional distribution of the anti-neutrino candidate events in the target and gamma catcher volumes.

Almost all of the anti-neutrino events are confined within the combined volume of the target and gamma catcher. It is important to mention two categories of events here: (1) Spill Out. These are events with the neutrino interaction in the target but with the neutron captured

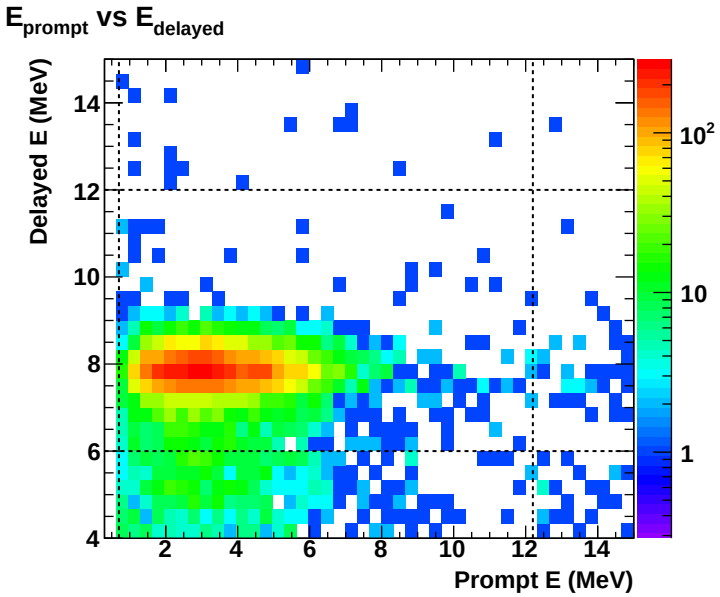


Figure 5.9: Prompt energy vs delayed energy for the neutrino candidates. The dashed lines show the selection cuts applied.

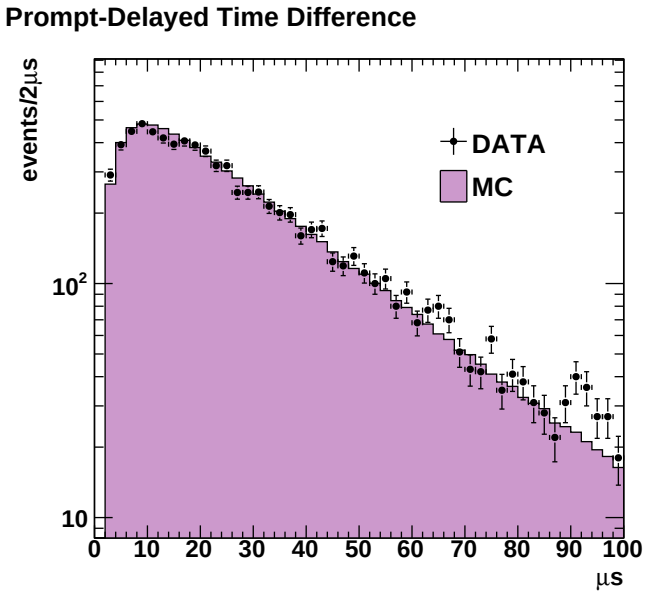


Figure 5.10: Time delay between the prompt and delayed candidates.

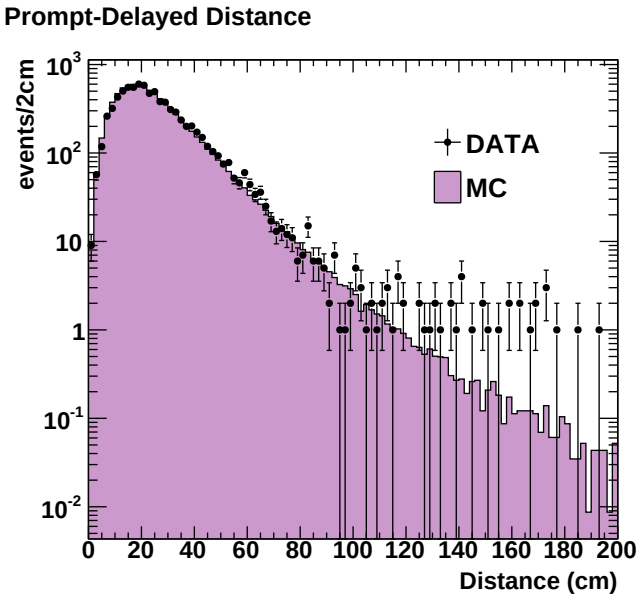


Figure 5.11: Distance between the prompt and delayed candidates.

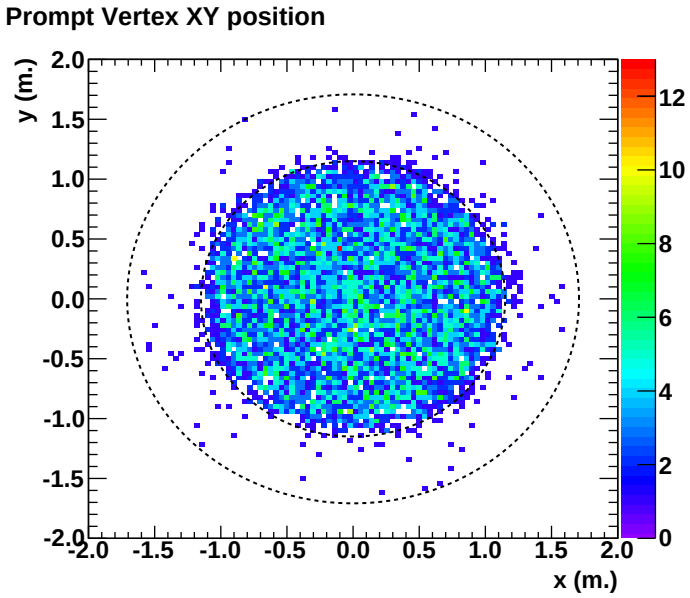


Figure 5.12: x-y vertices of the prompt candidates.

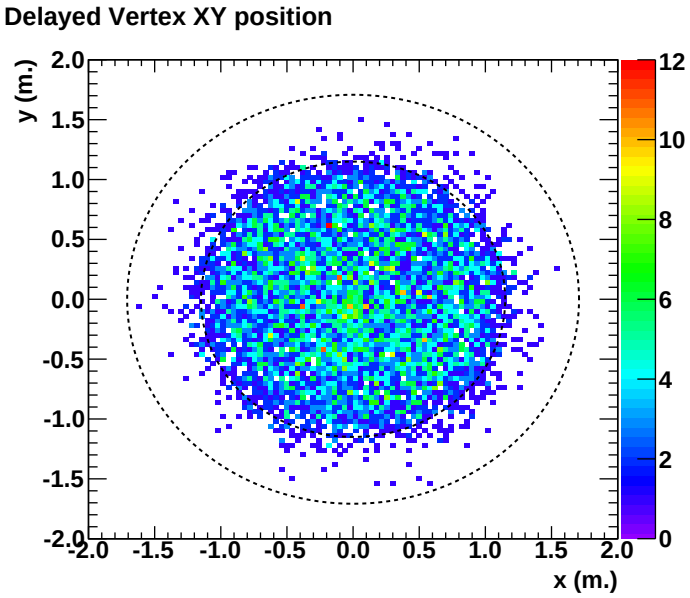


Figure 5.13: x-y vertices of the delayed candidates.

in the gamma catcher. (2) Spill In. These are events with the neutrino interaction in the gamma catcher with the neutron capture happening in the target.

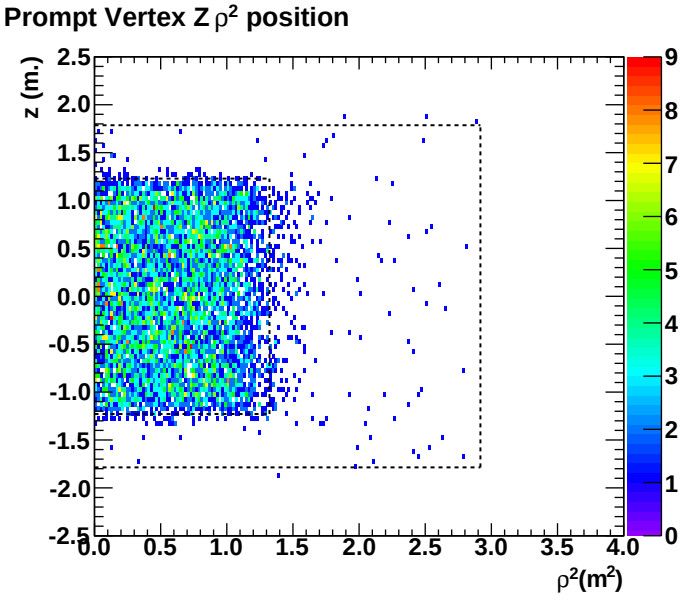


Figure 5.14: $Z - \rho^2$ vertices of the prompt candidates.

From Fig. 5.16 - 5.19, it is easy to see excess events in the data for vertices with high $z$-values and low $\rho^2$ values. These events are candidates for the stopping muon events which will be

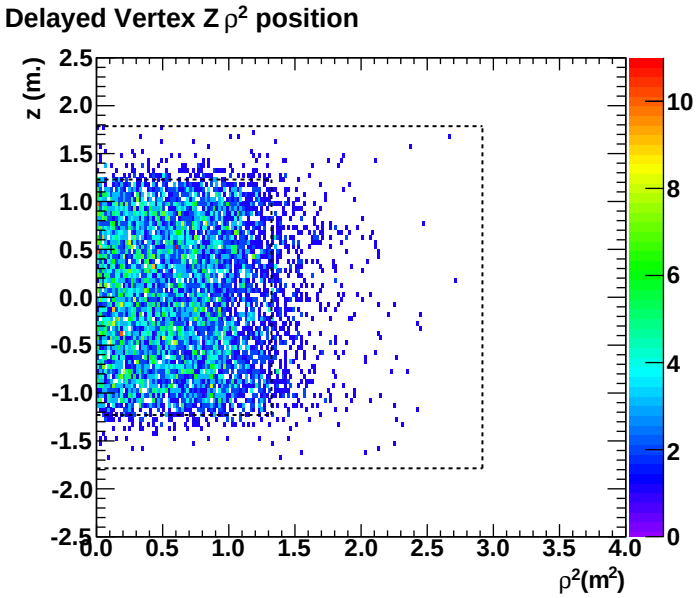


Figure 5.15: $Z - \rho^2$ vertices of the delayed candidates.

discussed in detail in Chapter 8.

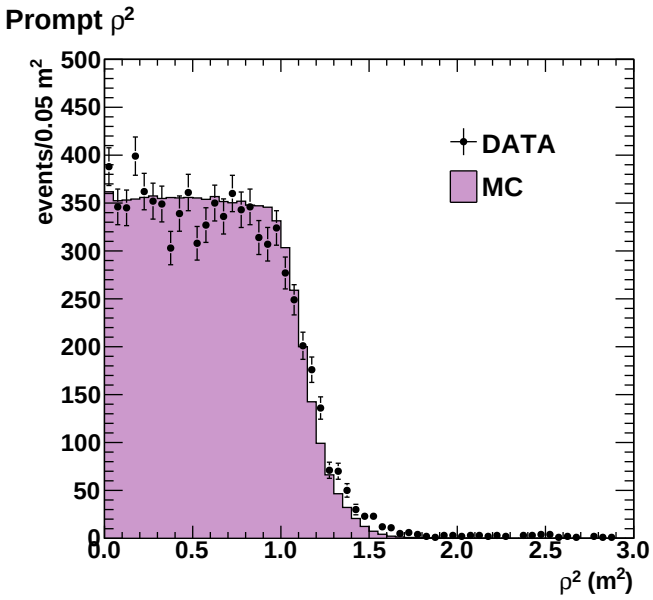


Figure 5.16: $Z - \rho^2$ vertices of the prompt candidates.

From the RMS($t_{\text{start}}$) plots shown in Figs. 5.20 - 5.21, it can be seen that there is a slight offset between the data and the MC but since the candidates are selected with a cut of RMS($t_{\text{start}}$) $< 40$ ns, this discrepancy does not affect the selection.

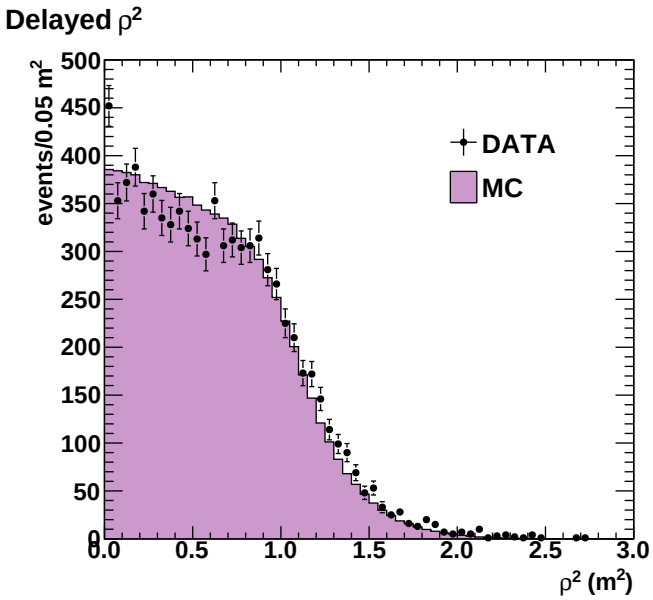


Figure 5.17: $Z - \rho^2$ vertices of the delayed candidates.

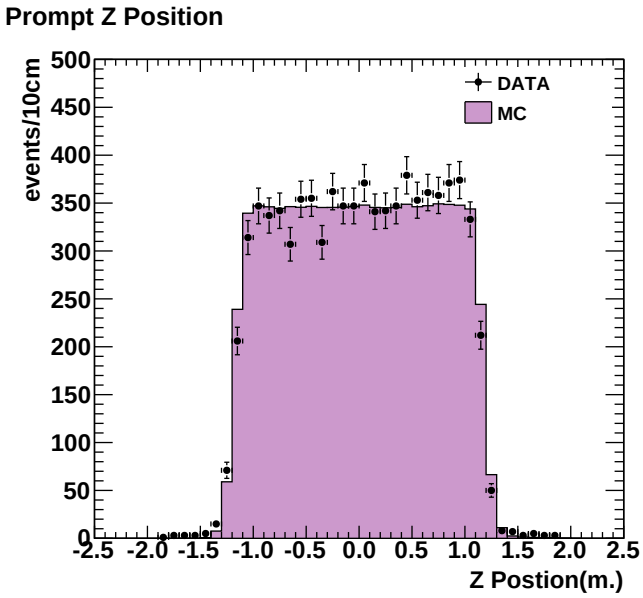


Figure 5.18: $Z - \rho^2$ vertices of the prompt candidates.

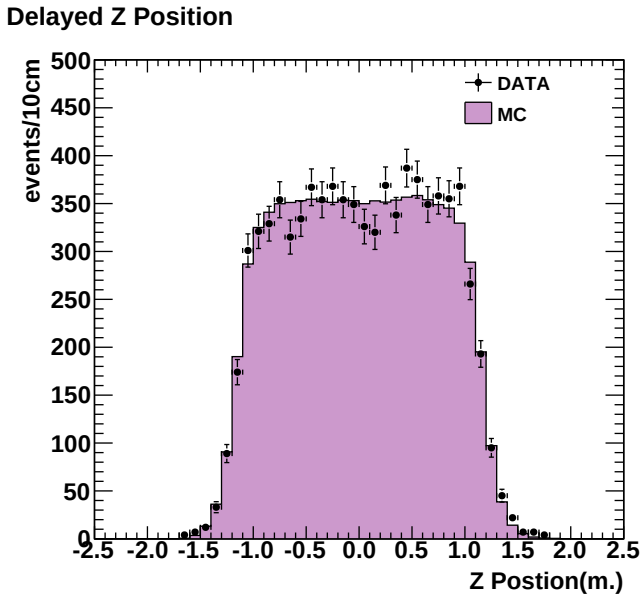


Figure 5.19: $Z - \rho^2$ vertices of the delayed candidates.

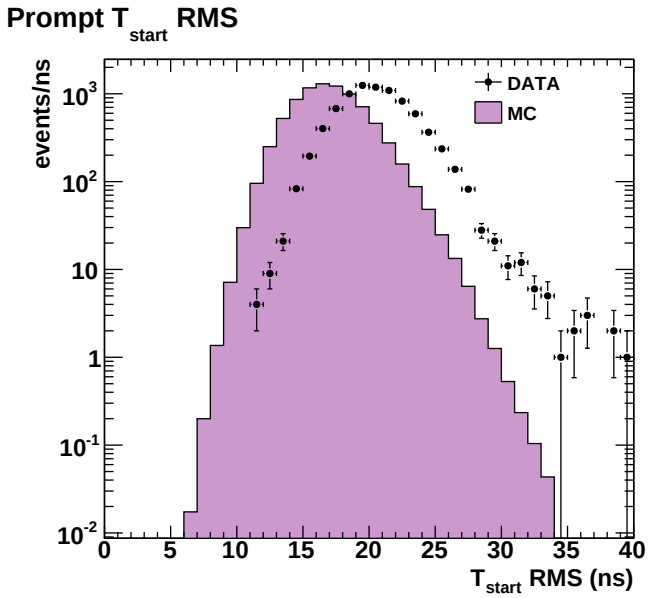


Figure 5.20: $t_{\text{start}}$ RMS for the prompt candidates.

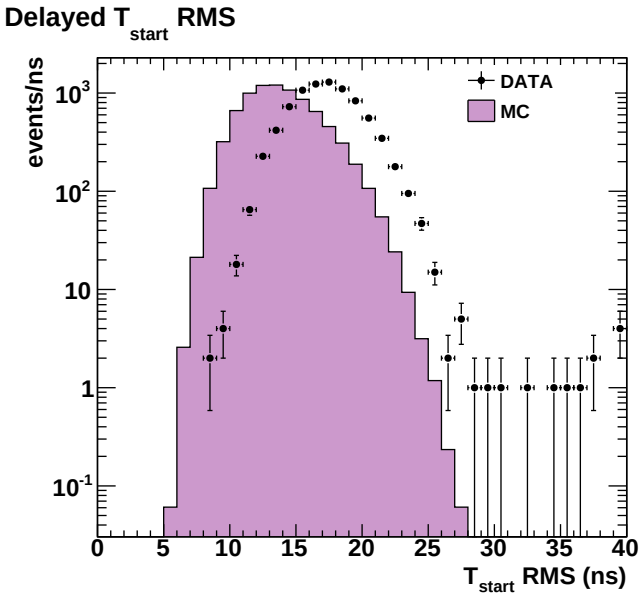


Figure 5.21: $t_{\text{start}}$ RMS for the delayed candidates.

The final important light noise reduction parameters are the maximum charge in a PMT to the total charge in an event (MQTQ), for both sets of events as shown in the Figs. 5.22 - 5.23 below.

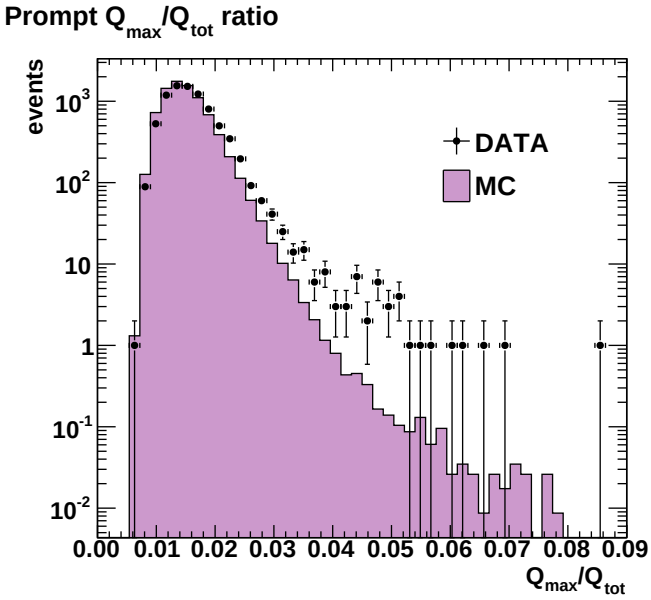


Figure 5.22: $Q_{\text{max}}/Q_{\text{tot}}$ ratio for the prompt candidates.

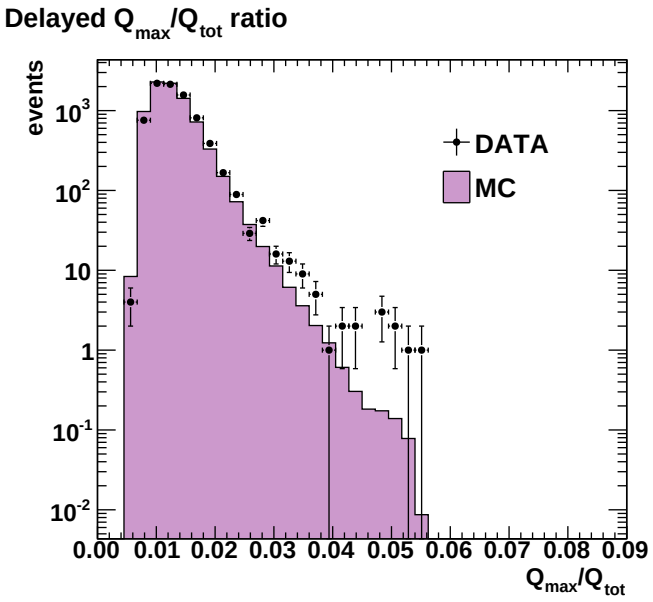


Figure 5.23: $Q_{\max}/Q_{\text{tot}}$ ratio for the delayed candidates.

## 5.3 Conclusion

In this Chapter, we discussed the selection of anti-neutrino candidates from the data as well as from the MC, were presented. The MC candidates were selected from a set of events with 100 times more statistics than the data. From the plots shown in this chapter, it can be concluded that the cuts used to select the anti-neutrino candidates are optimized to reduce the background and other sources of noise events. Also direct comparison of the data and MC selections shows the consistency between the two. The determination of $\theta_{13}$ based upon the candidates selected in this Chapter will be presented in Chapter 9.

# Chapter 6

# $^{252}$Cf Source

## 6.1 Spontaneous Fission Source

The radioisotope $^{252}$Cf is an intense source of neutrons which decays with 96.91% probability by $\alpha$ emission and 3.09% probability by spontaneous fission. It has a half life of 2.645 years and a specific activity of 0.536 mCi/$\mu g$. The average energy of the alpha particles emitted in its alpha decay is 6.1 MeV. During spontaneous emission 1$\mu$g of $^{252}$Cf can emit $2.314 \times 10^6$ neutrons per second. Both $\alpha$-decay and spontaneous fission are quantum mechanical barrier penetration phenomenon called "quantum tunneling" in which the wavefunction of a particle in a finite-sized potential barrier extends outside the barrier and so this paticle has a non zero probability to be outside the potential well [54].

Inside a nucleus the balance of forces is provided by the strong force and the Coulomb force. The strong force is a short range phenomenon and it can not even reach from one end to the other of a fair sized nucleus [33]. For a big nucleus, if a proton is at the edge of the nucleus, the srong force of attraction from the neighboring nucleons is much smaller than the Coulomb repulsion from the rest of the nucleons. In a case when the balance of the two forces is broken, the nucleus can break without acquiring any extra energy. The process of $\alpha$-decay results in an particle and the daughter nucleus as represented in general by the

following nuclear reaction

$$ {}^{A}_{Z}\mathrm{X}_{N} \rightarrow {}^{A-4}_{Z-2}\mathrm{X}_{N-2} + {}^{2}\mathrm{He} + Q_{\alpha} \tag{6.1} $$

where $Q_{\alpha}$ represents the energy released.

For example in the case of $^{238}$U, the value of $Q_{\alpha} \approx 6.22$ MeV. The emission of an $\alpha$ particle decreases the Coulomb energy of the nucleus without affecting the overall binding energy per nucleon because the $\alpha$ particle has nearly the same value of binding energy per nucleon as the parent nucleus. The half-life of a nucleus undergoing $\alpha$-decay is given by the Geiger-Nuttall law

$$ \log(\mathrm{t}_{1/2}) = A + \frac{B}{\sqrt{Q_{\alpha}}} \tag{6.2} $$

where A and B are constants.

The process of spontaneous fission is more complex than that of the $\alpha$-decay because the process depends on uncertainties like the masses of the two fragments, the number of prompt neutrons emitted and the energy released. Beyond the Bohr-Wheeler limit of $Z^2/A \approx 48$, a nucleus becomes unstable to spontaneous fission. In spontaneous fission, as the excited nucleus deforms the nuclear Coulomb energy decreases with the increase in distance between the nucleons while the nuclear surface energy increases with increase in the nucleus surface area.

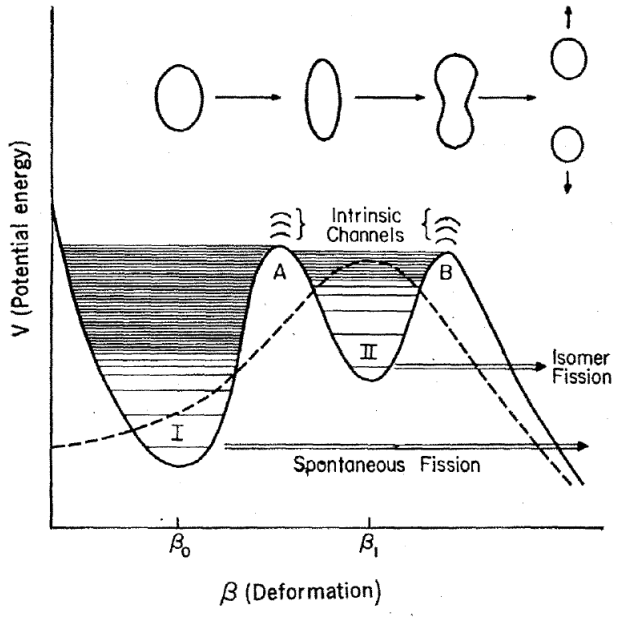


Figure 6.1: Schematic illustration of spontaneous fission [45].

At the saddle point the rate of change of the two energies are the same. After passing through this stage the nucleus very quickly separates into two fragments at the stage known as the "scission point". The energetic fission fragments emit "prompt neutrons" which take away most of their excitation energies. Prompt gammas are emitted in competetion with the last neutron, giving rise to the relation between the total number of prompt neutrons and the gamma energy. Sometimes the late $\beta$ emission of the fragments results in the emission of "delayed neutrons".

### 6.1.1 Theory of $^{252}$Cf Fission Source

The $\alpha$-decay of a $^{252}$Cf nucleus results in a $^{248}$Cm nucleus along with an $\alpha$ particle with a value of $Q_\alpha = 6.2169$ MeV. On the other hand, in the case of spontaneous fission the two fragments produced in a given energy, spin and parity distribution, de-excite first by emitting neutrons, mostly, thereby reducing their excitation energy but taking away very little spin. This is followed by a gamma cascade which removes most of their angular momentum.

### 6.1.2 Prompt Neutron Multiplicity and Energy Distribution

After the "saddle point", the nucleus moves irreversibly toward fission and at the "scission point" it breaks up into two fragments. The "hot" nuclear fragments cool down by emitting neutrons first, in a similar fashion to a heated liquid evaporating molecules. Hence one might expect the neutron energy spectra $N(E_N)$ of these evaporated neutrons to resemble a Maxwell-Boltzmann distribution with a corresponding effective temperature $T_{\text{eff}}$,

$$N_W(E) = \frac{2}{\sqrt{\pi}} \frac{\sqrt{E}}{T_{\text{eff}}^{3/2}} \exp(-\frac{E}{T_{\text{eff}}}.) \tag{6.3}$$

An improvement over the simple Maxwell-Boltzmann distribution is done by using a parameterized Watt spectrum which includes several factors such as (1) the motion of the fission fragments, (2) the distribution of the fission-fragment residual nuclear temperature, (3) the energy dependance of the cross-section for the inverse process of compound-nucleus formation and (4) the possibility of multiple-chance fission. A fit to the data to obtain a parameterized Watt spectrum was done by Frohner [36] and Mannhart [56] and the resultant energy spectrum for the prompt neutrons in the spontaneous fission of $^{252}$Cf is given by

$$N_W(E) = \frac{2}{\sqrt{\pi b a^3}} \exp(-\frac{ab}{4}) \exp(-\frac{E}{a}) \sinh(\sqrt{bE}), \tag{6.4}$$

where the Watt temperature $T_W = a$ and Watt energy $E_W = a^2 b/4$. Frohner showed the fit to the data resulted in $T_W = 1.174 \pm 0.008$ MeV and $E_W = 0.361 \pm 0.014$ MeV.

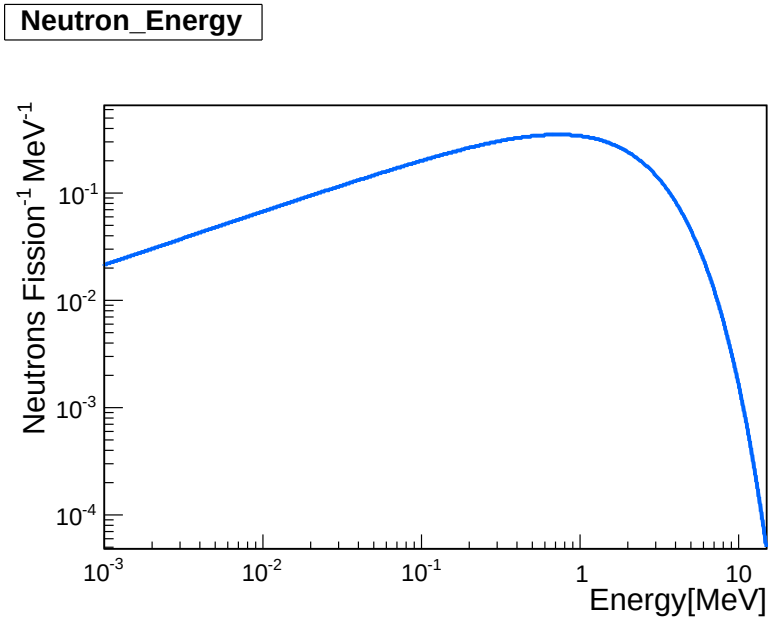


Figure 6.2: Neutron energy Watt spectrum in spontaneous fission of $^{252}$Cf using the parameters found by Frohner [36].

### 6.1.3 Gamma Multiplicity and Energy Distribution

The multiplicity of the prompt gamma rays in the spontaneous fission of $^{252}$Cf was experimentally measured by Brunson [49]. The distribution is a double Poisson model given by

$$\Pi(G) = 0.682\frac{7.20^G e^{-7.20}}{G!} + 0.318\frac{10.71^G e^{-10.72}}{G!}. \tag{6.5}$$

Here G is the gamma-ray multiplicity.

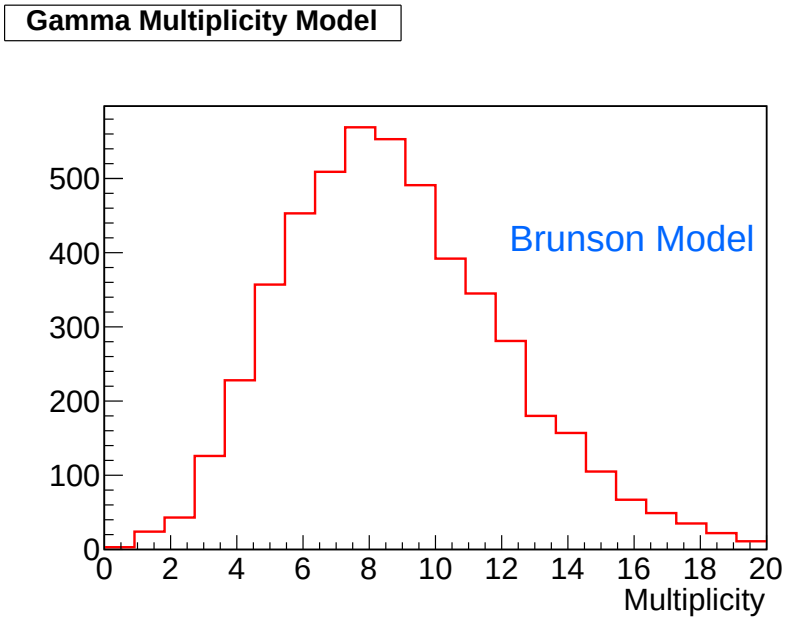


Figure 6.3: Brunson's model of gamma multiplicity in spontaneous fission of $^{252}$Cf.

The experimentally measured spectrum of the gamma ray energy for the spontaneous fission of $^{252}$Cf is well described by the relation [70]

$$N(E) = \begin{cases} 38.13(E-0.085)e^{1.648E}, & \text{E}< 0.3\text{MeV} \\ 26.8e^{-2.30E}, & 0.3\text{MeV} < E < 1.0\text{MeV} \\ 8.0e^{-1.10E}, & 1.0\text{MeV} < E < 8.0\text{MeV} \end{cases} \tag{6.6}$$

Eq. (6.6) comes from Valentine [69] and is a fit to the $^{235}$U measurement of Maienschein [55]. The reason for using the thermal fission of $^{235}$U data is that these are more precise than the $^{252}$Cf measurements. The resulting gamma energy spectrum is shown in Fig. 6.4 below

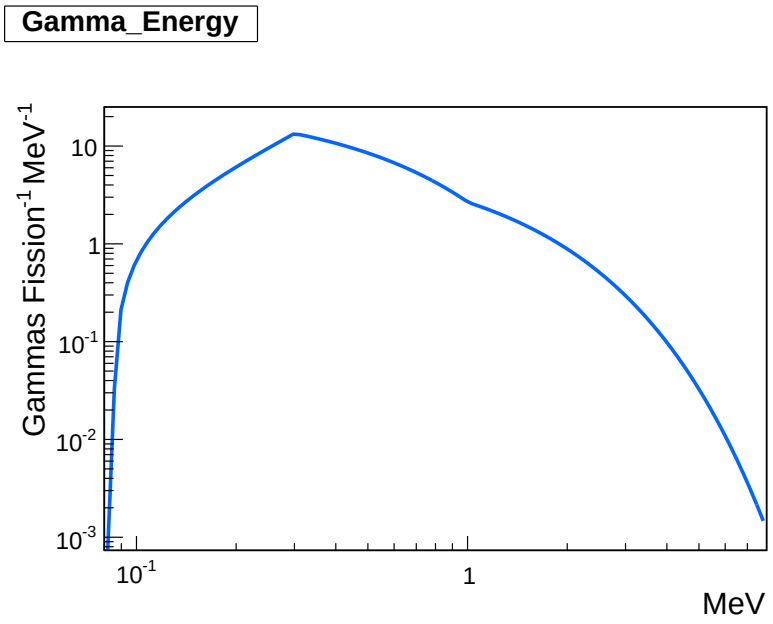


Figure 6.4: Gamma energy spectrum in spontaneous fission of $^{252}$Cf obtained from Eq. (6.6) which in turn is a parameterized fit to the measured spectra of thermal neutron induced fision of $^{235}$U.

The $^{252}$Cf Monte Carlo event generator for Double Chooz is based on the above formulation. This ensures that simulated events generated by the event generator have similar features to the experimental data.

### Neutron Efficiency with $^{252}$Cf Data and MC

As described in Chapter 5, the selection of IBD candidates depends upon several cuts, each of which remove some neutrino events along with the sources of background and noise. Hence it is essential to know the selection efficiencies of each of those cuts to good precision. This is achieved with the help of calibration source data and MC data in most cases.

The total efficiency of detection of the delayed neutrons $\epsilon_{\text{neut}}$ in the inverse beta decay reaction depends on the following fractions of (1) the fraction of neutrons captured on gadolinium, $\epsilon_{\text{Gd}}$, (2) the fraction of neutrons captured within the neutrino selection time window, $\epsilon_{\Delta T}$, and (3) the fraction of neutrons captured within the delayed energy range within, $\epsilon_{\Delta E}$ [5]

$$\epsilon_{\text{neut}} = \epsilon_{\text{Gd}} * \epsilon_{\Delta T} * \epsilon_{\Delta E}. \tag{6.7}$$

The relative error between the efficiencies with data and MC is assigned as the uncertainty in the central value of the given efficiency. We present here the comparison of the $^{252}$Cf data and MC and a way to extract the neutron multiplicity from the MC and the same after background subtraction in the case of data. The data selection cuts used in the $^{252}$Cf source analysis are similar to those described in Chapter 5 for the IBD candidate selection, with the following differences:

- Energy Cuts:
  - Prompt Energy Cut: 0.7 MeV $< E_{\text{prompt}} <$ 30 MeV. The prompt energy spectrum for the $^{252}$Cf fission extends far beyond the usual neutrino prompt spectrum.
  - Delayed Energy Cut: 0.7 MeV $< E_{\text{delayed}} <$ 30 MeV. To account for the multiple neutron captures in the same event window, the delayed capture window is extended beyond the normal capture windows for hydrogen and gadolinium captures.

- Prompt-Delayed Coincidence:
  - Time between consecutive prompt and delayed triggers $1\mu$s $< \Delta$T $<$ 1ms . This time window ensures that all the captures in gadolinum (mean capture time $30\mu$s) and in hydrogen (mean capture time $200\mu$s) are included. The lower cut of $1\mu$s is placed to exclude the recoil proton signal due to the slowing down of prompt neutrons as well as to remove the delayed prompt gammas.

- Light Noise Cut: These are the same as the ones used for the IBD candidate selection in Chapter 5.
  - $\mathrm{rms}(t_{\mathrm{start}}) < 40\mathrm{ns}$.
  - $Q_{\mathrm{max}}/Q_{\mathrm{tot}} < 0.09$ (Prompt events).
  - $Q_{\mathrm{max}}/Q_{\mathrm{tot}} < 0.055$ (Delayed events).

- Multiplictiy and Isolation Cuts:
  - No additional triggers from 1.5ms preceding the prompt signal. This long isolation before every prompt event ensures that there is no contamination of delayed neutron captures into the prompt gamma spectrum. This is a special isolation cut applied to the $^{252}$Cf data and it was not used for the IBD candidates.

- Cuts for Background Subtraction in Case of Data:
  - Unlike in the case of the MC, the $^{252}$Cf data includes background event which must be subtracted before any comparison to the MC can be done. The backgrounds present in the data can be of two kinds: (1) The usual backgrounds as in the case of the neutrinos. This includes all the external backgrounds, accidentals and the noises present during a normal data taking period. This background is removed by normalizing a data from a normal neutrino data run to the livetime of the $^{252}$Cf data run and subtracting from it. (2) The source-related background which may include the presence of other fissioning isotopes not yet included in the MC or the signal from the proton recoil of the prompt neutrons during the process of slowing down. This background is subtracted by running the same analysis for an offtime window of the same width but offset by 4ms from the normal time window described above.

In addition to determining the neutron detection effiiciency, the $^{252}$Cf source and MC data is used to calculate the fraction of total IBD events that spill in or spill out as described in Chapter 5.

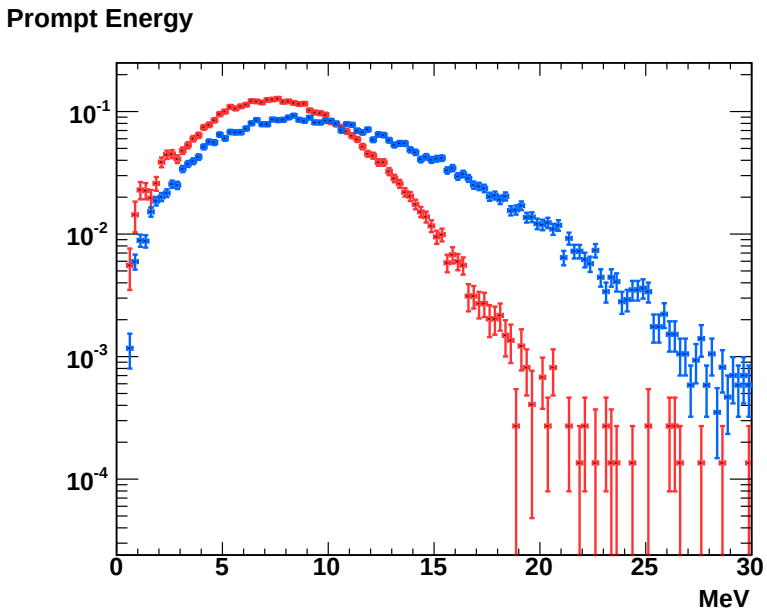


Figure 6.5: Comparison of prompt energy spectra for $^{252}$Cf fission, data (red) and MC (blue).

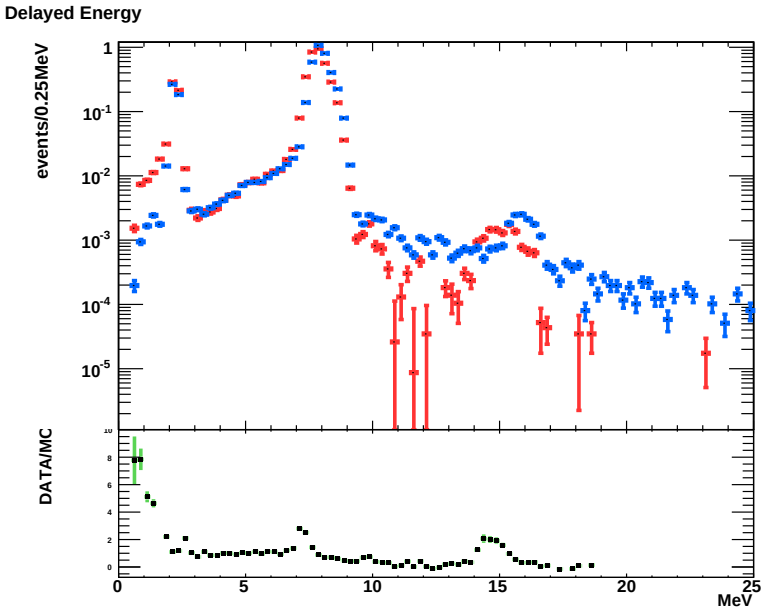


Figure 6.6: Comparison of delayed energy spectra for $^{252}$Cf fission, data (red) and MC (blue).

The apparent lack of agreement between the $^{252}$Cf source data and MC is clearly visible in Fig. 6.5. The data and MC agree much better for the delayed spectrum in Fig. 6.6 and the prompt-delayed $\Delta$T plot in Fig. 6.7. This could be indicative of the fact that the understanding of the gamma spectrum of $^{252}$Cf spontaneous fission must be improved by performing more precise measurements. However, it must be noted that due to very close agreement in case of the delayed neutron capture energy and the prompt-delayed $\Delta$T, a loose cut of 0.7MeV [51] or a tight cut of 7MeV [5] has little effect on the outcome of the calculations for the neutron detection efficiency or the Gd fraction.

From Fig. 6.6 we see that the data compares fairly well to the MC as far as the presence of background in the low energy region is concerned. The agreement at the two capture peaks, especially at the Gd peak between $[6, 12]$ MeV is very good.

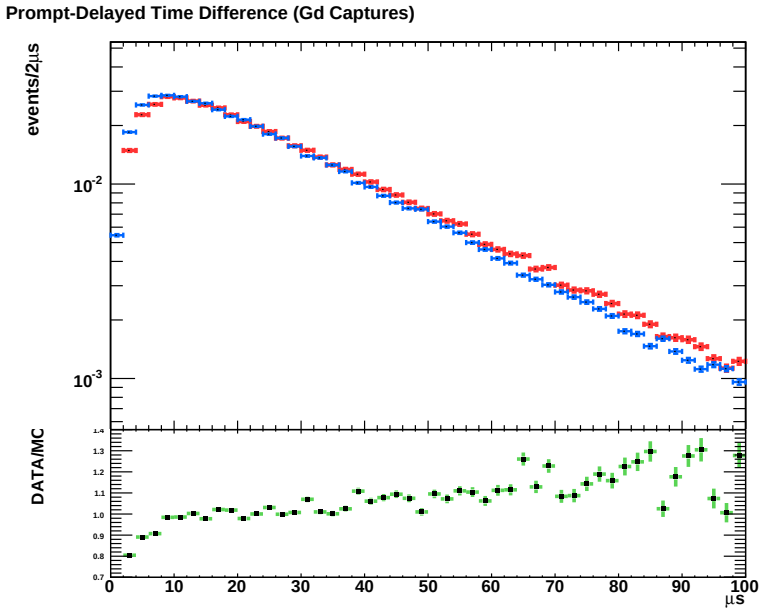


Figure 6.7: Comparison of prompt-delayed time difference for gadolinium captures, with data (red) and MC (blue).

From Figs. 6.7 and 6.8 we can see that there is a discrepancy between the neutron capture times from the data and the MC, especially at $\Delta T < 10\mu$ s. This was investigated and was concluded to be an imperfection in the modeling of neutron thermalization in the MC

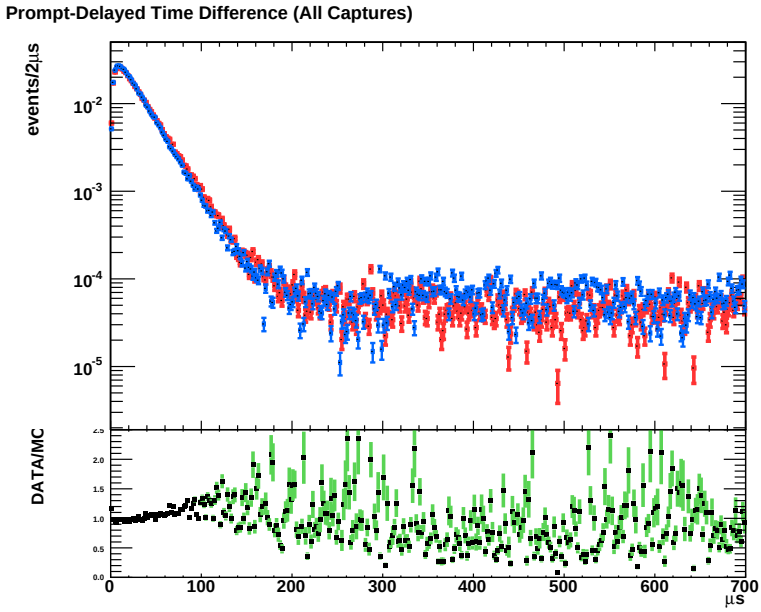


Figure 6.8: Comparison of prompt-delayed time difference for all hydrogen and gadolinium captures, data (red) and MC (blue).

rather than any kind of inefficieny of trigger [61]. The agreement between data and MC for the H-captures ($[0, 700]\mu$s) is very useful for calculating the $\Delta$T efficiency, ($\epsilon_{\Delta T}$).

Using the cuts for selection and background subtraction described above, the background subtracted prompt neutron multiplicity from the $^{252}$Cf source data were found to be

$$N_{MC} = 3.741 \pm 0.0078$$

,

$$N_{DATA} = 3.735 \pm 0.0082$$

. The numbers above give the number of neutrons emitted per fission of a $^{252}$Cf nucleus in the source data and the MC. Figs. 6.9 and 6.10 show the neutron multiplicty distribution in normalized and logarithmic scale respectively.

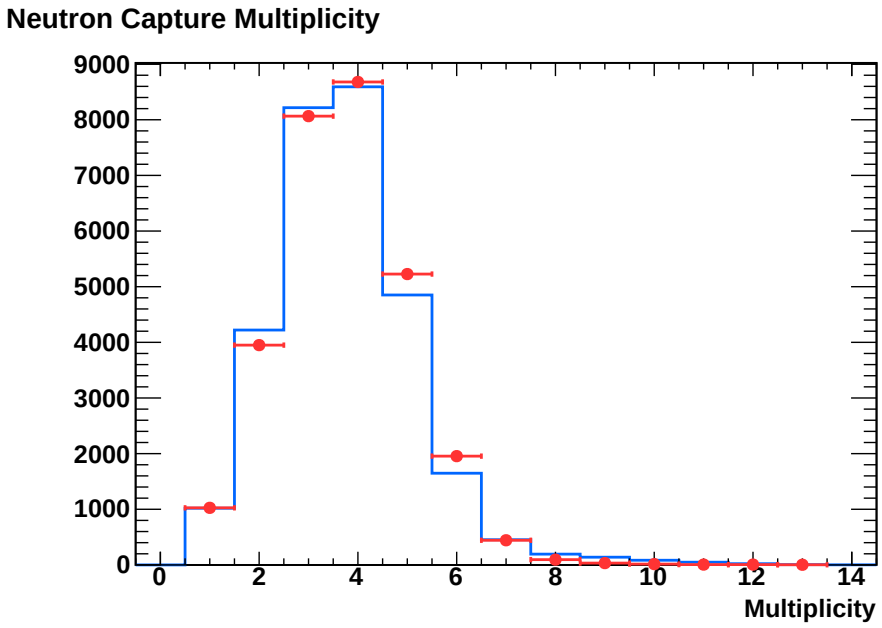


Figure 6.9: Comparison of prompt neutron multiplicity for the $^{252}$Cf fission, data (red) and MC (blue).

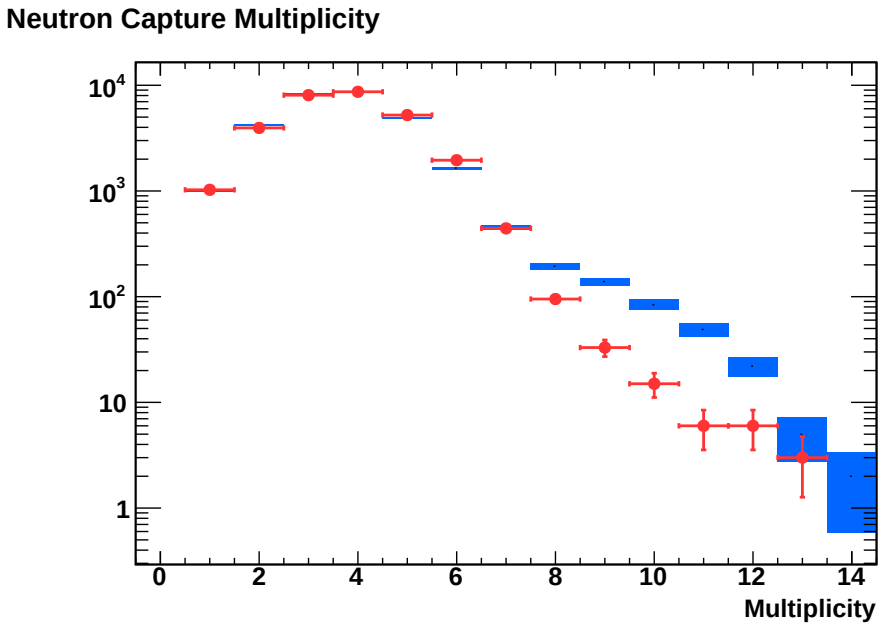


Figure 6.10: Comparison of prompt neutron multiplicity for the $^{252}$Cf fission, data (red) and MC (blue) in logarithmic scale.

### 6.1.4 Neutron Detection Efficiency with Prompt Neutron Multiplicity

The efficiency for the detection of the neutron captures in the detector can be directly determined by using the captures of the prompt neutrons coming from the calibration source $^{252}$Cf. Assuming an ideal source and detector and that the probability of detecting one neutron is independent of the probability of detecting any other neutron, if $n$ is the number of neutrons emitted in a fission, then the number of them being detected is given by

$$N_{det} = \epsilon n, \tag{6.8}$$

where $\epsilon$ denotes the single neutron detection efficiency. If the multiplicity of the prompt neutrons for $^{252}$Cf follows a distribution $G(n)$ then the mean number of neutrons detected is given by [4]:

$$N_{det} = \epsilon \sum_{j=1}^{\infty} nG(n). \tag{6.9}$$

The accepted value for $\sum_{j=1}^{\infty} nG(n)$ is $3.757 \pm 0.010$ [38]. Therefore, in principle, calculating the neutron detection efficiency using the neutron multiplicity should be straightforward. However, there is a difficulty in doing so in practice. It has been shown by Nifenecker [58], that for individual fragments, both the prompt neutrons as well as the prompt gammas show the same saw-tooth shape when plotted as a function of fragment mass [35]. From these data a linear relation between the prompt gamma energy and neutron multiplicity was derived which is given by Valentine [69] as

$$E_t(n) = 0.75n + 4.0. \tag{6.10}$$

However this has neither been experimentally verified nor been correctly modeled in the simulations. In fact, Bluel et al. [16] reported observing a lack of correlation between the two with uncertainties due to high background effects and potential bias introduced in the event selection. In Fig. 6.11 we present the measured correlation between the gamma ray energies and the neutron multiplicity in the Double Chooz detector.

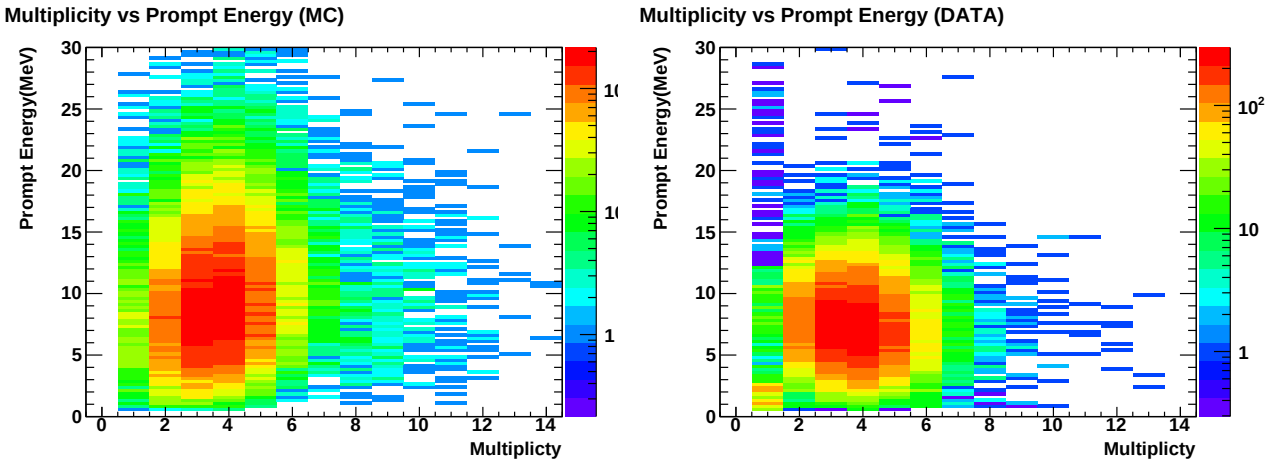


Figure 6.11: Prompt gamma energy vs neutron multiplicity for MC [left] and data [right].

The following plots, in Fig. 6.12 and Fig. 6.13, show the relation between the average value of gamma energy vs neutron multiplicity and vice-versa for both data and MC. All the data plots are drawn after background subtraction described earlier.

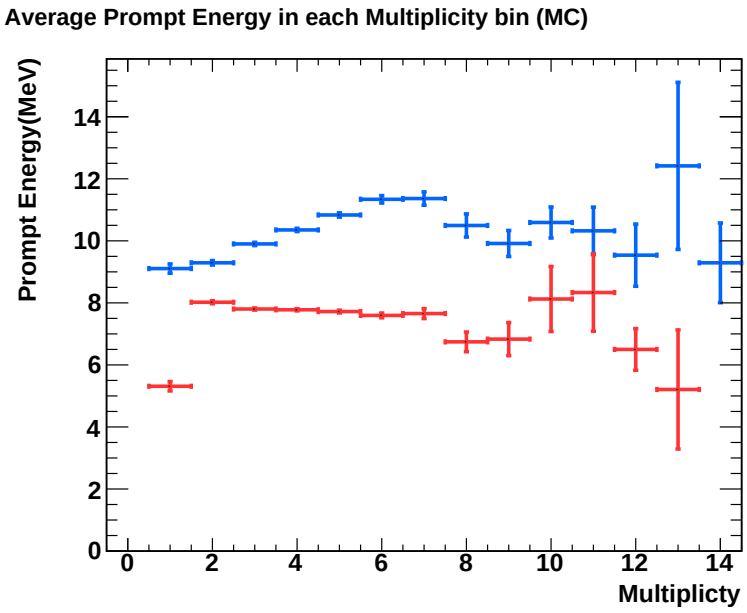


Figure 6.12: Variation of average prompt gamma energy with neutron multiplicity for data (red) and MC (blue).

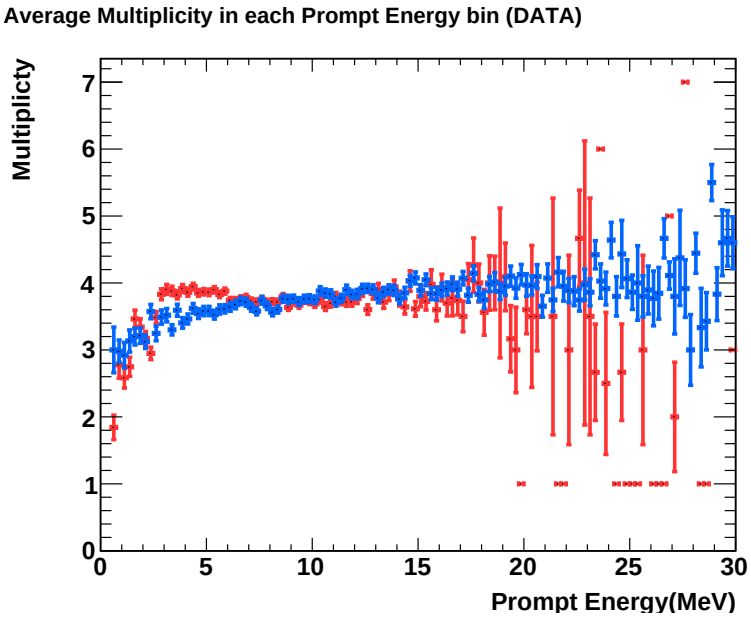


Figure 6.13: Variation of mean neutron multiplicity with prompt gamma energy threshold for data (red) and MC (blue).

No clear indication of such a correlation was obtained from the data and the MC. Such a correlation would imply a bias in the neutron multiplicity induced by any possible cut applied on the prompt gamma energy. The calculation of the neutron detection efficiency using the neutron multiplicity is a direct and powerful cross-check of the value for the neutron detection efficiency given in Eq. (6.8). However, such a direct comparison needs a good understanding of the expected number of fission for a given cut on the gamma energy. In other words a knowledge of the gamma-neutron correlation is extremely important for such a calculation. Continued studies are needed to enable future experiments to measure the neutron efficiency better using the detected neutron multiplicity, as well as improved nuclear fission models.

# Chapter 7

# Analysis of Reactor Off Data

Double Chooz was unique among the reactor neutrino experiments to have two significant periods when both the reactors were turned off. This gave the experiment an excellent opportunity to validate the previous analyses of various background candidates with the reactor-on data [29]. There were two separate periods in which both reactors B1 and B2 of the Chooz nuclear reactor were turned off. The first reactor-off period had a runtime of 0.93 days while the second period had a runtime of 6.6 days giving a total 7.53 days of complete reactor-off time. An analysis of the data during this period was done by selecting the candidates using the standard neutrino selection candidates as well as doing specialized analayses for specific background sources, namely correlated backgrounds and $^{9}$Li backgrounds. The selection was primarily done using two broader sets of cuts: The first set, "Standard" contained the minimal set of cuts applied for the neutrino candidate selection as discussed in Chapter 5, while the second set, "$^{9}$LiReduced + OV" contained additional cuts to reduce the cosmogenic $\beta - n$ background and the $\mu$/Fast-N candidates producing the correlated backgrounds. All these cuts are described in detail in Chapter 5. The details of the candidate selection with the two sets of cuts used are summarized below:

- Standard Cuts: (1) Prompt Energy Cut: 0.7 MeV $< E_{prompt} <$ 12.2 MeV. (2) Delayed Energy Cut: 6.0 MeV $< E_{delayed} <$ 12 MeV. (3) Time between consecutive prompt and

delayed triggers $2\mu s < \Delta T < 100\mu s$. (4) RMS($t_{start}$) $< 40$ ns. (5) $Q_{max}/Q_{tot} < 0.09$ (Prompt events). (6) $Q_{max}/Q_{tot} < 0.055$ (Delayed events). (7) No additional triggers from $100\mu s$ preceding the prompt signal to $400\mu s$ after it. (8) Muon Event: (a) Total charge in Inner Veto $> 10000$ DUQ. (b) Energy in the Inner Detector $> 30$ MeV. (9) 1 ms veto applied after the last muon.

- Additional Cuts: (1) To reject those candidates which are correlated, in time, to a showering muon ($E_\mu > 600$ MeV), an additional veto of 0.5 s is applied after each showering muon. (2) Also candidates whose prompt signal are coincident with an OV trigger, initiated by a muon passing through the OV, are excluded.

| Observable | Reactor Off-Off | | |
|---|---|---|---|
| | Period 1 | Period 2 | Total |
| Runtime (days) | 0.93 | 6.6 | 7.53 |
| Livetime (days) | 0.804 | 6.022 | 6.84 |
| Average Muon Rate (Hz) | $45.99 \pm 0.025$ | $46.498 \pm 0.009$ | – |

Table 7.1: The runtime, livetime and muon rates for the two reactor off-off periods with "$^9$LiReduced + OV" cuts.

The values of the runtime, livetime and muon rates are listed in Table 7.1. For the "Standard" cuts, the total livetime was found to be 0.85 days and 6.34 days for the first and second reactor off-off periods respectively resulting in a total livetime of 7.19 days. The results of the candidate selection for the reactor off-off periods are shown in the following histograms. Fig. 7.1 and Fig. 7.2 show the distribution of prompt energy and the delayed energy plots for the selected candidates both with the "Standard" cut as well as the "$^9$LiReduced + OV" cuts. Fig. 7.2 shows the delayed energy spectrum of the candidates superimposed on the anti-neutrino Monte Carlo (MC) spectrum. The histograms have been drawn with markers also showing the empty bins without data.

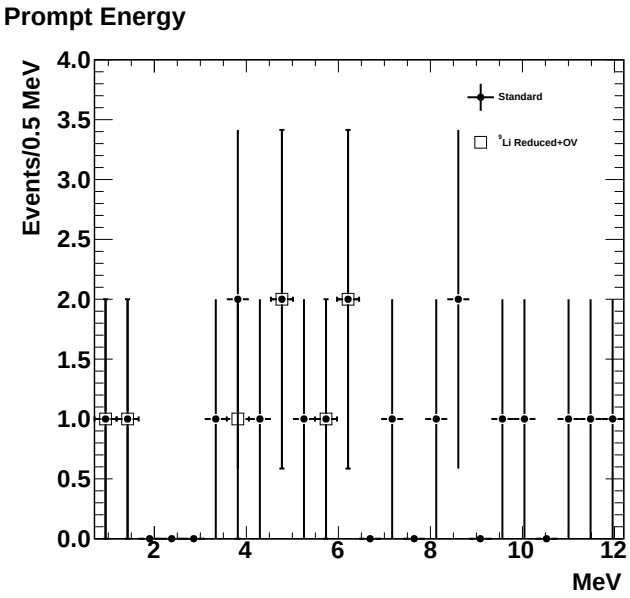


Figure 7.1: Prompt energy spectrum for the off-off candidates.

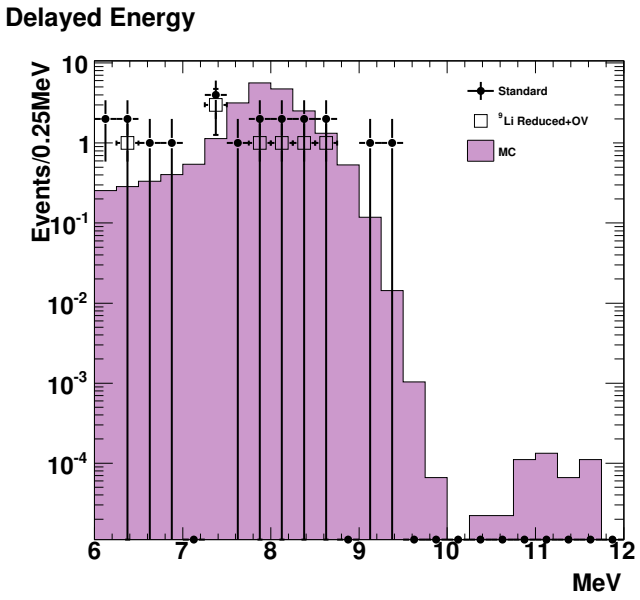


Figure 7.2: Delayed energy spectrum for the off-off candidates.

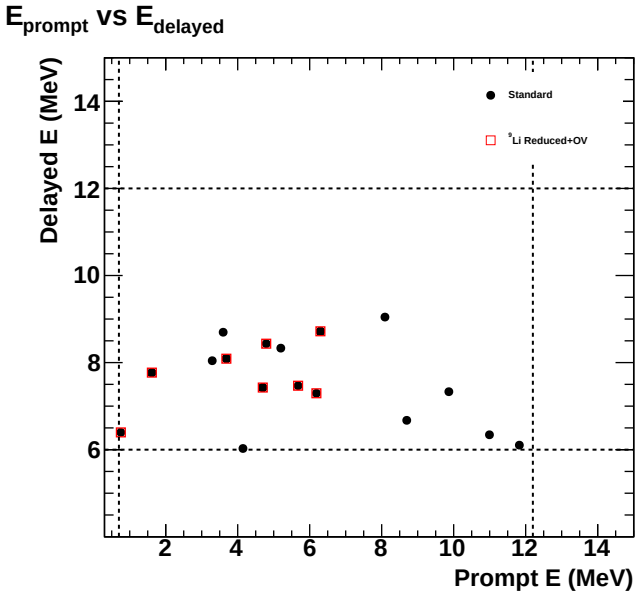


Figure 7.3: Prompt energy vs delayed energy for the off-off candidates. The dashed lines show the selection cuts applied.

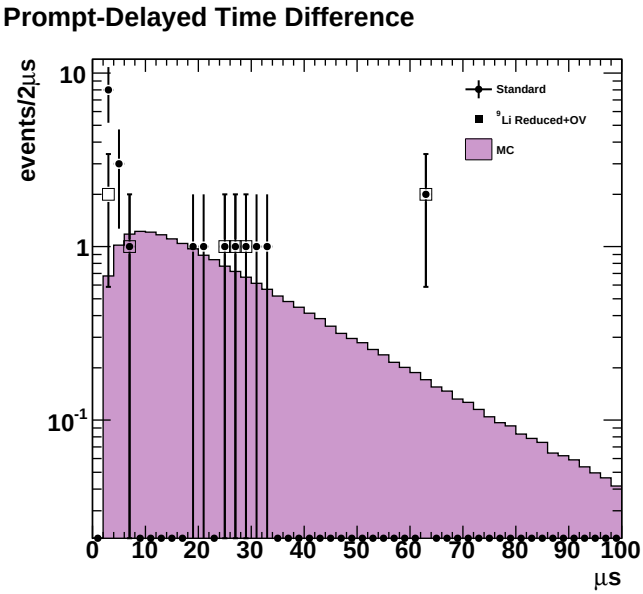


Figure 7.4: Time delay between the prompt and delayed candidates for the off-off candidates.

In Fig. 7.4, due to presence of a data point which is far off from the MC, a $\chi^2$-test was performed to compare the data and the MC results. The test resulted in a $\chi^2$/NDF of 21.83/48 with a probability of 0.999583.

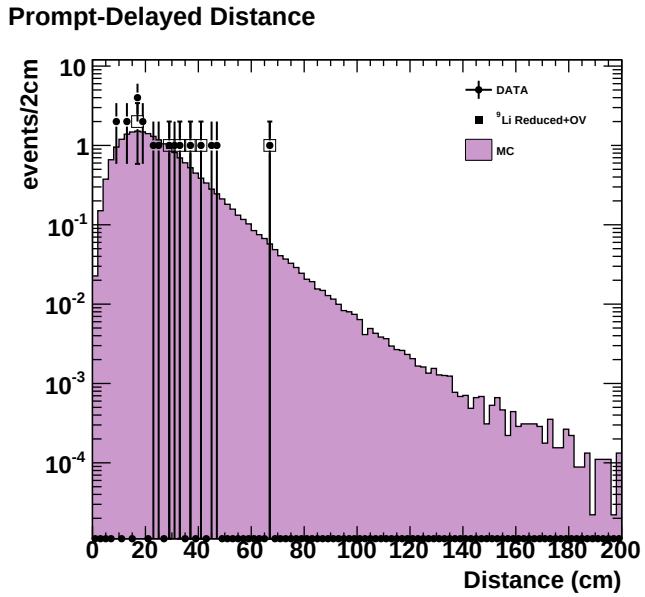


Figure 7.5: Distance between the prompt and delayed candidates for the off-off candidates.

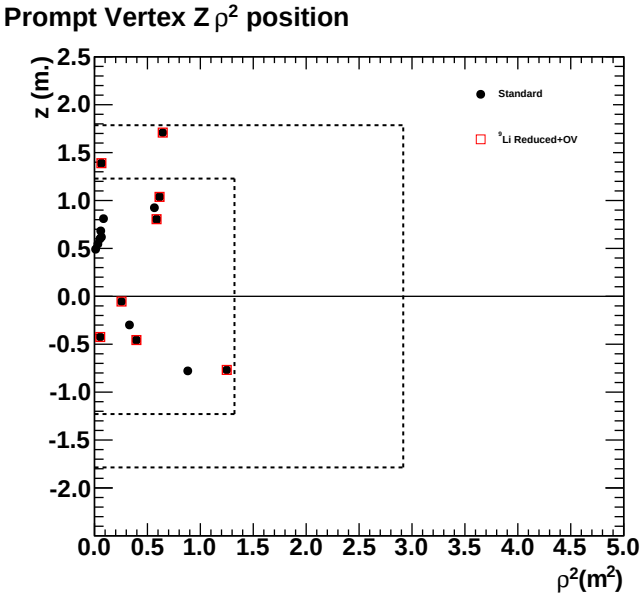


Figure 7.6: $Z - \rho^2$ vertices of the prompt candidates for the off-off candidates. The dotted line squares show the Target and Gamma Catcher volumes respectively.

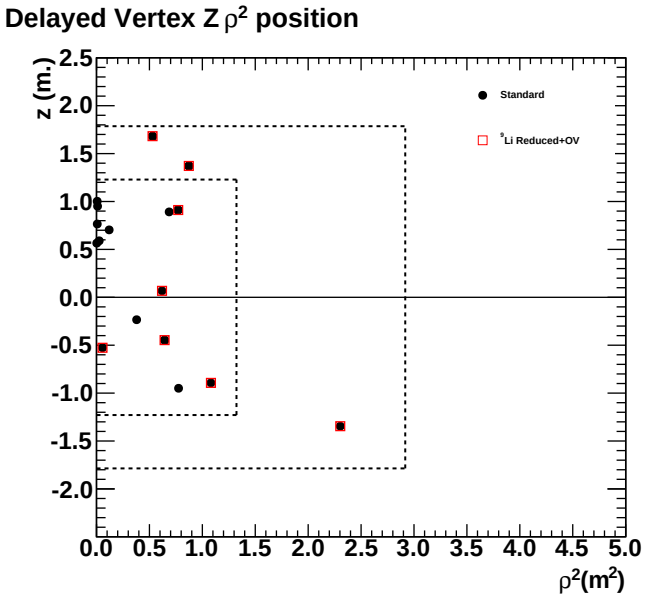


Figure 7.7: $Z - \rho^2$ vertices of the delayed candidates.

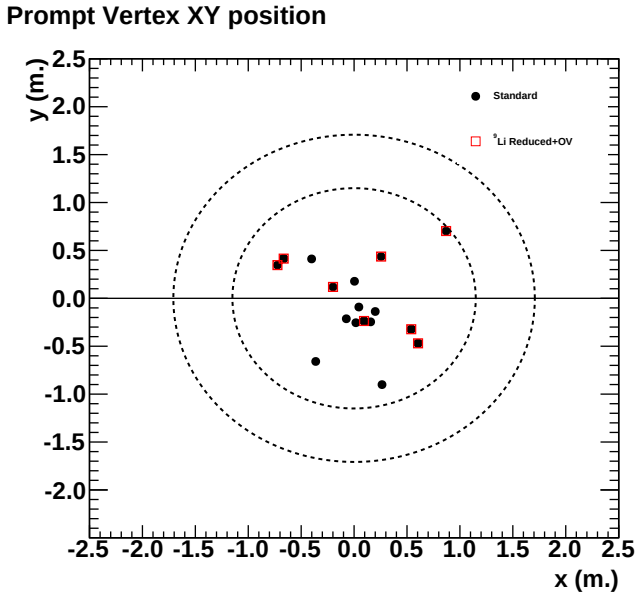


Figure 7.8: x-y vertices of the prompt candidates. The dotted line cirlces show the Target and Gamma Catcher volumes respectively.

From Figs. 7.6 - 7.9, it is easy to see the cluster of events with high z-value and low radial distance which are candidates for stopping muons sneaking through the target chimney.

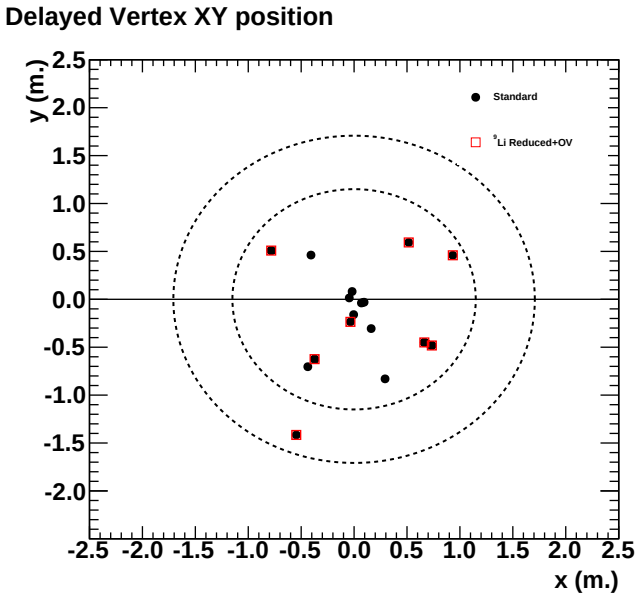


Figure 7.9: x-y vertices of the delayed candidates for the off-off candidates.

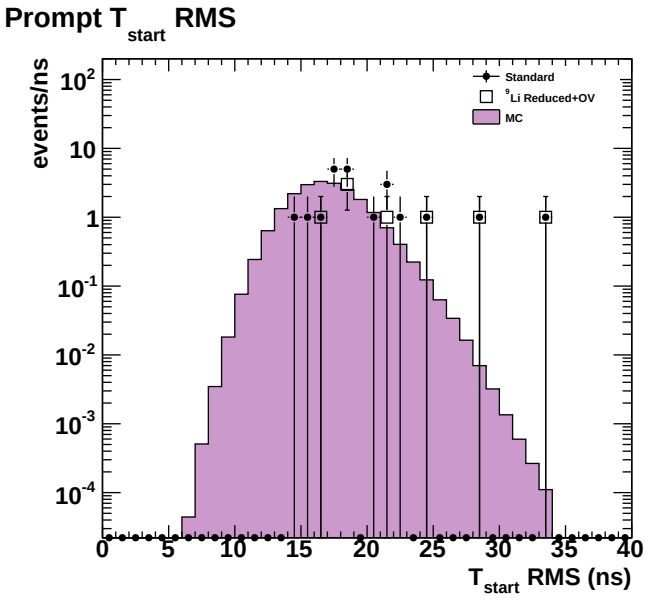


Figure 7.10: $T_{\text{start}}$ RMS for the prompt candidates for the off-off candidates.

Another $\chi^2$-test of histogram comparison was performed for Fig. 7.10 and Fig. 7.11 because of the apparent lack of data points below 14ns. The test yielded a $\chi^2$/NDF of 12.74/27 with a probability of 0.991 and 25.79/22 with a probability of 0.26 for the two figures respectively.

It must be noted that the cut on the RMS of the arrival time of the pulses at the PMT used is RMS($T_{\text{start}}$) < 40ns. The efficiency of this cut is 100% and no other use of this cut is made.

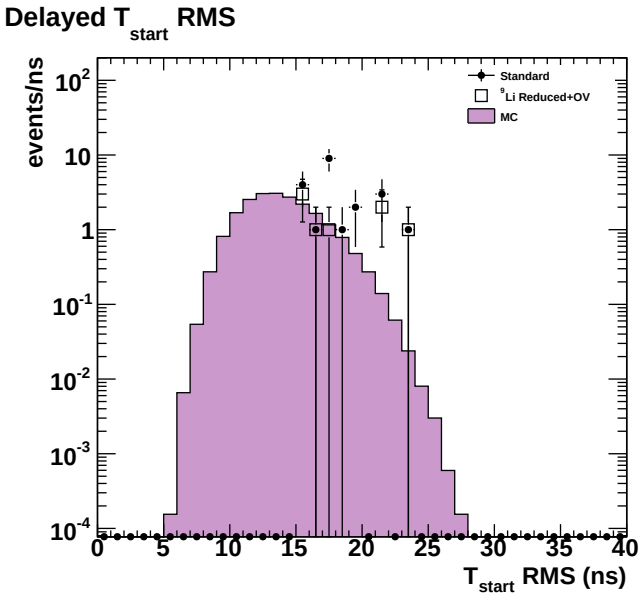


Figure 7.11: $T_{\text{start}}$ RMS for the delayed candidates for the off-off candidates.

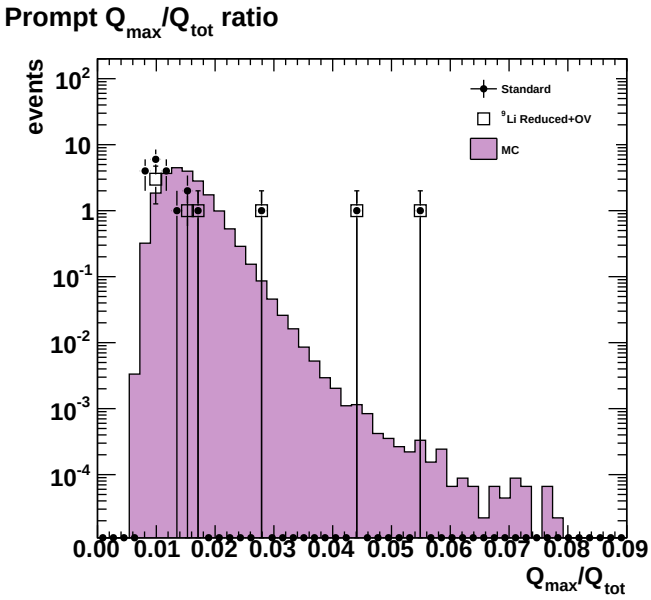


Figure 7.12: $Q_{max}/Q_{tot}$ ratio for the prompt candidates for the off-off candidates.

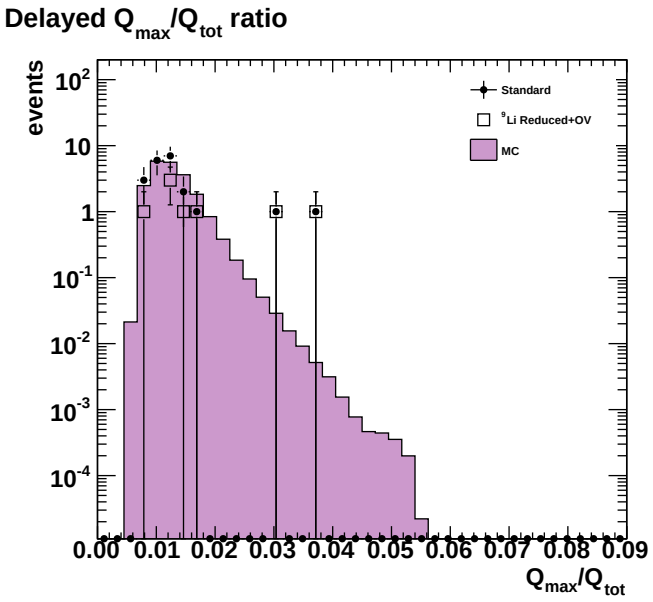


Figure 7.13: $Q_{max}/Q_{tot}$ ratio for the delayed candidates for the off-off candidates.

## 7.1 Background Estimation

The "Standard" cuts resulted in 21 candidate events while the "$^9$LiReduced + OV" cuts yielded 8 candidates during the same period. At the same time, it is very possible for an actual neutrino event to be present in these candidate events due to the delayed activity of the long-lived isotopes in the reactor fuel. A dedicated simulation of the residual neutrino spectrum was done with FISPACT [34], an evolution code predicting the isotope inventory in the reactor cores. The neutrino spectrum is then computed using the BESTIOLE [25] database. The resulting total number of neutrino interactions during the reactor-off period after veto and efficiency correction is $2.49 \pm 0.60$ ($1.42 \pm 0.57$) for the two selection cuts respectively.

After subtracting the expected number of neutrinos during this period, the measured total background is given by $2.7 \pm 0.60$/day ($1.0 \pm 0.4$/day) [27]. These measurements are consistent within uncertainties with background estimates of $3.4 \pm 0.6$/day ($2.0 \pm 0.6$/day) made with the reactor-on data [29].

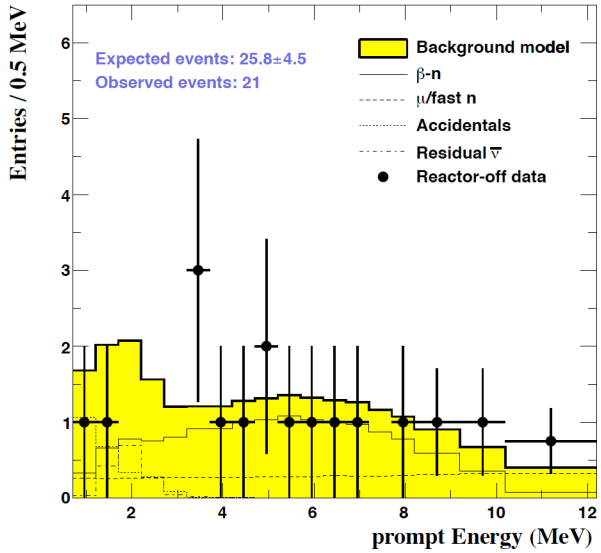


Figure 7.14: Anti-neutrino ($\bar{\nu}_e$) candidates in reactor-off data selected with "Standard" cuts [27].

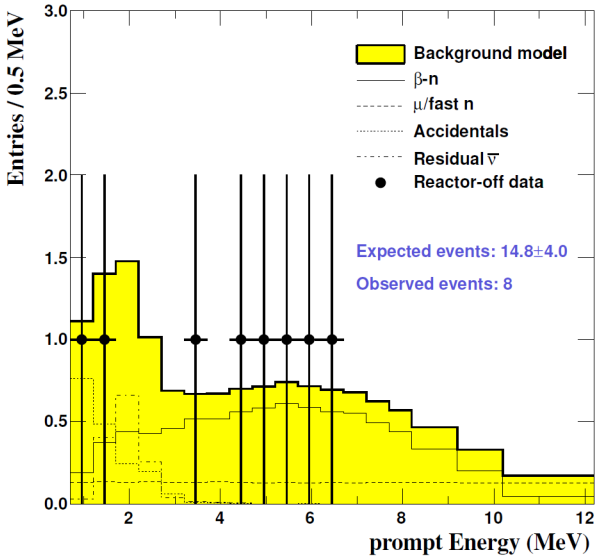


Figure 7.15: Anti-neutrino ($\bar{\nu}_e$) candidates in reactor-off data selected with"$^9$LiReduced + OV" cuts [27].

## 7.2 Scaling Relations for Cosmogenic Products

The text in this section is closely based on the text written by me for the internal Double Chooz technical note [13]. The rates of the IBD candidates coming from the sources like the correlated backgrounds (excluding the stopping scaling relations numbersmuon ($\mu$'s)) and $\beta$-n backgrounds can be scaled to other experimental sites such as Daya Bay, RENO and the future Double Chooz Near detctor. The scaling rules for a cosmogenic product between any two experiments can be derived using simple relations. Let us define a few symbols used in the derivation of these single relations. We define a cosmogenic isotope "b", the various observables related to "b" will be measured in units of length $[l]$, mass $[m]$ and time $[t]$. The various symbols for these observables are shown in the Table 7.2 below.

| Symbol | Description | Dimension |
|---|---|---|
| $N_b$ | Count of b | [b] |
| $N_{b_\mu}$ | Number of b per $\mu$ | $[b.\mu^{-1}]$ |
| $n_b$ | Number density of b per volume | $[b.l^{-3}]$ |
| $\lambda_b$ | Number linear density of b | $[b.l^{-1}]$ |
| $\lambda_{b_\mu}$ | Number linear density of b | $[b.\mu^{-1}l^{-1}]$ |
| $Y_{b_\mu}$ | Specific(mass) yield of b per $\mu$ | $[b.\mu^{-1}l^2.m^{-1}]$ |
| $\alpha_{X->Y}$ | Cross section for process $X->Y$ | $[l^2.Y.X^{-1}]$ |
| $m_b$ | Molar mass of substance b | $[m.mole^{-1}]$ |
| $M_X$ | Total mass of object X | $[m]$ |
| $\rho_X$ | Density of X | $[m.l^{-3}]$ |
| $R_b$ | Total productin rate of b | $[b.t^{-1}]$ |
| $r_b$ | Specific(mass) production rate of b | $[b.m^{-1}.t^{-1}]$ |
| $N_A$ | Avogadro's number | $[mole^{-1}]$ |

Table 7.2: The list of symbols and their dimension, used in the derivation of the scaling relations.

## General Relations

We now derive the general relations. The carbon number density in a liquid scintillator (LS) with $N_{C_{\rm LS}}$ carbon atoms per LS molecule is

$$n_c = \frac{N_A N_{C_{\rm LS}} \rho_{\rm LS}}{m_{\rm LS}}$$

. The linear number density of b produced per $\mu$ in LS is

$$\lambda_{b_\mu} = n_c \sigma_{(C+\mu->b+\text{anything})}.$$

The number of b produced per $\mu$ in the LS over an average muon track length $\langle L_\mu \rangle$ is

$$N_{b_\mu} = \lambda_{b_\mu} \langle L_\mu \rangle.$$

The specific yield of b per $\mu$ in LS of density $\rho_{LS}$ is

$$Y_{b_\mu} = \frac{\lambda_{b_\mu}}{\rho_{LS}} = \frac{N_{b_\mu}}{\rho_{LS}\langle L_\mu \rangle} = \frac{N_A N_{C_{LS}}}{m_{LS}} \sigma_{(C+\mu->b+\text{anything})}. \tag{7.1}$$

Total rate, from specific rate and total mass $M$ is given by

$$R = rM$$

. Also, the number b per $\mu$ from total numbers or total rates is

$$N_{b_\mu} = \frac{N_b}{N_\mu} = \frac{R_b}{R_\mu}$$

.

## Scaling Relations

The cross-section scales with average muon energy E as:

$$\sigma \propto \langle E \rangle^{\alpha}$$

So the scaling relation between two experiments expt.1 and expt.2 can be derived as follows:

The specific yield can be written from Eq. (7.1) as :

$$\frac{Y_{b_\mu[\text{expt.1}]}}{Y_{b_\mu[\text{expt.2}]}} = \frac{\sigma_{[\text{expt.1}]}}{\sigma_{[\text{expt.2}]}} \frac{N_{C_{LS}[\text{expt.1}]}}{N_{C_{LS}[\text{expt.2}]}} \left(\frac{m_{LS[\text{expt.1}]}}{m_{LS[\text{expt.2}]}}\right)^{-1}$$
$$= \left(\frac{\langle E \rangle_{[\text{expt.1}]}}{\langle E \rangle_{[\text{expt.2}]}}\right)^{\alpha} \frac{N_{C_{LS}[\text{expt.1}]}}{N_{C_{LS}[\text{expt.2}]}} \left(\frac{m_{LS[\text{expt.1}]}}{m_{LS[\text{expt.2}]}}\right)^{-1}$$

.

The number of b per $\mu$ scales as:

$$\frac{N_{b_\mu[\text{expt.1}]}}{N_{b_\mu[\text{expt.2}]}} = \frac{Y_{b_\mu[\text{expt.1}]}}{Y_{b_\mu[\text{expt.2}]}} \frac{\rho_{LS[\text{expt.1}]}}{\rho_{LS[\text{expt.2}]}} \frac{\langle L_\mu \rangle_{[\text{expt.1}]}}{\langle L_\mu \rangle_{[\text{expt.2}]}}$$
$$= \left(\frac{\langle E \rangle_{[\text{expt.1}]}}{\langle E \rangle_{[\text{expt.2}]}}\right)^{\alpha} \frac{N_{C_{LS}[\text{expt.1}]}}{N_{C_{LS}[\text{expt.2}]}} \frac{\rho_{LS[\text{expt.1}]}}{\rho_{LS[\text{expt.2}]}} \frac{\langle L_\mu \rangle_{[\text{expt.1}]}}{\langle L_\mu \rangle_{[\text{expt.2}]}} \left(\frac{m_{LS[\text{expt.1}]}}{m_{LS[\text{expt.2}]}}\right)^{-1}$$

.

The rates of production can be derived from the above general relations between various quantities. The total rate of production of the quantity b is $R_b = N_{b_\mu} R_\mu$

and the specific rate is

$$r_b = \frac{R_b}{M} = \frac{N_{b_\mu} R_\mu}{M}$$

. Applying the above prescription, the scaling law for $r_b$ becomes

$$\frac{r_{[\text{expt.1}]}}{r_{[\text{expt.2}]}} = \left(\frac{\langle E \rangle_{[\text{expt.1}]}}{\langle E \rangle_{[\text{expt.2}]}}\right)^{\alpha} \frac{N_{C_{LS}[\text{expt.1}]}}{N_{C_{LS}[\text{expt.2}]}} \frac{\rho_{LS[\text{expt.1}]}}{\rho_{LS[\text{expt.2}]}} \frac{R_{\mu[\text{expt.1}]}}{R_{\mu[\text{expt.2}]}} \frac{\langle L_\mu \rangle_{[\text{expt.1}]}}{\langle L_\mu \rangle_{[\text{expt.2}]}} \left(\frac{m_{LS[\text{expt.1}]}}{m_{LS[\text{expt.2}]}} \frac{M_{[\text{expt.1}]}}{M_{[\text{expt.2}]}}\right)^{-1}$$

. It can be shown from the definition of the average length $\langle L_\mu \rangle$ that the product $R_\mu \langle L_\mu \rangle$ is equal to the average muon flux (muons per unit time per unit area) times the volume of the active area.

Therefore $\phi = \rho R_\mu \langle L_\mu \rangle / \mathrm{M}$ is simply the average muon flux. So we can write

$$\frac{r_{[\text{expt.1}]}}{r_{[\text{expt.2}]}} = \left( \frac{\langle E \rangle_{[\text{expt.1}]}}{\langle E \rangle_{[\text{expt.2}]}} \right)^{\alpha} \frac{N_{C_{LS}[\text{expt.1}]}}{N_{C_{LS}[\text{expt.2}]}} \left( \frac{m_{LS[\text{expt.1}]}}{m_{LS[\text{expt.2}]}} \right)^{-1} \frac{\phi_{[\text{expt.1}]}}{\phi_{[\text{expt.2}]}} \tag{7.2}$$

## Corrections due to Scintillator Compositions

In this section we discuss in detail the effect of the factors related to the scintilator composition for the different experiments. Table 7.3 shows the scintillator compositions for the experiments.

| Double Chooz | KamLAND | Daya Bay | RENO |
|---|---|---|---|
| Dodecane(80%) $[CH_3(CH_2)_{10}CH_3]$ O-PXE(20%) $[C_{16}H_{18}]$ | Dodecane(80%) $[CH_3(CH_2)_{10}CH_3]$ Pseudocumene(20%) $[C_9H_{12}]$ | LAB $[C_6H_5C_NH_{2N+1}]$ | LAB $[C_6H_5C_NH_{2N+1}]$ |

Table 7.3: Chemical compositions of the various scintillators. The scintillators for Daya Bay and RENO have been assumed to be pure LAB based with N=12.

The total number of scintillator molecules $X$ in a unit volume is

$$N_{LS_X} = \frac{\rho_{LS} N_A}{m_{LS}}$$

. The carbon number (C) per volume of the scintillator $X$ with $N_{C_{LS}}$ carbon atoms per molecule is

$$n_c = \left[ \frac{\rho_{LS} N_A}{m_{LS}} \right] N_{C_{LS}}$$

and the corresponding hydrogen number (H) with $N_{H_{LS}}$ hydrogen atoms per LS molecule is given by

$$n_h = \left[ \frac{\rho_{LS} N_A}{m_{LS}} \right] N_{H_{LS}}$$

.

The values of the various quantities specific to the experiments under discussion are listed in Table 7.4.

| Detector | Density $(g/cc)$ | $N_{C_{LS}}$ | $N_{H_{LS}}$ | $n_c$ $(10^{28}\mathrm{Cm}^{-3})$ | $n_h$ $(10^{28}\mathrm{Hm}^{-3})$ | $m_{LS}$ | volume $(\mathrm{m}^3)$ |
|---|---|---|---|---|---|---|---|
| RENO | 0.86 | 18 | 30 | 3.78 | 6.31 | 246.43 | 16 |
| Double Chooz | 0.80 | 12.84 | 24.32 | 3.46 | 6.55 | 178.33 | 10.3 |
| Daya Bay | 0.86 | 18 | 30 | 3.78 | 6.30 | 246.43 | 20 |
| KamLAND | 0.78 | 11.22 | 22.34 | 3.35 | 6.60 | 160.31 | 1171 |

Table 7.4: Scintillator composition for the various experiments.

Based on the numbers from Table 7.4, the factors due to the scintillator compositions are listed in Table 7.5:

| Detector | $\left(\frac{N_{C_{LS}[\text{expt.}X]}}{N_{C_{LS}[\text{DC}]}}\right)$ | $\left(\frac{m_{LS[\text{expt.}X]}}{m_{LS[\text{DC}]}}\right)^{-1}$ | $\left(\frac{N_{C_{LS}[\text{expt.}X]}}{N_{C_{LS}[\text{DC}]}}\right)\left(\frac{m_{LS[\text{expt.}X]}}{m_{LS[\text{DC}]}}\right)^{-1}$ |
|---|---|---|---|
| RENO | 1.402 | 0.723 | 1.015 |
| Double Chooz | 1.0 | 1.0 | 1.0 |
| Daya Bay | 1.402 | 0.723 | 1.015 |
| KamLAND | 0.866 | 1.112 | 0.968 |

Table 7.5: Factors due to the scintillator composition for the various experiments, relation to that of Double Chooz.

From Table 7.5 we see that the combined factors due to the number of carbon atoms per LS molecule and the molecular mass of the LS molecules are within 3.2% of unity for the experiments we compare. Neglecting these small correction factors we are left with the scaling relations

$$r_{[\text{expt.1}]} \cong \left(\frac{\langle E\rangle_{[\text{expt.1}]}}{\langle E\rangle_{[\text{expt.2}]}}\right)^{\alpha}\left(\frac{\phi_{[\text{expt.1}]}}{\phi_{[\text{expt.2}]}}\right) r_{[\text{expt.2}]}, \tag{7.3}$$

$$R_{[\text{expt.1}]} \cong \left(\frac{\langle E\rangle_{[\text{expt.1}]}}{\langle E\rangle_{[\text{expt.2}]}}\right)^{\alpha}\left(\frac{\phi_{[\text{expt.1}]}}{\phi_{[\text{expt.2}]}}\right)\left(\frac{M_{[\text{expt.1}]}}{M_{[\text{expt.2}]}}\right) R_{[\text{expt.2}]}. \tag{7.4}$$

### 7.2.1 Scaling Results

The muon flux at the Double Chooz far detector site was estimated by dividing the measured muon rate with detector area and detector volume. The results of the two methods are consistent and are in agreement with the simulation using MUSIC/MUSUN code. The average of the two methods was taken as the value for the muon flux for the DC far site. The mean muon energy at the DC far site was calculated with MUSIC/MUSUN. The scaling of the muon flux to other experimental sites was done according to two different empirical methods, [64] and [18], both of which assume a flat overburden. The shape of the overburden was assumed to have minimal effect on the variation of the muon rate with depth. The mean muon energies as various depths were calculated using MUSIC/MUSUN simulation code [66]. An overall systematic error of 6.1% on the mean muon energies also takes into account the numerical approximations introduced in the simulation and the uncertainty on the primary muon flux.

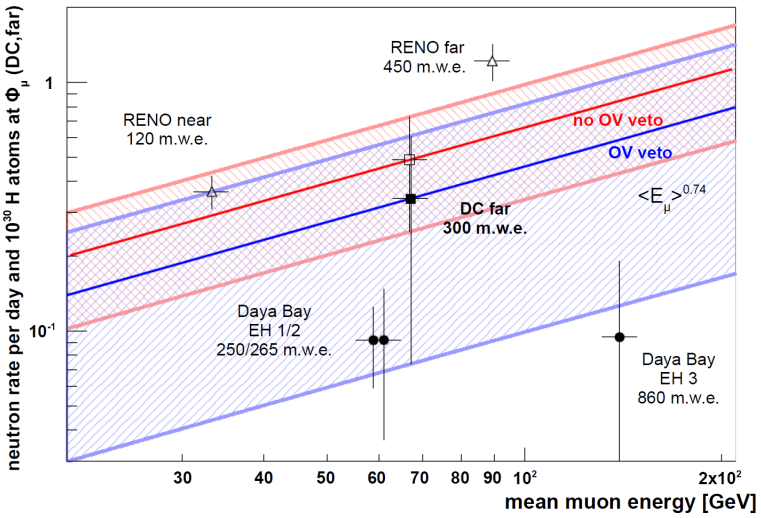


Figure 7.16: Scaling of DC fast-$n$ background rates. Empty (full) markers indicate quoted results using a selection without (with) an external muon veto; lines and shaded bands represent our scaling of the DC measurements with their uncertainty. Values were scaled by the number of $H$ atoms and normalized to muon flux at DC far site [13].

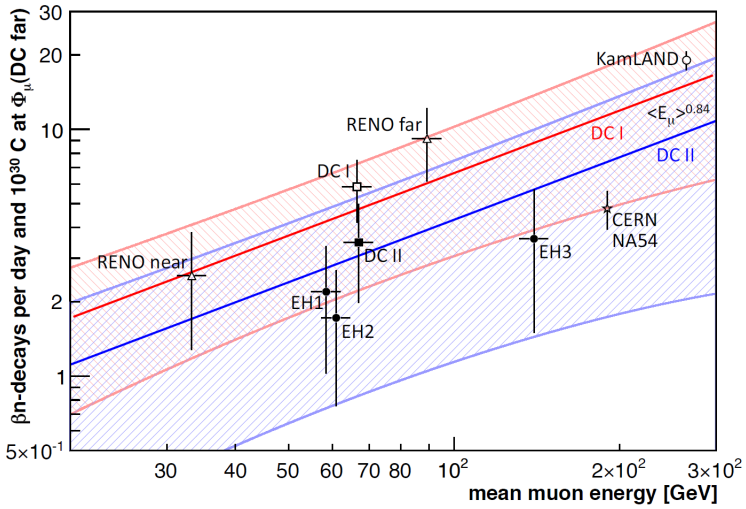


Figure 7.17: Scaling of DC $\beta$-n decay rates. Results were scaled by number of carbon atoms and normalized to muon flux at DC far site. Solid lines and shaded regions correspond to rate and scaling uncertainties in reactor-off analysis: "Standard" (red solid line) and open data points show the total $\beta$-n rate, while "$^9$LiReduced + OV" (blue solid line) and filled data points correspond to analyses with an extended veto following showering muons [13].

The value of the exponent $\alpha$ was chosen conservatively to be $\alpha = 0.84 \pm 0.22$, ranging from the lower bound of [21] to the result of [26]. The results of the scaling of the DC Fast-N background rates and the $\beta$-n rates according to Eq. (7.2) are shown in Figs. 7.16 and 7.17.

# Chapter 8

# Neutron Background Production and Detection Rates in Double Chooz

The correlated background is one of the most important backgrounds in an underground neutrino experiment especially one like Double Chooz which is at a relatively shallow depth with large cosmogenic backgrounds. For these backgrounds, both the prompt and delayed events, similar to the inverse beta decay (IBD) events, come from a single original process eg, a muon spallation, hence the name "correlated background". The neutrons or neutron-like backgrounds is one of the major sources of correlated backgrounds. Neutrons are produced through spallation processes by cosmic muons, either in the nearby rock surrounding the detector or by ones that just clip the inner veto (IV) region of the detector so that they avoid being tagged by the IV. These neutrons are often very energetic with initial kinetic energies reaching up to 1 GeV. Due to their high kinetic energies, these neutrons are referred to as "Fast Neutrons". These neutrons have large interaction lengths and readily travel through the intervening matter to reach the active volume of the detector. Fast neutrons are often produced in high multiplicities and may reach the detector in bunches of primary neutrons from the parent muon activity or secondary neutrons from the primary.

In a case when a fast neutron penetrates into the target volume of the detector, the pair of prompt and the delayed events happen to have a time delay between them that is comparable

to that of the true neutrino events. Therefore, in such a case we have a candidate event for the correlated background which could easily mimick a neutrino event in the detector. The actual processes that create the prompt-delayed pair of events in case of the correlated backgrounds in Double Chooz will be described in due course in this chapter. Methods to estimate the production rate of these neutrons inside and in the surroundings of the Double Chooz detector are presented in the following sections.

## 8.1 Neutron Interaction with Matter

Being a neutral particle, the neutrons undergo extremely weak electromagnetic interactions. Hence the neutrons pass through matter mostly unimpeded before undergoing strong interaction with the atomic nuclei. The interaction of high energy neutrons with matter can be devided into three categories: (1) Diffraction, (2) Scattering and (3) Absorption.

- Diffraction: Neutrons are perfect probes specially for condensed matter. They are not sensitive to charge distributions but are sensitive to magnetic fields due to their spin.

- Scattering: The scattering of energetic neutrons in matter can further be divided into (a) Elastic and (b) Inelastic scattering.

  During elastic scattering, a fraction of the kinetic energy of the neutron is transferred to the nucleus. The nucleus then ionizes the material surrounding the point of interaction. This is known as "proton recoil" and is most efficient when the target nuclei are of comparable mass to the neutrons. Hence this occurs preferentially on $^{1}$H and $^{2}$H. For a neutron of energy E, the average energy lost in an elastic collision with a nucleus of atomic weight $A$ is

  $$\Delta E = \left[\frac{2A(1-\cos\phi)}{(A+1)^2}\right]E. \tag{8.1}$$

  Here $\phi$ is the angle between the final neutron velocity in the center of mass and the laboratory frames of reference. On average, in case of collision with hydrogen

nuclei with $A = 1$, the number of collisions required for a 2 MeV neutron to become thermal ($0.025eV$) is $\approx 18$. On the other hand, in case of an inelastic collision, the total kinetic energy of the outgoing neutron and the nucleus is less than the incoming neutron as a part of the energy is used to excite the nucleus. The nucleus, as a result, undergoes internal rearrangement into an excited state from which it comes to the ground state with the emission of gamma radiation. This inelastic neutron scattering is more probable for heavier nuclei and there is a threshold for the incident neutron energy for a given nucleus. The threshold energy is infinity for hydrogen (which means inelastic scattering of neutrons can not occur on hydrogen), 6 MeV for oxygen and less than 1 MeV for uranium.

- Absorption: At thermal energy ranges, the probability of absorption of a neutron in a material is inversely proportional to its velocity. Neutron captures on $^1$H depend upon their velocities of thermal neutron while that on gadolinum is independant of it which will be explained in the later section.

### 8.1.1 Cross Sections

The probability of an interaction between a neutron and a target nucleus is called the "microscopic cross section ($\sigma$)" for the given nucleus for the particular interaction. This probability varies with the nucleus involved in the interaction as well as the energy of the neutron. The probability of a neutron interacting with a given volume of a material depends on the microscopic cross section as well as on the number of nuclei within the volume. The "macroscopic cross section ($\Sigma$)" can be defined as the probability of a given interaction ocurring per unit distance travelled by the neutron. The relation between the two kinds of cross sections is [60]

$$\Sigma = N\sigma. \tag{8.2}$$

where N is the number density of atoms in the material.

The macroscopic cross section for the interaction of a neutron in a material determines the probability of one neutron performing a specific interaction per unit length travelled in the material. Therefore the inverse of it should, on an average, give the distance that a neutron would travel before undergoing an interaction. This distance travelled by a neutron between any two successive interactions is called the "mean free path ($\lambda$)" for that interaction. The mean free path is related to the macroscopic cross section as

$$\lambda = \frac{1}{\Sigma}. \tag{8.3}$$

The total number of interactions can be determined by using the flux of the neutrons incident on the material. The flux of the neutrons ($\Phi$) indicates how many neutrons are travelling through the medium and what distance they cover in unit time. It can be defined as the total pathlength covered by the neutrons in unit volume in unit time and is

$$\Phi = nv. \tag{8.4}$$

Here, $n$ is the neutron number density and $v$ is the neutron velocity.

### 8.1.2 Rate of Neutron Interaction in a Material

From the definitions, the flux of the neutrons gives the total pathlength of all the neutrons in unit volume in unit time while the macroscopic cross section gives the probability of neutron interaction per unit pathlength. Hence the product of these two quantities would give the number of neutron interactions taking place in unit volume in unit time. This is known as the interaction rate

$$R = \Phi\Sigma. \tag{8.5}$$

Using Eq. (8.2) we have

$$R = \Phi N\sigma. \tag{8.6}$$

A neutron interacts either through scattering, diffraction or absorption. The probability of a neutron being scattered or absorbed by an atom of the material is determined by

the microscopic cross section. For light nuclei, the absorption cross section for neutrons is proportional to the inverse of its velocity. For medium to heavy nuclei, the region of the $1/v$ dependence is accompanied by sharp peaks, called the resonances, when the energy of the neutron plus the binding energy of the nucleus is equal to one of the discrete quantum energy levels in the nucleus.

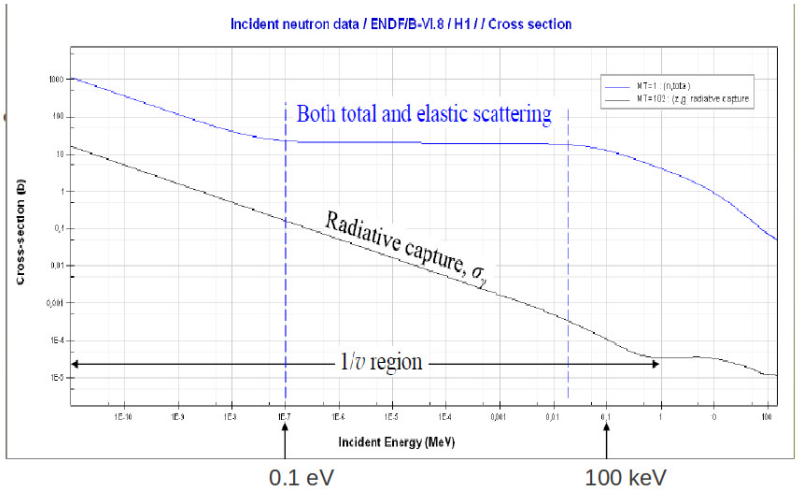


Figure 8.1: Schematic of the various cases for production of correlated background and the tagging schemes.

For most elements, the inelastic scattering, which is small for light elements, shows the same $1/v$ trend of the absorption process, for energies upto 1 MeV, while the elastic scattering cross section is nearly constant. Both elastic and inelastic scattering cross sections show resonance behavior. The total cross section can be either constant or decrease as $1/v$ depending upon which process dominates. In general the variations in the scattering cross sections are small compared to that in the absorption cross sections. For $^1$H, the scattering is predominantly elastic in nature and is a constant at low energies upto 1 MeV. With a good approximation, the elastic scattering cross section can be considered as constant for light elements. This is shown in Fig. 8.1.

## 8.2 Analysis with Data-Overview

The technique to estimate the daily rate and the spectral shape of the neutron background for the Double Chooz experiment involves identifying the parent muons which clip one of the detector systems before producing the fast neutrons that get inside the active volume of the detector. These events involve a muon triggering a "tag" in at least one of the two veto systems in the same event qualified as a anti-neutrino prompt event in the inner detector. The underlying physics arguments behind this tagging logic and the two tagging systems will be described in the following sections. There are two detector components dedicated to tagging the incoming muons which could be a potential source of a neutron-induced correlated background in the detector: (1) Outer Veto (OV) and (2) Inner Veto (IV) described in Chapter 2. We will now explain what a "tag" means for each of these two tagging systems.

### 8.2.1 Outer Veto Tagging

The Outer Veto (OV) system consists of two separate panels above the detector. Each of them consists of plastic scintillator strips placed above each other in XY direction. All the analysis results that are going to be presented in this chapter were determined from data taken using only the lower panel of the OV. The OV can identify the muons that pass through the OV and the inner detector and such events are rejected using the OV anti-coincidence condition as discussed in Section 5.2. Most of these events are tagged by the IV as well and are readily rejected. There are cases when the IV fails to identify any muon in such a event because of the fact that the muon could be either missing or just clipping the IV and does not deposit enough energy in the IV to create an "IV Tag". In such cases the OV provides a great handle to study those events as the IV has relatively low efficiency for identifying those events. An "OV Tagged" event consists of a "antineutrino-like" event in the inner detector within 224 ns of a muon event in the OV. The fact that these events

have a "coincident" muon tagged by the OV, means it is highly likely that it is caused by the activity of the parent muon around the detector. These events will be studied to estimate their spectral shape and rate.

### 8.2.2 Inner Veto Tagging

For relatively shallow detectors, as in the Double Chooz experiment, background rejection with the help of the Inner Veto (IV) is very important. The IV is filled with liquid scintillator equipped with 78 8 inch diameter photomultiplier tubes to detect any charge deposited by an ionizing particle like a muon passing through it. For a minimum ionizing particles like muons, the energy deposited per unit track length is 2 MeV/cm. A rough calibration of the IV gives about 2000 DUQ/MeV of energy deposited, where DUQ (Digital Unit of Charge) is an arbitrary unit of deposited charge. The antineutrino events selected in the inner detector have a deposited charge $< 10000$ DUQ in the IV. Any event with deposited charge $> 10000$ DUQ in the IV is said to be "tagged" by the IV. The physics argument behind using the "IV Tag" as an identification of a neutron event is that we can get the spectrum of the neutron background from the muons missing or clipping the IV without producing an "IV Tag" by studying the neutrons that are produced by muons producing an "IV Tag".

The details of the tagging techniques adopted during the dedicated neutron analysis during the first and the second publication stages for the experiments are summarised in the following Table 8.1.

| IBD Selection Condition | | | Reference Background Tag | | |
|---|---|---|---|---|---|
| Publication | OV | IV | OV | IV | Tag Name |
| $1^{st}$ | NA | 0 | NA | 1 | IV Tag (No OV Data available) |
| $2^{nd}$ | 0 | 0 | 0 | 1 | IV Only |
| | 0 | 0 | 1 | 0 | OV Only |
| | 0 | 0 | 1 | 1 | IV,OV Both |

Table 8.1: Available muon taggaing schemes in Double Chooz.

### 8.2.3 Doule Chooz Second Publication Data Set

The data set used for the second publication for Double Chooz came added with an extremely powerful tool to tag the muons that could potentially produce the neutrons around the detector. The OV eventually proved to be equally effective in tagging the muons that get into the chimney region for which the IV efficiency is very low. In the following sections we will demonstrate and utilize this power of the OV with a simple but effective technique to estimate the neutron as well as stopped muon backgrounds for Double Chooz. The availability of the OV data for almost two-third of the data for the second publication for Double Chooz made possible the use of all the possibilities described in Table 8.1.

### 8.2.4 OV Only Tagging Analysis

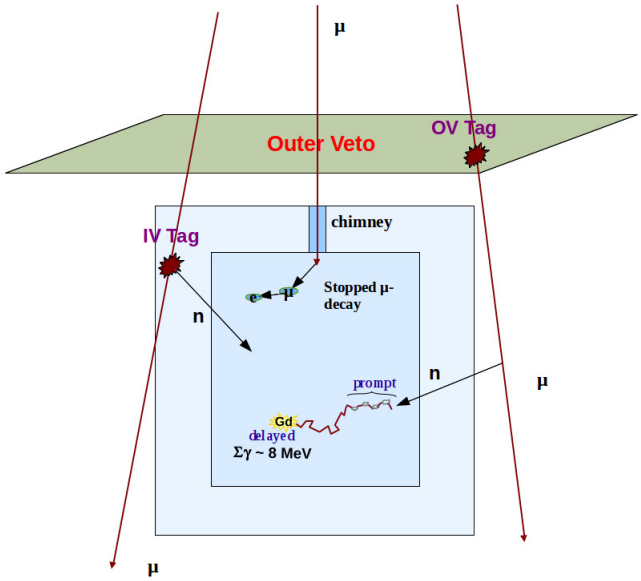


Figure 8.2: Schematic of the various cases for production of correlated background and the tagging schemes.

The most important physics scenario in which we need to determine the neutron background

for Double Chooz, when there is a "tag" only in the OV in the same event as an IBD-like prompt event inside the inner detector, is that a muon goes through the OV and close to the detector either missing the IV or clipping it so that there is no "tag" in the IV. The OV scintillator modules cover a rectangular aea of $14.1m \times 7.2m$ on top of the detector. The mechanical constraints due to the walls of the cavity prevent wider coverage along one side but it has a fairly large coverage on the other. Because of this the OV can provide the identification of the muons which either just miss the IV or just clip it so that the IV efficiency for these muons is small. The following Fig. 8.5 shows the events that have an "OV Tag" but are missed by the IV i.e, these events are "IV-Untagged".

### 8.2.5 Observations and Determination of Cuts

The fast neutrons produced by muon spallation come screaming into the detector producing an IBD-like event due to intial proton recoil and the subsequent capture in gadolinium. Different physics is responsible for another bckgound signal when a muon, after creating a signal in the OV sneaks into the inner detector through the chimney, producing very little light because of the very small amount of scintillator in the chimney. In this "stopped muon" case, the muon then stops in or around the chimney and decayes with a mean lifetime of $2.2\mu$s giving out a "Michel electron". The ionization energy from the intial muon appears as the prompt energy while that from the "Michel electron" gives the delayed energy, thus mimicking a typical IBD event.

Before deciding on the selection cuts to chose the neutron and stopped muon contributions to the correlated background, let us look at the muon hit positions on the outer veto shown in Fig. 8.3 below.

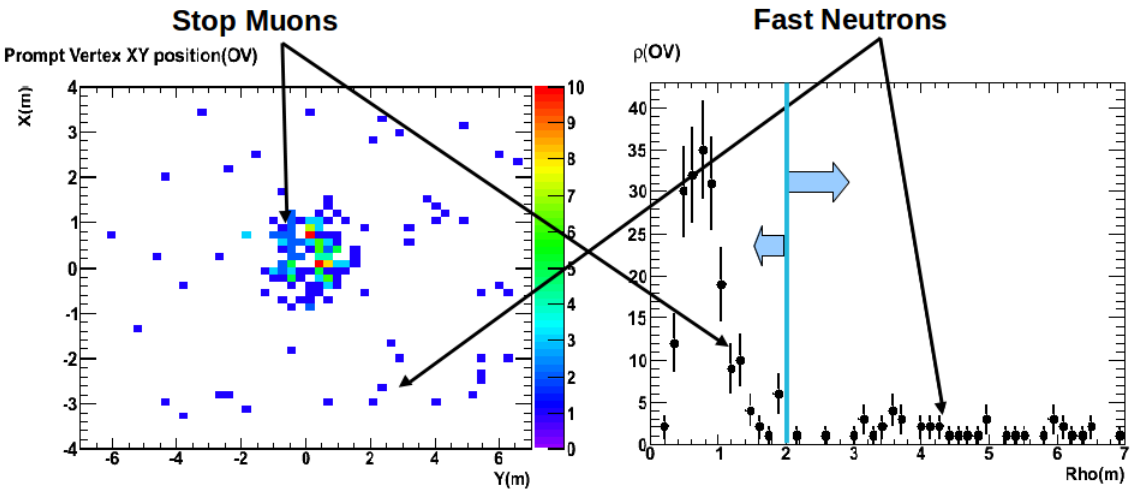


Figure 8.3: OV muon hit positions.

It is easy to see from Fig. 8.3 that there is a pattern in the hit muon positions on the OV. The muons contributing in the "stopped muon" part of the correlated background hit the OV close to the chimney region while the muons that either miss the detector or clip the IV, hit the OV further away from the central chimney region. Fig. 8.3 also highlights the efficiencies of the OV in selecting the two kinds of events. While the efficiency for the stopped muons is very high, the OV also selects a fair number of fast neutron candidates. The ratio of the stopped muon events and the neutron candidate events as selected by the OV is 77% : 23%. Still the number of neutron candidates are large enough for us to perform a study on their prompt energy spectral shape based upon their hit positions on the OV which will be dicussed in detail in thsi section.

From Fig. 8.4, which is a plot between the muon hit position on the OV against the charge deposited in the IV for events which have an IBD-like signal in the inner detector, we see that a large portion of the candidates for potential correlated background sources have a IV charge deposit $< 10,000$ DUQ which means these are tagged by the IV and could be selected as IBD candidates if it were not for the OV. Hence we can choose a large pool of such candidates selected by the OV but are under the IV-tag threshold.

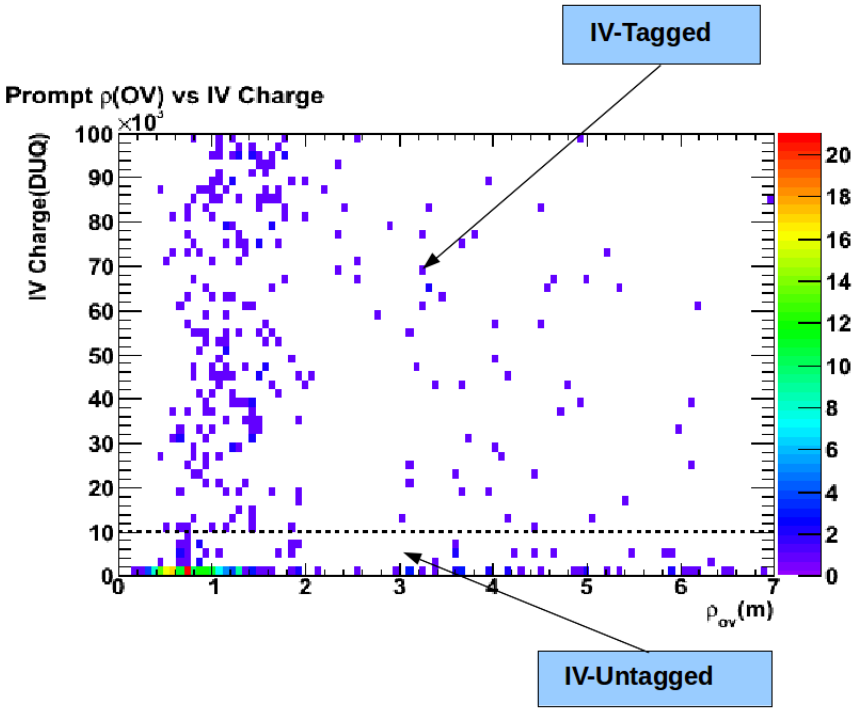


Figure 8.4: OV muon hit positions vs IV Charge.

Another factor affecting the selection of the neutron and stopped muon events is the $\Delta T$ between the prompt and delayed events for each type. The fast neutron candidates, with their capture on gadolinum, should show the typical time delay of $30\mu$s between their prompt and delayed events just as in the case of the IBD events. On the other hand the stopped muon events should have a $\Delta T$ showing the muon decayed at rest with a mean lifetime

of 2.2$\mu$s.

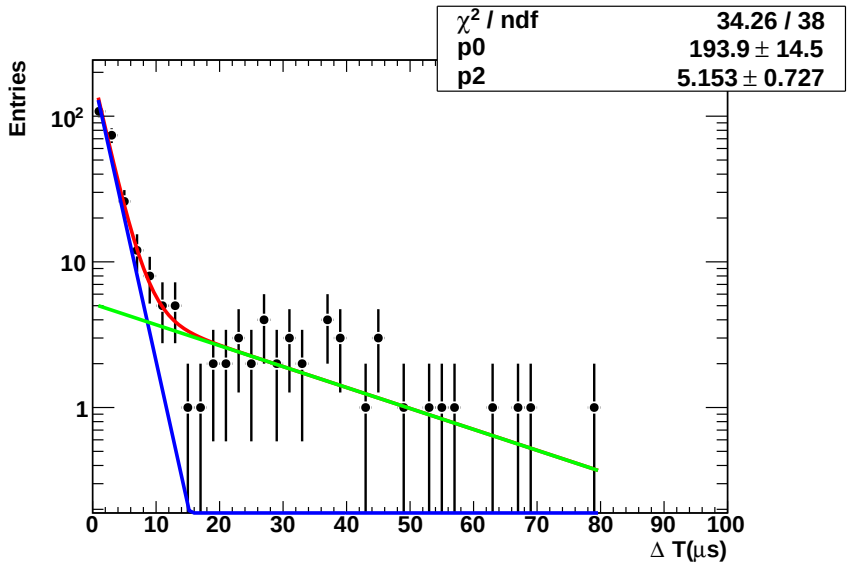


Figure 8.5: $\Delta T$ for ovtagged events.

From Fig. 8.5 we see that each of the neutron and the stopped muon contributions to the correlated background have distinct time signature between their prompt-delayed events. Here the the histogram is again fit with two exponentials with time constants 2.2$\mu$s for the stop muons and 28.74$\mu$s for the neutrons. The $\Delta T$ of 28.74$\mu$s is obtained from the time difference between the prompt and delayed events in the selected IBD events. As mentioned above, the ratio of fast neutrons and stopped muons in OV-selected events is 77% : 23%. This shows that the OV is predominantly efficient in selecting the stopped muons.

Based on the above figures, a correlation between the muon hit positions on the OV and the $\Delta T$ of these events can be established and is shown in Fig. 8.6 which clearly shows the clustering of the stopped muon events separating them from the neutron events. The dotted lines in the figure show the selection cuts applied to separate the two samples by using both the variants.

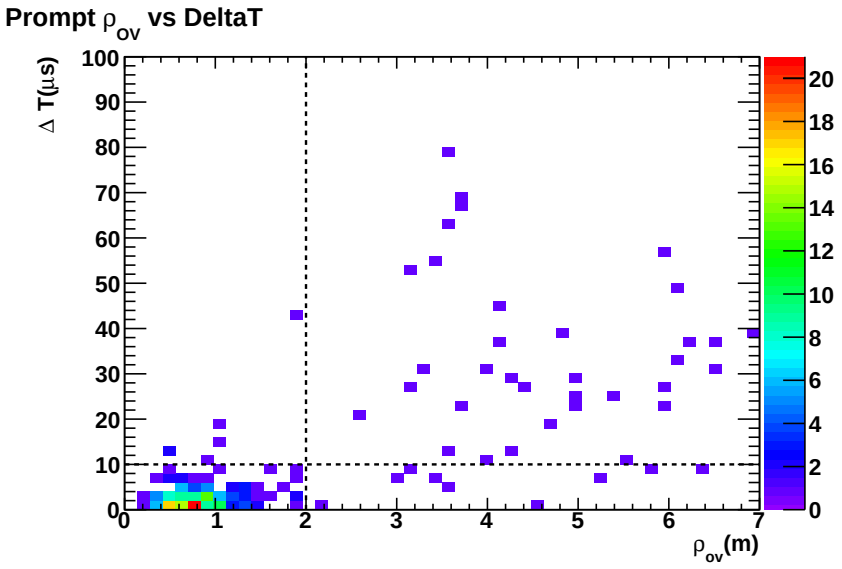


Figure 8.6: Correlation between muon hit position and $\Delta T$ for OV-tagged events. Amplitudes of the two exponential fits are also shown in the histogram.

| | Prompt Energy (MeV) | Delayed Energy (MeV) | $\Delta T$ ($\mu$s) | OV Tag | IV Tag | OV $\mu$ hit position (m.) |
|---|---|---|---|---|---|---|
| Fast Neutrons | $[12.2, 30]$ | $[6, 12]$ | $[10, 100]$ | 1 | 0 | $\rho_{ov} > 2$ |
| Stop Muons | $[12.2, 30]$ | $[6, 12]$ | $[0.5, 10]$ | 1 | 0 | $\rho_{ov} < 2$ |

Table 8.2: Selection conditions for fast neutron and stop muon candidates

In addition to the cuts mentioned in Table 8.2 all the data were subjected to the so called "$^9$Li-reduced cut" in which an additional veto of 0.5 s is applied after each showering muon of energy $E_\mu > 600$MeV, to reject those candidates which are correlated to these muons.

The neutron as well as stopped muon background is estimated using the extended prompt energy range $[12.2, 30]$ MeV and the final spectrum is normalized to the "untagged" spectrum in the same range with the part of it between $[0.7, 12.2]$ MeV giving the desired spectral and rate information inside the IBD region.

### Stopped Muon Candidates

The vertex positions of the stop muon candidates selected according to the above mentioned cuts are shown in Fig. 8.7 below. As predicted earlier, the events are mostly concentrated in a narrow region around the target chimney. It is important here to notice that the use of OV as a tag of these stopping muons, makes the use of any fiducial volume cut to select them, redundant.

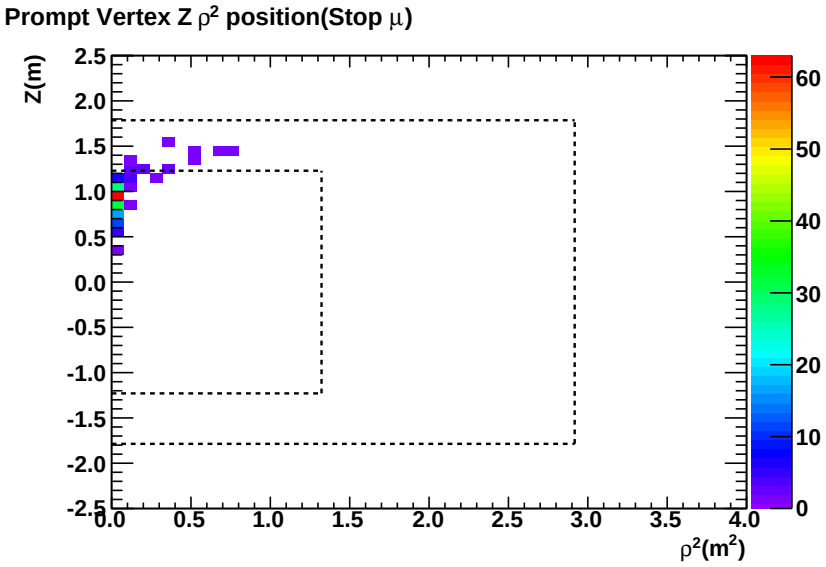


Figure 8.7: Vertex distribution of the stopped muon candidates in the detector.

Another feature of the stopped muon events should be that the $\Delta T$ between the prompt and delayed events should show the muon decay at rest with a mean lifetime of $2.2\,\mu$s. This is clearly seen in Fig. 8.8 where the $\Delta T$ distribution is fitted with an exponential, whose exponent $-2.188\,\mu$s, is very close to the mean muon life time.

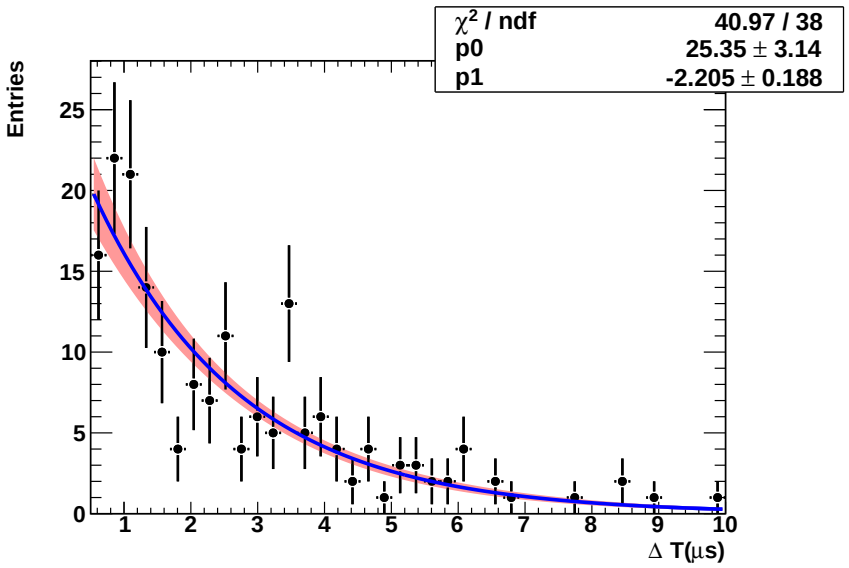


Figure 8.8: $\Delta T$ of the stop muon candidates in the detector.

In addition to their distinct vertex distribution, which is concentrated in a small region around the target chimney, and the $\Delta T$ distribution which agrees very well with model of the decay of a muon at rest with a mean half-life of 2.2$\mu$s, there are further physics reasons that confirm that the selected events are the chimney stopped muons.

While the neutron events must have a distinct signature of 8 MeV peak due to their delayed capture in gadolinum, in the case of the stopped muons, the ionisation energies due to the Michel electrons do not have such a characteristic peak. They have a very distinct energy spectrum with an end point at 52.8 MeV, which is equal to half the muon rest mass. This analysis considers the energy of these electrons only in the range $[6, 12]$ MeV, just as in the case of the IBD events. Fig. 8.9 shows the delayed energy for these events further strengthen the above argument.

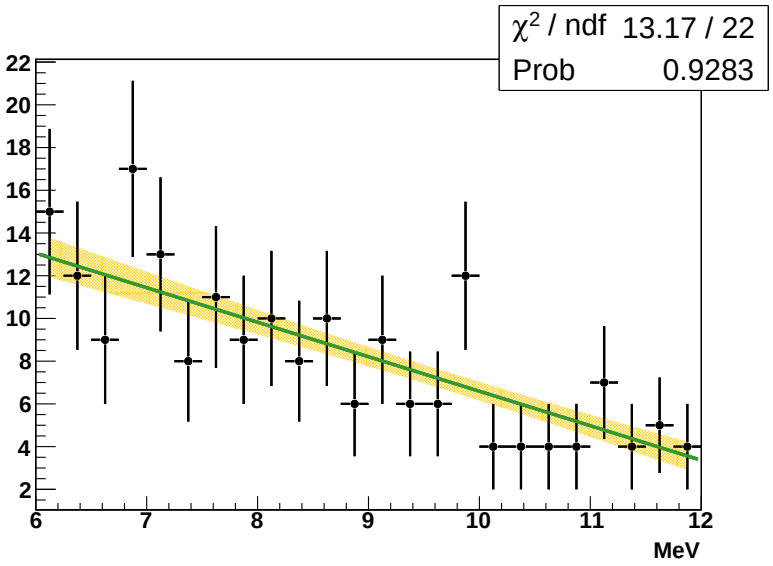


Figure 8.9: Delayed energy for the stopped muon candidates along with the parameters of the exponential fit with the fit parameters.

### 8.2.6 Fast Neutron Candidates

In this section, we will show the results of the neutron candidate selection according to the selection cuts described in Table 8.2. The vertex positions of the neutron candidates are expected to be rather uniformly distributed throughout the target volume due to the fact that the neutrons should be produced isotropically in the rock surrounding the detector.

This shows that in case of a muon just missing or clipping the detector, these neutrons come in mostly from the sides of the detector. This feature is quite clearly established in Fig. 8.10.

The $\Delta T$ between the prompt and delayed events for the neutrons should show the same characteristic neutron capture time as in the case of the IBD events. This is clearly seen in Fig. 8.11. where the $\Delta T$ distribution is fitted to an exponential and results in an exponent of 30.23$\mu$s which is close to the $\Delta T = 28.74\mu$s for the IBD events.

As expected, the delayed events show a peak at 8 MeV, characteristic of neutron captures on gadolinium, as shown in above Fig. 8.12. This figure makes it clear that the cuts applied

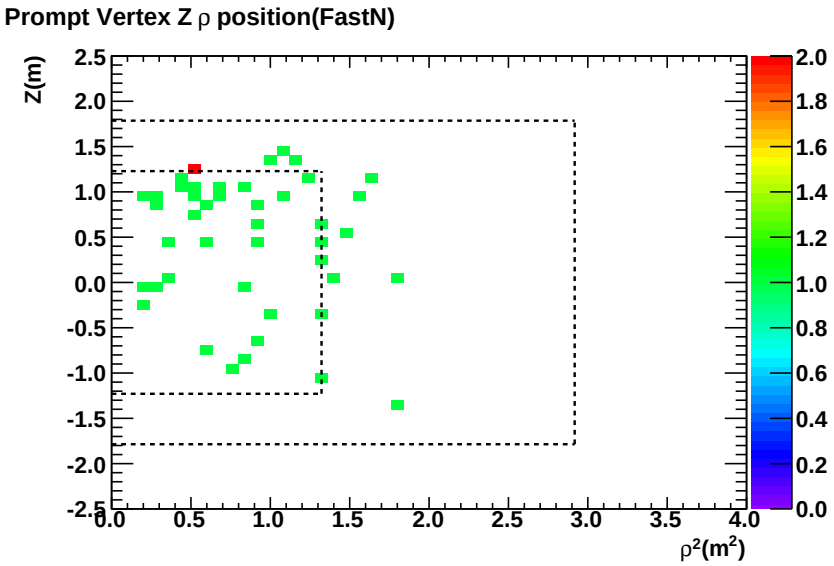


Figure 8.10: Vertex distribution of the fast neutron candidates in the detector.

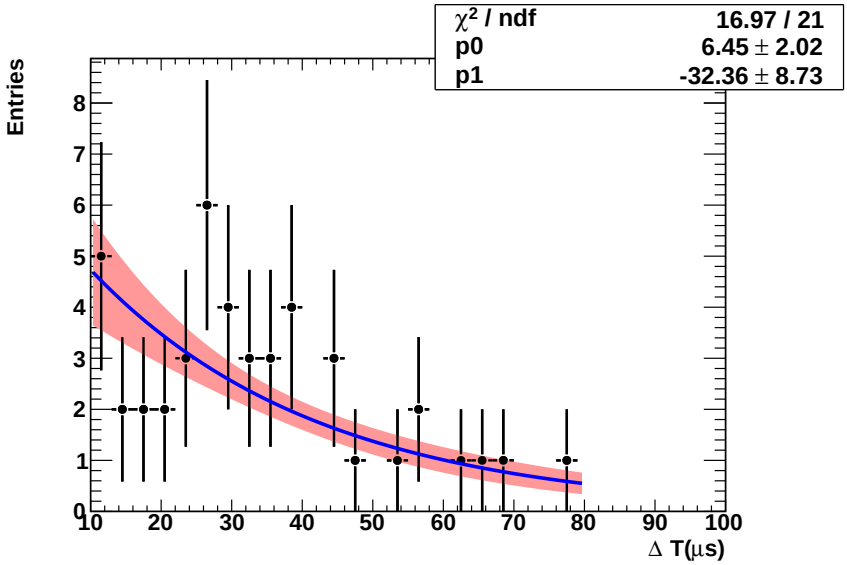


Figure 8.11: $\Delta T$ of the fast neutron candidates in the detector.

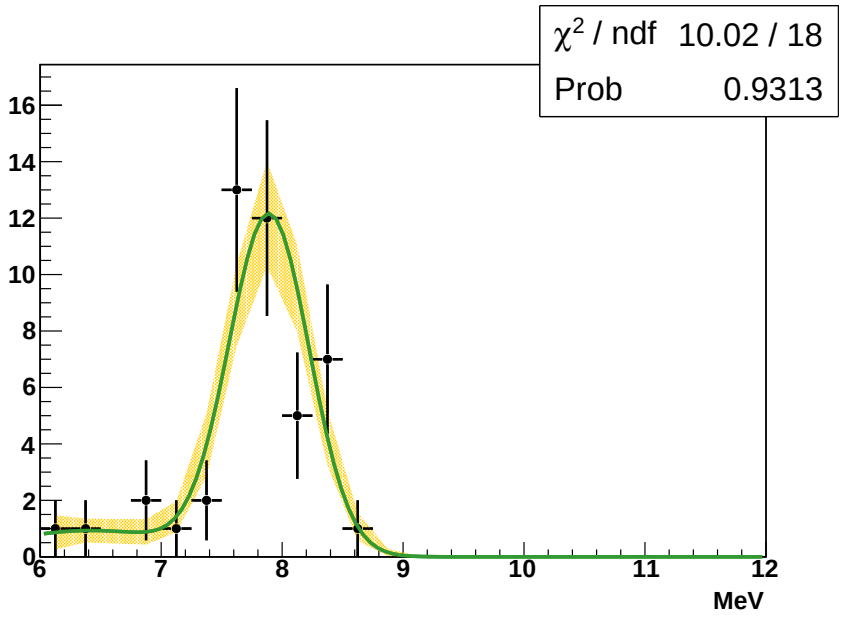


Figure 8.12: Delayed energy spectrum of the fast neutrons in $[12.2, 30]$ MeV.

have been neccessary and sufficient to descriminate between the muon and neutron part of the correlated background. Furthermore, there is little to no hint of any cross contamination among the two categories of candidates and each of them appear to have been selected with high enough purity. This will be verified in the following section where we will caluclate the cut efficiencies and purities of selection.

### 8.2.7 Efficiency and Purity of Selections

In this section we will describe the method used to identify the neutron and stopped muon candidates. Loosening a cut increases its efficiency at the cost of the purity of the sample selected and vice-versa. The efficiency of a cut is obtained by calculating the number of canidates passing the cut and the candidates selected through all other cuts. On the other hand, the purity of a cut is obtained by calculating the ratio of the sample selected through the cut over the total sample space within the cut.

In terms of hypothesis testing, if P denotes the probability, the efficiency of a selection can

be defined as the fraction of the selected events that are true events,

$$\text{efficiency} = \frac{P(\text{selected} \quad \&\& \quad \text{true})}{P(\text{true})}$$

On the other hand the purity of the selected sample can be defined as the fraction of the true events in the total selected events,

$$\text{purity} = \frac{P(\text{selected} \quad \&\& \quad \text{true})}{P(\text{selected})}$$

The plots used to compute the efficiencies of each of the cuts are shown in Fig. 8.13 - 8.16 below. The efficiency for a given cut is simply the ratio of entries in the selected and true events histogram (shaded) over the entries in the true events (colored) histogram.

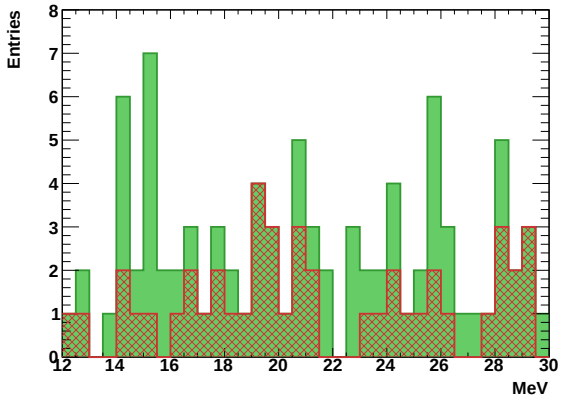


Figure 8.13: $\epsilon_{\Delta T}$ for fast neutrons.

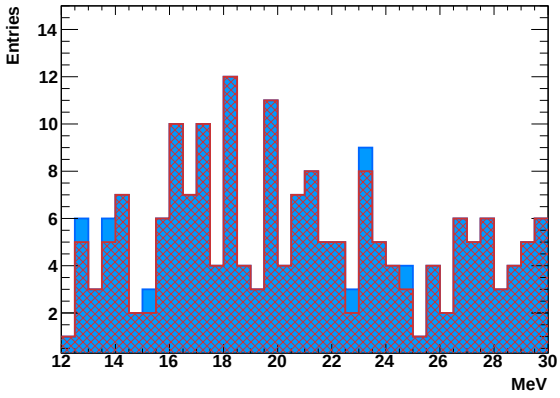


Figure 8.14: $\epsilon_{\Delta T}$ for stopped muons.

The purities are not used to directly evaluate the number of candidate events. The plots used to calculating the purity of each selection are shown in Fig. 8.17 - 8.20 below. The purity for a given cut is computed as the ratio of the entries in the selected and true events (shaded) histogram over that in the selected events (colored) histogram.

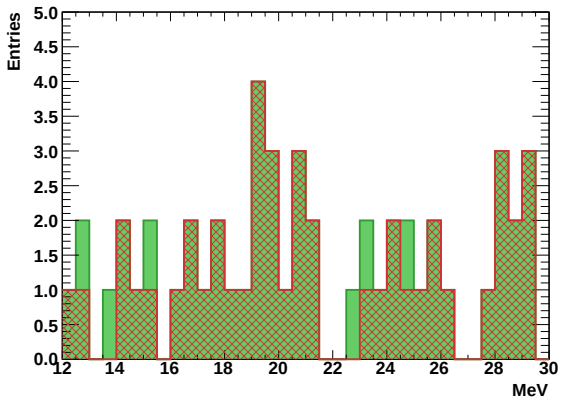


Figure 8.15: $\epsilon_{\rho_{ov}}$ for fast neutrons.

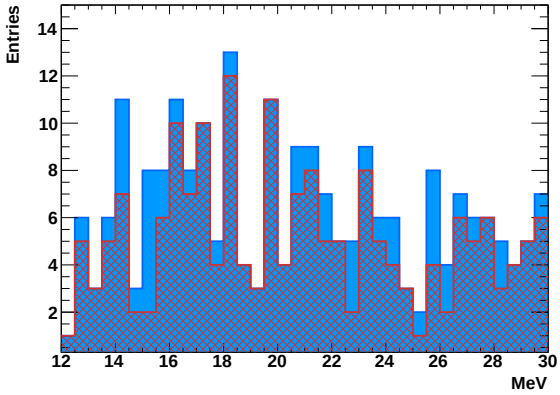


Figure 8.16: $\epsilon_{\rho_{ov}}$ for stopped muons

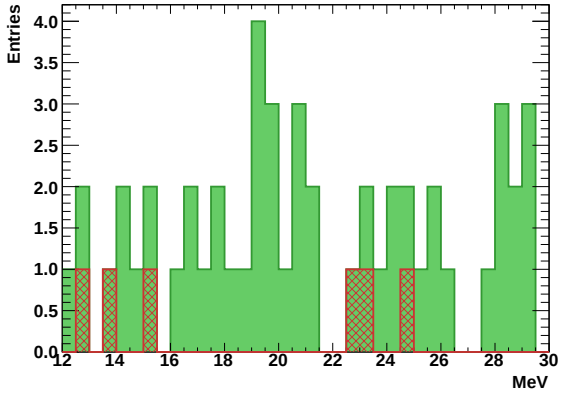


Figure 8.17: $Purity_{\Delta T}$ for fast neutrons

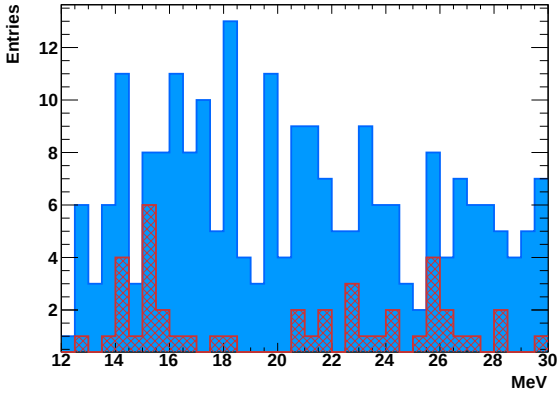


Figure 8.18: $Purity_{\Delta T}$ for stop muons

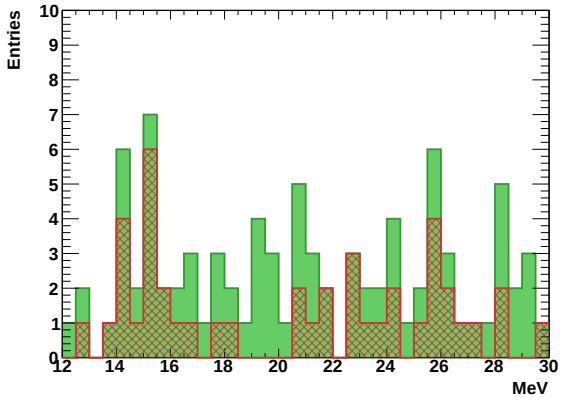


Figure 8.19: $Purity_{\rho_{ov}}$ for fast neutrons

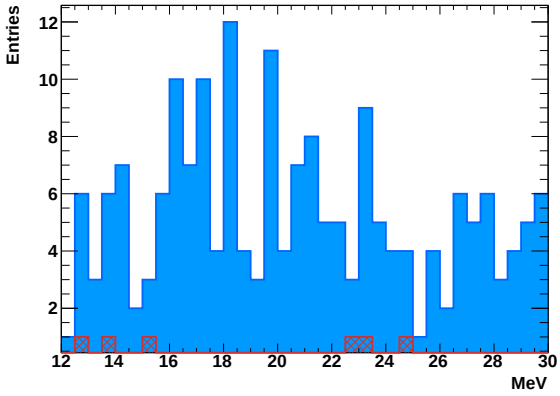


Figure 8.20: $Purity_{\rho_{ov}}$ for stop muons

From the above figures, we see that both the neutron and stopped muon populations causing the correlated background are separated and selected with optimum efficiency and purity. The computed values of the efficiencies and purities for each of the cuts are lised in the following Table 8.3

| Background species | Efficiency of cut | | Purity of cut | |
|---|---|---|---|---|
| | $\epsilon_{\rho ov}$ | $\epsilon_{\Delta T}$ | $Purity_{\rho ov}$ | $Purity_{\Delta T}$ |
| Fast Neutrons | $0.88 \pm 0.18$ | $0.51 \pm 0.094$ | $0.67 \pm 0.07$ | $0.89 \pm 0.095$ |
| Stop Muons | $0.81 \pm 0.08$ | $0.97 \pm 0.10$ | $0.97 \pm 0.07$ | $0.84 \pm 0.06$ |

Table 8.3: Efficiency and purity numbers of the selection of the fast neutron and stop muon candidates

The cut systematic uncertainties were added in quadrature and then added to the cut statistical error in a similar fashion to determine the final listed errors.

### 8.2.8 Prompt Energy Spectra Normalization

In order to estimate the spectrum of each background species as well as their daily rates within the IBD selection energies we normalize the "OV-tagged" spectra for the neutrons and the stopped muons to the "OV-untagged" spectra in the $[12.2, 30]$MeV region according to their respective ratio in that data. The tail of this normalized data, inside the neutrino selection energies, gives the spectral shape as well as the rates for these background candidates.

The prompt energy spectra for stopped muons and fast neutrons were corrected for the efficiencies of the selection cuts and the two spectra were added together in their proper ratio to give the total correlated background estimate. In order to achieve the proper ratio of each kind, the total $\Delta T$ distribution for the "OV-untagged" events in $[12.2, 30]$MeV was fitted with a double exponential, see Fig. 8.21. On this log-linear plot the slopes of the two fitting functios were fixed to $2.2\mu$s in the range $[2, 10]\mu$s for the stopped muons and $28.74\mu$s

in the range $[10, 100]\mu$s for the neutrons.

The two prompt spectra were then scaled to get the correct ratio of neutrons and stopped muons. The number of each type of candidate in these data was computed from the integrals of the two fit functions over the respective fit ranges. After computing the scale factors for the neutrons and the stopped muons, each was scaled to get them in the same ratio as the "OV-untagged" events in $[12.2, 30]$MeV.

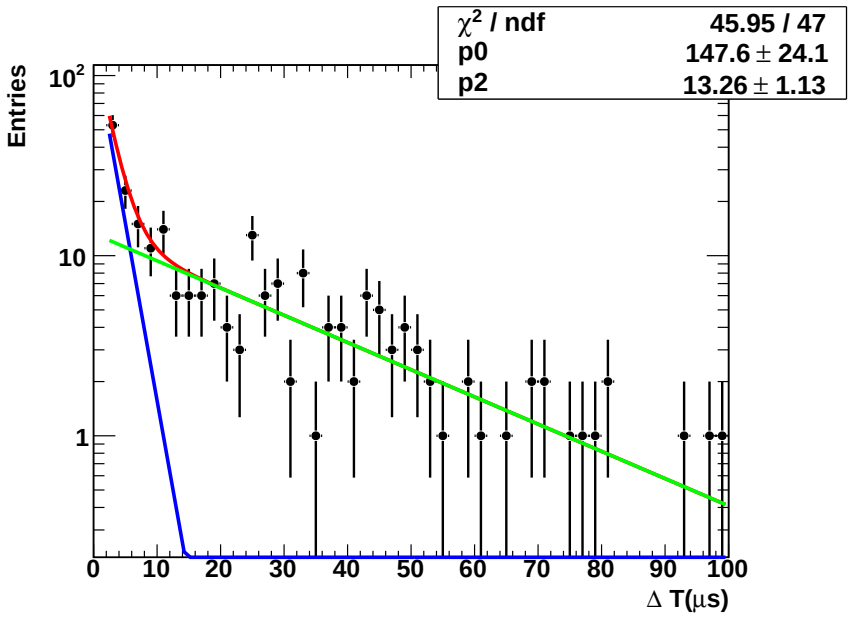


Figure 8.21: $\Delta T$ for the events in the range $[12.2, 30]$ MeV that were un-tagged by the OV or IV.

The choice of the slopes for the exponentials used to fit the $\Delta T$ plot were taken as the standard $2.2\mu$s mean muon lifetime in case of the stopped muons and $28.74\mu$s for the neutrons, as obtained from the mean capture of the neutrons from the IBD events.

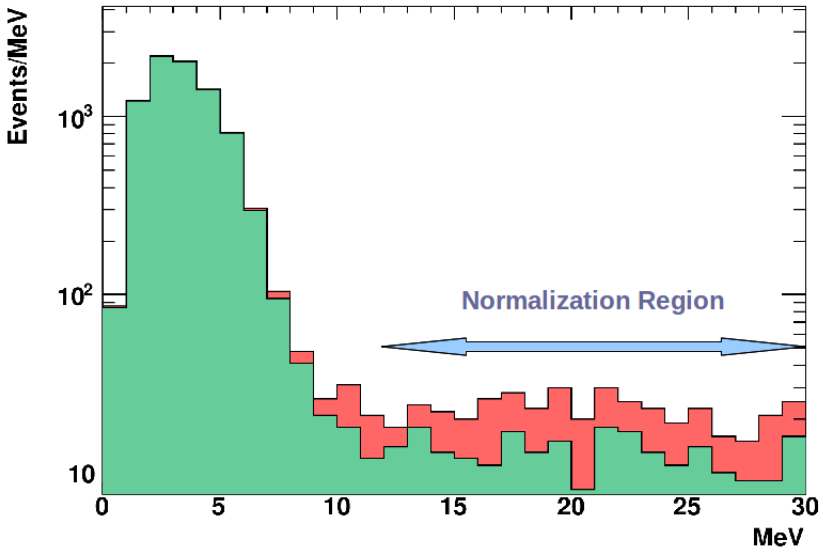


Figure 8.22: Prompt energy spectra for total events(Red) and the events after OV veto(Green). Normalization is performed over the [12.2,30] MeV range of the green histogram shown.

The following Table 8.4 lists the ratios of the two background species, their individual scale factors by normalizing the extended IBD spectrum over the same range $[12.2, 30]$ MeV and the total number of each of them in the IBD energy region of $[0.7, 12.2]$ MeV.

| Un-tagged events in $[12.2, 30]$ MeV | Fraction of candidates | | scale factors | | OV-tagged candidates in $[0.7, 12.2]$ MeV | |
|---|---|---|---|---|---|---|
| | Fast-N | Stop-$\mu$ | Fast-N | Stop-$\mu$ | Fast-N | Stop-$\mu$ |
| 235 | 0.67% | 0.33% | 3.53 | 0.42 | 86.14 | 45.88 |

Table 8.4: Ratios and scale factors for the fast neutron and stopped muon candidates.

### 8.2.9 Stopped Muon Spectral Shape

Since the stopped muon prompt energy spectrum falls a.t both lower and higher energies, it was fit with a 3-parameter Landau function, see Fig. 8.23. The fit spectrum clearly shows a gradual fall towards the lower energies inside the IBD energy range of $[0.7, 12]$ MeV.

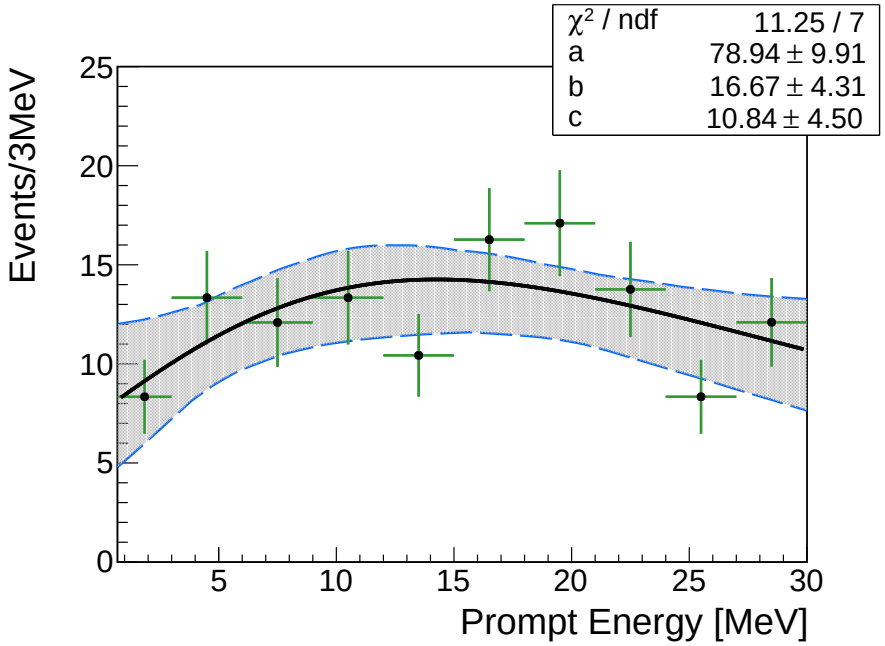


Figure 8.23: Stopped muon prompt energy spectrum, data at a Landau function fit.

Another attempt to model the spectral shape for the stopped muons was made by fitting it to a linear model as shown in Fig. 8.24. Both models show a slight fall in the spectrum toward low energies. The fit models are drawn along with a 68.3% CL or $1\sigma$ uncertainty region around the best spectrum fit. The "IV-untagged" condition of "IV Charge $<$ 10,000 DUQ" identifies the stopped muon vertices high up and close to the chimney region of the inner detector. This constraints low energy depositions from getting into the target region. This might be one reason behind the negative slope of the stopped muon spectrum at low energies.

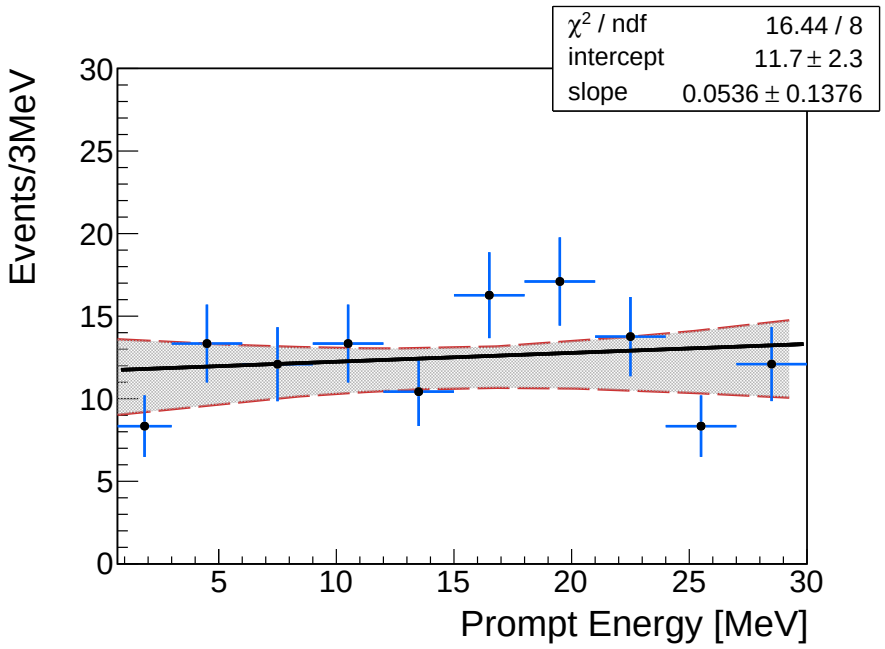


Figure 8.24: Stopped muon prompt energy spectrum, data at straight line fit.

### 8.2.10 Fast Neutron Spectral Shape

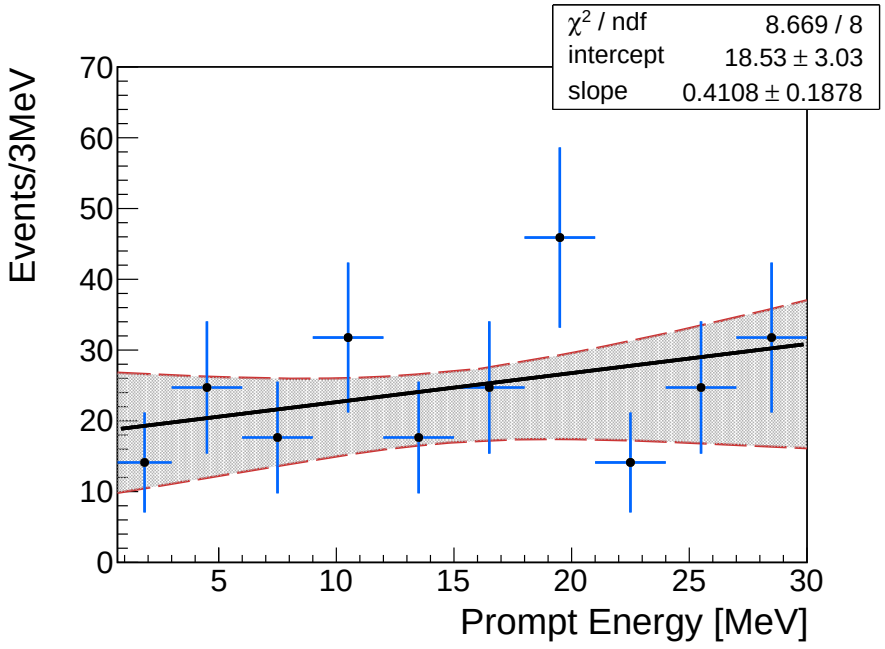


Figure 8.25: Fast neutron prompt energy spectrum, data at straight line fit.

### 8.2.11 Rate of Events

The rate of the neutron and stopped muon events are computed over a total livetime of 227.9294 days. The following Table 8.5 summarises each of the two categories of events. The uncertainties quoted are combined statistical and systematics.

| Candidate | Total number | Rate ($\text{day}^{-1}$) | Slope (Linear Fit) | Intercept |
|---|---|---|---|---|
| Fast Neutrons | 86.14 | $0.38 \pm 0.25$ | $0.41 \pm 0.43$ | $18.53 \pm 3$ |
| Stop Muons | 45.88 | $0.20 \pm 0.13$ | $0.053 \pm 0.13$ | $11.7 \pm 2.3$ |

Table 8.5: Daily rate and spectral shape information about the fast neutron and stopped muon candidates

### 8.2.12 Combined Spectral Shape

The two spectra are combined using the ratios listed in Table 8.4. The combined spectrum is approximated with a linear function and fit in the range $[0.7, 12]$ MeV.

For the record, the extended IBD spectrum in the energy range $[0.7, 30]$ MeV was fit outside the IBD selection range and the fit function was extrapolated to the IBD region to estimate the number of correlated background candidates inside the neutrino selection region of $[0.7, 12]$ MeV. This fit was performed in the range $[12.2, 30]$ MeV with a 1-parameter and a 2-parameter straight line. The 1-parameter fit and extrapolation is termed the "flat extrapolation" while that with the 2-parameter lineis called the "free extrapolation". The following figures show the results of these two fits:

In Fig. 8.27, the fit parameter obtained from the range $[12.2, 30]$ MeV was used to extrapolate the line into the region $[0.7, 12.2]$ MeV. The blue band shows the $1\sigma$ confidence region around the fit.

Similar to that in the previous case, Fig. 8.27 shows the "free extrapolation" with the fit

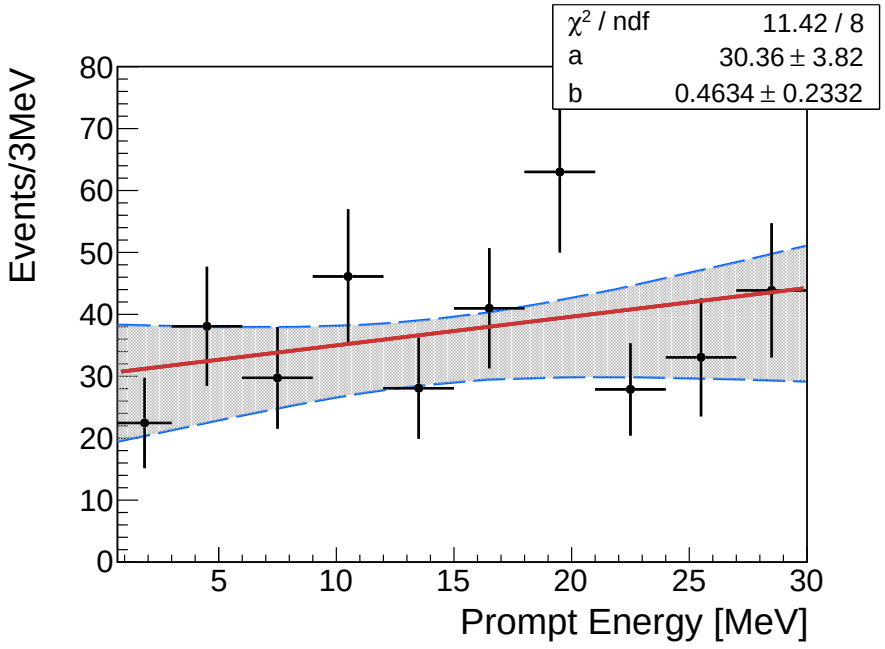


Figure 8.26: Fast Neutron prompt spectral shape fitted with a linear model.

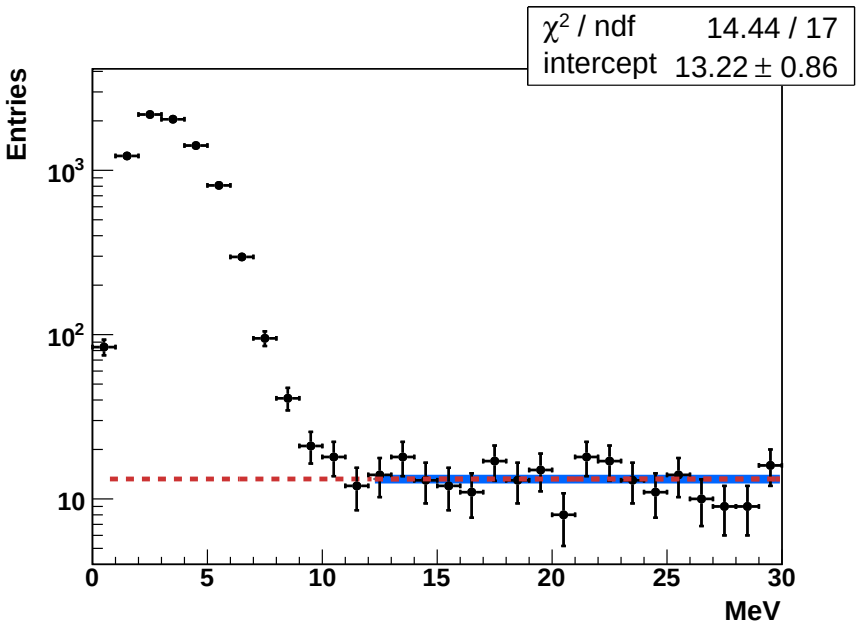


Figure 8.27: Flat extrapolation extended from [12.2,30] MeV into the IBD region of [0,7,12.2] MeV

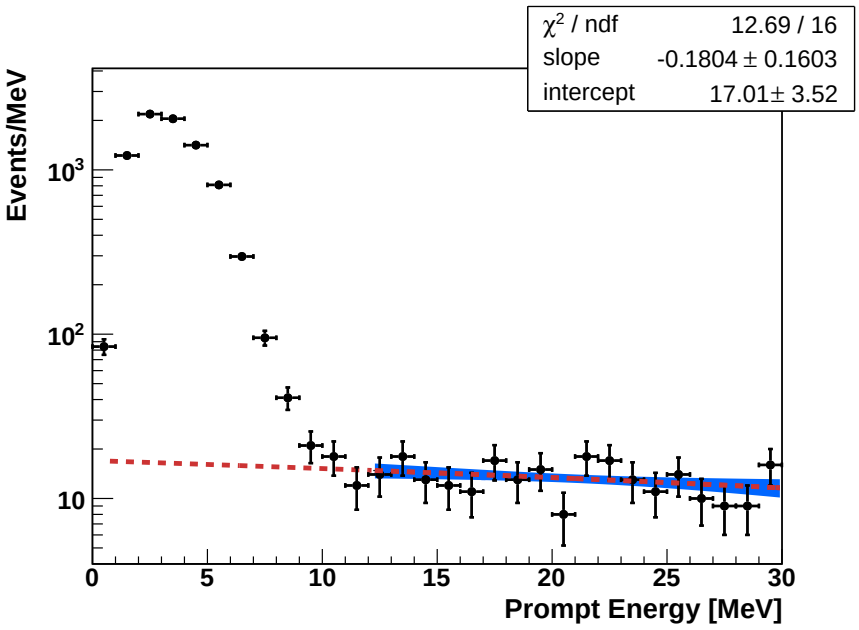


Figure 8.28: Free extrapolation extended from [12.2,30] MeV into the IBD region of [0,7,12.2] MeV

parameters obtained from data in the range $[12.2, 30]$ MeV used to extrapolate the line into the region $[0.7, 12.2]$ MeV. The blue band shows the $1\sigma$ confidence region around the fit.

### 8.2.13 Summary table

Table 8.6 summarizes the total numbers and daily rates for background candidates estimated using the diffeent techniques.

| Method | Total Number | Rate $(\text{day})^{-1}$ | Overall Slope $(\text{MeV})^{-1}$ | Intercept $(\text{MeV})^{-1}$ |
|---|---|---|---|---|
| OV Tagged | 132 | $0.58 \pm 0.28$ | $0.166 \pm 0.077$ | $9.932 \pm 1.25$ |
| Flat Extrap. | 153 | $0.67 \pm 0.04$ | 0 | $13.22 \pm 0.86$ |
| Free Extrap. | 182 | $0.80 \pm 0.13$ | $-0.18 \pm 0.16$ | $17.01 \pm 3.52$ |

Table 8.6: Summary of the total number and rates of background candidates estimated using different methods.

The OV trigger rate is 224 kHz and the item window for the coincidence between the OV signal and an inner detector signal is 224 ns. Hence the probability of an coincidence between a OV muon and an accidental event in the inner detector is neglected as being too small. An overlay of the extended IBD spectrum, the combined correlated background specturm as well as the $1\sigma$ and $2\sigma$ uncertainty regions are shown in the Fig. 8.29 below. The correlated background data and the spectral shape is overlayed on top of the extendend IBD spectrum obtained after the OV veto. The extended region in the range $[12.2, 30]$ MeV is where the two spectra have been normalized to each other.

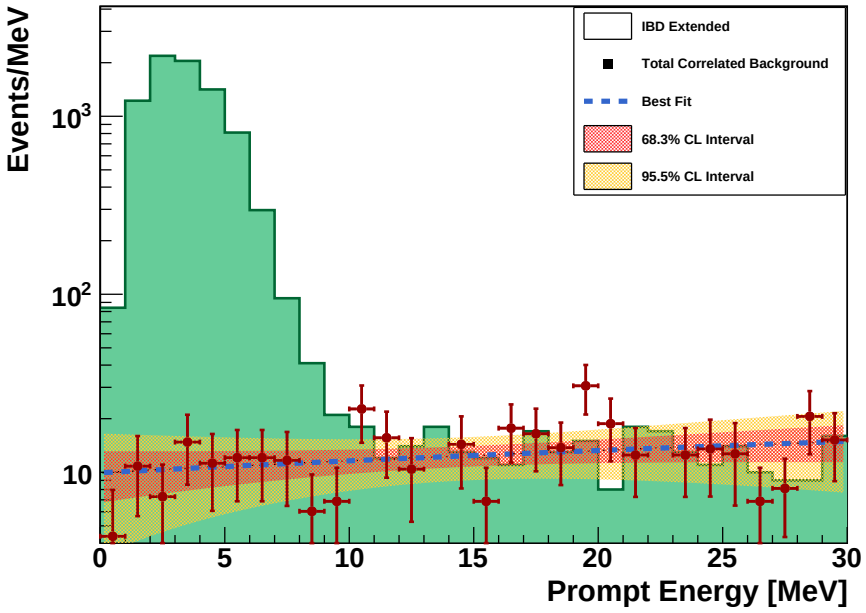


Figure 8.29: Total correlated background data and spectral shape overlayed on the extended IBD spectrum.

### 8.2.14 Slope of the Neutron Spectrum

The positive slope of the stopped muon spectrum at lower energies is most likely due to the fact that the muons which are not identified by the inner veto are relatively low energy muons. These muons are spatialyl constrainted from reaching the inner detector and so very

few of them reach the active volume. On the other hand, the positive slope of the prompt energy spectrum for the neutrons could imply that the cross section for the interaction of the fast neutrons with the nuclei increases with increasing energy. Elastic scattering is the most pobable interaction process between a fast neutron and light elements like hydrogen. Elastic scattering cross sections are more or less independant of neutron energy upto 1 MeV. Beyond that too, it shows very little variation and there are no resonance peaks in the cross section for $^1$H and $^2$H. Hence it is assumed that the prompt energy spectrum for the neutrons in Double Chooz was expected to be rather flat. Since neutrons tagged by the OV are likely to be the ones that are either "IV-clipping" or "IV-near miss", most of them probably will come into the detecor from the rock outside the detecor volume. We decided to investigate this by plotting neutron prompt energy spectra as a function of increasing radial cut on the OV muon hit position. This will allow us to look for neutrons getting into the detector due to muon spallation in rock. The results are shown in the following Figs. 8.30 - 8.38.

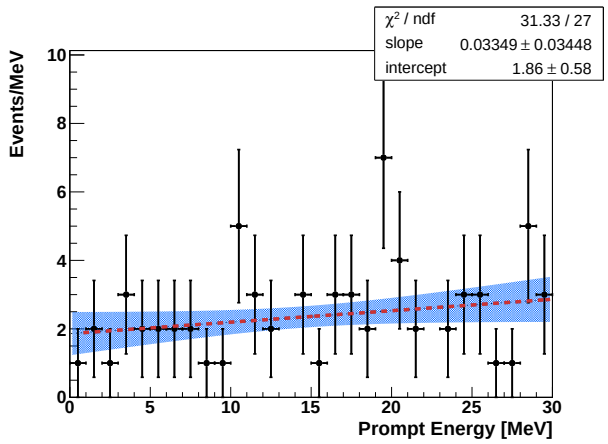


Figure 8.30: Fast neutron prompt energy spectrum for $\rho_{ov} > 2$ m.

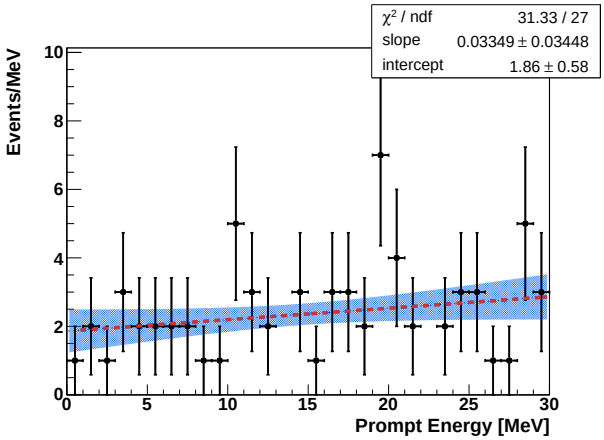


Figure 8.31: Fast neutron prompt energy spectrum for $\rho_{ov} > 2.5$ m. Due to the lack of any statistics between $2m. < \rho_{ov} < 2.5$m., the values remain unchanged from Fig. 8.30.

The results of the above study reveals that with an increasing threshold cut on the radial muon hit position, so the closer we get to getting a sample of fast neutrons produced mainly due to muon spallation on the rock, the flatter is the spectrum due to their recoil on the

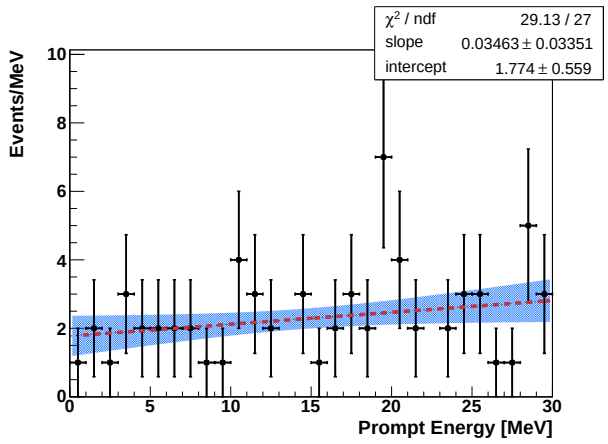


Figure 8.32: Fast neutron prompt energy spectrum for $\rho_{ov} > 3$m.

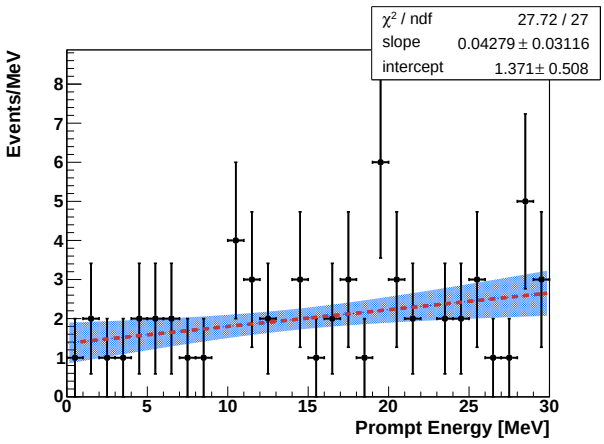


Figure 8.33: Fast neutron prompt energy spectrum for $\rho_{ov} > 2$m.

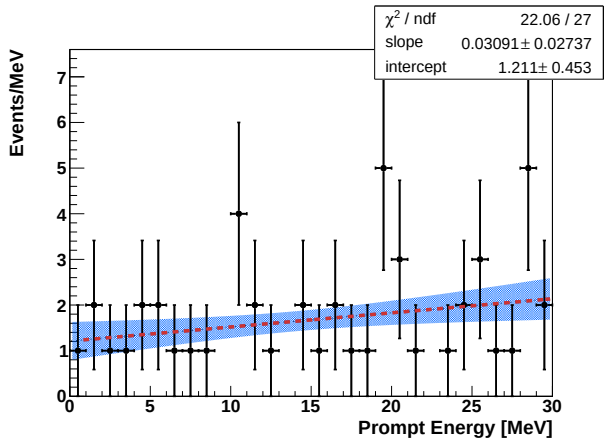


Figure 8.34: Fast neutron prompt energy spectrum for $\rho_{ov} > 4$m.

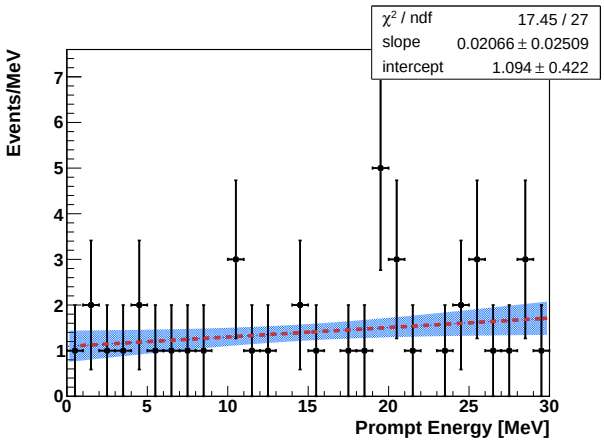


Figure 8.35: Fast neutron prompt energy spectrum for $\rho_{ov} > 4.5$m.

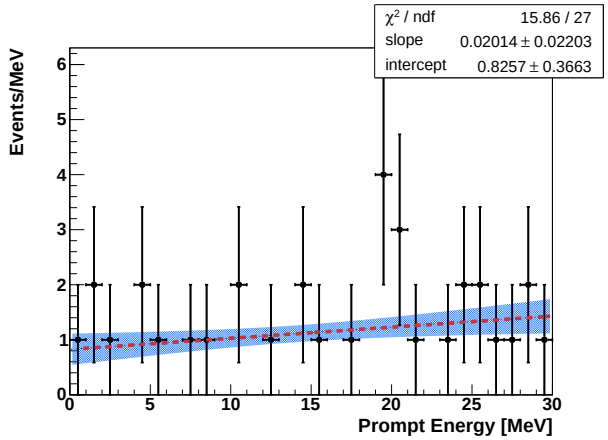


Figure 8.36: Fast neutron prompt energy spectrum for $\rho_{ov} > 5$m.

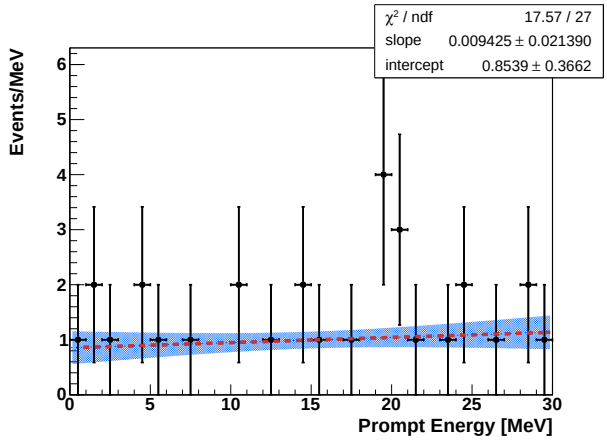


Figure 8.37: Fast neutron prompt energy spectrum for $\rho_{ov} > 5.5$m.

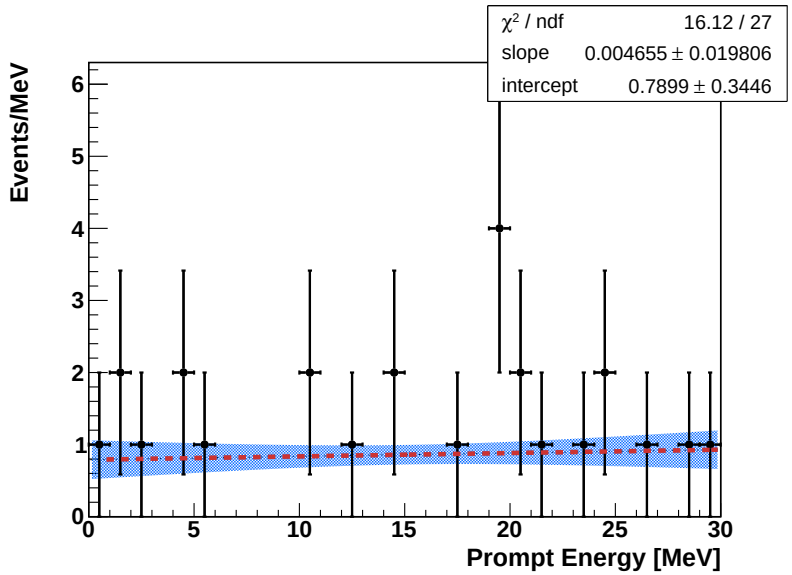


Figure 8.38: Fast neutron prompt energy spectrum for $\rho_{ov} > 6$m.

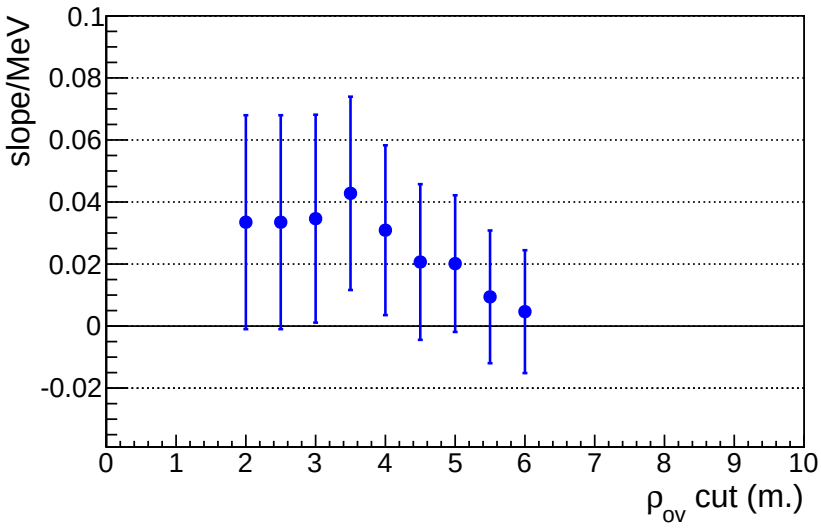


Figure 8.39: Graph showing the variation of the slope of the fast neutron prompt energy spectrum as a function of radial distance cut.

protons in the scintillator. With the neutron scattering cross section dominated by elastic scattering on 1H, assuming a constant flux $8 \times 10^{-7} cm^{-2} s^{-1}$ [47] of neutrons coming into the detector, the total interaction rate of neutrons in the inner detector is expected to be independant of the neutron energy.

### 8.2.15 Conclusions from OV-only Tagging Method

The primary purpose of the tagging scheme is to estimate the neutron background for Double Chooz by tagging muons that either clip or nearly miss the inner veto (IV) volume of the detector. The "OV-only tagged" method, described in this section, is successful in tagging these "IV-clipping" or "IV-near miss" muons, and hence provides a good estimate of the rate of the external neutrons coming into the detector.

At the same time the method is very powerful in tagging muons that get into the detector without triggering the IV. Hence the method was equally suitable for computing the stopped muon part of the correlated background. Hence the "OV-only" method, both in the case

of neutrons as well as stopped muon events, can be used to estimate potential background events with the same IV tagging criteria as for the IBD events. This shows the power and usefulness of this simple but effective technique to estimate both the neutron as well as stopped muon events causing the correlated background for Double Chooz.

## 8.3 IV Only Tagging

The "OV-Tagged" method is very powerful for the external fast neutrons as well as for the chimney stopped muons for computing their rates and spectral shapes using the same IV-tagging scheme as for the neutrino events. For the stopped muons espcially, it provides a very efficient method as the IV efficiency for these events is low. Also the stopped muon events have a limited topology in the sense that they are concentrated in a small region in or around the chimney region of the detector and the "OV-tagged" method can identify a sufficient number of these events to allow for an analysis. The neutron events on the other hand have a wider range of topology as their angular distribution around the detector is much more varied. The OV, due to its structural constraints, has little coverage over the detector on two sides closer to the walls of the laboratory and it is possible for the neutrons to enter the inner detector from the sides of the detector due to spallation on rock of near-miss or clipping muons which do not trigger a hit on the OV. In such cases an analysis technique involving "IV-only" tagging would give a totally idependant way to estimate the neutron background. In this case the muon that possibly causes the background candidates would be "IV-only" tagged and there would be no related OV-signal.

This method could give accurate estimate for neutron events that are produced in the rock near the detector with the responsible muon completely missing the detector. The topology of these events would differ from "OV-only Tagged" ones and therefore they would provide a good independant confirmation of the results obtained in the previous section. The following

Fig. 8.40 shows some of the key aspects of tagging the neutrons with this technique.

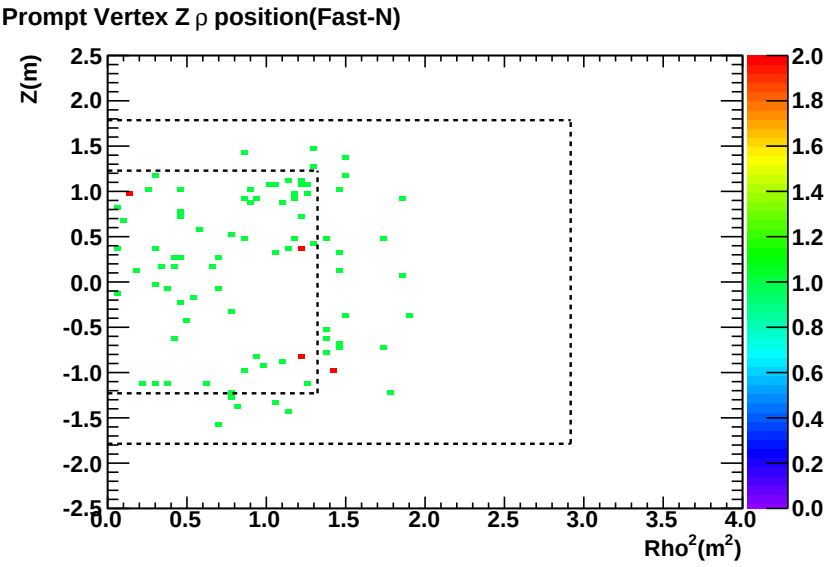


Figure 8.40: Vertex distribution of the fast neutrons tagged by the IV alone.

The vertex distribution of the fast neutron candidate events are, as expected, distributed rather uniformly in the inner detector. One difference from the similar plot obtained with "OV-only" selection is that there are a few more events near the bottom of the detector. These are the neutron events caused by the muons that clip the bottom corner of the detector. It has only been possible to detect these events because of the "IV-tagging" of the muons.

From Figs. 8.41 and 8.42, that show the delayed energy and $\Delta T$ for the fast neutron candidates, we can conclude that the selected events show the characteristic gd-peak and the timing of a neutron capture event.

### Summary Table

We see that the neutron rate observed by using "IV-only" tagging gives a value for the rate of the neutrons that is consistent with that obtained by using "OV-only" tagging unit. It

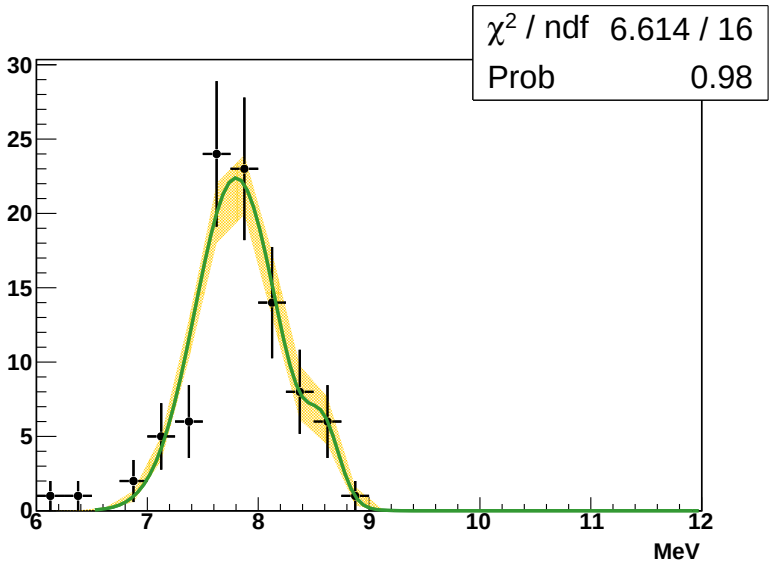


Figure 8.41: Delayed capture energy of the IV-tagged neutrons, data and fit.

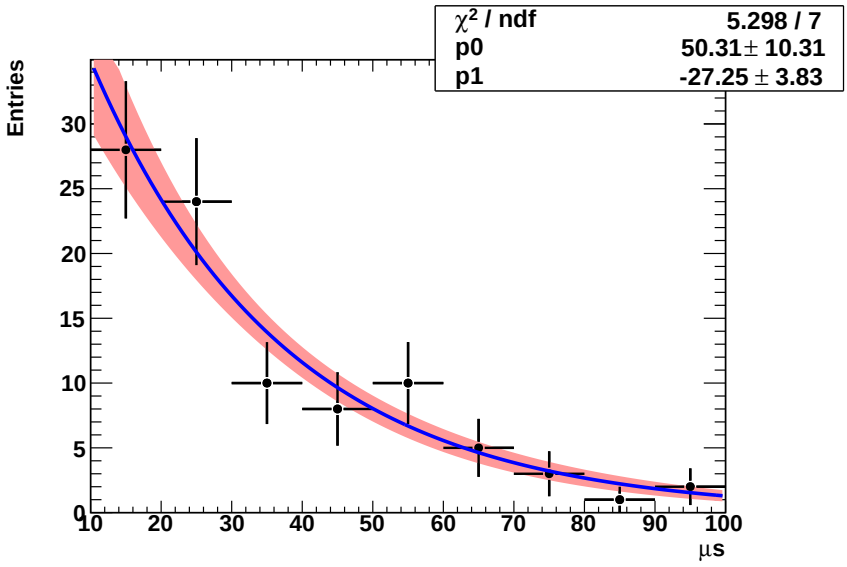


Figure 8.42: $\Delta$T distribution for the IV-taged neutrons, data and fit.

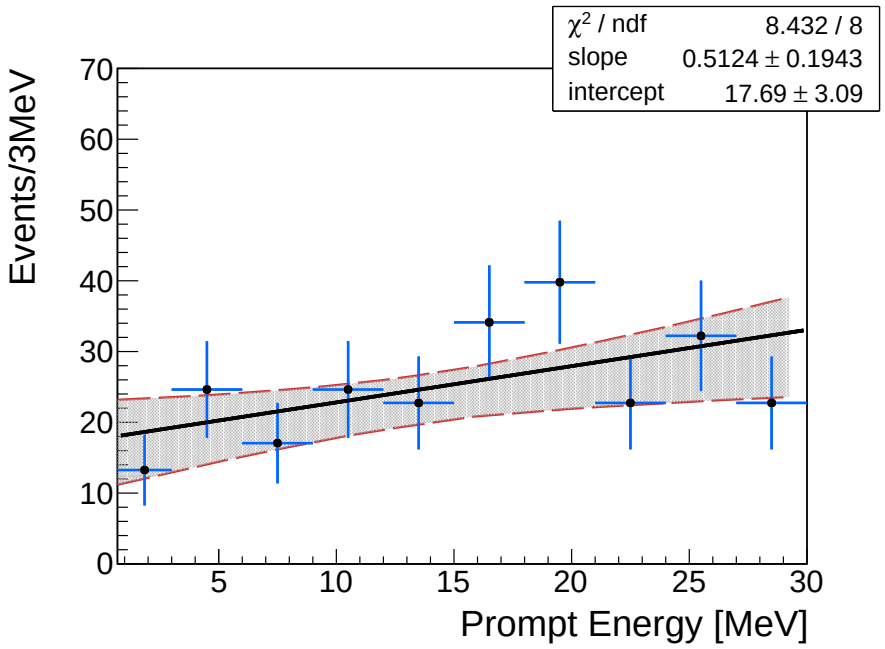


Figure 8.43: Prompt energy spectrum for the fast neutrons tagged by the IV-only, data and fit.

| Method | Total Number | Rate $(day)^{-1}$ | Overall Slope $(MeV)^{-1}$ | Intercept $(MeV)^{-1}$ |
|---|---|---|---|---|
| IV Tagged | 71 | $0.31 \pm 0.10$ | $0.28 \pm 0.074$ | $6.85 \pm 1.14$ |

Table 8.7: Summary of the total number and rates of neutons background candidates estimated with the "IV-tagged" method.

is reassuring that both of these independent detector components have consistent tagging efficiencies for external fast neutrons.

### 8.3.1 Neutron Rate from Multiplicity of Events Following a Muon

In an experiment like Double Chooz primary neutrons from near-miss muons, along with the secondary neutrons, are two of the most serious backgrounds. Double Chooz applies an offline veto of 1 ms after each muon event to remove such events from the candidates selected. Most of the correlated background sources, such as neutron-like events, are rejected

by the muon veto of 1 ms. In this section we study the events that survive on increasing time cut since the last muon and estimate the neutron-like events remaining in the selected neutrino sample. As mentioned earlier, muons which either nearly miss or clip the detector produce neutrons that get into the active volumes of the detector which in turn could be followed by secondary neutrons. These neutrons can be a source of correlated background, as explained in earlier sections, or they could fall into the time window opened by a $e^+$ or $\gamma$ creating event with varying multiplicities (M) in the delayed time window following a prompt event. We will study these events separately and from the number of events of M$\geq$ 2, we will provide an estimate of the neutron events with M = 1 which could easily be mistaken as an IBD event.

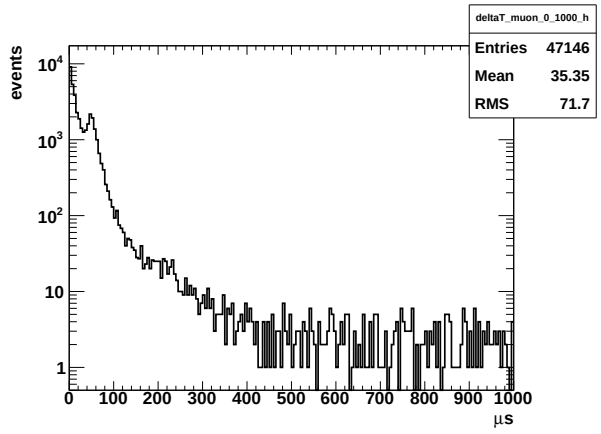


Figure 8.44: Time of an event since the last muon.

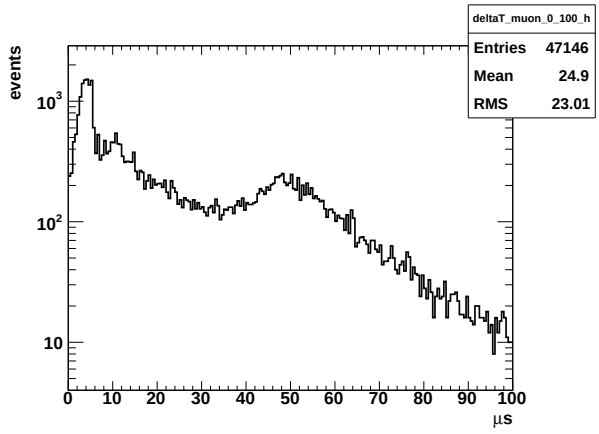


Figure 8.45: Events since a muon at t=0, showing inefficiency at times $< 50$ $\mu$s

Fig. 8.44 shows the variation of the IBD-like events following a muon. It shows that after a veto time cut of 1 $\mu$s since the passage of the muon cuts out almost all the events correlated with the muon. Fig. 8.45 shows the fluctuations in the event rate immediately following a muon. To perform this study of the multiplicity of the delayed events, we have chosen to follow the event rate starting 50 $\mu$s after the muon event.

Events with multiplicity of the delayed events equal to 1, as shown in Fig. 8.46, can represent either an IBD event ($e^+$ + n) or a double neutron event (n + n). Ideally all of these should be

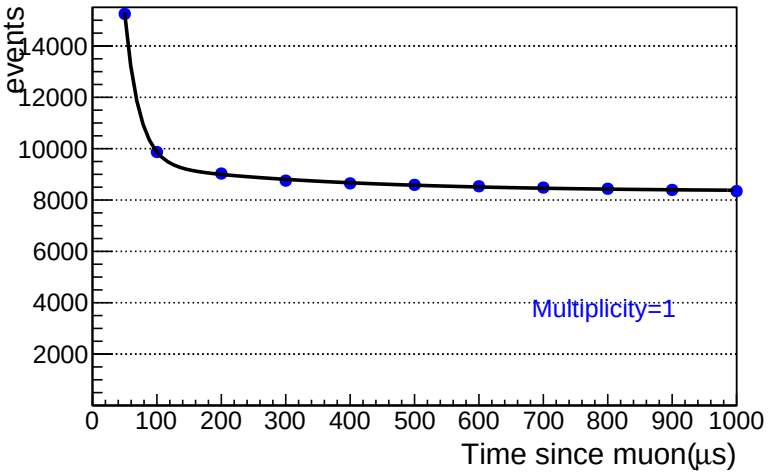


Figure 8.46: Survival of events of multiplicity1 with time since the last muon

IBD events but there could be a small contamination of neutron-like events in this category of events.

Events with multiplicity of the delayed events equal to 2, shown inf fig. 8.47, can represent either an (IBD + n) or [$\gamma$ + (n + n)] or an [n + (n + n)] event. The graph is fit with a combination of an exponential and a straight line, with the exponential part vanishing before reaching the 1 ms veto cut, after which all that remains is the flat linear remainder.

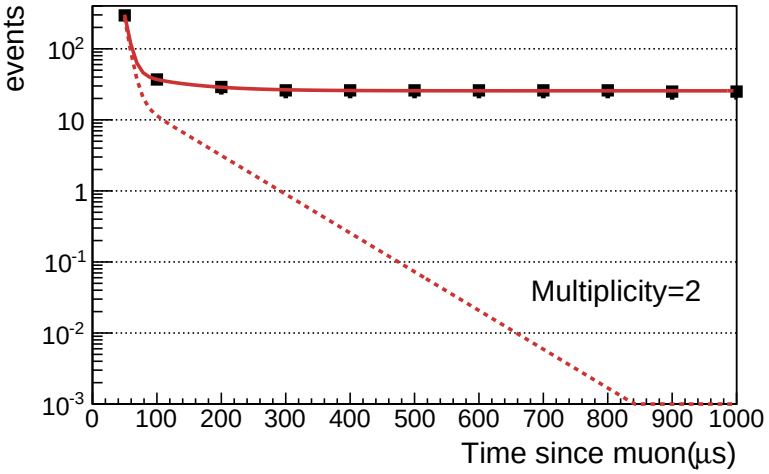


Figure 8.47: Survival of events with M = 2 with time since the last muon.

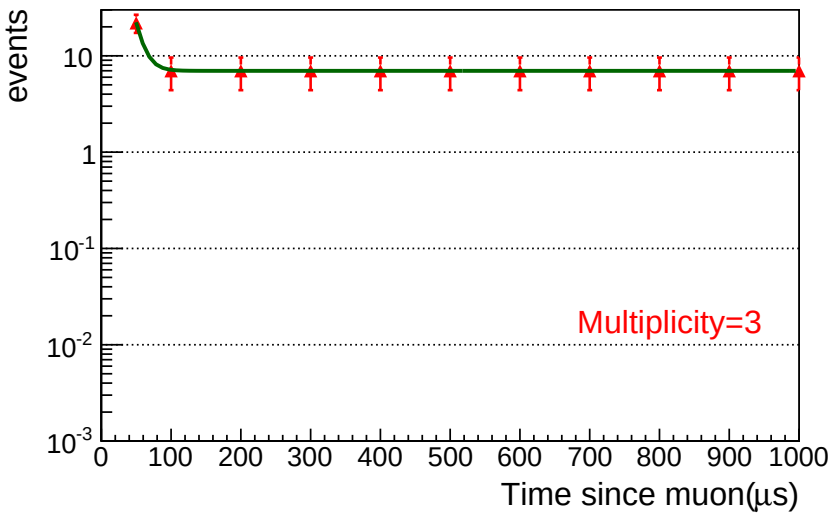


Figure 8.48: Survival of events with multiplicity = 3 with time since the last muon.

Events with multiplicity of the delayed events equal to 3 can represent either an [IBD + (n + n)] or [$\gamma$ + (n + n + n)] or an [n + (n + n + n)] event as shown in Fig. 8.48.

Similarly, events with multiplicity of the delayed events equal to 4 can represent either an [IBD + (n + n + n)] or [$\gamma$ + (n + n + n + n)] or an [n + (n + n + n + n)] event, as shown in Fig. 8.49

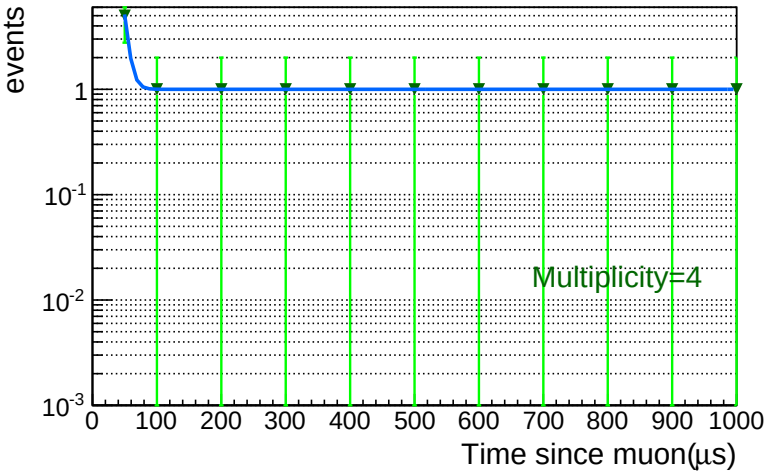


Figure 8.49: Survival of events with M = 4 with time since the last muon.

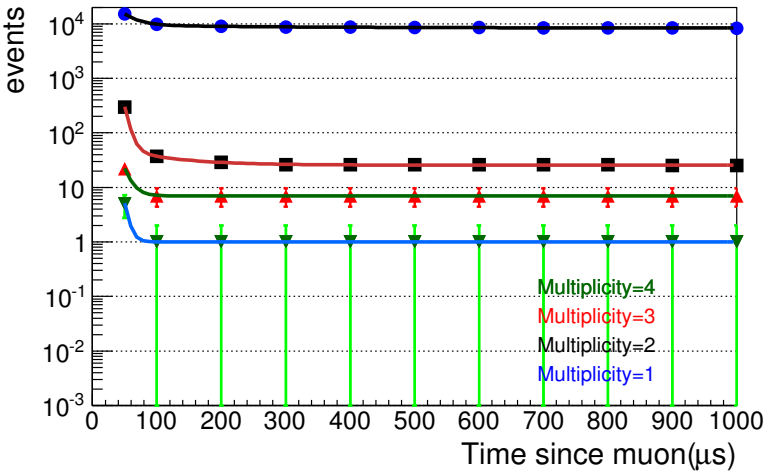


Figure 8.50: Survival of events with M=1 through M=4 with time since the last muon.

Fig. 8.50 shows all the events and their daily rates after the 1 ms veto cut since the last muon. An offtime selection was done for all events with an offtime event window of [3,4] ms after the muon, to find any accidental events. All the numbers quoted below are the result of the subtraction of any such events from the events in the ontime event window.

| Candidates with | Total number | Rate ($day^{-1}$) |
|---|---|---|
| M=2 | 25 | 0.11 ± 0.022 |
| M=3 | 7 | 0.03 ± 0.0011 |
| M=4 | 1 | 0.0044 ± 0.0043 |
| M=5 | 1 | 0.0044 ± 0.0043 |

Table 8.8: Total number and rates of the neutron candidates surviving the time cut since the last muon.

The graph of Fig. 8.51 plotting the numerical values from Table 8.8 is fit with a 2 parameter Poisson function given by

$$f(x) = \frac{P_0 P_1^x e^{-x}}{\Gamma(x+1)} \tag{8.7}$$

The fit was performed between the $x$-axis values [2,6] and extrapolated to $x$=1 to estimate the neutron background of multiplicity 1 events after the 1 ms veto cut since a muon. All

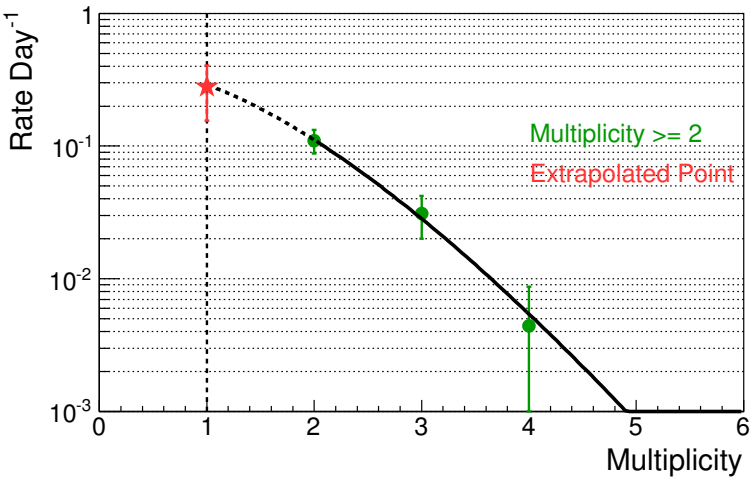


Figure 8.51: Rates of events of varying multiplicities surviving the veto cut since last muon. The fit function is extrapolated to estimate the rate of neutron-like events surviving the veto cut.

the uncertainties quoted in Table 8.9 are of statistical nature.

| Candidates with M=1 | Total Number | Livetime (day) | Rate ($day^{-1}$) |
|---|---|---|---|
| Extrapolated from Fit | 69 | 227.9294 | 0.29±0.12 |

Table 8.9: Extrapolated rate of neutron-like background with statistical uncertainty

This study of events with various multiplicities surviving the time cuts since the passage of the last muon gives another simple but good estimate of the neutron or neutron-like background for Double Chooz. The study was performed using both reactor-on and reactor-off data, and the results were consistent with each other.

## 8.4 Summary

In this chapter we have attempted to estimate the rate of the background caused by neutrons coming into the detector from outside rock and mimic an anti-neutrino event. The rate of such events have been estimated using various techinques, including the use of the "reactor off-off" data. The values of the daily rates for such events are consistent between the various analyses and are summarised in the following Table 8.10.

| Analysis technique | Total Number | Livetime (day) | Rate ($day^{-1}$) |
|---|---|---|---|
| OV Tagging | 86 | 227.9294 | 0.38±0.25 |
| IV Tagging | 71 | 227.9294 | 0.31±0.10 |
| Extrapolated from Fit | 69 | 227.9294 | 0.29±0.12 |

Table 8.10: Rates of neutron backgrounds for Double Chooz experiment estimated using various methods.

## 8.5 Estimation of Fast Neutron Incidence Rate

The daily rates of the fast neutron background presented in Table **??** are the measured rates inside the detector. In reality the incidence rate of the fast neutrons into the active volume of the detector could be higher. Some of these neutrons may be interacting inside the detector without meeting the conditions to produce a background or some of them may not be interacting at all. In order to estimate the efficiency for the detection of these fast neutrons, a Monte Carlo (MC) based study was performed mainly to establish an order of magnitude estimate for the actual incidence rates for these neutrons in the detector. Neutrons with energy (E> 1 MeV) were generated in a thin (1 mm) outer layer of the target scintillator using the Double Chooz MC simulation package DCGLG4sim [40].

The study was performed separately by (1) varying the initial kinetic energy of the neutrons from 1 MeV to 15 MeV, and by (2) varying the incident angle from 0° to 180°. Fig. 8.52

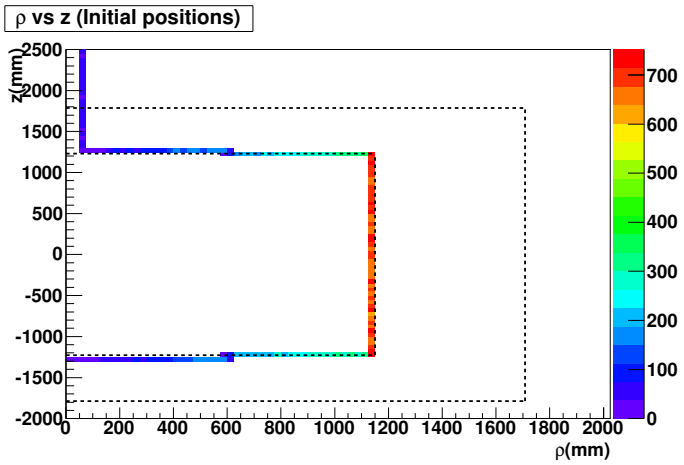


Figure 8.52: $\rho$ vs z plot showing the simulated initial positions of the neutrons.

shows the initial positions of the simulated neutrons. The neutrons were allowed to be captured in the target volume and a delayed coincidence analysis was performed. Fig. 8.53 shows the final capture positions of the neutrons while Fig. 8.54 shows the time difference ($\Delta T$) between the prompt and delayed events due to these neutrons. A fit to the $\Delta T$ plot shows a capture time of $24.7 \pm 0.7$ $\mu$s.

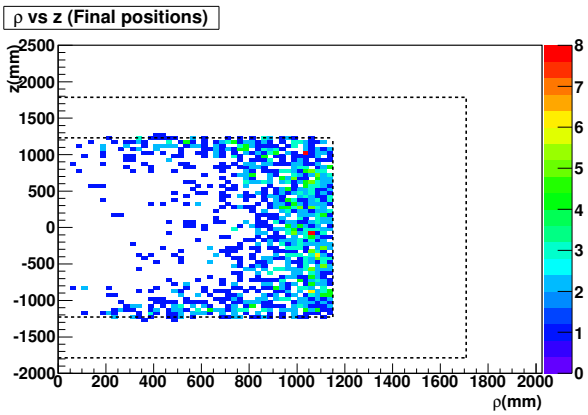


Figure 8.53: $\rho$ vs z plot showing the final capture positions of the neutrons.

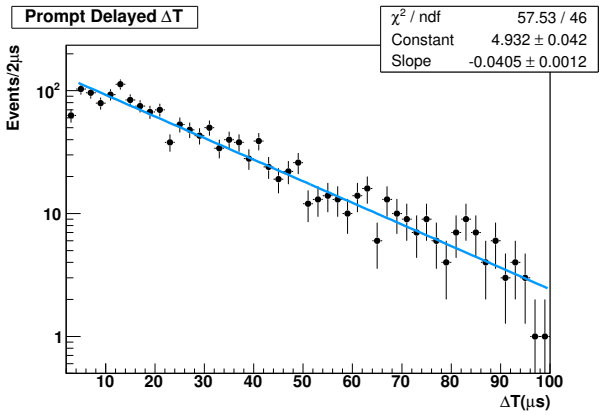


Figure 8.54: Prompt-Delayed $\Delta T$ for the captured neutrons.

Figure 8.55: $\rho$ vs z plot showing the final capture positions of the neutrons (Left) and the $\Delta T$ for the captured neutrons (Right).

The efficiencies of detection of these neutrons, based upon the principle of delayed coincidence, for each incident kinetic energy, were calculated by taking the ratio of the number of

neutrons detected by the number of neutrons initially generated for each incident energy. A

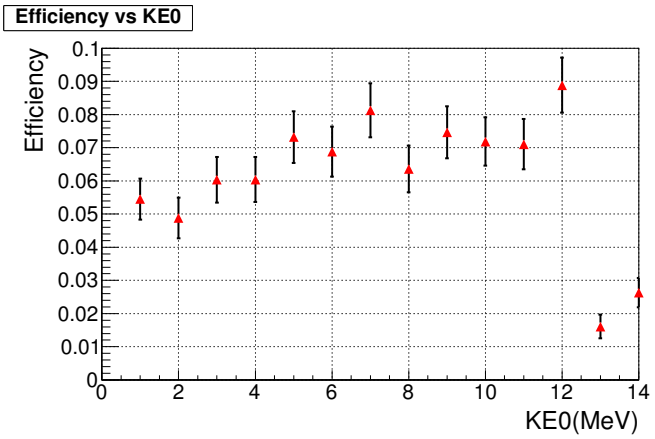


Figure 8.56: Detection efficiency for the neutrons as a function of their incident kinetic energies.

graph of the calculated efficiencies as a function of the incident neutron kinetic energies are shown in Fig. 8.56 which clearly shows some dependency of the efficiency on the incident kinetic energy.

The efficiency to detect these neutrons as a function of their incident angles was performed for two different energies 6 MeV and 10 MeV. The incident angles were all measured from the inward normal to each face of the detector, top, bottom and the side. The detection efficiencies of these neutrons calculated for each incident angle is shown in Fig. 8.57 and Fig. 8.58.

The grapha are fit with a hyperbolic tangent function

$$f(x) = P_0 + P_1 + \tanh[(x - P_2)/P_3]. \tag{8.8}$$

An average estimate of the detection efficiency for the incident angles from 0° to 90° is made by taking the integral of the fit function in that range for each face. The mean of such average efficiencies comes out to be 0.042. Hence dividing the value of the neutron background from Table 8.5 by this efficiency, we get an order of magnitude estimate of the neutron incident rate in the Double Chooz detector equal to $\approx$9 day$^{-1}$.

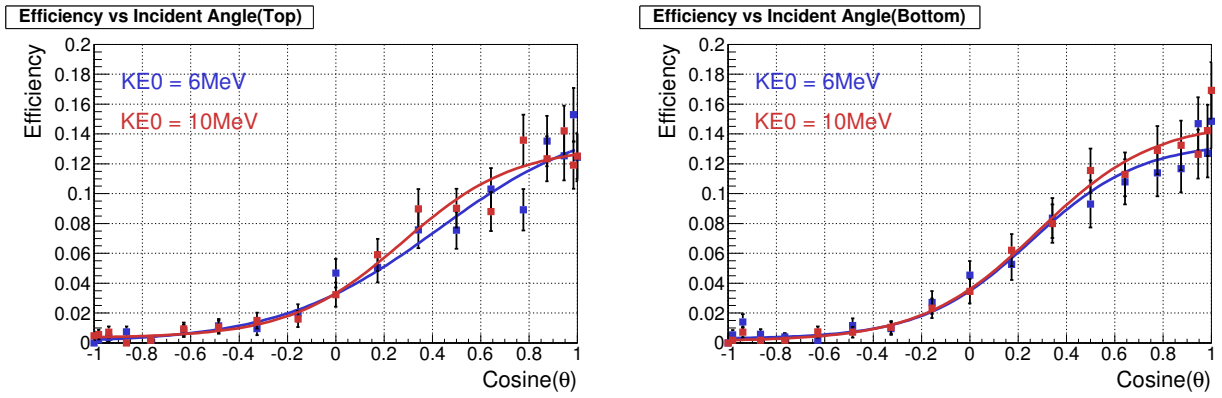


Figure 8.57: Detection efficiency for the neutrons as a function of the incident angles on the top (Left) and bottom (Right) faces of the detector.

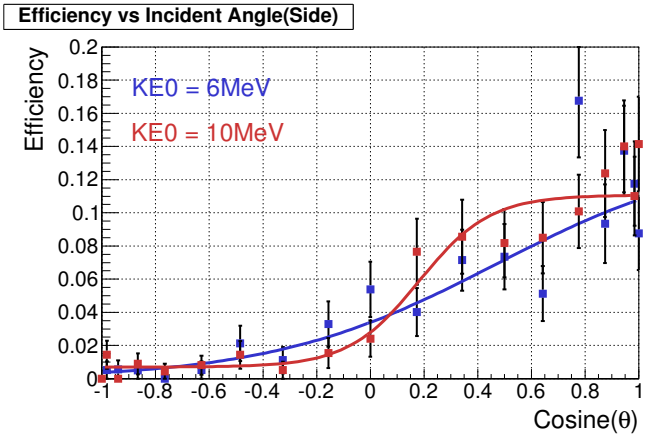


Figure 8.58: Detection efficiency for the neutrons as a function of the incident angles on the side face of the detector.

## 8.6 Summary of Neutron Incident Rate Study

An order of magnitude estimation of the possible incident rate of the fast neutrons for the Double Chooz experiment was presented. It is important to mention here that this MC study is a rather crude way to estimate the incident rate for the fast neutrons in the Double Chooz detector. The results of this study can be improved by repeating it with a realistic energy and angular distribution for the neutrons.

# Chapter 9

# Double Chooz $\theta_{13}$ Result

## 9.1 Double Chooz Final Oscillation Fit

Double Chooz was the first experiment to report the measurement of the non-zero value of $\theta_{13}$ with the results published in [28] and [29]. In this chapter I will summarize mainly the analysis results published in the second publication [29]. The analysis results, as presented in Chapter 8, contribute toward the final estimation of the correlated background, one of the key component of the overall $\theta_{13}$ anaylsis. Additionally, the analysis technique presented in this chapter involves the use of both the rate and spectral shape of the various components of the analysis. This is different from the my independant analysis of $\theta_{13}$ based solely upon the observed and predicted rates of the antineutrino events, as presented in chapter 10.

The final analysis to measure the value of $\theta_{13}$ from the Double Chooz data requires figuring out a few more things. We need to measure the rate and shape of the various background sources for the experiment. In the following sections we will describe briefly the estimation of each background. The oscillation analysis is based on a combined fit to antineutrino rate and spectral shape. The IBD candidates, as selected and described in Chapter 5, are compared to the Monte Carlo signal and background events from high-statistics samples. Two integration periods are used in the fit to help separate background and signal flux. If the minimum power of either reactor is below 20% of peak during a particular detector run,

then that detector run is placed in "IP1", else, the detector run is placed in "IP0". Each type of background population was computed based on the measured rates and the livetime of the detector during each integration period.

### 9.1.1 Accidental Background

The accidental background is primarily produced by the random coincidence of a prompt signal from natural radioactivity and a neutron-like signal. To estimate the accidental background the same selection cuts used to select the IBD candidates in Chapter 5 are used except now the delayed coincidence window is offest by 1s in order to avoid any prompt-delayed correlations within the time window for neutron captures in Gd and H. To obtain a large enough sample of such events, 198 successive time windows were opened, each 500$\mu s$ after the other. The rate of the accidental background was found to be $0.261 \pm 0.002$ day$^{-1}$, see Fig. 9.1.

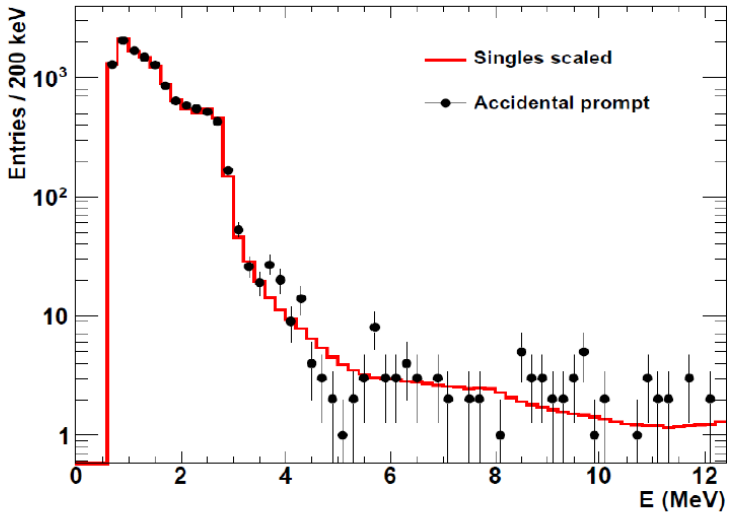


Figure 9.1: Accidental prompt energy spectrum (black) with the measured radioactivity energy spectrum.

### 9.1.2 $^{9}$Li Background

Muons interacting with $^{12}$C through spallation create unstable radioisotopes such as $^{8}$He and $^{9}$Li. These isotopes decay by emitting $\beta$-particles and neutrons which combine together to create a background for IBD candidate selection. Most of these isotopes have long half lives with the half life of $^{9}$Li being 178 ms while that of $^{8}$He is 119 ms and therefore it is not practical to veto these events. Hence a rate for these events are estimated using an exponential fit to the time between an IBD candidate-pair and the muon immdiately preceeding it. The analysis to determine the rate was performed in three energy ranges for the showering muons: (1) $E_{\mu}^{vis} < 275\,\text{MeV}$ (2) $275\,\text{MeV} < E_{\mu}^{vis} < 600\,\text{MeV}$ and (3)$E_{\mu}^{vis} > 600\,\text{MeV}$. An additional cylindrical fiducial cut on the distance of closest approach from the muon to the IBD candidate, $d\mu\nu < 80\,\text{cm}$ was applied to case (1) and (2) to select the events correlated to the showering muons. An overall rate of $2.05^{+0.62}_{-0.52}$ events $day^{-1}$ was found, see Fig. 9.2.

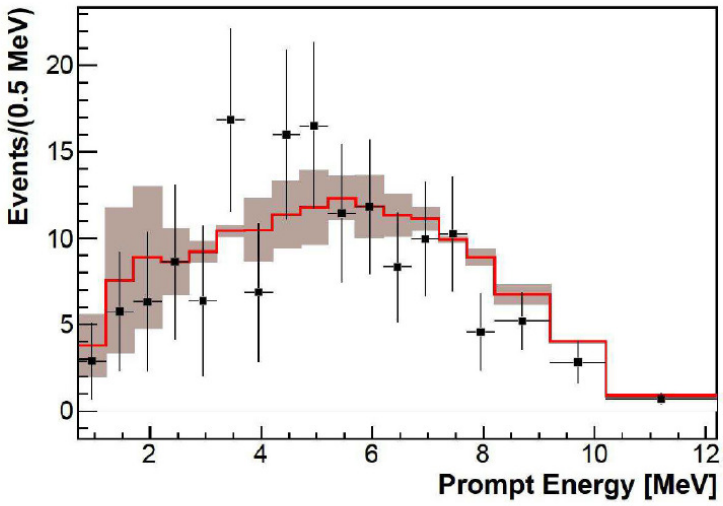


Figure 9.2: Prompt energy ($\beta$)-spectrum of the $\beta n$ emitters $^{9}$Li and $^{8}$He (black) with the Monte Carlo (red).

### 9.1.3 Fast Neutron and Stopped Muon Background

The production mechanism of the fast neutron and the stopped muon background has been discussed in Chapter 8. Several analyses dedicated to estimating the overall correlated background were performed using different combinations of IV and OV tagging. The analysis from which the central values for the above two backgrounds were taken uses the IV-tagging of the prompt triggers with OV veto applied for the IBD selection while rejecting the sources of further backgrounds in the selected events. The total rate of this background with this analysis was found to be $0.67 \pm 0.20$ day$^{-1}$ which is consistent with the analysis described in Chapter 8. The spectral shape of the total correlated background is also consistent within uncertainties with that presented in Chapter 8.

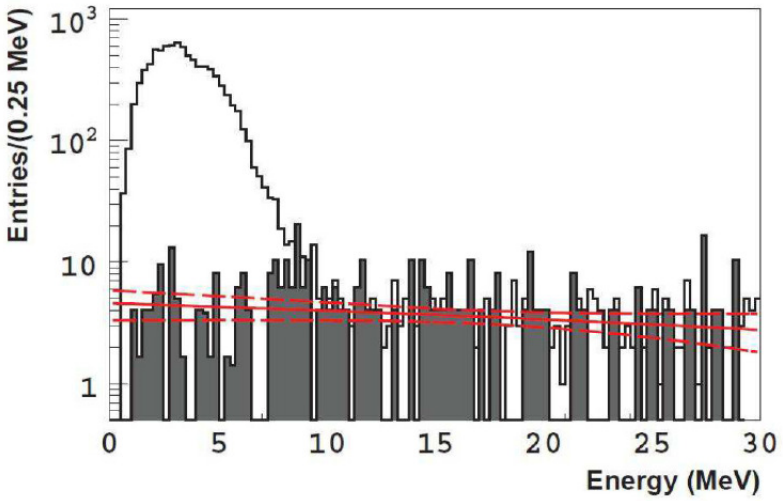


Figure 9.3: Official FastN and Stop Muon combined spectral model (solid red) with $\pm 1\sigma$ (dashed red).

## 9.2 Reactor Model for Oscillation Fit Analysis

In order to come up with a prediction for the antineutrino interaction in the Double Chooz detector, the complete modelling of the nuclear reactors is essential in terms of their power, fission rate and the fission cross section. In the following sections we will describe the various inputs that go into building a reactor model for the experiment.

### 9.2.1 Thermal Power

The sources of antineutrinos for the Double Chooz experiment are the reactor cores B1 and B2 at the Âť ElectricitÂťe de France (EDF) Centrale NuclÂťeaire de Chooz. The main isotopes that provide more than 99.7% of the antineutrinos through the decay of the fission products are: $^{235}U$, $^{239}Pu$, $^{238}U$, and $^{241}Pu$. Knowledge of the thermal powers of the reactor cores is neccessary in order for the precise prediction of the antinuetrino interaction rates. EDF conducts weekly in-core instrumentation calibration for the thermal power measurement. At the nominal full power of 4250 MW the final uncertainty is 0.5% $(1\,C.L.)$.

### 9.2.2 Fission Rate

The fractional fission rates $\alpha_k$ of each isotope is given in Eq. (9.2). Reactor simulations are used to accurately model the evolution of the $\alpha_k$ which are also neccessary to calculate the mean energy released per fission per reactor R:

$$\langle E_f \rangle_R = \sum_k \alpha_k \langle E_f \rangle_k. \tag{9.1}$$

Double Chooz used two complementary simulation codes: (1) DRAGON which is a 2D simulation code to model the neutron transport in the cores and (2) MURE which is a 3D simulation code to simulate the individual fuel assemblies. These codes were benchmarked against data from the Takahama-3 reactor and were found to be consistent other codes commonly used in the reactor industry for reactor modeling within the uncertainty in the

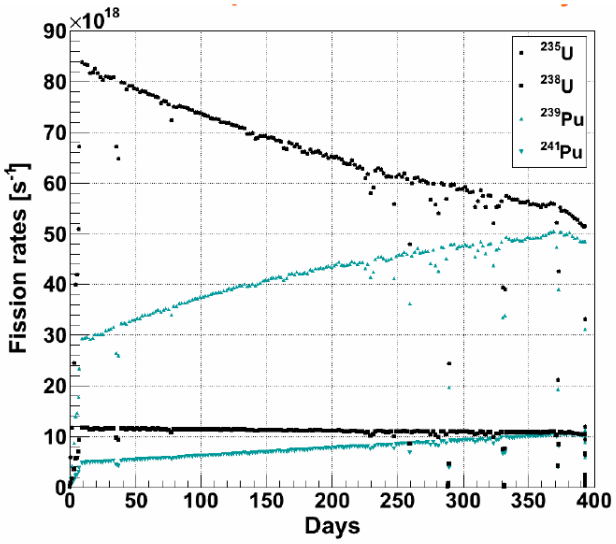


Figure 9.4: Time dependent fuel consumption rate in the cores.

Takahama data [48]. The initial composition of the fuel assemblies is determined first and then MURE is used to model the evolution of the full core to calculate the $\alpha_k$âĂŹs, and also the predicted antineutrino flux.

### 9.2.3 Mean Cross Section per Fission

The average cross section per fission is effectively a interaction cross section averaged over the whole energy spectrum for all the isotopes listed above. It is given by

$$\langle \sigma_f \rangle = \sum_k \alpha_k \langle \sigma_f \rangle_k = \sum_k \alpha_k \int_0^\infty dE\, S_k(E)\, \sigma_{IBD}(E) \tag{9.2}$$

where $\alpha_k$ is the fractional fission rate of the $k^{th}$ isotope ($k = {}^{235}U,\ {}^{239}Pu,\ {}^{238}U,\ {}^{241}Pu$), $S_k(E)$ is the reference spectrum of the $k^{th}$ isotope and $\sigma_{IBD}$ is the inverse beta decay cross section.

The antineutrino spectrum for each of the above listed isotopes are in Fig. 9.5. Corrections have been applied to the conversion of the $\beta$ spectra into the antineutrino spectra by using higher order energy corrections [44]. Also, corrections have been made using the so "off-equilibrium" effect caused by the long-lived fission products. These corrections lead to an

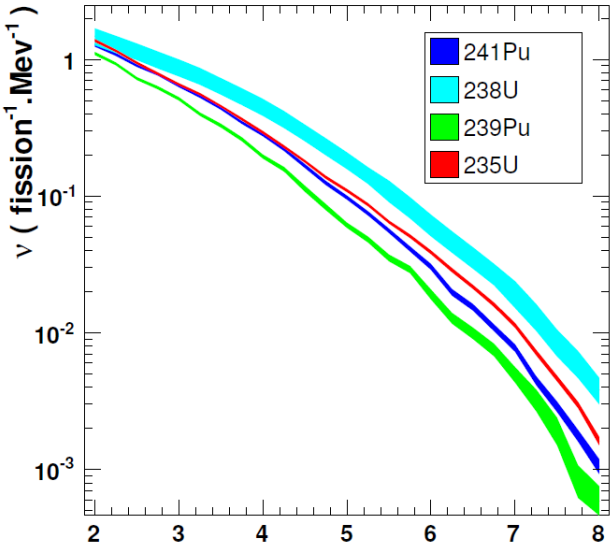


Figure 9.5: Reference antineutrino spectra after recalculations.

effect which results in a 3.5% increase in the antineutrino flux. The systematic uncertainty in these spectra is of the order of 3%.

## 9.3 Bugey4 Anchor for cross section normalization

The cross section per fission for each reactor $\langle\sigma_f\rangle_R$ is normalized to the total rate measurement of the Bugey4 experiment at 15m [31].

$$\langle\sigma_f\rangle_R = \langle\sigma_f\rangle^{Bugey} + \sum_k (\alpha_k^R - \alpha_k^{Bugey})\langle\sigma_f\rangle_k. \tag{9.3}$$

where R stands for each reactor. The Bugey anchor point has low associated systematics and as a consequence of this treatment the overall uncertainty in reactor normalization for Double Chooz decreases from 2.70% to 1.76%.

## 9.4 Antineutrino Predicted ate

For the oscillation fit for the value of $\theta_{13}$, the data is placed in 18 variably-sized bins between $[0.7, 12.2]$ MeV. The whole dataset was divided into separate integration periods as explained

in section 9.1. This technique of using multiple integration periods takes advantage of the different signal to background ratios in each period. We note here that the antineutrino signal varies with the reactor power but the background remains constant with time. A prediction of the observed number of signal and background events is constructed for each energy bin, following the same energy integration period division as the data. By using all the reactor related evaluations in the preceeding sections, the predicted rate of antineutrinos is

$$N_i^{exp,R} = \frac{\epsilon N_p}{4\pi} \frac{1}{{L_R}^2} \frac{P_{th}^R}{\langle E_f \rangle_R} \langle \sigma_f \rangle_R (E,t) \tag{9.4}$$

which, with the Bugey anchor point, gives the expected number of antineutrinos with no oscillation in the $i^{th}$ energy bin as:

$$N_i^{exp,R} = \frac{\epsilon N_p}{4\pi} \frac{1}{{L_R}^2} \frac{P_{th}^R}{\langle E_f \rangle_R} \times \left( \frac{\langle \sigma_f \rangle_R}{(\sum_k \alpha_k^R \langle \sigma_f \rangle_k)} \sum_k \alpha_k^R \langle \sigma_f \rangle_k^i \right) \tag{9.5}$$

Here $N_p$ is the number of target protons, $\epsilon$ is the efficiency of the cuts used to select the IBD candidates, $L_R$ is the baseline from point of neutrino creation to their interaction in the detector and $P_{Th}$ is the power of the reactor R. By using the expected number of neutrinos in each energy bin as obtained above and the total background calculated earlier, the predicted number of signal and background events in each energy bin is given by

$$N_i^{\text{pred}} = \sum_{R=1,2}^{\text{Reactors}} N_i^{\nu,R} + \sum_b^{\text{Bkgnds.}} N_i^b. \tag{9.6}$$

Here $N_i^{\nu,R} = P_(\bar{\nu}_e \to \bar{\nu}_e) N_i^{\text{exp},R}$; $P_{\bar{\nu}_e \to \bar{\nu}_e}$ is the neutrino survival probability from the well-known oscillation formula and $N_i^{\text{exp},R}$ is given by Eq. (9.6). The index $b$ runs over the three backgrounds: cosmogenic isotope; correlated; and accidental. The index $R$ runs over the two reactors, Chooz B1 and B2. Table 9.1 lists all the predictions for the no-oscillation signal as well as for the backgrounds.

The systematic and statistical uncertainties, as shown in Table 9.2, are propagated to the

| | **Reactors Both On** | **One Reactor $P_{th} <$ 20%** | **Total** |
|---|---|---|---|
| Livetime [days] | 139.27 | 88.66 | 227.93 |
| IBD Candidates | 6088 | 2161 | 8249 |
| $\nu$ Reactor B1 | 2910.9 | 774.6 | 3685.5 |
| $\nu$ Reactor B2 | 3422.4 | 1331.7 | 4754.1 |
| Cosmogenic Isotope | 174.1 | 110.8 | 284.9 |
| Correlated FN & SM | 93.3 | 59.4 | 152.7 |
| Accidentals | 36.4 | 23.1 | 59.5 |
| Total Prediction | 6637.1 | 2299.7 | 8936.8 |

Table 9.1: Summary of observed IBD candidates and corresponding signal and background predictions.

final fit by using the covariance matrix $M_{ij}$ which takes care of the bin to bin correlations.

$$M_{ij} = M_{ij}^{\text{sig.}} + M_{ij}^{\text{det.}} + M_{ij}^{\text{stat.}} + M_{ij}^{\text{eff.}} + \sum_{b}^{\text{Bkgnds.}} M_{ij}^{\text{b}} \tag{9.7}$$

| **Source** | **Uncertainty [%]** |
|---|---|
| Reactor Flux | 1.67% |
| Detector Response | 0.32% |
| Statistics | 1.06% |
| Efficiency | 0.95% |
| Cosmogenic Isotope Background | 1.38% |
| FN/SM | 0.51% |
| Accidental Background | 0.01% |
| **Total** | 2.66% |

Table 9.2: Summary of signal and background normalization uncertainties relative to the total prediction.

A fit of the binned signal and background data to a two-neutrino oscillation hypothesis was performed by minimizing a standard $\chi^2$ function

$$
\begin{aligned}
\chi^2 &= \sum_{i,j}^{36} \left(N_i - N_i^{\text{pred}}\right) \\
&\times \left(M_{ij}\right)^{-1} \left(N_j - N_j^{\text{pred}}\right)^{\text{T}} \\
&\quad + \frac{\left(\epsilon_{FN/SM} - 1\right)^2}{\sigma^2_{FN/SM}} + \frac{\left(\epsilon_{^9\text{Li}} - 1\right)^2}{\sigma^2_{^9\text{Li}}} \\
&\quad + \frac{\left(\alpha_E - 1\right)^2}{\sigma^2_{\alpha_E}} + \frac{\left(\Delta m^2_{31} - \left(\Delta m^2_{31}\right)_{\text{MINOS}}\right)^2}{\sigma^2_{\text{MINOS}}}
\end{aligned}
\tag{9.8}
$$

The fit parameters $\epsilon_{FN/SM}$ and $\epsilon_{^9\text{Li}}$ are free parameters in the fit and they are used to scale the rates of the correlated and the $^9Li$ background respectively while the rate of accidentals is not allowed to vary as its initial uncertainty is precisely measured.

The best-fit gives $\sin^2 2\theta_{13} = 0.109 \pm 0.030$ (stat.) $\pm 0.025$ (syst) at $\Delta m^2_{31} = 2.32 \times 10^{-3}$ eV$^2$, with a $\chi^2$/NDF $= 42.1/35$. as show in Fig. 9.6. The allowed region at 68%(90%) CL is $0.067(0.043) < \sin^2 2\theta_{13} < 0.15(0.18)$.

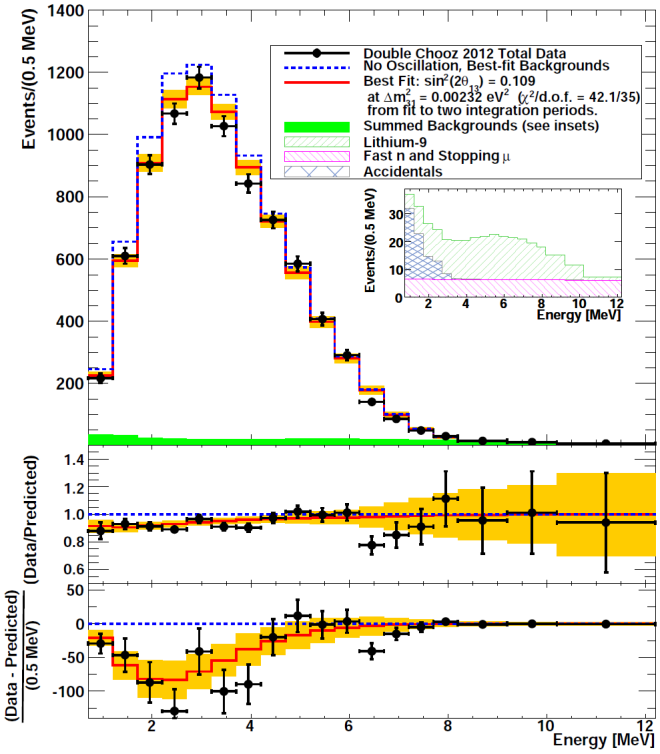


Figure 9.6: Measured prompt energy spectrum for both integration periods (data points) superimposed on the expected prompt energy spectrum, including backgrounds (green region), for the no-oscillation (blue dotted curve) and best-fit (red solid curve) at $\sin^2 2\theta_{13} = 0.109$ and $\Delta m^2_{31} = 2.32 \times 10^3 eV^2$. Inset: stacked spectra of backgrounds. Bottom: differences between data and no-oscillation prediction (data points), and differences between best fit prediction and no-oscillation prediction (red curve). The orange band represents the systematic uncertainties on the best-fit prediction.

An analysis comparing only the total observed number of IBD candidates in each integration period to the expectations produces a best-fit of $\sin^2 2\theta_{13} = 0.170 \pm 0.052$ at $\chi^2/NDF = 0.50/1$ as shown in Fig. 9.7. The compatibility probability for the rate-only and rate+shape measurements is about 30% depending on how the correlated errors are handled between the two measurements.

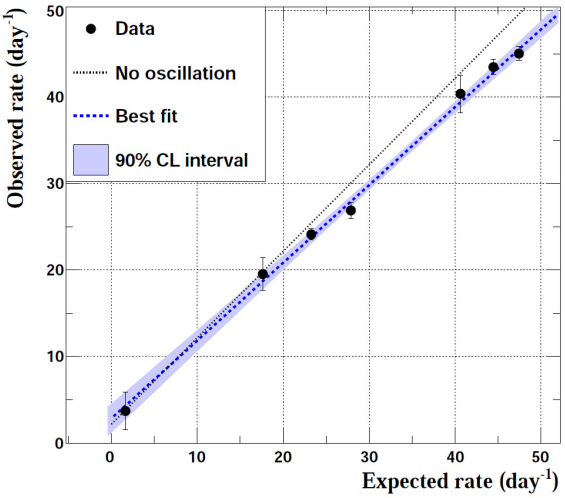


Figure 9.7: Daily number of ÂŕÎ¡e candidates as a function of the expected number of ÂŕÎ¡e. The dashed line shows the fit to the data, along with the 90% C.L. band. The dotted line shows the expectation in the no-oscillation scenario

### 9.4.1 Summary of Final Fit Analysis

Double Chooz has found evidence for a non-zero value of $\theta_{13}$ from the rate and energy spectrum of reactor neutrino candidates at a distance of 1050 m from two reactors. It is the first evidence for this parameter using the energy spectrum from reactor neutrinos, rather than simply their rate. We find a best fit value and 1ÏČ error to be $\sin^2 2\theta_{13} = 0.109 \pm 0.030$ (stat) $\pm$ 0.025 (syst). The data is inconsistent with the assumption that oscillations are absent with a CL of 99.9% ($3.1\sigma$). An analysis comparing only the total observed number of IBD candidates in each integration period to the expectations produces a best-fit of sin2 2Îÿ13 = 0.170Âś0.052 at An analysis comparing only the total observed number of IBD candidates in each integration period to the expectations produces a best-fit of $sin22\theta_{13} = 0.170 \pm 0.052$ at $\chi^2/NDF = 0.50/1$, see Fig. 9.7 .

### 9.4.2 Effect of Uncertainty in Central Value of Correlated Background on the Systematic Uncertainty on $\theta_{13}$

The results presented in Chapter 8 are consistent with the central value of the correlated background used for the final $\theta_{13}$ oscillation fit. A preliminay investigation of the effect of the uncertainty in the central value of the correlated background on the systematic uncertainty budget for $\theta_{13}$ shows that the effect is within $\pm 0.4\%$ and hence is very small.

# Chapter 10

# Rate-Only Analysis to Compute $\theta_{13}$ and the Overall Background

Double Chooz was the first among the reactor anti-neutrino experiments to publish its results. In fact there have been two separate publications by the Double Chooz collaboration [28] and [29] as presented in chapter 9. Both of those results were the results of an analysis that takes into consideration the rates as well as the spectral shapes of the neutrino candidates as well as the various background sources. The second publication also presented the result of an analysis using the rates as observed from data and that expected in the no-oscillation scenario. In this chapter we present result of an analysis based on comparing the daily observed rates of the neutrino candidates as well as the expected rates from Monte Carlo simulation to the expected rates according to the reactor power variations, assuming no oscillation. The analysis follows closely the technique used in [39]. The neutrino candidates for the analysis were selected using cuts for reducing the $^9Li$ candidates and the OV anti-coincidence of the prompt candidates in addition to the standard cuts explained in Chapter 5. The expectations for the neutrino candidate events from each reactor core of the Chooz reactor in each data taking run were provided for the Double Chooz detector in [53] and are shown in Fig. 10.1. These indicate the neutrino interaction rates inside the detector assuming no oscillation. The runwise expected number of neutrinos from each reactor core namely "B1" and "B2" were added together to get the total expected rate.

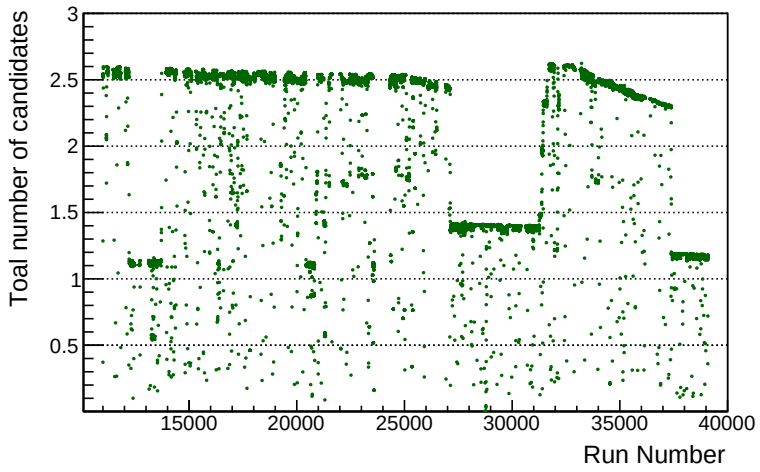


Figure 10.1: Predicted rate of neutrinos in each run assuming no oscillation.

The runwise expected number of neutrinos then added together for the total number of runs for each day to get the daily number of neutrino candidates as expected from the reactor condition. These are shown in Fig. 10.2.

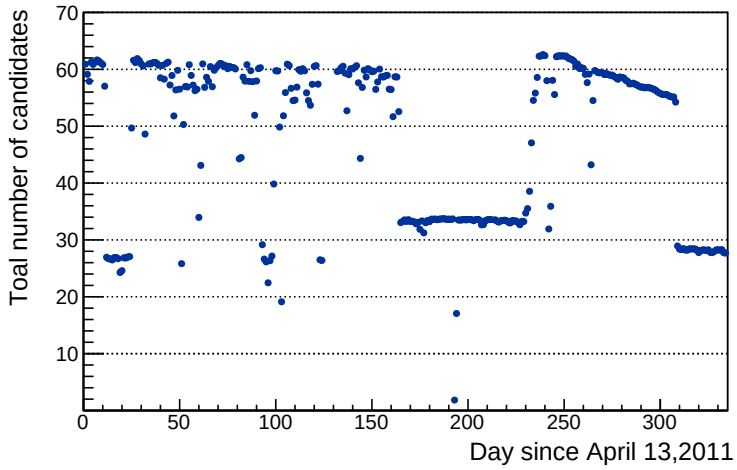


Figure 10.2: Predicted rate of neutrinos in each day assuming no oscillation.

The distribution of the daily rates of the expected neutrino interaction rates are in the following Fig. 10.3

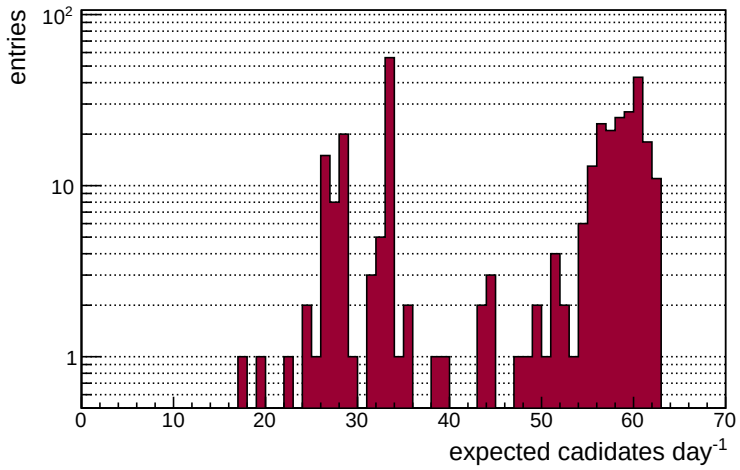


Figure 10.3: Distribution of expected neutrino (no oscillation) daily rates (day$^{-1}$)

With the total number of neutrinos per day as shown in Fig. 10.2, the days were then grouped according to the daily neutrino rates as: $(0-10)\text{day}^{-1}$, $(10-20)\text{day}^{-1}$, $(20-30)\text{day}^{-1}$, $(30-40)\text{day}^{-1}$, $(40-50)\text{day}^{-1}$, $(50-60)\text{day}^{-1}$ and $(60-70)\text{day}^{-1}$ of no oscillation bins.

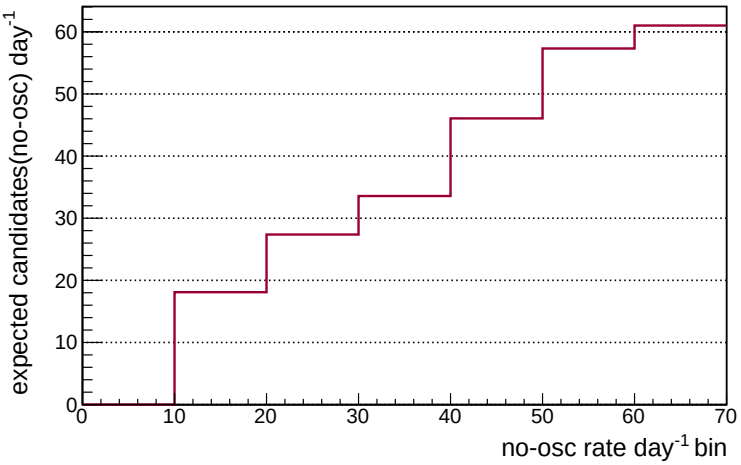


Figure 10.4: Binned expected neutrino daily rates (no oscillation).

Fig. 10.4 shows the histograms of the expected daily neutrino rates, under the no oscillation hypothesis, binned according to the grouping described above. Fig. 5.4 of Chapter 5, can be plotted against the daily rates of Monte Carlo events representing the expected signal for the duration of physics data-taking, based on the formalism of Eq. (9.5), as shown in Fig. 10.5 below.

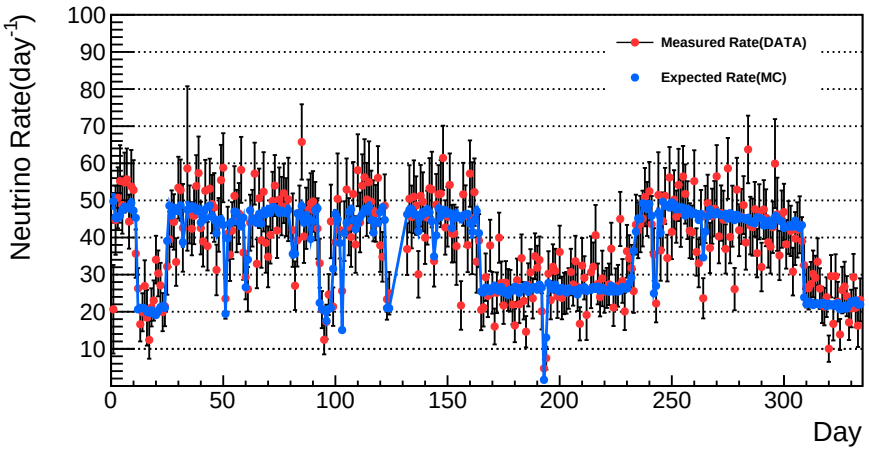


Figure 10.5: Neutrino daily rates: Observed in Red and expected MC(no oscillation) in Blue.

Organizing the expected MC (no oscillation) and the observed daily rates in the same groups as the reactor predicted rates, we get the plots shown in Fig. 10.6 and Fig. 10.7.

In this analysis technique, we can compare: (1) The observed rates from data to the expected interaction rates and (2) The expected interaction rate of neutrinos to their expected MC rate after applying the selection cuts. .

## 10.1 Comparison of Observed Data to Predicted Rates

Direct comparison between the observed daily rates of the neutrino candidates with the rates of their interactions in the detector represents the combined effects of neutrino oscillation and the detection efficiency. It is possible to disentangle the two effects by the use of the

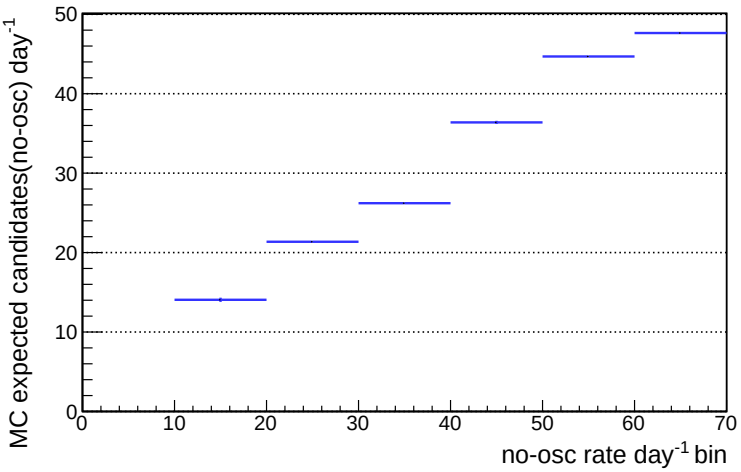


Figure 10.6: Binned expected neutrino daily rates from MC (no oscillation). The error bars are statistical and are almost too small to be seen.

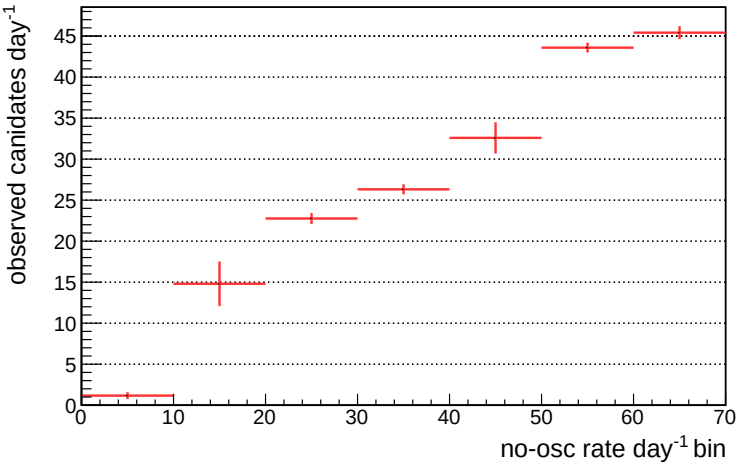


Figure 10.7: Binned observed neutrino daily rates (no oscillation).

corrected cut efficiencies listed in Table 10.1. The errors shown are purely statistical in nature, leaving the systematics to be treated separately. In Fig. 10.8 the blue dashed-line shows the no oscillation scenario.

Table 10.1 shows the neccessary inputs needed to calculate the total detection efficiency for the experiment by taking the product of the efficiencies of the individual cuts.

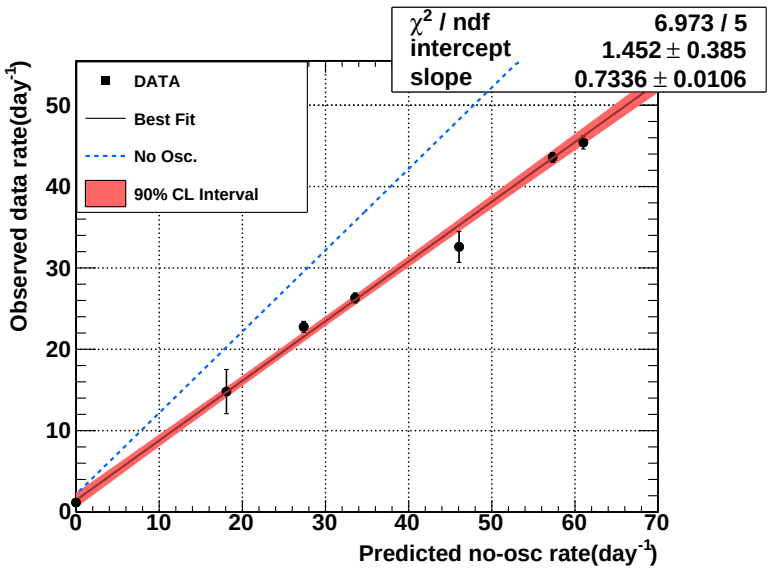


Figure 10.8: Observed neutrino daily rates vs the predicted rates

| Source(Cut) | Efficiency (Data) | Efficiency (MC) | Uncertainty(Syst) | MC Correction Factor |
|---|---|---|---|---|
| Reactor | – | – | 1.8% | – |
| Target H-atoms | – | – | 0.3% | – |
| Spill in/out | 1.01347 | – | 0.3% | 1.00 |
| Gd/(H+Gd) | 0.86 | 0.87 | 0.3% | 0.985 ± 0.3% |
| Δ T Cut | 0.962 | – | 0.5% | 1.00 |
| $E_{delayed}$ | 0.941 | – | 0.6% | 1.00 |
| Total | 0.789 | – | 0.0165 | 0.985 |
| Total(corrected) | 0.7772 | – | 0.0165 | 0.985 |

Table 10.1: Cut efficiencies for Double Chooz

Table 10.1 shows the calculation of the corrected efficiency for the selection cuts. The corrections for the livetime of the runs have already been considered while calculating the candidate rates. It also shows that the absolute efficiency is overestimated by just over the uncertainty range of the corrected efficiency.

### 10.1.1 Calculation of $\theta_{13}$ from observed data vs predicted rates

Dividing the slope of the fit in Fig. 10.8 by the corrected efficiency we can get the fraction of neutrinos that survive,

$$\Delta N_{\text{surviv}} = \frac{0.7336 \pm 0.0106}{0.7772 \pm 0.0165} = 0.944 \pm 0.011(\text{stat.}) \pm 0.016(\text{syst.}). \tag{10.1}$$

The corresponding fraction of neutrinos thus disappeared is D = 0.0561±0.0106(stat.)±0.0165(syst.)

In the equation for the survival probability in 2-flavor oscillation;

$$P_{\nu_\alpha \to \nu_\alpha} = 1 - \sin^2\theta \sin^2\left(1.27\Delta m^2 \frac{L(m)}{E(MeV)}\right) \tag{10.2}$$

The disppearance coefficient $\sin^2\left(1.27\Delta m^2 \frac{L(m)}{E(MeV)}\right)$ can be computed by considering the two integration period (IP) scenario for the Double Chooz final fit in which if the minimum power of either reactor is below 20% of reach during a particular detector run, then that detector run is placed in "IP1", else, the detector run is placed in "IP0".

For the atmospheric neutrino mass splitting given by $\Delta m^2 = 2.32^{+0.12}_{-0.08} \times 10^{-3}$ eV$^2$ [32], the correctly weighted disappearance coefficient comes out to be:

$$\alpha_{\text{disapp}} = 0.5037^{+0.0353}_{-0.0241} \tag{10.3}$$

The corresponding value of $\sin^2 2\theta_{13}$ is given by

$$\sin^2 2\theta_{13} = \frac{0.0561 \pm 0.0106 \pm 0.0165}{0.5037^{+0.0353}_{-0.0241}} = 0.111 \pm 0.028(\text{stat.}) \pm 0.040(\text{syst.}). \tag{10.4}$$

Eq. (10.4) gives an estimate of $\sin^2 2\theta_{13}$ based upon the absolute value of the cut efficiencies otained from table 10.1. The following section will show the estimation of $\sin^2 2\theta_{13}$ based

upon the corrected efficiency numbers by comparing the MC to the numerically predicted no-oscillation rates.

## 10.2 Comparison of Monte Carlo to Predicted Rates

Observed neutrino candidate rates from the data were compared to the rates expected from the reactor predictions assuming no oscillation. Comparing the two rates can provide a cross-check on the absolute efficiency estimate as well as an alternative way of calculating the survival probability of the neutrino candidates and, subsequently, the value of $\theta_{13}$. The result of the comparison is shown in the Fig 10.9 below.

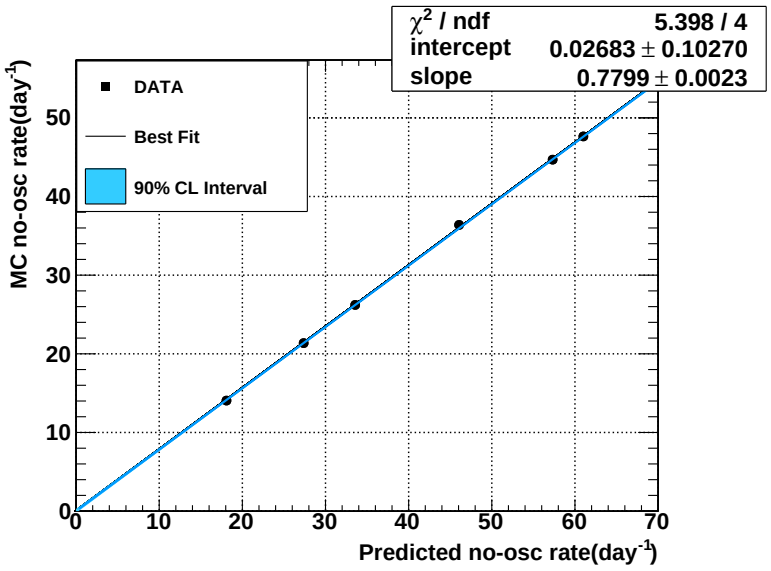


Figure 10.9: Neutrino daily rates from MC (no oscillation) vs the expected interaction rate.

The Monte Carlo candidates were selected from generated events with a factor of 100 and consequently the statistical errors reduced by a factor of 10. The MC candidates thus selected were then normalized to the live time of each day. The comparison of the expected daily rates from the Monte Carlo and the predicted daily rates from the interaction rates in the detector, gives an estimate of the absolute efficiencies of the cuts used to select the neutrino events from the neutrino interactions taking place in the detector. The scale factors

for the MC candidates and the statistical errors have already been taken care of. In fact the slope of Fig. 10.9 directly represents the overall MC candidate selection efficiency, before applying the MC correction factors, and it will be used later to determine the disppearance fraction of the neutrinos.

### 10.2.1 Calculation of $\theta_{13}$ from MC vs predicted rates

From Fig. 10.9, the MC selection efficiency comes out to be $0.7799 \pm 0.0023$. After applying the MC correction factor from table 10.1, we get a corrected selection efficiency computed directly by comparing the MC vs predicted neutrino rates, as $0.7682 \pm 0.0128$. By dividing the slope of the fit in Fig. 10.9, we get the fraction of neutrinos surviving as:

$$\Delta N_{\text{surviv}} = \frac{0.7336 \pm 0.0106}{0.7682 \pm 0.0128} = 0.955 \pm 0.011(\text{stat.}) \pm 0.013(\text{syst.}). \tag{10.5}$$

Following the same procidure as above, the value of $\sin^2 2\theta_{13}$ is

$$\sin^2 2\theta_{13} = \frac{0.045 \pm 0.011 \pm 0.013}{0.5037^{+0.0353}_{-0.0241}} = 0.089 \pm 0.028(\text{stat.}) \pm 0.032(\text{syst.}). \tag{10.6}$$

This value of $\sin^2 2\theta_{13}$ is consistent with those published in the second publication of the Double Chooz collaboration [29] as well as those of another analysis performed by comparing the observed and expected rates in [59]. Also the $y$-intercept Fig. 10.8 gives an estimate of an overall background rate for the Double Chooz experiment of $1.45 \pm 0.4\text{day}^{-1}$, which is consistent with those in the Double Chooz publications [27] and [59].

#### Uncertainty due to anti-neutrinos during the one or both reactor off periods

Even after the actual turn-off of a reactor, the nuclear fission reactions continue to take place for a while, releasing some residual anti-neutrinos in the process. Simulation studies were performed in [10] and [11] using the FISPACT evolution code and BESTIOLE $\beta$-decay library to estimate the expected number of anti-neutrinos during the periods when either one or both the reactors were off . The number of residual anti-neutrinos predicted during

the total reactor off-off period is $2.01 \pm 0.80$ in [11]. After correcting for livetime and the selection efficiency in Table 10.1, the number of residual neutrinos that are expected to be detected is $1.42 \pm 0.57$. Similarly the number of anti-neutrinos for the period when either reactor B1 or B2 was off, was calculated to be $9.3 \pm 2.8$ and $9.7 \pm 2.9$ respectively, [10]. A corrected number for the neutrinos expected to be detected were predicted in [59] as $5.5 \pm 1.65$ and $5.7 \pm 1.71$ for B1 and B2 respectively during the one reactor-off periods. Because of the number of residual anti-neutrios during the single reactor off periods are very small in comparison to that during the reactor-on period, this analysis ignores these anti-neutrinos for the calculation of $\sin^2\theta_{13}$. Instead they are treated as another source of systematic uncertainty. This is achieved by repeating the analysis by adding the residual neutrinos from 1 reactor-off data in the bins with rates of $20-30$ neutrinos day$^{-1}$ and $30-40$ neutrinos day$^{-1}$ because those are the two bins with the most number of days when either of the two reactors were off. The 2 reactor-off data was added to the first bin of $0-10$ neutrinos day$^{-}1$. The results with these additional systematics are

$$\sin^2 2\theta_{13} = 0.111 \pm 0.028(\text{stat.}) \pm 0.023(\text{syst.}), \tag{10.7}$$

for the comparison of observed vs. predicted candidates and

$$\sin^2 2\theta_{13} = 0.089 \pm 0.029(\text{stat.}) \pm 0.017(\text{syst.}). \tag{10.8}$$

comparing the MC vs predicted candidates. Similarly the overall background rate was $1.4 \pm 0.4\text{day}^{-1}$.

## 10.3 Summary

In this chapter, I have presented a technique to estimate the value of $\sin^2 2\theta_{13}$ as well as the overall background rate for the Double Chooz experiment based purely upon the daily rates of the neutrino candidates as: (1) Observed from the data, (2) Expected from the Monte

Carlo (nooscilllation) and (3) Expected according to the interaction rates in the detector (no oscllation). The results are in good agreement with the those previously published by the Double Chooz collaboration and presented in Chapter 9.

# Chapter 11

# Conclusions

Double Chooz was the first among a host of worldwide experimental efforts to measure the value of the neutrino mixing angle $\theta_{13}$. It achieved this goal by using only one detector, the far detector, and with possibly the shortest baseline among all the ractor neutrino experiments. The Double Chooz result of $\sin^2 2\theta_{13} = 0.109 \pm 0.030$ (stat) $\pm$ 0.025 (syst) [29] proved the mixing angle $\theta_{13}$ to be non-zero at 99.9% CL ($3.1\sigma$). Curently the near detector for the experiment is under construction and a combined result with both the detectors should appear by the end of the year 2014. The sensitivity on the measurement of $\theta_{13}$, after 5 years of data taking with the far detector and 3 years of running with both the far and the near detector, will much improved. Double Chooz has also used the data with delayed neutron captures in hydrogen to measure $\sin^2 2\theta_{13} = 0.097 \pm 0.034$ (stat) $\pm$ 0.034 (syst) [30]. With the ability to use neutron captures on gadolinum as well as on hydrogen, for the delayed coincidences in IBD candidate selection, an even more precise measurement of $\theta_{13}$ is with Double Chooz is just round the corner.

# Bibliography


[1] S. M. Bilenki. "Introduction to the Physics of Massive and Mixed Neutrinos". 2010.

[2] A. Blondel. "Future Neutrino Oscillations Facilities: Physics Priorities and Open Issues.". *Nucl.Phys.Proc.Suppl.*, 155:131–142., 2006.

[3] Rene Brun and Fons Rademakers. "ROOT: An Object Oriented Data Analysis Framework". *Proceedings AIHENP'96 Workshop*, 1996.

[4] J. Busenitz. "Measuring the Neutron Detection Efficiency with a Cf-252 Source". *Double Chooz internal note*, DC-doc 3097-v2.

[5] Pi-Jung Chang, Tomoyuki Konno, Igor Ostrovskiy, Alberto Remoto, Deepak Shrestha, Marc Bergevin, Jerrgy Busenitz, and Zelimir Djurcic. "Neutrino Efficiency Analysis Results.". *Double Chooz internal note*, DC-doc-3364-v3.

[6] C. Palomares (CIEMAT). "Study of a New Photomultiplier Distribution in the Double Chooz Experiment". *Double Chooz internal note*, 2007.

[7] E. Calvo (Ciemat). "PMT Support Status.". *Double Chooz internal note*, DC-doc-15-v1.

[8] Mainz Collaboration. "Final Results from Phase II of the Mainz Neutrino Mass Search in Tritium $\beta$ Decay". *arXiv:hep-ex/0412056*, 2004.

[9] T2K Collaboration. "About T2K". www.t2k-experiment.org.

[10] Antoine Collin and Alain Letourneau. "Expected Antineutrino Interactions Refueling Phase for for B1 core.". *Double Chooz internal note*, DC-doc-4125-v3.

[11] Antoine Collin, Alain Letourneau, and David Lhuillier. "Expected Antineutrino Interactions during Reactor Off-Off Period.". *Double Chooz internal note*, DC-doc-4125-v3.

[12] Herve de Kerret. "Results from Double Chooz". *Double Chooz internal note*, DC-doc-4292-v1.

[13] Dennis Dietrich, Lisa Goodenough, Anselmo Meregaglia, Deepak Shrestha, Alessandra Tonazzo, and Michel Wurm. "Off-Off Background Scaling Technote.". *Double Chooz internal note*, DC-doc-4163-v26.

[14] A.D. Dolgov. "Cosmology and Neutrino Properties". *arXiv:0803.3887 [hep-ph]*.

[15] B. Aharmim et al. "Low Energy Threshold Analysis of the Phase I and Phase II Data Sets of the Sudbury Neutrino Observatory". *arXiv:0910.2984 [nucl-ex]*.

[16] D.L. Bluel et al. "Gamma-Ray Multiplicity Measurement of the Spontaneous Fission Decay of 252Cf in a Segmented HPGe/BGO Detector Array". https://e-reports-ext.llnl.gov/pdf/360428.pdf, 2009.

[17] E. Calabrese et al. "Impact of "$h_0$" Prior on the Evidence for Dark Radiation". *Phys. Rev. D*, 86, 043520, 2012.

[18] E. F. Bugaev et al. "Atmospheric Muon Flux at Sea Level, Underground, and Underwater". *Phys. Rev. D*, 58, 054001.

[19] F. Boehm et al. "Final Results from the Palo Verde Neutrino Oscillation Experiment". *Phys.Rev.D*, 64, 2001.

[20] G. Hinshaw et al. "Nine-Year Wilkinson Microwave Anisotropy Probe(WMAP) Observations: Cosmological Parameter Results". *arXiv:1212.5226 [astro-ph.CO]*, 2012.

[21] J. F. Wang et al. "Predicting Neutron Production from Cosmic-Ray Muons.". *Phys. Rev. D*, 64, 013012.

[22] K. N. Abajazian et al. "Light Sterile Neutrinos: A White Paper". *arXiv:1204.5379 [hep-ph]*, 2012.

[23] M. Apollonio et al. "Search for Neutrino Oscillations on a Long Base-Line at the CHOOZ Nuclear Power Station". *Eur. Phys. J. C*, 27:331âĂŞ374, 2003.

[24] Pau Novella et al. "DCRecoPulse". *Double Chooz internal note*, DC-doc-649-v2.

[25] T. A. Mueller et al. "Improved Predictions of Reactor Antineutrino Spectra". *Phys.Rev.C*, 83:054615.

[26] T. Hagner et al. "Muon-Induced Production of Radioactive Isotopes in Scintillation Detectors.". *Astropart. Phys.*, 14:33–47, 2000.

[27] Y. Abe et al. Direct measurement of backgrounds using reactor-off data in double chooz. *Phys. Rev. D*, 87,011102.

[28] Y. Abe et al. "Indication for the Disappearance of Reactor $\bar{\nu}_e$ in The Double Chooz Experiment.". *Physical Review Letters*, 108, 131801, 2012.

[29] Y. Abe et al. "Reactor $\bar{\nu}_e$ Disappearance in The Double Chooz Experiment.". *Phys. Rev. D*, 86, 052008., 2012.

[30] Y. Abe et al. "First Measurement of $\theta_{13}$ from Delayed Neutron Capture on Hydrogen in the Double Chooz Experiment.". *Phys Lett B*, 723, 66-70., 2013.

[31] Y. Declais et al. "Study of Reactor Antineutrino Interaction with Proton at Bugey Nuclear Power Plant.". *Phys. Lett. B*, 338:383–389, 1994.

[32] P. Adamson et al. (MINOS Collaboration). "Measurement of the Neutrino Mass Splitting and Flavor Mixing by Minos". *Phys. Rev. Lett.*, 106, 181801, 2011.

[33] D. Ferreira and R. Pinto. "Gamow's Theory of Alpha Decay". https://dspace.ist.utl.pt/bitstream/2295/931523/1/Ex8Serie1.

[34] R. A. Forrest. "FISPACT-2007: User Manual, UKAEA-FUS-534". www.ccfe.ac.uk/.

[35] J. Frehaut. "Neutron Gamma Competetion in Fast Fission". *Physics of Neutron Emission in Fission. Proceedings of an IAEA Consultants' Meeting*, 1988.

[36] F.H. Fröhner. "Evaluation of $^{252}$Cf Prompt Fission Neutron Data from 0 to 20 Mev by Watt Spectrum Fit". *Nucl. Sci. Eng.*, 106:345, 1990.

[37] C. Giunti and M. Laveder. "Statistical Signifcance of the Gallium Anomaly". *Phys. Rev. C*, 83,065504, 2011.

[38] N.E. Holden and M.S. Zucker. "Neutron Multiplicities for the Transplutonium Nuclides. https://www.osti.gov/bridge/servlets/purl/5713065-Y1sT3k/5713065.pdf.

[39] G. Horton-Smith. "An Analysis of Observed Rate vs Predicted Rate.". *Double Chooz internal note*, DC-doc-3341-v1.

[40] Glenn Horton-Smith. "lytest.mac". *Double Chooz Offline Group Software (DOGS).*

[41] Glenn Horton-Smith. "plotspectra.c". *Double Chooz Offline Group Software (DOGS).*

[42] Glenn Horton-Smith. "supervis.mac". *Double Chooz Offline Group Software (DOGS).*

[43] Glenn Horton-Smith. "Photo of Double Chooz inner detector before placement of lid on buffer tank, credit CEA-Saclay / IRFU - SIS". http://neutrino.phys.ksu.edu/~dchooz/photos/, 2010.

[44] P. Huber. "On the Determination of Anti-Neutrino Spectra from Nuclear Reactors". *Phys.Rev.C*, 84:024617.

[45] J. R. Huizenga. "Nuclear Fission Revisited". *Science*, 168:1405âĂŞ1413, 1979.

[46] C. Jarlskog. "Commutator of the Quark Mass Matrices in the Standard Electroweak Model and a Measure of Maximal CP Nonconservation". *Phys. Rev. Lett.*, 55:1039âĂŞ1042, 1985.

[47] C. Jollet and A. Meregaglia(IPHC-Strasbourg). "Neutron Simulation BG Evaluation". *Double Chooz internal note,*, DC-doc-861-v1.

[48] C. L. Jones, A. Bernstein, J. M. Conrad, Z. Djurcic, M. Fallot, L. Giot, G. Keefer, A. Onillon, and L. Winslow. "Reactor Simulation for Antineutrino Experiments Using DRAGON and MURE". *arXiv:1109.5379v1.*

[49] G.S. Brunson Jr. *"Multiplicity and Correlated Energy of Gamma Rays Emitted in the Spontaneous Fission of Californium-252"*. PhD thesis, University of Utah, USA, 1982.

[50] B. Kayser. "Neutrino Physics". *SLAC Summer Institute on Particle Physics (SSI04)*, 2000.

[51] T. Konno and Pi-Jung Chang. "Delayed Energy Containment for the 2nd publication.". *Double Chooz internal note*, DC-doc-3835-v3.

[52] Thierry Lasserre. "Testing the Reactor and Gallium Anomalies with Intense $\bar{\nu}_e$ Emitters". *Neutrino 2012*, 2012.

[53] D. Lhuillier. "Prediction of Run by Run $\nu$-Rates for the 2nd Pub.". *Double Chooz internal note*, DC-doc-3878-v2.

[54] W. Loveland. "Alpha Decay". www.oregonstate.edu/instruct/ch374/ch418518.

[55] F.C. Maienschein, R.W. Peelle, and T.A. Love. "Neutron Phys. Ann. Prog. Rep. for Sept. 1, 1958".

[56] W. Mannhart. "Status of the Cf-252 Fission Neutron Spectrum Evaluation with Regard to Recent Experiments". *Physics of Neutron Emission in Fission. Proceedings of an IAEA Consultants' Meeting*, 1988.

[57] G. Mention, M. Fechner, Th. Lasserre, Th. A. Mueller, D. Lhuillier, M. Cribier, and A. Letourneau. "The Reactor Neutrino Anomaly". *Phys. Rev. D*, 83, 073006, 2011.

[58] H. Nifenecker. "Neutron and Gamma Emission in Fission". *A Review.*

[59] Pau Novella. "Rate Only $\theta_{13}$ Analysis.". *Double Chooz internal note*, DC-doc-4593.

[60] U.S. Department of Energy. "DOE Fundamentals Hanbook Nuclear Physics And Reactor Theory Volume 1 of 2". www.hss.doe.gov/nuclearsafety/techstds/docs/handbook/h1019v1.pdf.

[61] I. Ostrovskiy. *"Measuring The Neutrino Mixing Angle $\theta_{13}$ With The Double Chooz Detector"*. PhD thesis, University of Utah, USA, 2011.

[62] E. W. Otten. "The Q-Value of the $\beta$-Decay and the Neutrino Mass". *International Journal of Mass Spectrometry*, 2006.

[63] Chris Polly. "Updated Oscillation Results from Miniboone". *Neutrino 2012*, 2012.

[64] J. Reichenbacher. "Calculation of the Underground Muon Intensity Crouch Curve from a Parameterization of the Flux at Surface.". *arXiv:0706.1110.*

[65] T. Schwetz, M. Tortola, and J. W. F. Valle. "Where we are on $\theta_{13}$: Addendum to Global Neutrino Data and Recent Reactor Fluxes: Status of Three-Flavour Parameters". *arXiv:1108.1376 [hep-ph]*, 2011.

[66] Alfred Tang, Glenn Horton-Smith, Vitally A. Kudryavtsev, and Alessandra Tonazzo. "Muon Simulations for Super-Kamiokande, KamLAND and CHOOZ". *Phys.Rev.D*, 74:053007.

[67] M. Tanimoto. "Search for CP Violation with a Neutrino Factory". *arXiv:hep-ph/9906516*, 1999.

[68] M. Thomson. "Particle Physics". www.hep.phy.cam.ac.uk/~thomson/lectures/partIIIparticles/Handout11_2009.pdf.

[69] T.E. Valentine. "Evaluation of Prompt Fission Gamma Rays for the Use in Simulating Nuclear Safeguard Measurements". http://hcpl.knu.ac.kr/neutrino/renosim/252Cf/252cf_code/ref/252cf_gam_mult_2.pdf, 1999.

[70] J. M. Verbeke. "Simulation of Neutron and Gamma Ray Emission from Fission and Photofission". http://nuclear.llnl.gov/simulation/fission.pdf.

[71] Matt Worchester. "DCdetector3d.". *Double Chooz internal note*, DC-doc-1041-v1.

[72] Matt Worchester. "DCsite2009.". *Double Chooz internal note*, DC-doc-1037-v1.